SCANNING TUNNELING MICROSCOPY STUDIES OF FLUORINATED GRAPHENE FILMS AND FIELD-DIRECTED SPUTTER SHARPENING

BY

SCOTT W. SCHMUCKER

DISSERTATION

Submitted in partial fulfillment of the requirements
for the degree of Doctor of Philosophy in Electrical and Computer Engineering
in the Graduate College of the
University of Illinois at Urbana-Champaign, 2012

Urbana, Illinois

Doctoral Committee:

Professor Joseph W. Lyding, Chair
Professor John R. Abelson
Professor James J. Coleman
Assistant Professor Eric Pop

ABSTRACT

Graphene fluoride is a two-dimensional fluorocarbon, and the wide-gap analogue of graphene. Among chemical derivatives of graphene, graphene fluoride is unique in its ease of synthesis and stability, as well as the extensive study of its bulk form, graphite fluoride. Only in the last few years, however, has graphene fluoride been isolated experimentally, and our understanding of its atomic and electronic structure, stability, reduction, and use as a platform for lithographic patterning is still limited. In this dissertation, an ultra-high vacuum scanning tunneling microscope (UHV-STM) is employed for the characterization of exfoliated double-sided graphene fluoride (ds-GF) and of single-sided graphene fluoride (ss-GF) on Cu foil. We explore the structure and stability of each material and, in particular, identify ss-GF as a stable, well-ordered, wide-gap semiconductor. This dissertation offers the first atomic-resolution study of this novel material, and the first UHV-STM measurement of its electronic structure.

Furthermore, we develop the novel field-directed sputter sharpening (FDSS) technique for producing sharp metal probes with 1 – 5 nm radii of curvature, a prerequisite for high-resolution scanning tunneling microscopy (STM) imaging and nanolithography. We show that FDSS offers significant improvements in lithographic patterning, and is applicable to a range of materials, including the hard metallic-ceramic hafnium diboride (HfB_2). Finally, we explore the use of HfB_2-coated W wires for STM imaging and spectroscopy.

ACKNOWLEDGEMENTS

My tenure at the University of Illinois has been formative, in large part due to the uniquely inspiring atmosphere cultivated by Professor Joseph Lyding. I thank Joe for his guidance and insight, but also for the freedom he has given me to work creatively and collaboratively and to take an active role in choosing and developing my research program. It remains a joy to work with Joe and to develop as a researcher both through individual perseverance and from Joe's extensive experience and keen insight.

My days in the Illinois STM group might have proven unproductive without the camaraderie and support of my fellow sojourners. Among these, I would first thank those students and researchers who assisted directly with the completion of this dissertation. My work on field-directed sputter sharpening was enabled through collaboration with Navneet Kumar, Scott Daly, Aditya Gupta, Daniel Lukman, and Eric Lee. Navneet provided his expertise and time to deposit thin films of HfB_2 onto tungsten STM tips under the guidance of Professor John Abelson. Scott was the adept chemist who synthesized the $Hf(BH_4)_4$ precursor molecules in the lab of Professor Greg Girolami. Aditya and Daniel both worked in the Lyding STM Lab as undergraduate student researchers, and Eric Lee completed his M.S. degree while studying plasma-based sputter sharpening of STM tips. Studies of fluorinated graphene in all its forms were made possible only with the assistance of Josh Wood, Yang Liu, Dr. Chad Junkermeier, and Dr. Rick Haasch. Yang and Professor T.-C. Chiang's expertise in angle-resolved photoelectron spectroscopy, and willingness to contribute of their valuable beam time are appreciated, and added greatly to the impact of my studies. I was thrilled to meet Chad at the APS March meeting in 2011 where I learned of his theoretical treatment of fluorinated graphene. His computational support of this dissertation has been extremely valuable and provided a substantial theoretical basis for my understanding of single-sided graphene fluoride. Rick's expertise in X-ray photoelectron spectroscopy was invaluable for characterizing samples, and his assistance with data analysis and tolerance of my wandering into his lab with questions or new samples is appreciated. Additionally, I am indebted to Dr. Matt Sztelle for his guidance in the mysterious ways of UHV systems and lab operations, as well as his pasta sauce and many games of racquetball. Dr. Laura Ruppalt offered her valuable knowledge of the "Chamber A" system and trained me on its use. Kevin He helped to maintain Chamber A, and it has been a pleasure to converse with him on subjects ranging from electron tunneling and general relativity to monetary policy and chess. Josh Wood has been a valued colleague not only for his involvement in my studies of graphene fluoride and his expertise in graphene CVD and Raman spectroscopy, but also his passion for knowledge and hard work. I also thank Lea Neinhaus for her assistance in reading and understanding the early studies of fluorinated graphene, published in German. No member of the Lyding STM Lab has left without imparting useful knowledge to me, and I thank all current and former lab members for their contributions to my development: Dr. Peter Albrecht, Dr. Josh Ballard, Dr. Erin Carmichael, Dr. Kyle Ritter, Dr. Greg Scott, Sumit Ashketar, Yaofeng Chen, Jae Won Do, Kyong Hee Joo, Justin Koepke, Ximeng Liu, Pam Martin, Marie Mayer, Vineet Nazareth, Peter Ong, Adrian Radocea, Alan Rudwick, Aditya Vaidya, Bryan Walker, Wei Ye, and Fan Zhang.

Several other members of the Illinois community played integral roles in the success of my research program. Specifically, Scott Robinson and Cate Wallace have repeatedly contributed their expertise and enthusiasm for the transmission electron microscopy system employed in this dissertation. The Imaging Technology Group of the Beckman Institute at the University of Illinois maintains an excellent microscopy facility which has proven invaluable in the completion of my research. I have counted continually on the assistance and guidance of staff members in the Frederick Seitz Materials Research Laboratory throughout the course of my research, including Jim Mabon, Bharat Sankaran, Mike Marshall, and Tony Banks. Also, the expert machining skills of Craig Zeilenga and Scott MacDonald have been poured into much of the equipment of the Lyding lab. Our group secretary, Kelly Young, and storeroom manager, Suzie Rook, of the Beckman Institute have contributed continually to the successful operation of the laboratory.

I was privileged to spend several years as a teaching assistant in the ECE 444 undergraduate integrated circuit laboratory. I thank the lab director Professor Jim Coleman and lab engineer Dane Sievers for their work in making this course available to students at the University of Illinois, and in particular Dane for his insight into the maintenance and operation of the clean room laboratory and integrated equipment. I hope that I can bring some of his insights and inspirations with me into my career.

Additionally, I acknowledge the members of the Fermi Pinning bowling team, Josh Wood, Justin Koepke, Albert Liao, and Joe Lyding. Competing in the annual ECE Strike bowling tournament offered a welcome respite from the drudgeries of graduate school.

For all of their help to those of us seeking knowledge, I thank the staff of the University of Illinois library system, especially those who like to read the acknowledgements in the new theses. Yes, I mean you.

This dissertation would not have been possible without financial support, and I gratefully acknowledge the assistance of a National Defense Science and Engineering Graduate Fellowship from the Air Force Office of Scientific Research (2004 – 2007), and the National Science Foundation Graduate Research Fellowship (2007 – 2009). This research was further funded by

the Office of Naval Research under grant number N000140610120 and the Defense Advanced Research Project Agency and Space and Naval Warfare Center, San Diego under contract N66001-08-C-2040.

I thank my parents, my sister April, my beloved daughter Lydia, and my family and friends for their love and support in this and in all things. Finally, I thank my wife Christine. As my life and burdens are shared with her, so too is this dissertation, as are all my works.

TABLE OF CONTENTS

CHAPTER 1
INTRODUCTION

1.1 Motivation

Since its mainstream introduction,[1] graphene has become the focus of an extensive collection of experimental and theoretical studies. The benefits of graphene are many[2–4] and the limitations few, but one fundamental property which limits the widespread introduction of graphene electronic devices is the absence of an electronic band gap. Among the solutions offered to this problem are quantum-confined graphene ribbons,[5] Bernal stacked bilayer graphene,[6] and aligned graphene films on lattice-matched insulating substrates, such as boron nitride.[7] However, each of these techniques brings its own array of limitations and experimental challenges, and none have established dominance in the field. Another option is the introduction of a band gap in graphenic materials by chemical functionalization. Stoichiometric hydrogenated graphene films, termed graphane, have been both theorized[8] and experimentally realized.[9] Electron-stimulated desorption of hydrogen from graphane[10] could enable the fabrication of graphene structures confined in a graphane barrier.[11,12] However, the adsorption of small hydrogen clusters on graphene is thermodynamically unfavorable,[13] and it has been suggested that many forms of graphane are inherently unstable.[14] As probable evidence of this property, experimentally realized graphane films exhibit significantly lower resistivity than predicted.[9] As a thermodynamically-favorable alternative, graphene fluoride has garnered significant scientific interest, owing to its known stability in bulk form,[15,16] correspondingly high resistivity,[17] and ability to convert semi-metallic graphene into a wide-gap semiconductor.[18] The material also benefits from decades of experimental and theoretical graphite fluoride research,[19–23] owing to industrial applications and the importance of fluorine in the synthesis of graphite intercalation compounds. However, isolation of monolayer graphene fluoride has occurred only recently,[24] and interest in this chemical derivative of graphene has burgeoned accordingly.[25–29] Great uncertainty persists in the field, particularly as to the presence of long-range structural order in graphene fluoride films produced by disparate synthesis techniques,[24,25] the preferred ordering of fluorine in single-sided and double-sided configurations, and the prevalence and nature of defects upon reduction to graphene.

The scanning tunneling microscope (STM)[30] has long established itself amongst the dominant tools for surface science and structural analysis of materials. However, the STM is heavily dependent on the application of a sharp, resilient metallic probe used to spatially confine tunneling current during imaging.[31,32] As an element of this dissertation, we develop a modified sputter-erosion sharpening technique, field-directed sputter sharpening (FDSS), explore the sharpening influence of FDSS in comparison to existing sputter erosion sharpening techniques, and apply FDSS to novel probe materials, specifically the metallic ceramic hafnium diboride. We further apply FDSS tips for high-fidelity nanolithography of the Si(100) 2 × 1:H surface by electron-stimulated desorption.

As processing development draws nearer the limits of scaling in electronic and mechanical systems, we are faced with an intriguing limit of precision. With the invention of the scanning tunneling microscope and subsequent development of scanned probe technologies,[33] it has become increasingly possible to discuss the generation of structures and devices with near-atomic precision.

The remainder of this dissertation will explore fluorinated graphene films, in single-sided and double-sided configurations. We will consider the stability of both chemical configurations when substrate-supported under STM imaging and patterning conditions. We study at the atomic scale the structural decomposition of monolayer double-sided graphene fluoride on Si(100) 2 × 1:H and the chemical interaction between graphenic flakes and pristine substrates. Through STM, scanning tunneling spectroscopy (STS), and X-ray photoelectron spectroscopy (XPS) we elucidate the structure of one stable form of single-sided graphene fluoride (C_4F), resolve uncertainty as to the presence of structural long-range order in planar-sheet graphene fluoride prepared with XeF_2, and make the first STS measurements of the electronic band structure of this material.

1.2 Probe Sharpening Methodology

The sharpening of conductive probes is a broad field of research, commonly enmeshed with the study of electron beam sources for electron microscopy,[34] field emitter arrays for display applications,[35] and atomic probes for scanned probe microscopy.[31] The field has increasingly flourished since the advent of the scanning tunneling microscope,[30] an application generally dependent on the detailed structure of a scanned probe. Sharpening techniques have previously been the focus of book chapters[36] and review articles.[37] The techniques employed in this dissertation and the progression of sputter sharpening technology will be detailed. When quantifying the microstructure of a probe, a practice of measuring radius of curvature and cone angle will be adopted. As the cone angle may vary with length scale, we take this angle to refer generally to the angle of the smallest defined cone, proximally nearest the probe apex. A definition of these characteristics is shown schematically in Figure 1.1 (all figures at the ends of chapters). In the literature this method of quantifying tip form is commonplace, though in some cases the apex diameter is referenced, and defined as the width of the smallest distinguishable apex feature.[38] The term "cone angle" is frequently applied interchangeably with the "cone half angle," which is half of the cone angle described in this dissertation.

1.2.1. Electrochemical Etching of Metallic Probes

Most probe materials routinely employed offer well-understood chemical or electrochemical etch (ECE) procedures for production of sharp microtips. In one manifestation, tungsten probes can be etched in 3M NaOH or KOH solution under an applied DC bias, while platinum-iridium alloy can be successfully etched in $CaCl_2$ with an applied AC bias. Additional materials employ varied etchant and biasing conditions and may require subsequent etch steps.[39–41] In all cases, these etching procedures fall routinely into two distinct categories, herein termed "drop-off" and "cut-off" techniques.

Under drop-off, or lamellae, etching[42] the desired probe wire length is extended through an inert counter-electrode ring within which an etchant film is confined. While etching, this probe wire thins and breaks under applied bias, and the released wire is captured for use. All tungsten tips reported in this dissertation were initially etched using the drop-off technique.

Similarly, under the cut-off or emersion technique,[43] several diameters of wire are submerged in an etchant solution in the vicinity of a counter electrode. For this dissertation, and commonly for platinum-iridium etching, this counter electrode is composed of graphite.[39,44] In this configuration, a small tear-drop forms and detaches from the wire apex, while the top probe is collected for use. In many cases, cut-off circuitry can be employed to detect this completion event,[43] while in this dissertation some platinum-iridium probes employ a mild fine etch immediately prior to completion to reduce etch rate significantly and allow for manual cut-off. Platinum-iridium probes etched in-house for this dissertation were prepared using the cut-off process described with fine etch and manual cut-off.

1.2.2. Conventional Sputter Erosion Sharpening of Metallic Probes

Since the discovery of pyramidal microstructure on ion bombarded surfaces,[45] the physics of sputter erosion have been irrevocably linked to probe sharpening, and the ability to employ these sputter erosion techniques for the sharpening of probes has been extensively explored.[46–57] The sharpening of polycrystalline tungsten wire is widely reported, with resulting radii of curvature between 5 nm[56] and ~20 nm.[54] The physics of this sharpening technique will be described in Section 1.3.

1.2.3. Metallic Probe Sharpening by the Schiller Decapitation Process

Another intriguing technique for sharpening of metallic field emitters was described by Schiller et al.[58] and is sometimes termed the Schiller decapitation process.[59] Schiller decapitation can be conceptualized as the sputter erosion analog of a cut-off ECE, under which a metallic tip is modified by self-sputtering. With Schiller's technique, a negative bias is applied to a tip, inducing field ionization and subsequent sputter erosion of the probe apex and shank. The resulting probes offer a reported radius of curvature between 4 nm and 6 nm. However, the technique requires a monitored decapitation detection mechanism, limiting the ability of this technique to scale to highly parallelized probe arrays. The Schiller decapitation process is the only previous example known to the author of a field-influenced sputter erosion process, where the electric field surrounding a biased conductive serves to direct the flux of ions. However, the technique is differentiated from the field-directed sputter sharpening process most clearly by the polarity of the applied bias and by the ion source itself. Where the applied negative bias under Schiller decapitation attracts locally generated ions to the probe, under the field-directed sputter sharpening procedure described in Chapter 2 an applied bias repels remotely generated ions, which travel a hyperbolic path away from the probe.

1.2.4. Field-Assisted Nitrogen Reaction of Tungsten Nanotips

The process of tungsten tip etching by nitrogen in a field-directed environment represents a related sharpening technique which is in essence the chemical analog of the physical FDSS. One can visualize the relation between field-assisted nitrogen etching and FDSS as that between electropolishing and sand blasting, two distinct techniques with a shared objective. By the application of a probe bias, Rezeq et al. restrict the reaction of nitrogen gas to the shank of a tungsten tip, thereby producing a preferential sharpening process.[60,61] The primary advantage of FDSS over this technique is the immediate application of FDSS to multiple probe materials, including platinum-iridium alloy and hafnium diboride, without the need to devise novel etch chemistries. In contrast, field-assisted nitrogen etching of tungsten may produce a more chemically inert probe surface following sharpening, while FDSS probes composed of reactive materials such as tungsten are subject to oxidation upon removal from vacuum.

1.3 Sputter Erosion Physics

Sputter-induced erosion of materials and the resulting generation of predictable microstructured and nanostructured patterns has been a subject of research for more than fifty years.[62] Study of the stopping of particles in matter and the relation between sputter yield and angle of incidence from which this phenomenon is derived[63] dates back further still. In his experimental result of 1959, Wehner demonstrated the sharpening of 0.5mm diameter metallic spheres following extensive sputter erosion over hundreds of hours.[62] In this early work, similar to those which followed, the spheres are electrically connected to the grounded reference potential. The underlying physics of this sputter erosion are well described by the Sigmund model.[46] Understanding of sputter erosion physics was additionally refined through the work of Barber et al.[47] and Carter et al.[50] where the sputter erosion process is modeled with Frank's model of chemical dissolution of crystals by kinematic wave theory.[64,65]

In a straightforward model, sputter erosion of surfaces can be envisioned as a flux of energetic ions inducing vibration and displacement of atoms within a substrate by collision cascade.[46] We can describe sputter erosion by the sputter yield:

$$Y(\theta) = \frac{\text{atoms ejected}}{\text{incident ions}} \tag{1.1}$$

As expected, the sputter yield is a function of substrate material and structure, ion species, and ion energy. Additionally, the sputter yield exhibits a curious relationship with the angle of incidence (θ) between an ion path and the substrate, shown from theoretical modeling in Figure 1.2. When considered in terms of a cascade of atomic collisions and a non-zero penetration depth for each ion (Figure 1.3), this result is verified. Sputter yield is the number of displaced atoms with sufficient recoil action to reach the sample surface and sufficient energy to overcome surface binding forces. As a result, most sputtered atoms are surface atoms, and sputter yield is related to spatial overlap between the sputter cascade and the substrate surface (Figure 1.4). As the angle of incidence of an incoming ion varies from surface normal to glancing incidence, a greater fraction of available energy is distributed in the near-surface region, increasing the overlap between the energy distribution and surface plane, and therefore increasing the sputter yield. An energetic ion will penetrate the surface while slowing due to the influences of nuclear and electronic stopping. Energy from the ion is distributed within the surface through interaction with atomic nuclei, producing an energy distribution centered some distance beneath the surface with a distribution that is approximately Gaussian.[46] As the angle of incidence is increased, sputter yield will increase as overlap between the sputter cascade and the substrate surface increases, thus facilitating the escape of a larger fraction of surface atoms. Approaching glancing incidence, ion reflection becomes increasingly prevalent. Reflection results in a rapid sputter yield decline until erosion halts for an ion flux parallel to the surface.

In modeling conventional sputter erosion (CSE) sharpening, we consider two distinct regimes. Under the first-order model of sputter sharpening, topographical surface modification is considered on a scale significantly larger than the ion penetration depth. In this case, we can model a sharpening process from the relation between yield and angle of incidence. Modeling first-order CSE, we consider a probe of distinct, flat planes as shown in Figure 1.5. During sputter erosion, each plane will etch at a rate related to its angle by the Y(θ) curve. As competing planes propagate, those etching most rapidly will in time overtake more gradually etched planes, resulting in an arbitrarily sharp apex with cone angle corresponding to the global maximum of the Y(θ) curve. Experimentally, this maximum is found to produce cone angles of 60° – 80° for various substrate materials and ion species.[66]

This first-order model provides a clear understanding of microstructure produced by sputter erosion well beyond the nanometer scale, particularly of the probe cone angle. However, in understanding CSE at the nanometer scale, one must more explicitly consider the collision cascade as well as surface diffusion effects.

A second-order model of CSE follows directly from the collision cascade when the spatial extent of this cascade is modeled. From this model, with explicit consideration of atomic-scale effects within the cascade of influenced lattice atoms, one can derive the effects observed under the first-order erosion model, specifically the relation between sputter yield and angle of incidence. As described by Sigmund,[51] at the length scale of the collision cascade, sputtering of material from the target surface will preferentially occur downstream from the impact site. Additionally, the model predicts the formation of a depression surrounding the base of an eroded pyramid, a structural effect verifiable experimentally in the study of sputter-induced morphological changes on surfaces.[67] Sputter erosion is reduced at the probe apex, but enhanced along the neighboring slope, leading to a reduction of cone angle on the length scale of ion penetration.

Such collision-based erosion models do not readily explain the resulting radius of curvature of a probe under CSE. Ultimately, the sharpening process is limited by the ion penetration depth, and the minimum radius of curvature should be on this scale. Though this fundamental limitation exists, those sputter erosion models described neglect the effect of surface diffusion on the final tip shape. As explained by Carter[49] and Carter et al.[50] in a first-order erosion model, the resulting probe apex is further modified by the influence of thermally induced and radiation enhanced surface diffusion. A more thorough derivation of sputter erosion sharpening following the work of Carter[49] has been presented previously by the author.[68] This effect has been studied in detail by Bradley and Harper[53] and must be considered in the modeling of field-directed sputter erosion. Whereas sputter erosion tends toward the general reduction of probe radius, the influence is balanced by a preferential flux of diffusing surface atoms from the region of greatest curvature. Such diffusion can be induced by thermal influences, localized or distributed, or by radiation induced surface self-diffusion, described in detail by Cavaillé.[69] Additionally, the effects of surface diffusion are influenced by the local electric field,[70] further complicating analysis of sputter erosion sharpening.

1.4 Sputter Sharpening Apparatus

Sputter sharpening described in this dissertation was performed in the "Chamber A" UHV system shown in Figure 1.6, located within the laboratory of Professor J. Lyding in the Beckman Institute at the University of Illinois, Urbana-Champaign. Sputter erosion operations were performed in a high-vacuum antechamber with a nominal base pressure of 8×10^{-9} torr. The chamber is evacuated by a Pfeiffer-Balzers TPU-240 turbomolecular pump backed by an Alcatel 2008A mechanical roughing pump. An integrated ion source is available in the form of a Physical Electronics PHI 04-161 sputter ion gun and corresponding OCI Vacuum Microengineering IPS3 controller. Electrical contact to the probe is provided by dual high voltage vacuum feedthroughs which allow for biasing and, where desirable, resistive heating. During field-directed sputter sharpening, tip bias is applied by a Systron-Donner M107 precision DC voltage source adjustable to 1 kV. During sputter cycling the chamber is backfilled to 5.5×10^{-5} torr of Ar or Ne gas using a Varian variable leak valve. Chamber pressure is monitored by an in situ nude ionization gauge and Varian Multi-Gauge controller with corresponding UHV board (gas correction factor 1.0).

Probe characterization is performed in a Philips CM200 transmission electron microscope (TEM) operating at 200 kV with nominal achievable resolution of 2 Å. The CM200 includes an integrated CCD camera (2000 × 2000 pixels) for image collection. Prior to TEM characterization, probes are removed to ambient conditions for transfer.

Additionally, the high-vacuum sputter erosion chamber is interlocked with UHV preparation and STM chambers, both maintained below 1×10^{-10} torr, for which the probes are destined. Imaging and patterning work is performed in constant-current mode using a room temperature STM designed by Lyding et al.[71] comprising two concentric piezoelectric tubes. The inner tube provides fine probe motion and facilitates inertial probe translation[72] while the outer tube provides inertial sample translation. Microscope control is accomplished via a digital feedback control system[73] and custom software designed by Professor Joseph Lyding et al. An STM system of similar structure is shown schematically in Figure 1.7 and has been described previously.[74]

1.5 Electron-Stimulated Desorption

In addition to its use for atomically resolved topographic and spectroscopic imaging of surfaces, the local influence of the STM tips provides a high-resolution probe for the manipulation of surfaces, a diverse array of techniques that take many forms. Such ability was recognized from the early days of STM.[75] In early demonstrations, the STM was employed as a local probe for deposition of carbonaceous contamination,[75,76] transfer of single atoms and molecules to surfaces,[77,78] and direct writing of metal nanostructures from organometallic precursors.[79] Perhaps the most memorable demonstration of this nanomanipulative capability was the work of Eigler and Schweizer[80] from which came the iconic image of "IBM" written with 35 Xe atoms on Ni(110).

The study of electron-stimulated desorption (ESD) of atoms and molecules on surfaces predates the invention of the STM by decades,[81–84] and has been the subject of extensive review.[85,86] Like ion- and photon-stimulated desorption, ESD makes accessible desorption processes which are unachievable by thermal effects. In general terms, ESD proceeds by the electronic excitation of an adsorbed atom or molecule from a bonding to an anti-bonding configuration.

It was recognized early that the STM is uniquely suited to lithographic patterning due to the extreme spatial localization of the electron beam, leading directly to spatial localization in the lithographic patterns produced.[87] Indeed, several resist chemistries were employed for this purpose in early studies, including carbonaceous contamination,[76] calcium fluoride,[88] and polydiacetylene.[89] However, it was recognized that a single layer of chemisorbed atoms offered an ideal resist layer owing to its potential for high resolution patterning and chemical contrast,[90] with hydrogen as the obvious choice, given its applicability to the technologically relevant Si surface, low atomic weight, and compatibility with the preparation of atomically-pristine Si surfaces (unlike fluorine). An early study of STM nanolithography was performed in air by Dagata et al.[91] and demonstrated patterned oxidation of n-Si(111):H. The patterning effect was attributed to field-enhanced oxidation. This work was followed quickly by demonstrations of tip-induced hydrogen desorption. Lyo and Avouris[92] demonstrated induced desorption from Si(111) following decomposition of H_2O in a process then attributed to a combination of field-induced desorption and tip-surface chemical interaction. Their work was followed by an H desorption study from Becker et al.[93] who demonstrated removal of H from the Si(111) 1 × 1:H surface, leading to local formation of the Si(111) 2 × 1 reconstruction. ESD lithography with a hydrogen resist was first demonstrated by Lyding et al.[94] for the purpose of patterned oxidation on the Si(100) 2 × 1:H surface. Subsequent efforts introduced access to a vibrational heating desorption regime[95] and feedback controlled lithography (FCL), which extends to the controlled desorption of individual H atoms.[96] Early patterning work has since extended to such universal processes as atomically-precise doping of silicon,[97,98] and the creation of quantum-dot cellular automata structures from arrays of Si dangling bonds.[99] These techniques provide atomic resolution patterning, and FCL provides precise control over the number of atomic desorption events. Nevertheless, electron-stimulated modification techniques are inherently stochastic in nature, with patterning fidelity dependent on the spatial distribution of electron tunneling current between tip and sample, and subject to the influence of secondary electrons.[100] In the case of ESD this effect is manifested in spurious depassivation sites distant from the pattern center. The goal of reliable and atomically-precise lithographic control of H removal by ESD remains elusive, and becomes more important as technologically relevant patterns approach the atomic limit.

ESD from substrates by electron transport from STM tip to sample can occur in two distinct regimes, commonly called field emission and tunneling. Both are related and depend on the quantum mechanical tunneling mechanism. They are distinguished by the existence of a free electron during transmission. In the case of tunneling, the electron tunnels directly through the vacuum gap into a substrate state, in quantum mechanical terms never existing in the gap as a free electron. In contrast, under field emission, the electron is field-emitted from the tip, tunneling through a vacuum gap made narrower by the high electric field into free space before entering the substrate.

1.6 Hafnium Diboride

Hafnium diboride is one of an array of group IV diborides, and is a hard, brittle metallic ceramic characterized by an array of advantageous mechanical and electrical properties. In particular, in its bulk form, HfB_2 has a high Young's modulus of 504 GPa,[101] high bulk hardness of 31.5 GPa,[102] low room temperature electrical resistivity between 10.6[103] and 15.8 $\mu\Omega$-cm,[104] and a high melting point of 3240 °C.[105] Various applications for films of metal borides, and specifically hafnium diboride, have been proposed, including wear-resistant coatings,[106] resistive heating elements,[107] and Cu diffusion barriers.[108] Such properties and applications, combined with the high conductivity of HfB_2 films, makes them exceptional candidates for the synthesis of ultra-hard, chemically resistant, conductive probes for STM. The deposition process employed in this dissertation has been the subject of substantial research,[109–111] and will be reviewed here only briefly.

The synthesis of metal diborides has historically followed from high-temperature processing above 1000 °C,[112] chemical vapor deposition (CVD) from halogen-based precursor molecules,[113] or the reduction of metal oxides with boron.[114] By employing the binary tetrahydroborate hafnium borohydride ($Hf(BH_4)_4$) precursor, known to produce non-volatile metallic borides upon decomposition,[115] a low temperature CVD process is enabled that is free of carbon and halogen contamination,[116,117] with a substantial processing temperature reduction to temperatures as low as 200 °C.[108]

Films deposited at low temperature (200 – 400 °C) are amorphous and of high density.[108] For deposition above 400 °C, films are crystalline but are of lower density and possess a columnar microstructure.[108,118] In other work, the annealing of amorphous films above 700 °C was found to induce the formation of nanocrystalline HfB_2 and to result in a significant hardness increase from 20 GPa to 40 GPa.[119]

CVD of HfB_2 from hafnium borohydride precursors opens a new avenue to the deposition of carbon-free and halogen-free metallic films by electron beam induced deposition (EBID).[120] In particular, the probe tip of an STM has been employed for local deposition, producing 5 nm metallic wires.[121]

1.7 Graphene

Scientific interest in graphene has persisted since the earliest theoretical treatments of its unique structure and corresponding electronic characteristics.[122–124] In part, this interest arises from the importance of graphene as the fundamental building block for other carbon-based systems. Early work focused on graphene as the base unit of graphite, and more recently graphene has garnered further attention as the structural basis for fullerenes and carbon nanotubes.[125–127] However, for decades graphene was perceived primarily as a structure for academic treatment of other, practical materials.[128,129] It was predicted, and almost universally agreed, that such two-dimensional materials as graphene could not exist in a stable form in isolation from bulk support structures. In some sense, this view is warranted, and even in recent years it has been recognized that graphene will preferentially fold, buckle, and roll itself out of two-dimensional space given the opportunity, but the recent development of graphene exfoliation to insulating substrates[1] makes clear the limitations of this model.

1.7.1. Origins and Development of Graphene

One must note the body of experimental work that predates the mainstream introduction of graphene to the scientific community in 2004, and the manner in which this work has evolved to create the recent flurry of activity surrounding the study of monolayer, bilayer, and trilayer graphene.

Among early papers on the subject, the first claim of monolayer graphene known to the author came from the reduction of exfoliated graphite oxide in 1962.[130,131] Because the original texts are in German, we translate a relevant passage:

> The carbon films were obtained by the reduction of graphite oxide, which was dispersed in dilute sodium hydroxide. From the contrast of the electron microscope, i.e. from the electron scattering, the thickness of these films is determined to a few hexagonal carbon layers. The lowest values were 3 – 6 Å, and pointed to the presence of films that consist of a single carbon layer.[131]

Nevertheless, though the authors employed properly the technology and techniques available, in light of fifty years of hindsight, the methods available (comparison to a range of calibration standards of known thickness) introduce significant uncertainty when attempting to characterize atomically-thin materials. Nevertheless, it is understood that reduction of exfoliated graphite oxide is capable of producing monolayer films,[132] and therefore it may be reasonably suspected that Boehm et al. produced monolayer graphene from graphite oxide in their work. In intervening decades, graphite oxide films were studied extensively, and this interest has only continued to grow since 2004.[132–137]

The first conclusive evidence for monolayer graphene came in 1968 and 1969 when May et al.,[138] based on the observations of Morgan and Somorjai,[139] correctly identified monolayer graphene in low-energy electron diffraction (LEED) patterns on the Pt surface following exposure to various carbon precursors at temperatures from 25 °C to 1400 °C. Together with early demonstrations of few-layer graphene on Ni,[140] this work represents the earliest study of graphene chemical vapor deposition (CVD) on metal surfaces.

Since these early discoveries, graphene CVD has been reported on many transition metal surfaces, including Pt,[141–145] Ni,[146–149] Pd,[143] Re,[150] Co,[143] Ir,[151–153] Ru,[154–157] and Cu.[158–161] Growth kinetics, and thus graphene thicknesses, vary by substrate material depending on whether growth follows a precipitation[162] or surface adsorption[158] process. The distinction between growth processes can be clearly illustrated by isotope labeling during growth.[163] The example systems, Ni and Cu foils, demonstrate that growth on Ni proceeds by the absorption of C into the Ni bulk at high temperature, followed by a precipitation process during cooling. In contrast, graphene growth on Cu is found to follow a surface adsorption process, whereby graphene islands nucleate and grow until full surface passivation is achieved. The significance of this distinction arises primarily in the preferentially monolayer nature of graphene grown on Cu, where on Ni substrates growth conditions must be precisely controlled to minimize the formation of multilayer graphene.[148,149,164] CVD of graphene on Cu foil is a recent discovery[158] and a technique employed in this dissertation for the growth of monolayer graphene.

Further early work on the synthesis and etching of graphene nanostructures came from the laboratory of Sumio Iijima, who would later be credited with the discovery of carbon nanotubes.[165] In early studies of few-layer graphene by Iijima et al.,[166–168] transmission electron microscopy was employed not only to confirm the presence of few-layer graphene but to demonstrate thinning under electron bombardment and etching by W atoms.[166] By imaging of the rolled edges of graphene flakes, films as thin as trilayer graphene could be clearly identified,[166] and modified by the influence of the imaging electron beam and deposited W adatoms.[167]

The graphitization of SiC upon heating was first reported by Edward Acheson and patented in 1896 as a method for producing artificial graphite from low-quality carbon feedstock.[169] The graphitization of SiC(0001) above 800 °C (generally between 1200 °C and 1800 °C) was well understood by the 1970s.[170–172] In the decades following, the ability to produce monolayer and bilayer graphene on the Si face of SiC was developed,[173–180] ultimately leading to the development of transfer-free graphene electronic devices such as field-effect transistors (FETs) operating at speeds up to 100 GHz.[181]

By 2004 it remained unclear whether monolayer graphene existed, as it was generally agreed to be fundamentally unstable in its two-dimensional form. Numerous researchers worked extensively to isolate graphene by exfoliation, a process that, in hindsight, was limited more by their ability to identify monolayers than to produce them. It is likely that monolayer graphene is created with every pencil mark,[182] but without a mechanism to efficiently evaluate the resulting flakes, an exhaustive search becomes overwhelmingly costly. Although thin graphite films had been produced by mechanical exfoliation,[183] the scaling of this technique to monolayer films proved difficult. This limitation was finally overcome by Novoselov et al. in 2004,[1] when they demonstrated sufficient optical contrast in few-layer graphene to distinguish monolayer and bilayer films. The key to this discovery was the observation of an interference effect on SiO_2 films of specific thicknesses (e.g. 300 nm). As a result of this crucial discovery, the vetting of graphene flakes produced by mechanical exfoliation (the “scotch tape” method) became practical. Ultimately, this led to the demonstration of certain physical phenomena in graphene[184,185] including the half-integer quantum Hall effect (QHE) and Berry's phase.

Thereafter, the study of monolayer graphene rapidly expanded to the extent that the original 2004 paper from Novoselov and Geim has been cited between 6207 (Web of Science) and 7477 (Google Scholar) times in the scientific literature. Between January 1, 2012 and February 28, 2012 (2:57 PM central time) 162 new research articles have been posted to arxiv.org which contain "graphene" in their title. This phenomenon was driven not only by the curious physics of monolayer graphene, but perhaps more so by a low barrier to entry in a field that had been previously explored only cursorily. Suddenly every research scientist on earth had the ability to produce monolayer graphene, literally in their garage if they desired, and a massive body of research rushed in to the fill the vacuum. It is beyond the scope of this discussion to review this work in its entirety, though several books and reviews have followed the subject.[2,3,186–189]

We will, however, discuss recent studies of graphene growth, particularly on Cu substrates, following the techniques employed in this dissertation for the synthesis of single-sided graphene fluoride. As we have seen, CVD of graphene on transition metal surfaces was one of the first techniques available for monolayer synthesis, and by 2009 similar techniques had been applied to a wide range of metals. In particular, the formation of graphitic films on Ni was discovered as early as the 1960s,[140,190] and this substrate has remained popular due to ease of growth, low cost, and easy transferability.[164] However, given the high carbon solubility of Ni, limiting graphene film thickness becomes a major challenge.[191] Recently, Peng et al. demonstrated the reproducible, transfer-free growth of bilayer graphene on SiO_2 with a Ni catalysis layer.[192] Carbon applied to the top surface of a 400 nm Ni film is absorbed during high-temperature processing, and on cooling produces a bilayer graphene film at the Ni-SiO_2 interface. Chemical etching of the Ni leaves a bilayer graphene film at the surface. Other surfaces, such as Pt and Ir have been used to produce monolayer graphene,[138,152] but high cost and limited transferability prevent their wholesale acceptance as growth substrates. Other researchers worked to grow graphene films directly on insulating surfaces,[193] but the quality of CVD graphene remains highest on metals.

Although in some early work, the formation of graphitic films on Cu substrates was demonstrated as an element of diamond nucleation,[194,195] it was not until 2009 that the field began to develop rapidly due to demonstration of consistently monolayer CVD graphene on Cu by Li et al.[158] Due to Cu's extremely low carbon solubility,[196] graphene growth on Cu proceeds by a surface adsorption process instead of bulk precipitation.[163] As a result, large grains of monolayer graphene were preferentially formed under favorable growth conditions.[197] The low cost of polycrystalline Cu enables a scalable growth process which ultimately led to demonstration of a roll-to-roll growth and transfer process for 30 inch graphene films with Hall mobilities as high as 7350 $cm^2V^{-1}s^{-1}$.[160]

1.8 Fluorinated Graphite

There has been a recent burst of interest in the chemical functionalization of graphene films, in part as a means of improving control of its exciting, yet restrictive, electronic band structure. As in many research fields, recent studies can draw readily on decades of work by hundreds of early researchers. Although chemically modified monolayer graphene is a relatively new material (with the notable exception of exfoliated graphene oxide), the chemical modification of bulk graphite has been studied extensively over more than 60 years, and has been the focus of many published works.[21–23,198,199] In particular, fluorinated graphite has been the subject of extensive study, due in part to industrial applications as a lubricant superior to graphite[200–203] and as an excellent cathode material for lithium ion batteries.[204,205] Additionally, interest in graphite intercalation compounds (GICs)[206,199,207] directed substantial interest to fluorinated graphite due to the intercalation of F into graphite, and its importance in the formation of many other metal fluoride GICs.[22] While countless fluoride intercalation compounds have been synthesized and studied,[19,198,20–23] for our purposes the most relevant are planar-sheet graphite fluoride (a fluorine-graphite intercalation compound) and the related covalent compound, puckered-sheet graphite fluoride (variously termed carbon monofluoride, polycarbon monofluoride, or graphite fluoride). Planar and puckered forms of graphite fluoride are the bulk lamellar analogues of single-sided and double-sided graphene fluoride, respectively. We do not attempt a comprehensive discussion of the wide-ranging field of fluorinated graphite, but rather introduce the bulk materials most closely related to the monolayer films explored in this study, and highlight the most fundamental characteristics of each.

1.8.1 Puckered-Sheet Graphite Fluoride

In its most stable form, fluorinated graphite is a covalent fluorocarbon in which the planar aromatic backbone is converted to a puckered film of sp^3 carbon. The resulting compound generally takes the form $(CF)_n$ or $(C_2F)_n$, and in the former case has been variously termed graphite fluoride, carbon monofluoride, polycarbon fluoride, polycarbon monofluoride, or poly(carbon monofluoride). It is the most highly fluorinated of the various forms of fluorinated graphite, and generally exists as a gray-white powder, or a transparent crystal in the case of highly fluorinated HOPG.[208]

Graphite fluoride was first synthesized by Ruff and Bretschneider[15] in 1934 by the exposure of graphite to fluorine at temperatures between 280 °C and 430 °C to produce a fixed-valence compound of composition $C_{1.09}F$. Subsequently, C_xF ($1.02 \leq x \leq 1.48$) was produced by Rüdorff and Rüdorff in 1947 between 420 °C and 500 °C.[209] The original model proposed for this compound[210,211] was refined by the Rüdorff model,[209] and independently through the work of Palin and Wadsworth,[212] which drew on the structure proposed by London[213] in private discussions, and was published by Bigelow[214] with acknowledgement. With a growing interest in graphite intercalation, the related planar-sheet graphite fluorides attracted substantial interest starting in the 1970s, and will be discussed in Section 1.8.2.

$(CF)_n$ graphite fluoride is generally believed to prefer the form of a trans-linked cyclohexane chair,[209] rather than a cis-trans-linked cyclohexane boat,[215] despite early dispute arising in part due to NMR studies indicative of a boat configuration.[20] This conclusion is also supported by the first density functional theory (DFT) study of puckered-sheet graphene fluoride,[18] wherein Charlier et al. modeled $(CF)_n$ in both boat and chair configurations. The chair configuration was found to be energetically favorable (0.145 eV/C-F bond), though the boat configuration was also a metastable state with a significant (>2.7 eV) barrier for likely transition paths, suggesting that the boat configuration may be realizable, though unfavorable, depending on the kinetics of fluorination.

Electronically, strong covalent C-F bonding in $(CF)_n$ results in an insulating gray or white compound with a large (>3 eV) band gap. Charlier et al. report a 3.5 eV direct band gap at the Γ point, with a 2.7 eV direct band gap at the A point.[18]

Interest in puckered-sheet graphite fluoride has reemerged in the last decade, due to renewed interest in chemical functionalization of monolayer and few-layer graphene materials. Recent experimental studies of graphene fluoride will be discussed in Section 1.9.3, but we will describe first the process and difficulties of extracting graphene from bulk graphite fluoride.

The first experimental studies of graphene fluoride[17] were enabled by mechanical exfoliation of bulk $(CF)_n$ prepared using conventional techniques. Multilayer graphene films were exfoliated to SiO_2, with thicknesses ranging from 6 to 10 nm. Transport measurements made on these films verified their high resistivity (~30 GΩ), a result consistent with the large anticipated electronic band gap. Absent in this early study was the presence of monolayer or even few-layer graphene samples. Several groups, including researchers in the Lyding STM Laboratory, have since observed the difficulty of exfoliating monolayer $(CF)_{n.}$[17,25,27,216] Although Withers et al. exfoliated monolayer C_4F, their efforts to produce monolayer $(CF)_n$ from bulk led them to describe the process as “impossible.”[27] Subsequently, Nair et al.[25] did successfully demonstrate monolayer exfoliation of 1 μm flakes, likely due to a less destructive, lower temperature fluorination process, but described these monolayer flakes as “extremely fragile and prone to rupture,” resorting to the on-surface fluorination of exfoliated graphene for the synthesis of larger samples. As we shall see, the work of this dissertation supports their observation.

1.8.2 Planar-Sheet Graphite Fluoride

A related form of fluorinated graphite can be produced by the exposure of graphite to fluorine, generally in the presence of fluoride compounds (e.g. HF, LiF, AgF). Synthesis is often performed below 100 °C, sometimes at room temperature. In contrast to puckered-sheet graphite fluoride, the planar form of fluorinated graphite that results lacks the strong covalent bonding characteristic of $(CF)_n$ and $(C_2F)_n$, and is the result of graphite intercalation by atomic fluorine. The nature of chemical bonding between C and F varies with F concentration.[217–219] For low F concentrations, roughly below $C_{20}F$, C-F bonding is ionic, and F acts as a dopant, resulting in p-doped graphite, and increasing the electrical conductivity above that of pristine graphite.[218] Conductivity increases until F concentration reaches ~12 at%,[220] above which the increasingly covalent character of C-F bonding leads to a decrease in electrical conductivity. In the case of C_4F, results vary. In some studies, conductivity is nearly unchanged from that of bulk HOPG,[220] whereas others report a two order of magnitude decrease in conductivity when fluorinated.[16] As we shall see, this is in contrast to monolayer C_4F graphene fluoride, where room-temperature conductivity at the charge neutrality point decreases between one and six orders of magnitude.[24,27] The characteristic change from ionic to semi-covalent bonding with increasing F concentration can also be observed in C 1s and F 1s binding energies, measured by XPS, which increase with increasing fluorine concentration.[22,218,219,221,222] These data indicate three distinct configurations of C_xF, purely ionic bonding for $x > 20$

(F 1s: ~684.5 eV, C 1s: ~284 eV), nearly ionic bonding with F locally bound to a C atom for $4 < x < 20$ (F 1s: 685.7 eV, C 1s: 284 eV), and semi-covalent bonding for $x \leq 4$ (F 1s: >685.7 eV, C 1s: >284 eV with C-F peak offset by 3.3 eV). The influence of such variable bonding character is also seen in C-C bond length, which varies with increasing F concentration.[22] While the graphite lattice constant is 2.461 Å, a decrease of 0.24% is seen for fluorine concentrations up to $C_{3.5}F$, for which a lattice constant of 2.455 Å is measured by X-ray diffraction.[223] At higher fluorine concentrations, this lattice constant increases to 2.478 Å for $C_{1.3}F$.[224]

The first experimental realization of tetracarbon monofluoride was by Rüdorff and Rüdorff in their 1947 paper.[16] Planar-sheet graphene fluoride of the form C_xF ($3.6 \leq x \leq 4.0$) was formed by reaction with atomic fluorine in the presence of HF at 80 °C. It was determined that HF was necessary for the reaction to occur, and that the fluorination process ultimately produced tetracarbon monofluoride, being unable to proceed to the formation of CF or C_2F. The product of the reaction was found to be inert towards many acids and bases, but to decompose slowly in H_2SO_4 above 100 °C. Also, Rüdorff and Rüdorff provided the first measurements of electrical resistivity in planar-sheet graphite fluoride, finding an increase over graphite by two orders of magnitude, from 0.02 Ω-cm in graphite to 2-4 Ω-cm in C_4F. However, the resistivity of C_4F was still significantly lower than the electrically insulating $(CF)_n$ previously studied.[15,209] From their X-ray diffraction (XRD) study, Rüdorff and Rüdorff proposed the first structural model of C_4F, a model that has since been further verified and is similar to the single-sided structure presented in this dissertation. In particular, they found that the aromatic structure of graphite was preserved, with no indication of buckling characteristic of puckered-sheet graphite fluoride. Perhaps most importantly for this dissertation, early XRD studies of C_4F suggested the alternation of F on the top and bottom faces of each graphene sheet, a hypothesis again proposed in recent studies of exfoliated monolayer C_4F,[27] but incompatible with the single-sided fluorination presented in this dissertation. Although discussed in a later text,[19] this early work was not continued until 1970, when Lagow et al. improved on the Rüdorff process by a static bomb synthesis technique[225] during his graduate study at Rice University.[198,226,215]

Experimental exploration of the in-plane structure of fluorinated graphite suggests a number of viable structures. These include the Rüdorff structure of C_4F,[219] the orthorhombic system of $C_{3.5}F$,[227] and a hexagonal structure in C_6F.[228]

There was a limited body of theoretical work on the electronic properties of planar-sheet graphite fluoride before the advent of fluorinated graphene in recent years. This was limited to preliminary results presented by Holzwarth et al. in 1983.[229] Holzwarth, et al. assumed the Rüdorff model of C_4F and computed a self-consistent band structure from first principles. The results of this simulation suggested that C_4F is a semiconductor with a 2 eV band gap.

1.9 Chemically Modified Graphene

In order to enable greater control of the mechanical, thermal, and electronic properties of graphene, various forms of graphene chemical modification have been explored. Recent studies of graphene's chemical derivatives follow primary on early studies of graphite intercalation compounds (GICs)[23,230,231] together with covalent forms of functionalized graphite: graphite oxide[136] and graphite fluoride.[21] GICs are non-covalent lamellar structures where intercalate molecules are interspersed between sp^2 bonded carbon sheets. Structures are characterized by the number of carbon layers between intercalate layers, termed the "stage number." For instance, a stage 1 compound comprises alternating layers of monolayer graphene and intercalate. Stage 2 compounds (e.g. bromine GICs) comprise bilayer graphenic films separated by intercalate.

Two distinct classes of chemically modified graphene occur in practice: covalent and non-covalent chemistries. The most extensively studied covalent chemistries include fluorine, hydrogen, and oxygen (in the form of graphene oxide), which produce gapped insulators due to disruption of the graphene π-bonded network. In contrast, non-covalently functionalized graphene generally preserves the metallic nature of graphene but can influence various characteristics of the film including doping[232] and solubility.[233]

1.9.1. Graphene Oxide

Graphene oxide is the earliest form of chemically modified graphene to be discovered, and remains of profound importance today due to its increased solubility, gapped structure, and reducibility. However, the structure of graphene oxide is non-stoichiometric, and the reduction process results in a high density of defects. As a result, graphene oxide has not yet been seriously considered as an electronic material. However, recent work by Hossain et al. has indicated the possibility of a related method of graphene functionalization, whereby oxygen is bonded in an epoxy configuration.[234]

1.9.2. Hydrogenated Graphene

Early interest in the interaction of hydrogen with graphite and graphene[235–237] centered on the development of hydrogen storage technologies,[238] rather than the electronic implications of such a structure. In graphite, hydrogen intercalation is not generally observed, though hydrogen is incorporated into certain ternary intercalation compounds containing alkali metals.[239,240] Theoretical works have predicted a stable hydrogenated form of monolayer graphene.[8] Other studies, however, have noted a significant nucleation barrier to hydrogenation,[13] suggesting the difficulty of producing such a material. Although hydrogenated graphene films have since been realized experimentally,[9] their stability in isolated form remains uncertain due to low resistivity,[9] and their formation appears strongly dependent upon graphene-substrate interaction.[241]

Although the structure of hydrogenated graphene as a trans-linked cyclohexane chair has been predicted,[8] no experimental verification of this structure is known to the author, perhaps due to its recent discovery or to its thermodynamic unfavorability. Other proposed single-sided structures include C_2H, where H atoms bind to a single graphene sublattice,[242] and 1-D hydrogen chains separated by rippled sp^2 graphene.[243]

The electronic band structure of fully hydrogenated graphene was predicted theoretically,[8] and measured experimentally by angle-resolved photoelectron spectroscopy (ARPES).[244] In the same ARPES/STM study, a significant substrate influence on hydrogen absorption was observed, where hydrogen chemisorption was templated preferentially in the Moiré superstructure positions of the Ir(111) substrate and graphene overlayer where graphene-substrate interaction was greatest.[244] In a subsequent study,[241] the complementary influence of hydrogenation and substrate interaction was explored in detail. Covalent interaction of adsorbed hydrogen with graphene is enhanced on highly interacting substrates, ultimately enabling a graphane-like structure with 50% H coverage on one side, due to substrate interaction with the downward puckered C atoms pairing with H interaction on the upward puckered C atoms. In other work by Guisinger et al., the hydrogenation of monolayer graphene was observed by STM[245] and subsequently patterned by ESD by Sessi et al.[10] Their work experimentally introduces the theorized possibility of creating confined graphene nanostructures in hydrogenated graphene barrier,[11] but such goals have remained elusive to date.

1.9.3. Fluorinated Graphene

In direct contrast to hydrogenated graphene, and like bulk fluorinated graphite, fluorinated graphene is thermodynamically stable and readily synthesized. Recently, three distinct forms of graphene fluoride have been produced, which we characterized by their fluorine concentration and atomic configuration.

The first, dilute fluorinated graphene (DFG), is characterized by an extremely low concentration of fluorine, which serves to introduce p-type doping into the graphene sheet. In prior studies of DFG, an unexpected colossal negative magnetoresistance effect was seen, with a significant (×40) reduction in resistance under magnetic fields of 9 T.[246]

The second, ss-GF, is a covalent form of fluorinated graphene where fluorine is confined to a single side due to the presence of some barrier to double-sided adsorption (typically a substrate). In many ways, ss-GF is analogous to planar-sheet graphite fluoride. For example, under typical fluorination conditions, both materials saturate in the form of C_4F, and will not readily proceed to full coverage. Additionally, ss-GF is six orders of magnitude more resistive than graphene.[247] As we will show, the atomic structure of monolayer C_4F is similar to the Rüdorff structure of graphite fluoride, despite its single-sided nature. In an early demonstration of ss-GF, Robinson et al. employ an XACTIX XeF_2 etching system similar to the one used in this dissertation to functionalize the top side of a Cu-bound graphene sheet.[247]

In a different approach, Withers et al. produced graphene fluoride by the mechanical exfoliation of planar-sheet graphite fluoride (C_4F).[27] While the structure of this material approximates ss-GF, it is not strictly single-sided. Indeed, Withers et al. suggest the alternating orientation of the Rüdorff structure, although this hypothesis remains untested.

The third, ds-GF, or fluorographene, is a covalent form characterized by full fluorination, CF in saturation. Ds-GF is analogous to puckered-sheet graphite fluoride, with similarly high resistivity. Another common characteristic of ds-GF is ease of rupture during exfoliation,[25,27] possibly due to the creation of defects during the fluorination process. In this dissertation we demonstrate ds-GF produced by mechanical exfoliation from bulk graphite fluoride, further probing this instability by STM. In other cases, graphene can be fluorinated on both sides after exfoliation[25] or growth,[247] resulting in monolayer ds-GF. In early studies of few-layer ds-GF, Cheng et al. demonstrated mechanical exfoliation from bulk CF.[17] Subsequently, Robinson et al. demonstrated the double-sided fluorination of CVD graphene by exposure to XeF_2 on a SOI substrate, on which Si etching facilitated the exposure of graphene's bottom surface and creation of CF ds-GF.[247] Shortly thereafter, Nair et al. demonstrated both mechanical exfoliation of micron-sized monolayer flakes from graphite fluoride, noting their propensity to rupture, and the fluorination of pre-exfoliated graphene by exposure to solid XeF_2 at 120 °C over days to weeks.[25] Subsequently, Zbořil et al. demonstrated a liquid-phase exfoliation process to produce monolayer ds-GF from puckered-sheet graphite fluoride.[248]

The goal of reducing fluorinated graphene to recover pristine graphene, particularly in a lithographically patterned manner, has been pursued by several groups, each with their own methods. One primary goal of ongoing study is the creation of electronic nanostructures within fluorinated graphene films,[14,249] which would enable the production of graphene-only integrated circuits with a combination of metallic graphene and semiconducting graphene nanowires confined within a graphene fluoride barrier. In their earliest work, Cheng et al. reduced graphene fluoride films by annealing at 500 – 600 °C in Ar/H_2 gas, a process that reduced the material and recovered a conductive graphenic material.[17] As shown later by Robinson et al. this thermal annealing process introduces a substantial density of defects in the graphene, seen in Raman spectra. To resolve this issue, a hydrazine treatment process[250] was employed at lower temperatures between 100 and 200 °C, resulting in efficient reduction while enabling a partial recovery of graphene's aromatic carbon backbone.[247] Zbořil et al. contributed a chemical approach to graphene fluoride reduction, conversion to graphene iodide by halide exchange using KI.[248] In the first demonstration of patterned reduction, Withers et al. developed an e-beam lithographic technique for patterned reduction of C_4F flakes exfoliated from bulk planar-sheet graphene fluoride.[29] Feature sizes achieved in this work were as small as 40 nm. By the inverse approach, patterned fluorination, Lee et al. created 35 nm graphene ribbons in ss-GF.[251] A polystyrene mask is applied by thermal dip-pen nanolithography with a heated AFM tip, and a wide range of control experiments employed to verify the negligible influence of polystyrene and fluorinated polystyrene on the resulting devices. Upon exposure to XeF_2, graphene is converted to wide-gap C_4F, but with the polystyrene films acting as a mask, graphene nanoribbons are produced.

1.9.4. Chlorinated Graphene

The formation of chlorine-based GICs dates back to 1957,[252] and is being studied extensively. Although Cl_2 does not intercalate into graphite[253] due to poor lattice matching with the graphite lattice,[254] molecular chlorine is an important element in the intercalation process of other species, and is cointercalated together with some materials with which it is miscible, such as Br_2[255] and $I_{2,}$[256] thereby providing the required lattice match. Most metal chlorides will intercalate in the presence of Cl_2, and in some cases spontaneously, where the molecule dissociates to produce Cl_2.[23]

Unlike as for fluorine and hydrogen, it is not yet clear whether covalent chlorinated graphene structures are experimentally realizable. In a recent study by Li et al.,[257] the existence of covalently functionalized chlorinated graphene on SiO_2 was suggested. In that work, a photochlorination procedure was employed for graphene functionalization, wherein monolayer graphene was exposed to atomic chlorine produced by irradiation with a Xe arc lamp. The resulting graphene exhibited covalent C-Cl bonding with 8 at% coverage, an increase in electrical resistivity, and an increase in the Raman D peak, indicating increased sp^3 bonding character. However, these results conflict with a subsequent study by Wu et al.[258] in which graphene was exposed to chlorine plasma, resulting in ionically bound chlorine and p-type doping, coupled with slow etching of graphene and resulting decrease in conductivity. The disagreement between these papers was explored theoretically by Ijäs et al.[259] whose simulations were consistent with the results of Wu, et al. and suggested that the results of Li et al. could be explained by the predicted fracturing of graphene into chlorine-terminated nanodomains. However, the work of Ijäs et al. did not exclude the possibility of substrate-mediated covalent functionalization of graphene by chlorine, particularly in light of earlier observations that the substrate has a substantial influence on the covalent adsorption of hydrogen on graphene.[260,261] In fact, simulations of chlorinated graphene on various silicon oxide surfaces suggest covalent functionalization to be achievable.[259]

In light of these works, we conclude that chlorinated graphene is generally characterized by ionic C-Cl bonding, consistent with previous studies of chlorine GICs. However, given the slow rate of etching, chlorination of graphene may offer a useful alternative to substitutional doping for conductivity modulation. Furthermore, given an apparent preference for covalent functionalization of graphene edges, and the instability of adatoms bound to the graphene basal plane, Cl may have applications for edge state passivation on graphene nanoribbons.

1.9.5. Brominated Graphene

Molecular bromine forms a GIC of stage 2 or higher,[262] with a rectangular superlattice generally of the form $C_{7n}Br_2$ or $C_{8n}Br_2$.[263–266] The interlayer spacing of Br_2 GICs varies from 7.03 Å for stage 2 compounds to 6.99 Å for stage 5 compounds.[264] This stage 2 intercalation structure scales in a simple way from bulk graphite to monolayer graphene, as explored by Jung et al.[267] Bromine adsorbs on outer surfaces of monolayer and few-layer graphene, and intercalates into every second plane, but does not form covalent C-Br bonds.

1.9.6. Interaction of Iodine with Graphene

It is almost universally agreed that molecular iodine does not intercalate into bulk graphite. This result is attributed to the low electronegativity of iodine and the lattice mismatch between molecular iodine and graphite.[254] However, I_2 can be cointercalated with other halogens such as Cl_2,[256] and several related interhalogens form GICs.[23] In the case of monolayer and few-layer graphene, surface adsorption of I_2 is observed by Jung et al.,[267] leading to p-type doping, an upward shift in the position of the Raman G peak, and quenching of the Raman 2D peak. The doping influence of I_2 is less than that of Br_2.[267] Additionally, Zbořil et al. have demonstrated the chemical reduction of fluorinated graphene by an intermediate graphene iodide phase,[248] indicating both the instability of graphene iodide and the possible application of graphene iodide chemistry for the reduction of more stable derivatives.

1.9.7. Non-Halogen Non-Covalent Chemistries

In addition to hydrogen and halogen-based forms of CMG, numerous other non-covalent chemistries have been explored to tune a range of graphene's properties. These include non-covalent functionalization for doping,[232,268] nucleation promotion for subsequent deposition steps,[269] increased graphene solubility,[233] lithographic patterning,[270] and band gap modulation.[271] One can imagine employing a non-covalently bound molecule as a mask for further covalent chemistries. For example, Wang and

Hersam demonstrated their ability to deposit continuous monolayers of 3,4,9,10-perylene-tetracarboxylic dianhydride (PTCDA) on the graphene surface, without regard for defects and substrate steps.[272] These films were subsequently patterned by feedback-controlled lithography,[270] and the resulting pattern employed as a mask for the deposition of N,N′-dioctyl-3,4,9,10-perylene-tetracarboxylic diimide (PTCDI-C8) on graphene. One can imagine a similar process by which a molecular mask is deposited, patterned, and employed for patterned fluorination of graphene. Although PTCDA may be unsuitable for the task, the range of adsorbates worthy of consideration is virtually limitless.

1.10 Graphene Growth and Fluorination Apparatus

Graphene studied in this dissertation was grown by CVD in the Micro and Nano Technology Laboratory and separately in the Micro/Nanofabrication Facility of the Frederick Seitz Materials Research Laboratory at the University of Illinois. In both cases, growth surfaces were held in a 1 inch quartz tube and heated from room temperature to 800 – 1000 °C by a split single-zone tube furnace. Gas delivery is provided by means of three independent mass flow controllers which deliver Ar, CH_4, and H_2. Precise growth conditions vary, and will be reported for each independent sample.

Fluorinated graphene samples are produced by two methods. Ds-GF is produced by mechanical exfoliation from bulk poly(carbon monofluoride) commercially available from Acros Organics (Geel, Belgium). Ss-GF is produced by exposure of monolayer graphene to XeF_2 gas at room temperature using an XACTIX XeF_2 etching system in the

Micro and Nano Technology Laboratory. Fluorination times are 7 minutes and nominal XeF_2 pressure is 3 torr.

1.11 Thesis Statement

This dissertation demonstrates FDSS of tungsten, platinum-iridium alloy, and hafnium diboride-coated tungsten, which results in a consistent improvement in scanned-probe lithographic patterning compared with CSE and standard ECE procedures. Using sharpened STM tips, we have identified monolayer CF flakes on the Si(100) 2 × 1:H surface, and observed a marked fluorine instability and flake decomposition concurrent with halogen etching of the underlying silicon substrate. In a comparison with CF, we synthesize monolayer C_4F on copper foil and characterize its structure and stability by STM. Unlike CF, which is fluorinated on both sides, single-sided C_4F is sufficiently stable at room temperature under low-energy electron bombardment to enable atomic-resolution imaging and the assignment of fluorine configuration by STM. We have verified the structure of C_4F by STM as well as STS, with exceptional agreement with theoretical models of isolated, infinite C_4F sheets. Furthermore, we characterize single- and double-sided graphene fluoride by XPS, providing additional information about the covalent C-F bonding in both forms of graphene fluoride. We conclude that fluorinated graphene, in particular ss-GF, is a wide-gap semiconductor with potential for future lithographic patterning and band gap modulation.

1.12 Figures

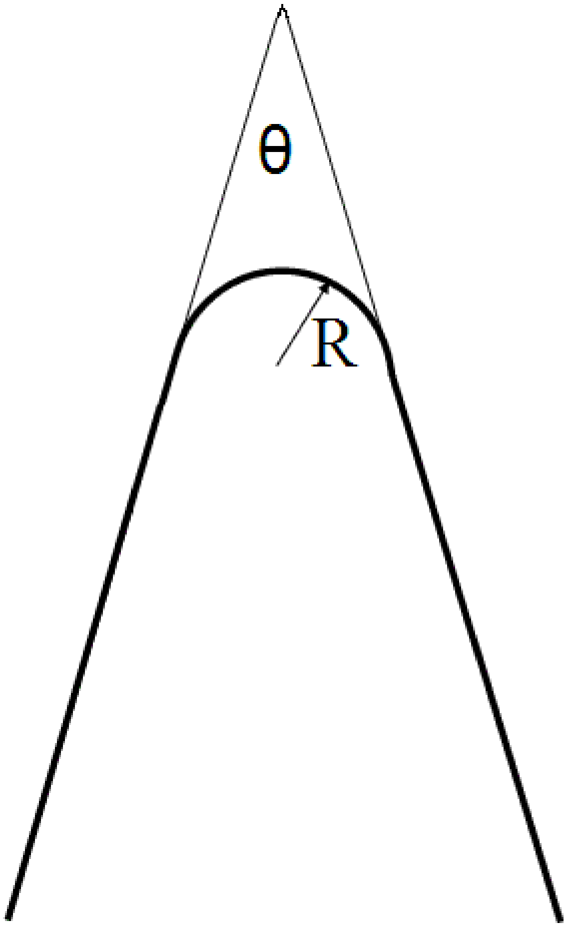

Figure 1.1: Schematic representation of the relevant geometric characteristics of a sharpened probe. The cone angle (θ) and radius of curvature (R_t) completely describe the typical form of the near-apex region of probes processed by sputter erosion sharpening.

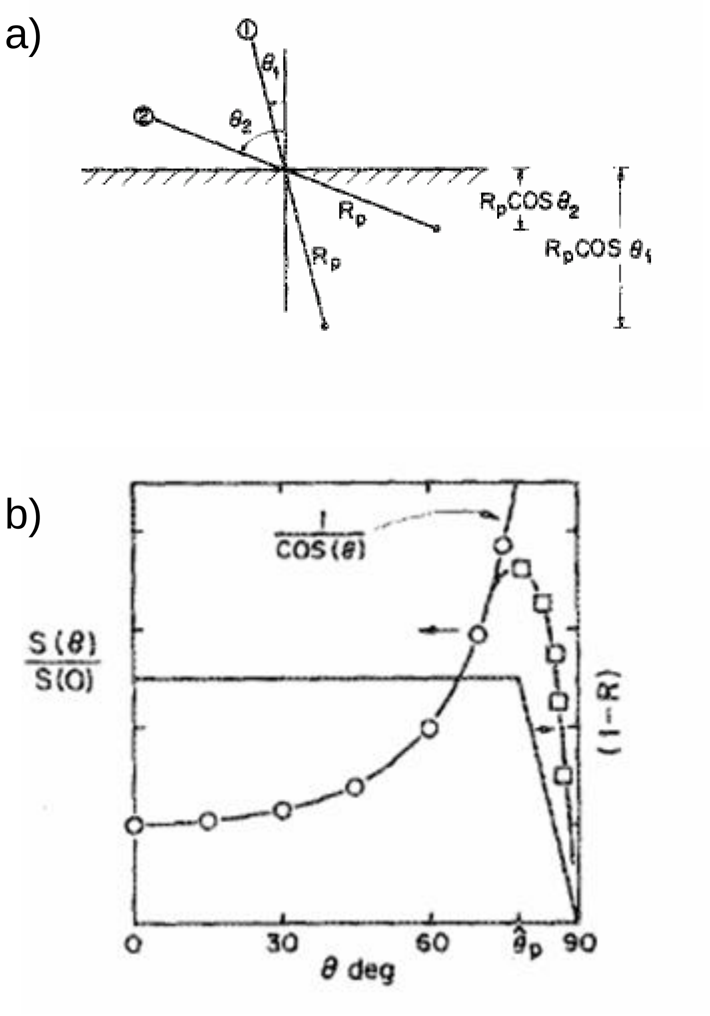

Figure 1.2: Theoretical representation of the dependence of sputter yield on angle of incidence. (a) Cosine dependence of energy distribution depth on angle of incidence. (b) This relation displays a typical peak and decline resulting from the ion reflection coefficient, R. The angular dependence of sputter yield is shown to increase for increasing angle of incidence, before peaking at critical angle θ_p and falling to zero for grazing incidence. Reprinted with permission from the Journal of Vacuum Science and Technology B, copyright 1986, American Vacuum Society.[273]

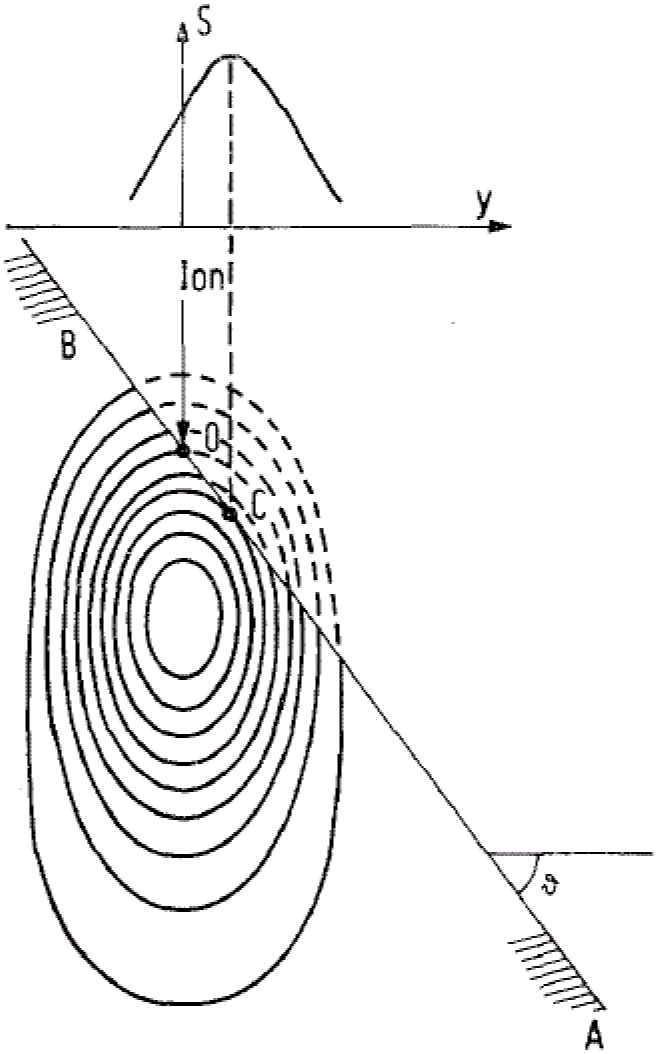

Figure 1.3: Schematic representation of sputter depth profile. Sigmund demonstrates the influence of ion penetration depth and the distribution of the sputter cascade on sputter erosion. The offset between the point of ion impact and the point of maximal sputter yield is shown to result. Reprinted with permission from the Journal of Materials Science, copyright 1973, Springer.[51]

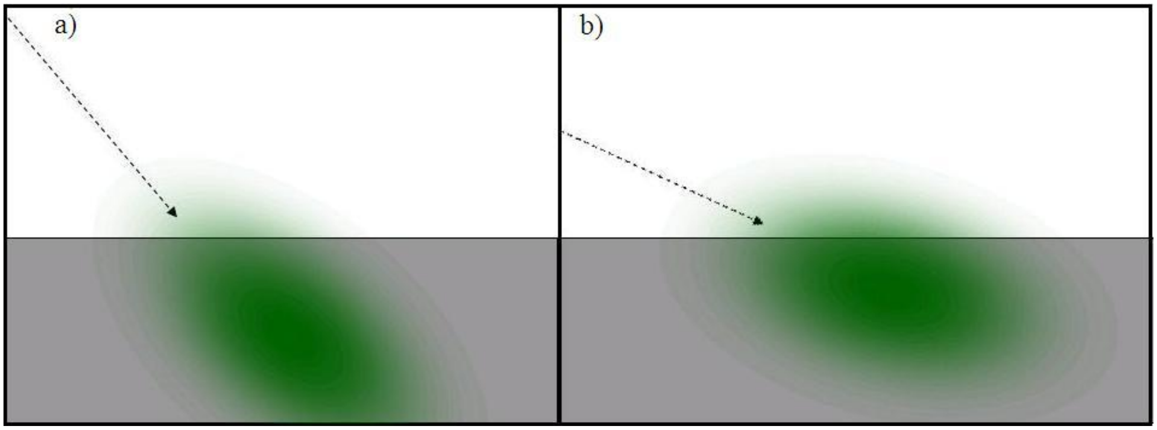

Figure 1.4: Schematic representation of the distribution of ion energy within the target substrate. The arrows demonstrate path of ion approach for two distinct angles of incidence. The distribution of ion energy is shown in green. Sputtering occurs most frequently at points where the energy distribution and surface overlap. (a) For a steeper angle of incidence, the overlap is less. (b) For glancing incidence, this overlap increases, leading to an increased sputter yield.

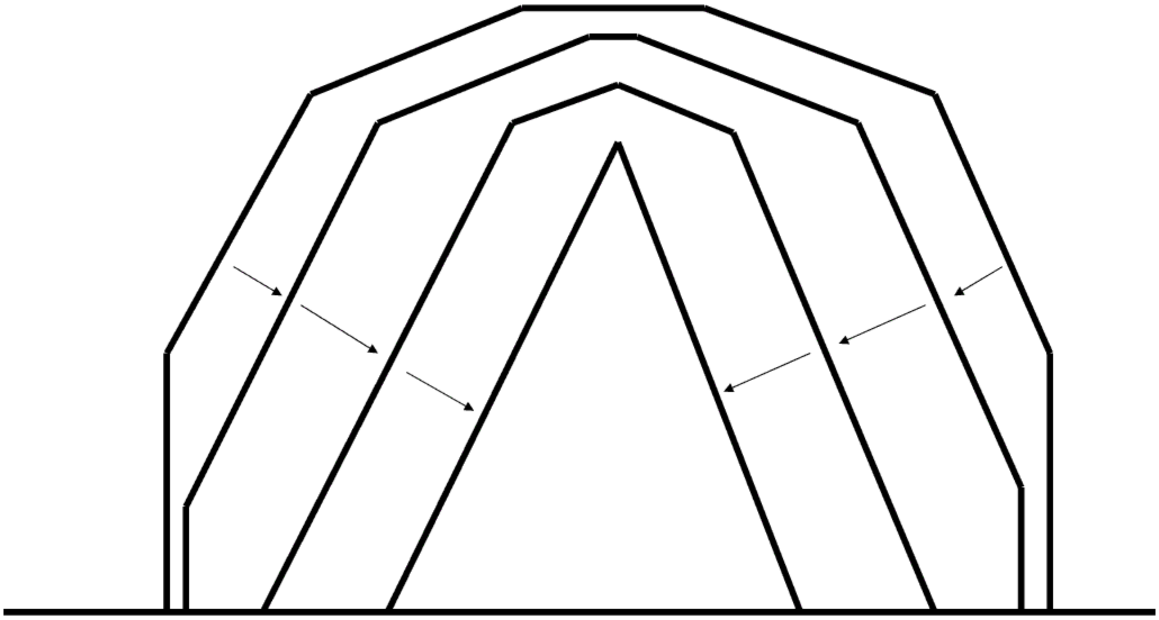

Figure 1.5: Flat-plane representation of first-order sputter erosion sharpening. Each plane erodes at a velocity related to the sputter yield at the corresponding angle of incidence. Ultimately, those planes which translate at maximal velocity are found to supersede all other planes. This simple model explains the relationship between the resulting cone angle and the relation between sputter yield and angle of incidence. The cone angle is twice the angle corresponding to maximal sputter yield.

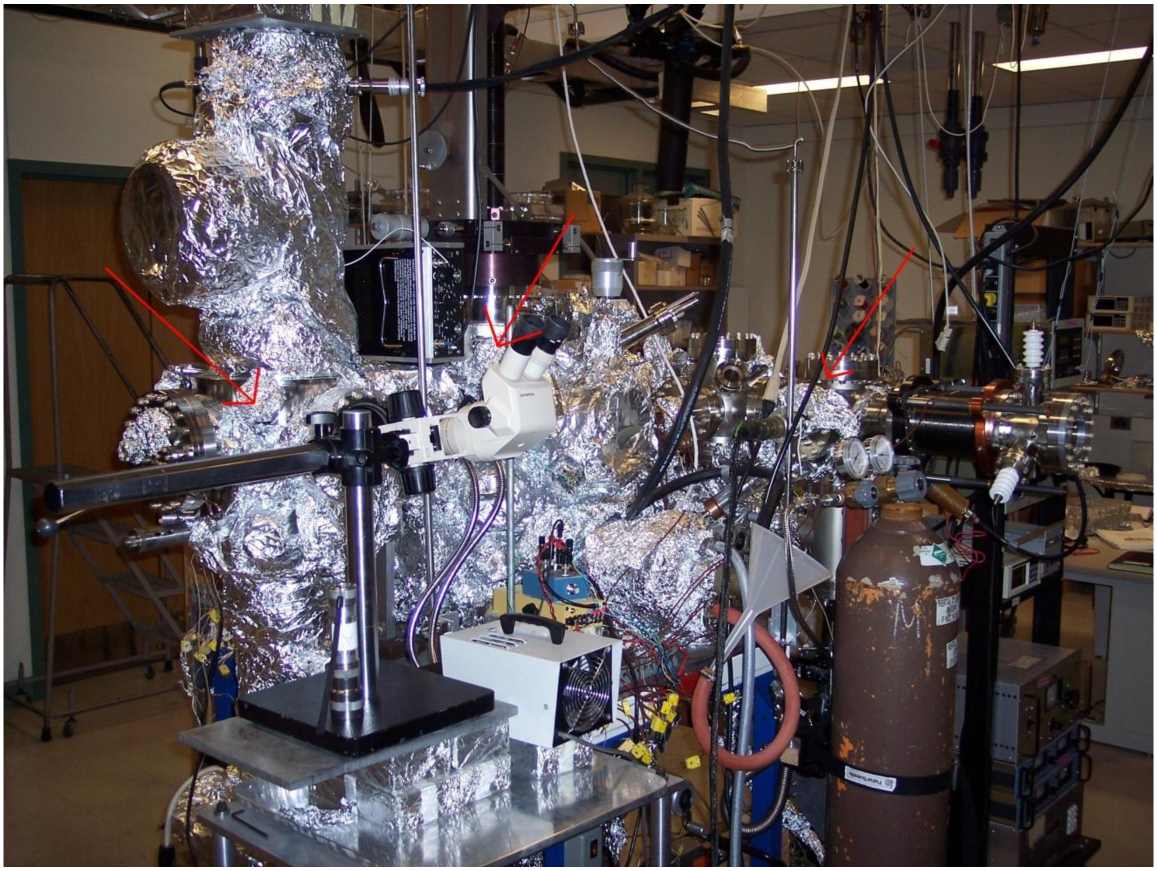

Figure 1.6: The "Chamber A" UHV system employed in this dissertation. Indicated with red arrows are the sputtering chamber where sputter erosion is performed (right), the preparation chamber where sample and tip cleaning and other preparation techniques are performed (center), and the scanning tunneling microscope (STM) chamber, where the microscope is located (left).

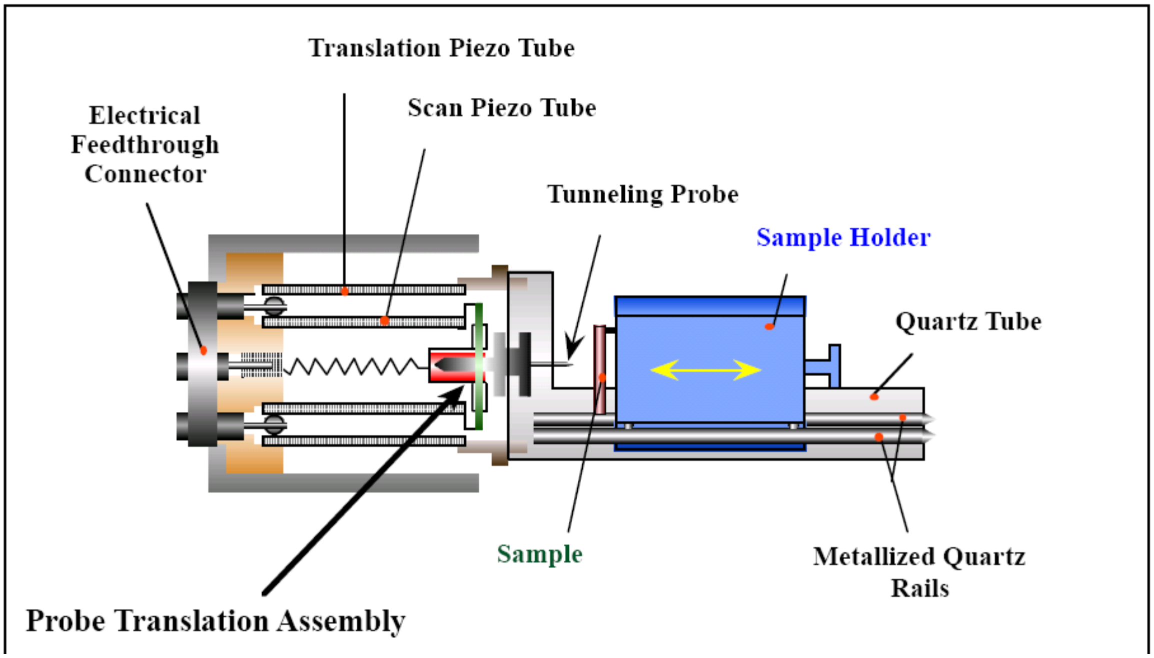

Figure 1.7: A schematic representation of the Lyding model scanning tunneling microscope employed in this dissertation. Diagram courtesy of Professor J. Lyding.

CHAPTER 2
FIELD-DIRECTED SPUTTER SHARPENING

In this chapter we explore FDSS, a modified sputter erosion sharpening process capable of producing metallic tips with 1 – 5 nm radii of curvature. We will explain the sharpening procedure in detail and demonstrate its efficacy for sharpening of platinum-iridium alloy, polycrystalline tungsten, and diamond-like carbon (DLC). We also explore the subject of off-axis FDSS, for cases where the ion beam is unidirectional but oriented non-axially to the probe, and provide experimental demonstration of this effect.

We then offer a theoretical model for an ion flux in the vicinity of a biased probe, based on the simplifying assumption of the probe tip as a perfectly conducting biased wire in isolation, model the variation of ion flux with probe bias, and simulate the sputter erosion process. Some of the elements of this chapter we have discussed previously by the author.[68] These results will be reviewed here, and additional data presented.

Section 2.1 will describe the FDSS process in general, and specific experimental results will be presented in Section 2.2 for Pt-Ir alloy, and in Section 2.3 for W. We will discuss off-axis sputtering in Section 2.4. Section 2.5 will discuss FDSS of less conductive materials such as DLC. Section 2.6 will describe theoretical models of FDSS, including a mathematical model of ion paths, finite element analysis of ion paths, and a Monte Carlo simulation of sputter erosion for FDSS and CSE.

2.1. Field-Directed Sputter Sharpening

FDSS is a process related to CSE, but altered by the application of a positive probe bias, which serves to deflect the ion beam from the probe apex in a controllable manner. A flux of inert gas ions is oriented axially along the axis of the probe wire and tip, which has been previously sharpened to radius < 1 μm using other methods. These energetic ions are deflected by the electric field surrounding the probe, and some ultimately impinge upon the tip. From the point of impact, erosional processes follow the physics described in Section 1.3 for CSE.

Two related factors influence the results of FDSS processing: modification of the ion path and therefore angle of incidence, and a controllable and preferential reduction of flux and surface diffusion in the apex region. We also gain the additional benefit of tip shank shielding, where the deflected ion beam does not impact areas distant from the apex. This shielding effect leads to a reduced etching rate and preserves any desirable structure on the probe shank.

2.2. Sharpening of Platinum Iridium Alloy Probes

To demonstrate the FDSS process, we employ an STM tip composed of Pt-Ir alloy (90% Pt, 10% Ir). This is a popular probe material due to its resistance to oxidation, acceptable mechanical properties, and the high work function of Pt (5.64 eV). For our purposes, the main advantage is oxidation resistance and the resulting ability to transfer probes between sputtering and characterization chambers without concern for the chemical and structural changes induced in other materials (e.g. tungsten) under ambient conditions.

Pt-Ir probes are prepared by two techniques. Those reported here were purchased commercially from Materials Analytical Services (MAS) Incorporated (Suwanee, Georgia). We refer to these tips as Pt-Ir-MAS probes. In other cases, we etch probes from Pt-Ir wire[39] in $CaCl_2$ solution. We refer to these as etched Pt-Ir probes. A typical TEM micrograph of a Pt-Ir-MAS probe is shown in Figure 2.1. Note that the typical probe has a single apex with a radius of curvature of approximately 100 nm. There is typically a thin layer of contamination on the probe apex, which we attribute to carbon contamination arising from the etch process.[274] On some occasions we observe significantly thicker contaminant films, but these are easily removed by sputtering.

In one experiment, a Pt-Ir-MAS probe is characterized by TEM and then processed by FDSS. The probe is biased at 400 V relative to vacuum chamber ground while 2000 eV Ne ions are directed along the axis of the probe wire. Several subsequent processing cycles are carried out under identical conditions, and the tip geometry is found to change significantly. Initial and final TEM micrographs are shown in Figure 2.2, and we see that the initial 100 nm tip radius is reduced to less than 1 nm. During the sputter sharpening process, successive TEM micrographs are taken at various sharpening stages. As seen in Figure 2.3, the tip radius progressively decreases towards equilibrium.

The final radius of curvature of the Pt-Ir probe is substantially smaller than those previously reported for tips prepared by CSE and represents the sharpest known STM tip prepared by sputter erosion.

Additionally, in comparison to later experiments discussed in this dissertation, this experiment employed a reduced ion current density (resulting in slower sharpening) and a lighter ion species (Ne rather than Ar). Both of these variables are expected to further reduce the achievable radius of curvature.

2.3. Sharpening of Tungsten Probes

Polycrystalline tungsten probes are commonly employed in STM due to their ease of preparation and low cost. Tungsten probes produced by NaOH ECE can be further sharpened with the FDSS procedure, under conditions similar to those employed for Pt-Ir alloy. As a disadvantage, the ambient exposure required before TEM characterization commonly results in oxidation of the probe apex prior to analysis. This difficulty is eliminated if electron microscopy is foregone in favor of immediate transfer to UHV. Results of STM characterization will be discussed in Chapter 4.

Several demonstrations of tungsten probe sharpening are provided in Figures 2.4 and 2.5. In each case, the probe radius is found to be significantly reduced from initial conditions, and such a result is found to be typical for similarly prepared probes. Starting from an initial radius between 10 nm and 100 nm, we find final tungsten probe radii to fall to within a range of 1 – 5 nm, a substantial improvement over previous results from the literature discussed in Chapter 1. It is believed that ambient exposure and electrostatic discharge adversely affect these tungsten probes during transfer, resulting in oxide growth. This growth appears predominantly at the probe apex, as expected, and results in detectable blunting of the tip prior to characterization.

2.4. Off-Axis Sputter Erosion Sharpening

We now explore the nature of off-axis FDSS, where the ion beam is unidirectional, but is misaligned with the axis of the probe wire. In a result consistent with CSE of surfaces, we note that sharpening produces a similarly sized, sharp single-apex when compared to axially aligned FDSS. However, the tip is oriented along the path of the ion flux, rather than the axis of the probe wire. Starting from a polycrystalline W tip prepared by ECE (Figure 2.6a), we process the tip by FDSS (V_{beam} = 2000 V, V_{tip} = 400 V: V_r = 0.2). The resulting tip has a <5 nm radius of curvature on the primary apex, but this apex is no longer axially oriented to the wire. This demonstration of off-axis FDSS suggests that precise alignment of the probe wire to the ion beam is not required for FDSS and that creation of novel tip geometries may be enabled by control of the sputtering geometry.

2.5. Sharpening of Diamond-Like Carbon Probes

Given its dependence on a field-directed ion flux, FDSS is generally applicable only to conductive materials. In the case of a more insulating tip, charge accumulation resulting from bombardment by a positive charged ion species counteracts the deflective influence of biasing. Sharpening occurs in the case of highly resistive materials, but the result more closely approximates that of CSE, with a larger equilibrium radius of curvature.

We have explored several materials in this dissertation, often targeting materials with properties suggestive of a stable, long-lived STM tip. In Chapter 3 we explore HfB_2 for this purpose, but in earlier work we considered a resistive coating of diamond-like carbon (DLC), deposited by physical vapor deposition (PVD) by Richter Precision (East Petersburg, Pennsylvania).

We first prepare a polycrystalline W tip by ECE and sharpen it by FDSS (V_{beam} = 1200 V, V_{tip} = 200 V: V_r = 0.167). The resulting tip has a sharp single-apex, but oxidized significantly following ambient exposure (Figure 2.7a). This tip was spot welded to the head of a stainless steel bolt passed through a threaded hole in a Cu block. The screw was then recessed into the Cu block for protection during shipping and handling. After receipt, with the tip still recessed, the entire block was coated using Richter Precision's Titankote^{TM} C11 DLC PVD coating technology. This process produces a film with the specifications shown in Table 2.1.[275]

Table 2.1: Properties of PVD Titankote^{TM} C11 DLC films from Richter Precision

Composition	DLC (a-C:H)
Thickness (μm)	1.0 – 4.0
Micro-hardness (HV)	2000 – 3000
Coefficient of friction	0.1
Process temperature (°C)	204

After coating, the tip was shipped back to the University of Illinois for characterization. It exhibited a single rounded apex with a ~300 nm radius of curvature (Figure 2.7b). The original W core was clearly visible through the deposited film. Adhesion of the continuous DLC coating to the W core was good, with a smooth surface at the tip apex. The gaps visible on the coated tip are a result of the wire orientation within the recess, where one side of the tip was oriented away from the PVD source. Away from the apex, the films exhibited a columnar microstructure.

The tip was then processed by FDSS (V_{beam} = 1600 V, V_{tip} = 400 V: V_r = 0.25), resulting in a single apex with a 15 nm radius of curvature, significantly blunter than conductive FDSS probes, but sharper than the initial tip and consistent with CSE (Figure 2.7c). It is important to note that this sharpening process was completed without stripping the DLC coating from the W tip. Therefore, even for insulating coatings, it is possible to sharpen a very thin DLC film (e.g. for AFM applications).

Attempts to employ this tip for STM were limited by its low conductivity. Stable scanning and spectroscopy were ultimately achieved; however, subsequent TEM images clarify the origin of this stability. As shown in Figure 2.7d, the DLC probe apex fractured during scanning, exposing the W core.

We conclude that DLC is a poor material for STM tips, due to its low conductivity. However, the use of DLC for non-conductive AFM tips is worthy of further exploration. Furthermore, increasing the conductivity of diamond or diamond-like materials by doping may improve sharpening efficacy. Although FDSS is generally incompatible with resistive materials, the benefit of sputter erosion sharpening remains, and the resulting 15 nm radius of curvature remains exceptional for the sharpening of DLC.

2.6. Simulation of Field-Directed Sputter Sharpening

Here we describe a simple model for ion deflection during FDSS and compute the variation of apex ion current density as a function of probe bias. We model the tip apex as an infinite, perfectly conducting cylinder, which is bombarded transversely with a positively charged energetic ion beam while biased positively. Following the derivation that we have described previously,[68] we write the well-known equation of the electric potential in which a singly ionized atom sits when in the vicinity of this infinite wire:

$$U(\vec{r}) = U(r) = \frac{qV_t R_t}{r} \equiv \frac{k}{r} \tag{2.1}$$

This represents a repulsive Kepler potential,[276] and thanks to the study of planetary motion (a related, attractive Kepler potential) by Johannes Kepler, we can immediately write an equation describing the motion of a singly-ionized atom passing near the wire, which follows a hyperbolic path:

$$\frac{1}{r} = C\left(e\cos\left(\theta - \theta_0\right) - 1\right) \tag{2.2}$$

$$C = \frac{km}{L^2} \tag{2.3}$$

$$e = \sqrt{1 + \frac{2EL^2}{mk^2}} \tag{2.4}$$

Where m is the mass of the ion species, E is the initial ion energy (qV_{beam}), (r,θ) are polar coordinates describing the position of the ion, θ_0 is a constant of integration, and L is the angular momentum given by:

$$L = x_0\sqrt{2mE} \tag{2.5}$$

Since we can assume the ion approaches from an infinite distance, $r \rightarrow \infty$ as $\theta \rightarrow \pi/2$, we can determine the constant of integration:

$$\theta_0 = \frac{\pi}{2} - \arccos\left(\frac{1}{e}\right) = \arcsin\left(\frac{1}{e}\right) \tag{2.6}$$

From here, given initial conditions (ion energy, initial offset from the probe apex, ion species) we can compute the path of each ion, determining when and where the probe is impacted. In Figure 2.8 we model several typical paths for a 2 keV initial ion energy and 1 keV probe bias ($V_r = 0.5$). The probe in our model has a 10 nm radius of curvature, and we show ion offsets of 5 nm, 7 nm, 9 nm, and 12.5 nm. As expected, each ion follows a hyperbolic path away from the probe apex.

This deterministic model then allows us to calculate the expected ion current density at the probe apex under various sputtering conditions. We will first assume that the initial ion flux is uniformly distributed. Although the ion flux actually has a Gaussian distribution, this assumption is reasonable because the ion beam diameter is ~2 mm and our region of interest is ~100 nm.

To determine average ion flux across the probe tip, we need simply to determine which range of initial positions leads to sputter erosion of the probe, and which range leads to full deflection such that no sputtering occurs. We note that the largest initial offset for which impact occurs will be that for which the ion impacts at a 90° glancing angle of incidence (Figure 2.9). This condition relates to the case where the ion path is perpendicular to the vector **r**, at the point where **r** equals the tip radius, R_t. To determine this, we compute:

$$\frac{\partial r}{\partial \theta} = \frac{e \sin(\theta - \theta_0)}{C(e \cos(\theta - \theta_0) - 1)} = 0 \tag{2.7}$$

Noting that C and e are finite and e is non-zero in the case of a repulsive potential, the solution to this equation corresponds to the case where the sine term is zero:

$$\theta = \theta_0 = \arcsin\left(\frac{1}{e}\right) \tag{2.8}$$

The case for which this occurs at the outer edge of a tip of radius R_t corresponds to:

$$\frac{1}{r} = \frac{1}{R_t} = C\left(e \cos\left(\arcsin\left(\frac{1}{e}\right) - \arcsin\left(\frac{1}{e}\right)\right) - 1\right) = C(e-1) \tag{2.9}$$

Solving this equation, we note that the tip bias and initial ion energy enter the equation only as the ratio, and we introduce the V_r term as follows:

$$\frac{qV_t}{E} \equiv V_r \tag{2.10}$$

In route to solving for x_0 we combine Equations 2.2 and 2.9 to produce:

$$\sqrt{1 + \frac{4x_0^2}{V_r^2 R_t^2}} = \frac{2x_0^2}{R_t^2 V_r} + 1 \tag{2.11}$$

This equation has a simple solution:

$$x_0 = R_t\sqrt{1-V_r} \qquad (2.12)$$

From these calculations, and an approximation of the relationship between yield and angle of incidence, it becomes possible to explain the influence of modified angle of incidence on sputtering. In Figure 2.10a, we show the calculated sputter yield at each position across the tip apex for a 5 nm radius probe. The zero point corresponds to the tip apex, and the 5 nm point corresponds to the edge of the tip. In the CSE case, as expected, yield increases as we move away from the apex, and the angle of incidence changes accordingly. Because the tip is modeled as an isolated wire, this yield drops to zero at 5 nm. For FDSS, a similar increase in yield is seen, but we see increased sputtering yield along the sides of the tip and an inward shift in the point of maximal sputtering yield. As the size of the tip decreases, the curve scales proportionally. Calculating this result demands the approximation of the dependence on angle of incidence of the sputtering yield. We employ a simple model which represents the basic trend, as shown in Figure 2.10b. The leading edge of the curve is a cosine relationship, and the falling tail is accommodated by multiplying by a correction factor at shallow angles.

We compare this mathematical analysis to a finite element model of a more realistic tip structure in two dimensions, shown in Figure 2.11a. We simulate a number of ion paths around the tip by an iterative electric potential computation on a 2.5 Å square mesh, with an iterative Poisson solver and the Jacobi method. Zero field-conditions are applied at the left and right boundaries, and the electric potential is fixed to ground at the upper edge and V_t at the lower edge. The tip is assumed to be at a uniform electric potential. Within each square of the mesh the ion path is computed deterministically by Newtonian mechanics, and the path is computed recursively until impact with the tip occurs or the ion leaves the system. For various values of V_r, the average ion current density is determined by simulating ion flux and determining the range of initial positions for which probe impact occurs. The results of these simulations are plotted in Figure 2.11b. Also shown is the solid curve corresponding to Equation 2.12, in exceptional agreement with the results of finite element analysis.

We further simulate the FDSS process by a Monte Carlo simulation of the sputter erosion process similar to the work of Hartmann et al.[277] Following an ion impact event, "atoms" corresponding to pixels in the tip image are removed from the system with a probability determined from Sigmund's second-order sputter erosion theory,[46] with spread determined by TRIM and a "deflection" parameter inserted manually to account for ions with a high angle of incidence. The process is calibrated to experimentally determined sputter yields for the ion species and substrate material employed (Ar and W).[66] The sputter erosion process then proceeds, with ions injected randomly and uniformly across the tip, and is allowed to follow the electric potential induced by the tip bias. The electric potential surrounding the probe is recalculated iteratively following ion impact. Though the process is inefficient, it is suitable for the small systems here studied. The results of sputter erosion are shown in Figure 2.12. We find that the tip sputtered under CSE ($V_{beam} = 1600$ V, $V_{tip} = 0$: $V_r = 0$) has a more significant microstructure along the shank, with ~10 nm features. In contrast, the tip processed by FDSS ($V_{beam} = 2000$ V, $V_{tip} = 400$ V: $V_r = 0.2$) has a smooth edge, with ~1 nm features. Because the simulation does not fully account for surface diffusion, we do not consider the simulated radius of curvature of the apex to be a suitable metric, yet the distinction between sputtering techniques is clear.

2.7. Discussion

The FDSS technique is found to produce exceptionally sharp probes and to be self-limiting and reproducible. Of note is the relative improvement seen when compared with the CSE technique. The radius of curvature for some probes was found to be ~1 nm, below the 1.6 nm projected range for 1.6 keV Ar in Pt reported by TRIM, although in general this range was expected to offer a lower bound for sharpening procedures. We find that sharpening of less conductive materials, such as DLC, leads to blunter tips, likely as a result of charge accumulation neutralizing the influence of probe bias. Simulation results suggest that the improved sharpening efficacy of FDSS is due to a combination of modulated ion path and reduced ion current density at the probe apex.

2.8. Figures

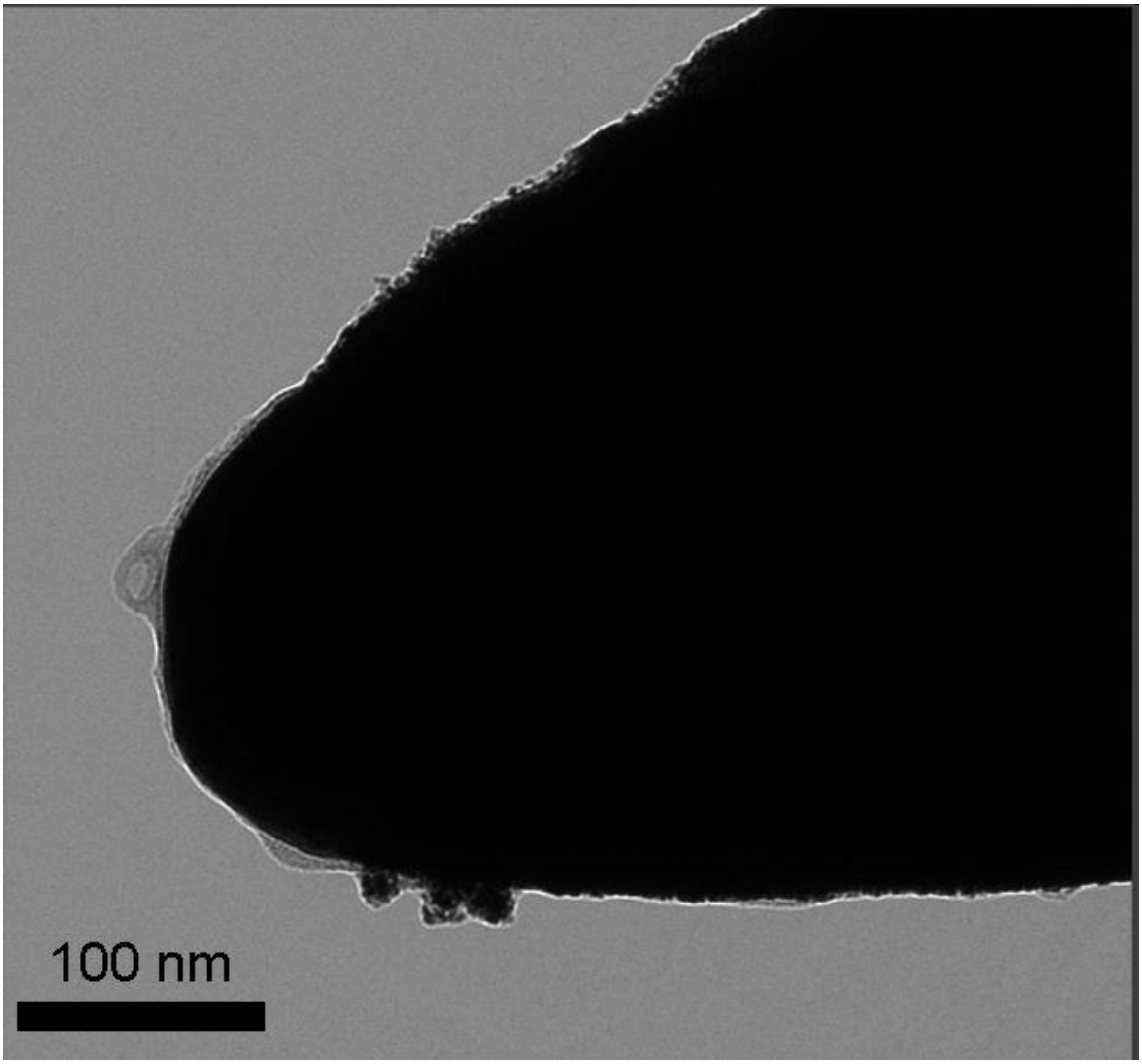

Figure 2.1: Transmission electron micrograph of a typical MAS Pt-Ir probe. The radius of curvature is approximately 100 nm and a mild surface contamination layer is visible.

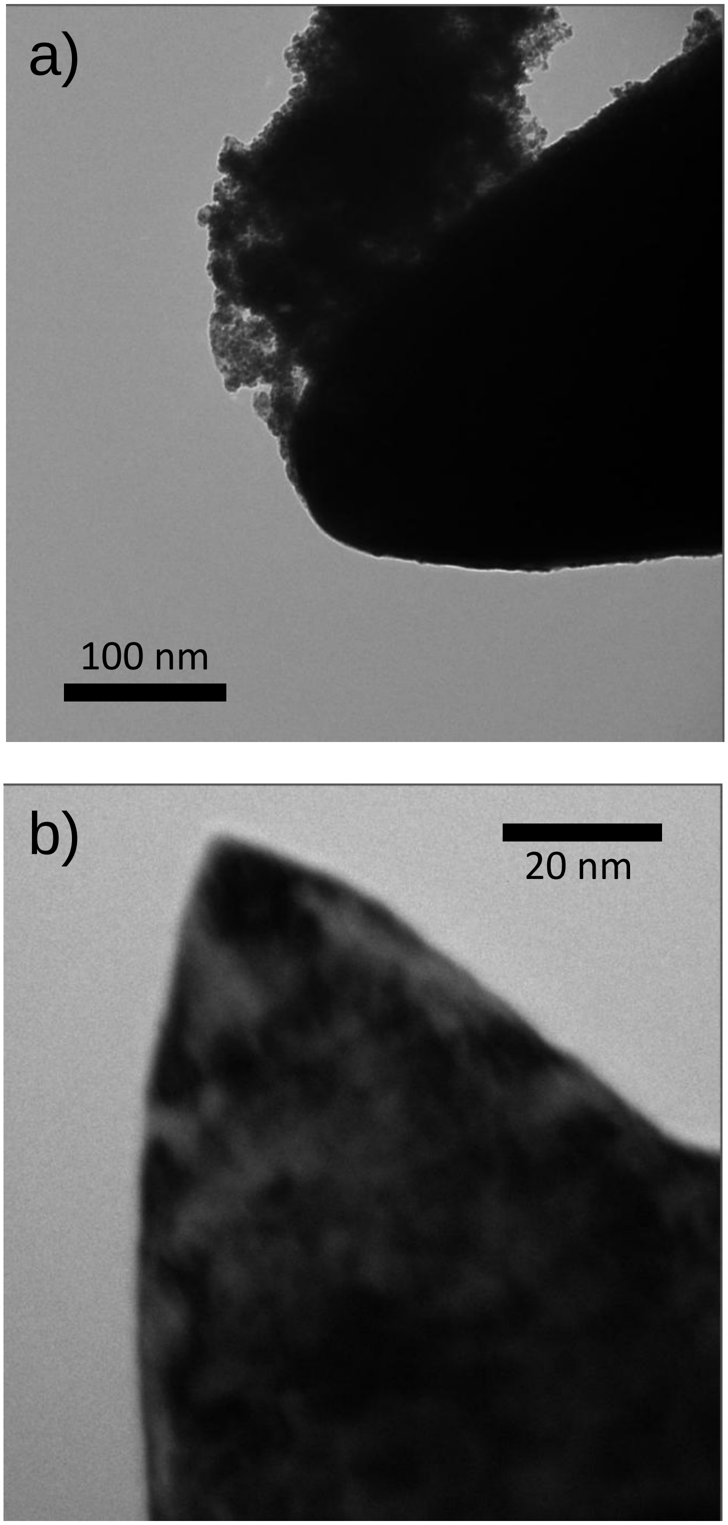

Figure 2.2: Sharpening of a MAS Pt-Ir probe subjected to FDSS. An ion energy of 2 keV and probe bias of 400 V were employed for 195 minutes. (a) Initial probe form. (b) Final probe form. Radius of curvature is reduced to ~1 nm.

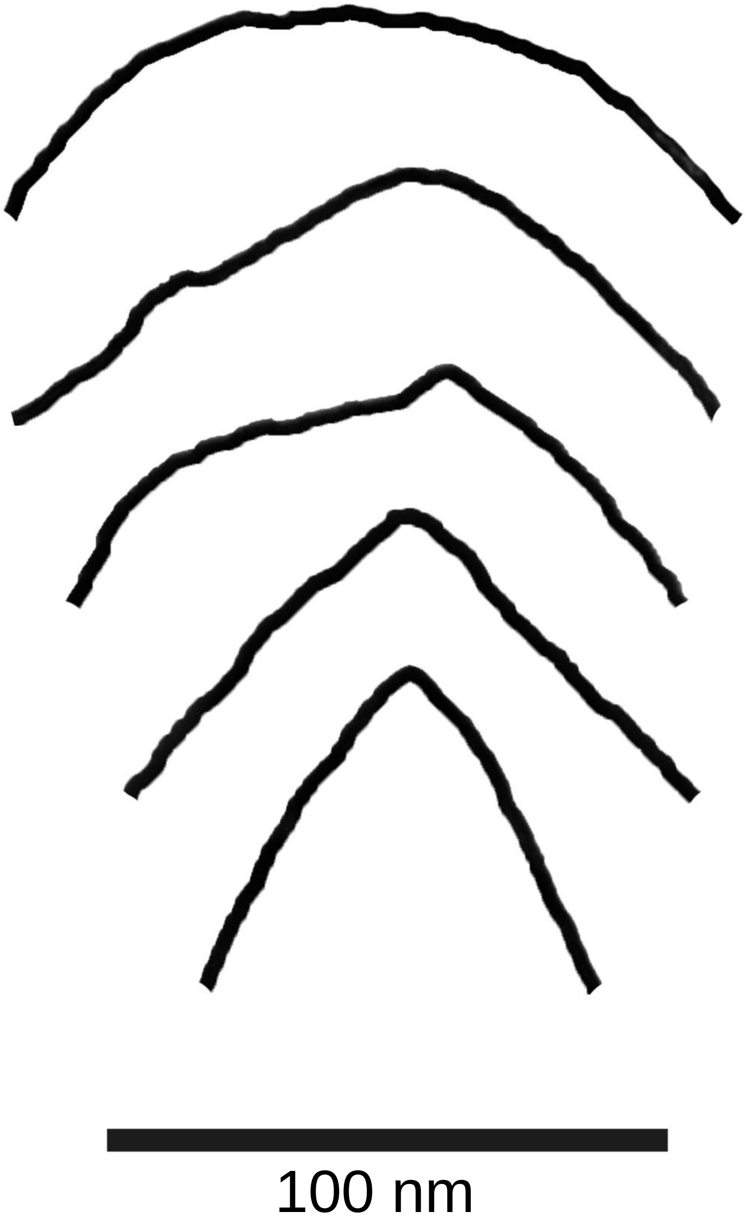

Figure 2.3: Comparison between subsequent erosion stages of a platinum iridium probe subjected to FDSS. An ion energy of 2 keV and probe bias of 400 V were employed. Time intervals between images are (from top to bottom): 75 min, 60 min, 30 min, 30 min. Initial and final images correspond to those shown in Figure 2.2.

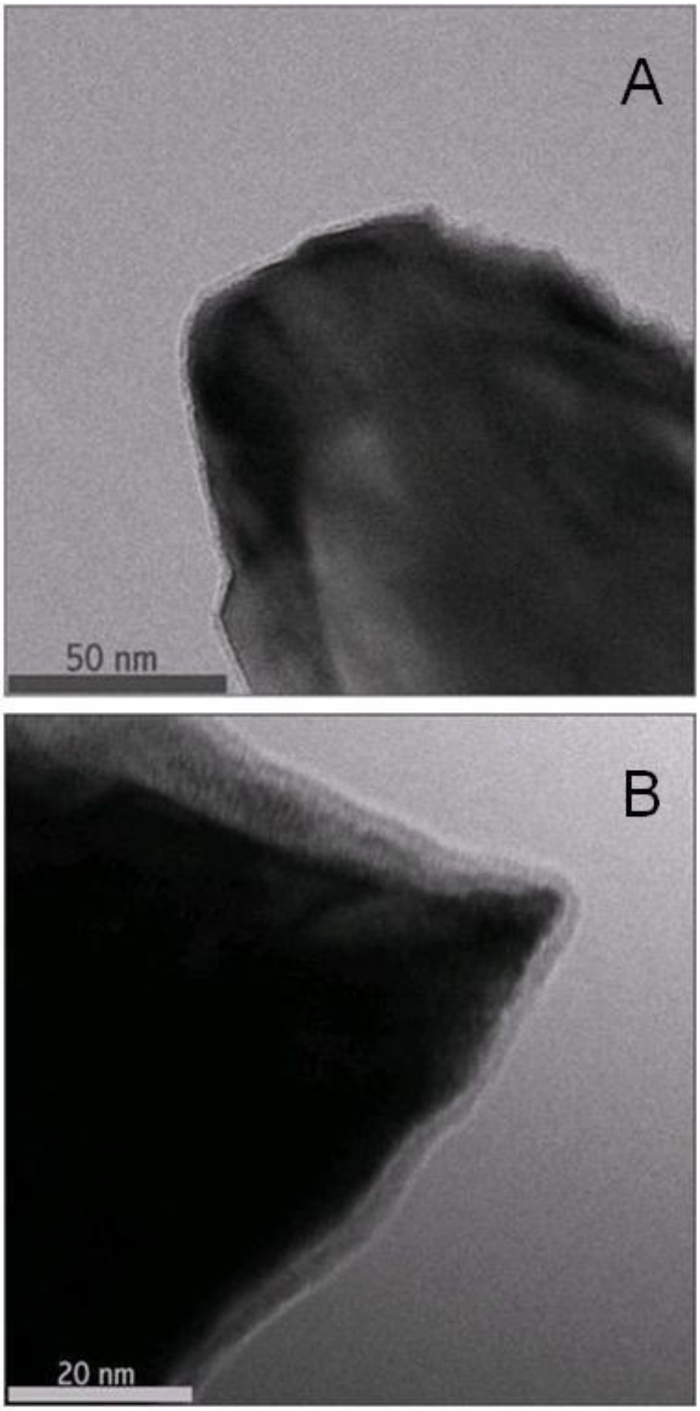

Figure 2.4: Demonstration of FDSS on a polycrystalline W probe. (a) Initial probe. (b) Final probe. Ion energy of 2 keV and probe bias of 400 V were employed for 15 min. The final probe radius of curvature is 1 – 2 nm when measured at the subsurface W layer.

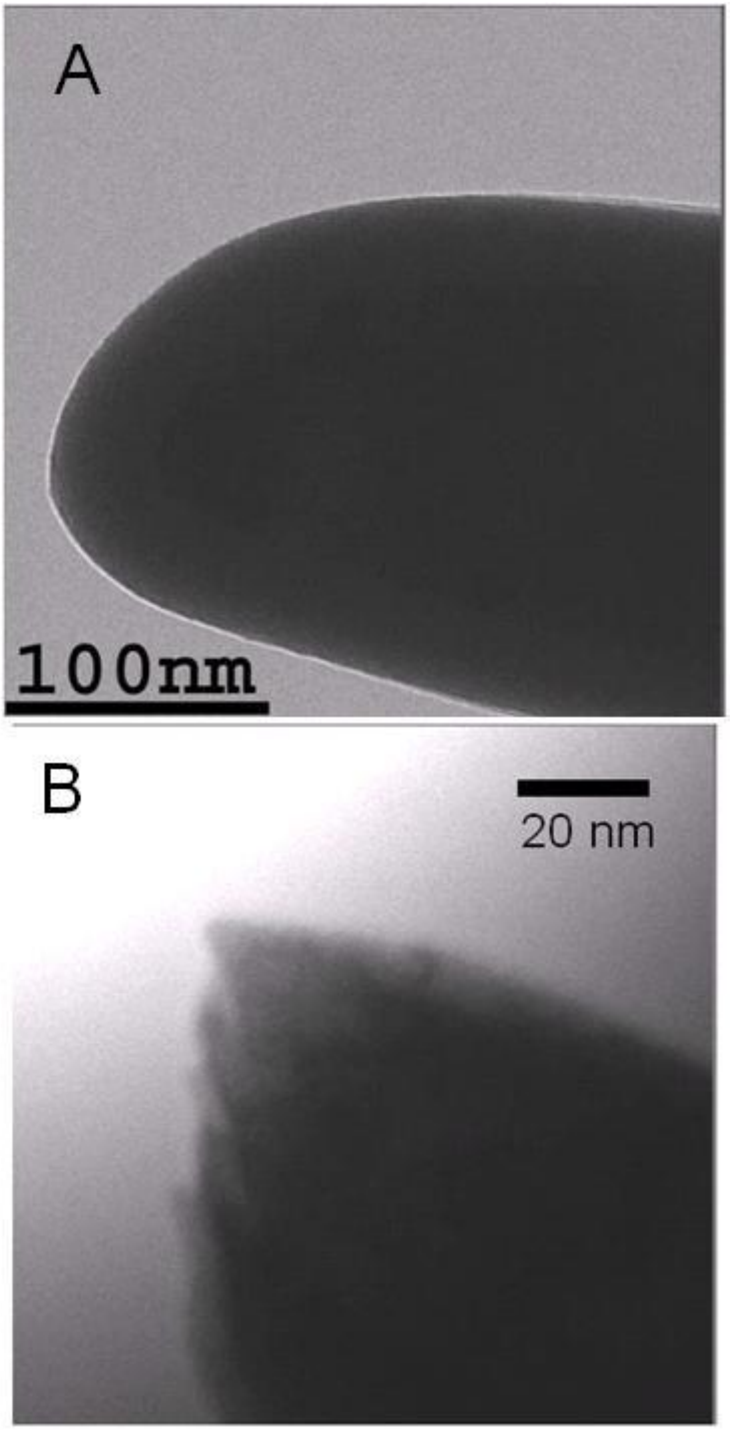

Figure 2.5: Further demonstration of polycrystalline tungsten sharpening. Ion energy of 2 keV was employed and a probe bias of 400 V was applied during sputtering, which proceeded for 35 min. (a) Initial probe. (b) Probe following FDSS.

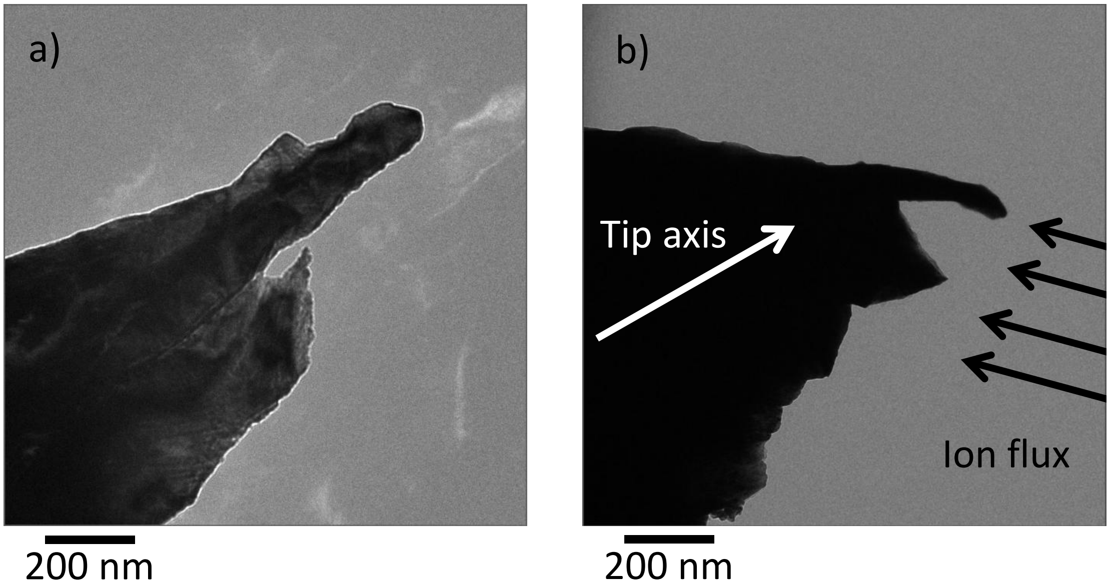

Figure 2.6: Demonstration of off-axis sputter erosion sharpening of W. (a) Initial tip. (b) The sharpened tip, following off-axis sputter erosion. The tip axis and ion flux direction are shown, and the sharpened apex is aligned with the ion flux.

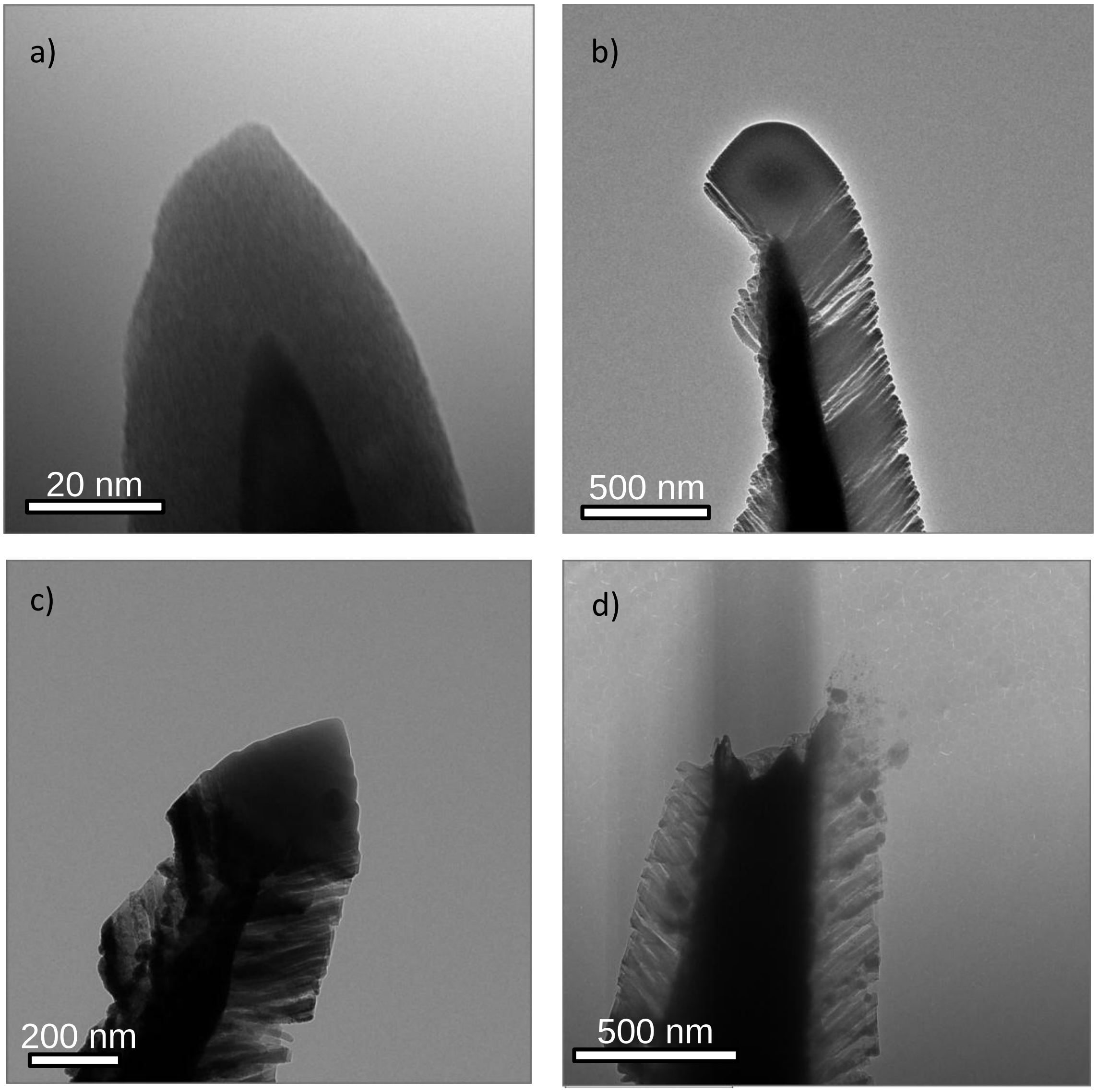

Figure 2.7: Preparation and sharpening of a DLC STM tip. (a) W tip has been sharpened by FDSS to a <5 nm radius of curvature. (b) This tip has been coated commercially with a DLC film to a thickness of ~300 nm, resulting in a ~300 nm radius of curvature. (c) This tip has been sharpened by FDSS, resulting in a ~15 nm radius of curvature DLC tip. (d) After use in the STM, this tip was damaged.

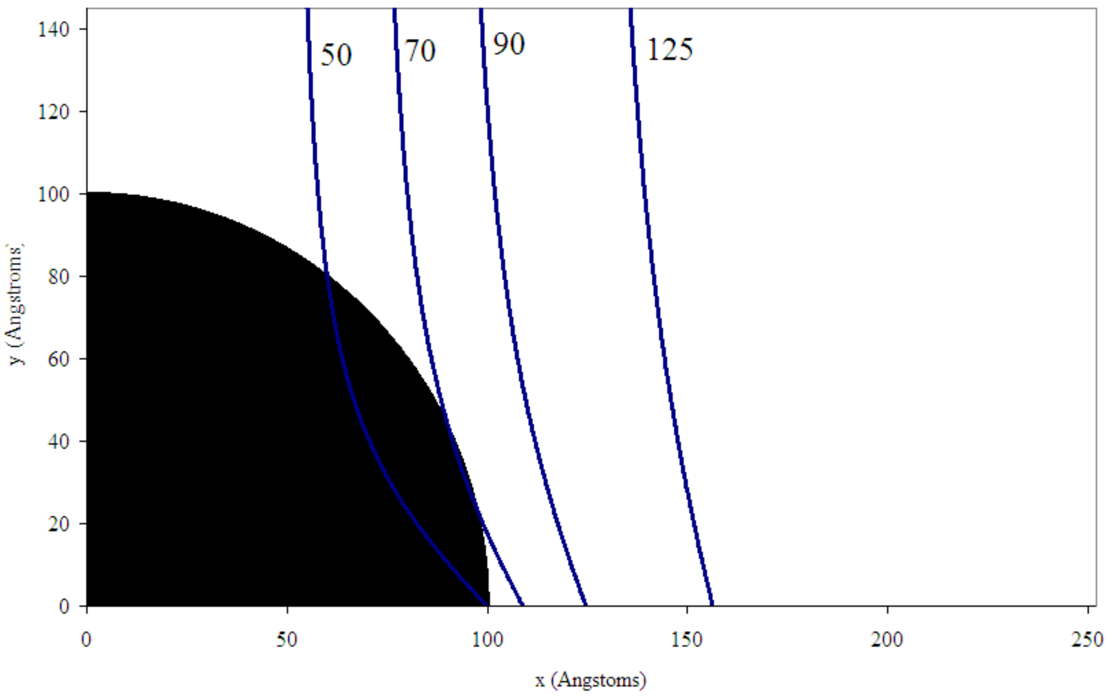

Figure 2.8: Simulation of several singly ionized Ar ion paths around a biased probe. Probe bias is 1 kV with initial ion energy of 2 keV and tip bias of 1 kV ($V_r = 0.5$). Initial ion positions are shown (50 Å, 70 Å, 90 Å, 125 Å).

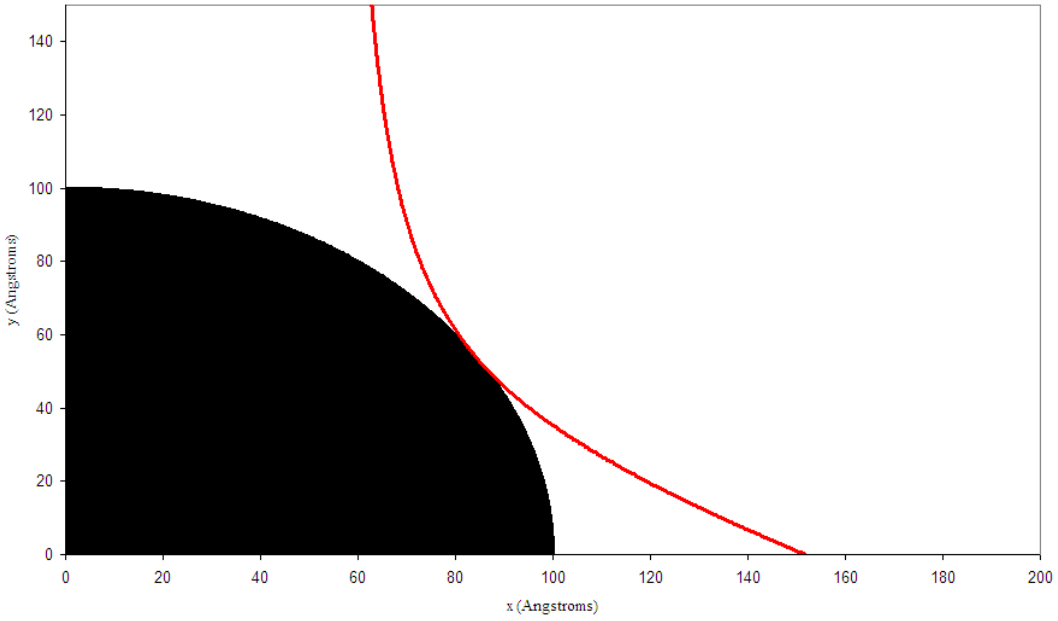

Figure 2.9: Calculated ion path for a glancing impact, as determined by Equation 2.9. In this system, ion energy was 2 keV, and the probe was biased to 1.4 keV. The radius of the probe was fixed at 100 Å, and singly ionized argon ions were assumed.

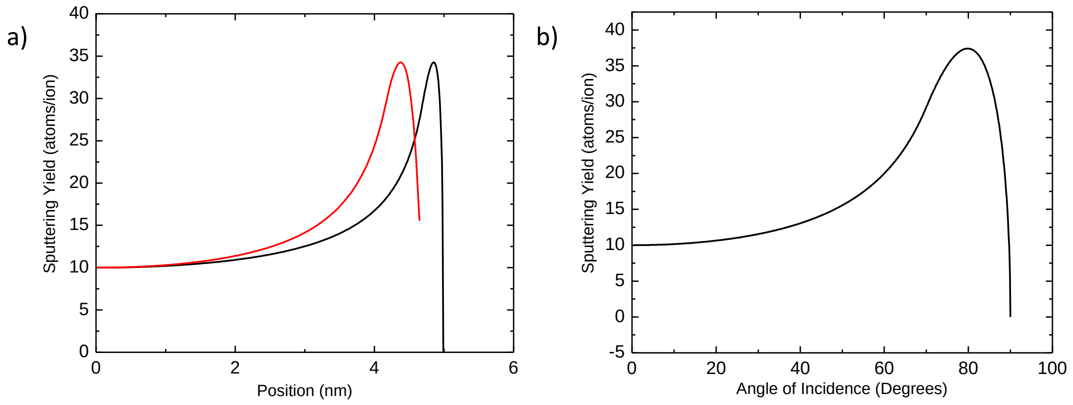

Figure 2.10: Calculated sputter yield data. (a) Calculated sputtering yield relative to distance from the apex of a 5 nm diameter tip for both CSE (black) and FDSS (red) sharpening where FDSS uses 2000 eV ions with a 1000 V tip bias and CSE uses 1000 eV ions with a grounded tip. Sputtering yield is compressed near the tip apex; with an increase in yield across the edge of the tip. (b) Curve representing the approximated yield versus angle relationship employed to calculate the curves in (a).

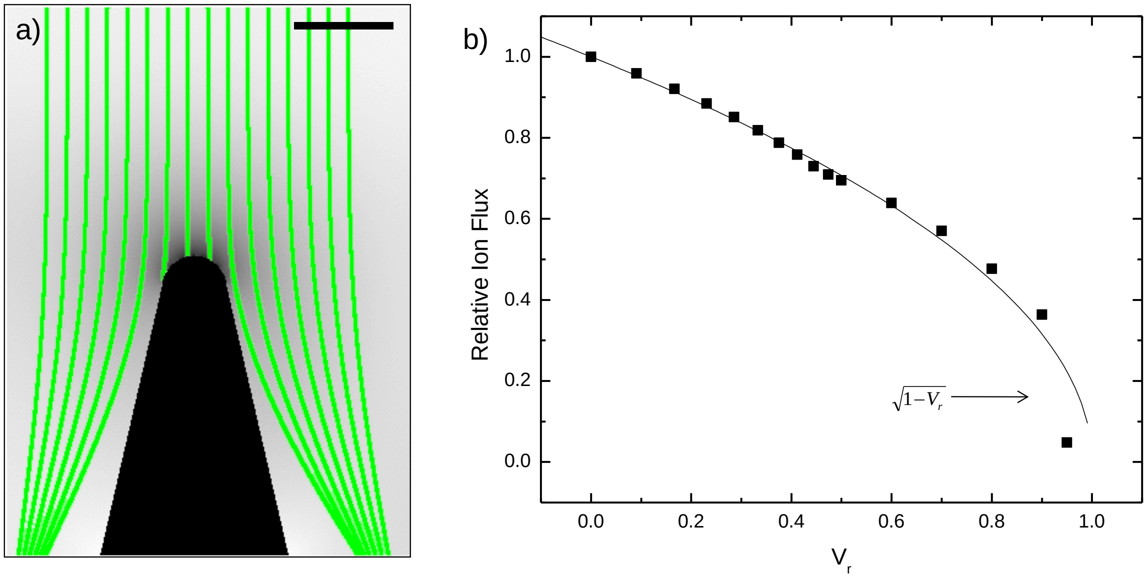

Figure 2.11: Simulation of ion flux in FDSS. (a) Simulated ion paths resulting from finite element analysis. Scalebar: 20 nm. (b) Variation of average ion flux at the tip apex as a function of V_r (squares). This result agrees well with the calculation based on the simple model of an infinite, perfectly conductive wire (solid line).

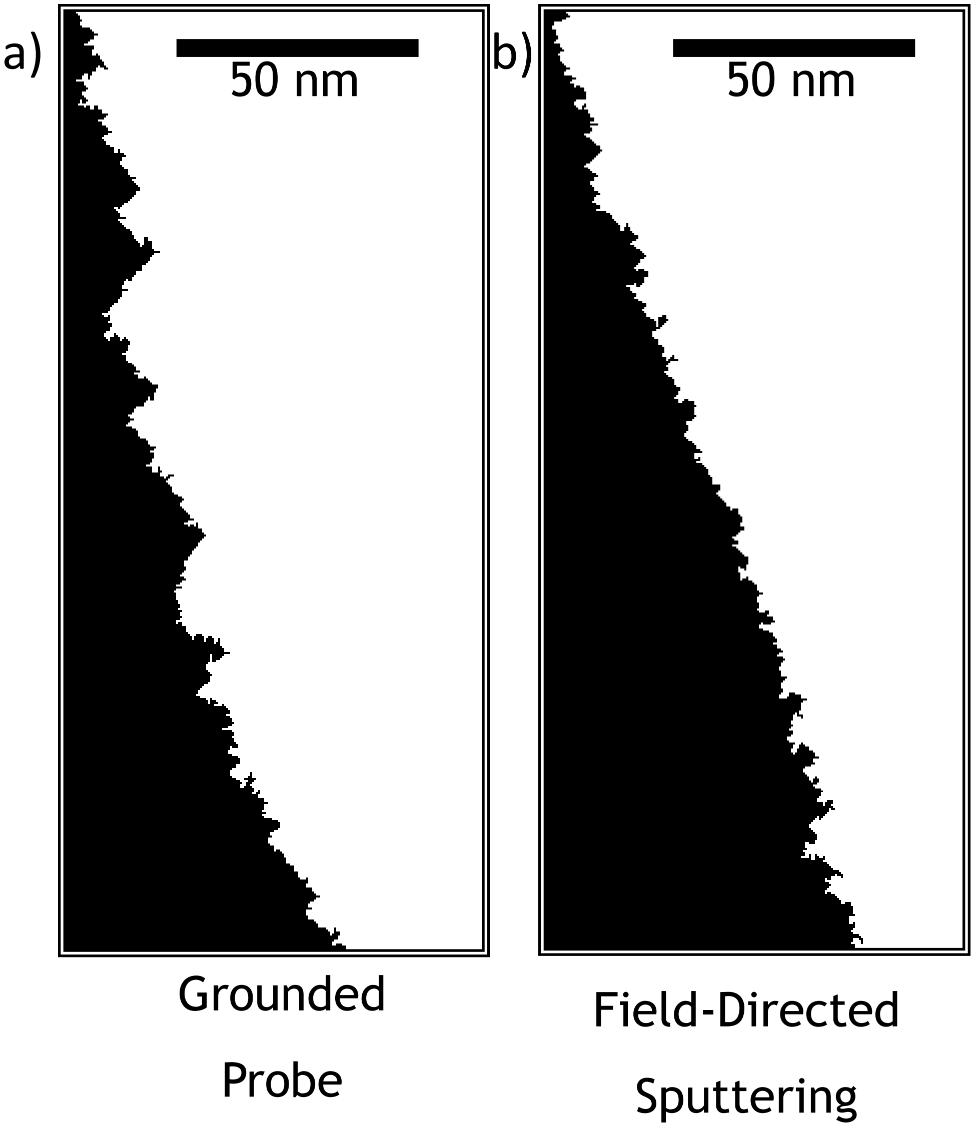

Figure 2.12: Monte Carlo simulations of FDSS performed on W tips with singly ionized Ar atoms. (a) The grounded probe (1600 eV ions) has a significant roughness of ~10 nm. (b) The FDSS probe (2000 eV ions, 400 V tip bias) has much smaller surface roughness of ~1 nm.

CHAPTER 3
HAFNIUM DIBORIDE AS A PROBE MATERIAL FOR SCANNING TUNNELING MICROSCOPY

One long-standing goal of the STM community is the fabrication of ultra-sharp, stable, and resilient probe tips designed to provide reliable atomic resolution imaging and patterning while resisting the detrimental influences of tip-sample interaction and remaining structurally invariant under the influence of adsorbate transfer from the surface. Many materials have been explored to address several of these issues. For example, the use of Pt tips eliminates the troubles of tip oxidation during transfer between preparation and scanning equipment. Tungsten is a common choice due to its hardness and relative affordability. In the case of AFM, diamond tips are popular, but diamond films sufficiently conductive for STM are difficult to fabricate.

Because different applications demand different characteristics in their probes, no single material is the perfect choice. Because tips with tailorable electronic, chemical, and mechanical properties are ideal, we seek a universal technique for the coating of pre-sharpened STM tips with a range of materials, which can then be sharpened with FDSS without the removal of the applied coating. As an example, we explore HfB_2. As discussed in Chapter 1, HfB_2 can be deposited as a conformal coating onto a variety of materials, including W. Among its attractive properties are extremely high hardness (20 GPa in the amorphous state, versus 3.4 GPa for W) and chemical stability. Perhaps most importantly for our purposes, HfB_2 has a high electrical conductivity (for a ceramic).

In Section 3.1 we will present our HfB_2 deposition technique, performed in collaboration with Dr. Navneet Kumar and Professor John Abelson of the Department of

Materials Science and Engineering at the University of Illinois at Urbana-Champaign. Then, in Section 3.2 we will present the results of coating sharpened W STM tips, and sharpening these films by FDSS. In Section 3.3, we will present our STM results demonstrating the successful application of HfB_2 tips to microscopy and spectroscopy.

3.1. Hafnium Diboride Chemical Vapor Deposition

Deposition of hafnium diboride film is performed in a turbo pumped high-vacuum chamber with a background pressure $< 5 \times 10^{-8}$ Torr. During deposition, the probe is heated and exposed to the $Hf(BH_4)_4$ precursor. Film thickness is measured on an adjacent silicon wafer by ellipsometry during growth and verified by transmission electron microscopy of the STM tip. During deposition, tip temperature is nominally maintained at 290 °C, and growth rate is approximately 2.5 Å/s. Following deposition, the film is characterized by scanning electron microscopy (SEM) (Figure 3.1a) and energy-dispersive X-ray spectroscopy (EDX) (Figure 3.1b).

3.2. Coating and Field-Directed Sputter Sharpening: Hafnium Diboride

The procedure for fabricating HfB_2 probes has four steps. We first produce a W tip with a 10 – 100 nm radius of curvature by ECE. With TEM, we verify that the tip radius is within this acceptable range and has a single apex. We then sharpen this tip by FDSS, producing a W tip with a <5 nm radius of curvature. Next, we deposit a ~100 nm film of HfB_2 on the W tip, increasing the radius of curvature to ~105 nm. We then sharpen the HfB_2 tip by FDSS, producing a tip with the properties of HfB_2 and a radius of curvature below 5 nm, without the need for fabricating HfB_2 wires or ECE of bulk HfB_2.

The entire process flow is shown schematically in Figure 3.2a, where W is shown in black and HfB_2 in semi-transparent green.

Following deposition of a 75 nm nominal coating of HfB_2, we are left with a W-HfB_2 tip with a 75 nm radius of curvature, shown in Figure 3.2b. This is consistent with deposition atop a sharp W tip. Note that the film coats the extremely sharp probe apex conformally. The surface of the tip has a roughness of approximately 5 – 10 nm, but as we shall see this is reduced following FDSS.

We then sharpen the W-HfB_2 tip by FDSS (V_{beam} = 1200 V, V_{tip} = 200 V, time = 60 min), after which the radius of curvature has been reduced to 4 nm, surface roughness reduced to ~1 nm, and most asymmetry eliminated. The resulting tip is shown in Figure 3.2c.

The resulting tip is extremely sharp in comparison with the deposited film, but we also note that CSE has been used previously to produce molybdenum tips of a similar size.[38] Therefore, seeking to verify that the use of field-direction has significantly influenced equilibrium radius of curvature, we run a control experiment intended to compare FDSS with CSE. The tip shown in Figure 3.2c is returned to the sputtering chamber and further processed under similar CSE conditions (V_{beam} = 1000 V, V_{tip} = 0). After sputtering, TEM indicates that the radius of curvature has increased to 13 nm. Furthermore, the tip apex has become rougher, and additional asymmetry has been introduced, as shown in Figure 3.2d.

3.3. Scanning Tunneling Microscopy and Spectroscopy: Hafnium Diboride

Given that the tip is half of the STM system, during spectroscopy a tip's density of states can substantially convolve with the density of states of the sample. Typically, the tip density of states is assumed to be constant, a reasonable first-order assumption in the case of a free-electron-like metal. If a tip is resistive, any voltage drop across the tip distorts the observed band structure of the substrate (e.g. a band gap will appear larger than anticipated).

As we are employing a novel tip material such as HfB_2, we must explore not only the stability and lifespan of probes during microscopy, but also the stability and accuracy of spectroscopy. To do so, a HfB_2-coated W tip is sharpened by FDSS, transferred to a UHV preparation chamber for a 600 °C degas, then transferred to a UHV-STM chamber for imaging of the well-understood Si(100) 2 × 1:H surface.

We first note, as seen in the representative image of Figure 3.3a, that HfB_2 STM tips provide stable imaging with immediate and consistent dimer resolution. We do note that this tip had a slight multiple tip with apex separation <1 nm, an observation consistent with the 4 nm tip radius produced, but not seen in the case of W tips. HfB_2 tips are found to provide stable scanning without any noticeable intrinsic tip changes over several weeks, a substantial improvement over W tips, which typically experience intrinsic changes over 60 – 300 min.

Also shown in Figure 3.3a are STS points, where STS data was collected with HfB_2 STM tips. Those marks shown in black were excluded from our data set because they are directly above a visible surface defect, such as a dangling bond or surface adsorbate. Those marks shown in red are included in our analysis. In Figure 3.3b we show a collection of constant-spacing STS data for this surface. Curves plotted in light gray are the original I-V data for each point, shown together. The thick black curve overlaid is the average of all data.

Several noteworthy observations can be made from this data. First, the electronic structure of the surface is nearly invariant across multiple spectra points. The variation we do observe is generally a doping effect, which leads to a shift in the Fermi level, and can be a result of nearby adsorbates or dopant atoms, and is therefore attributed to variations in the surface, rather than the tip. The measured band gap is invariant across data points, and is consistent with the 1.1 eV band gap of Si when extrapolated to account for the noise floor in constant-spacing STS.

HfB_2 STM tips are also employed for the ESD of H from Si(100) 2 × 1:H. In Chapter 4 we will discuss in detail the improvements offered by FDSS over alternate tip preparation techniques, but here we demonstrate that HfB_2 tips afford stable, high-resolution nanolithography. The influence of desorption and its byproducts on the tip is minimal. Figure 3.4a shows an example of a dimer-row desorption pattern in a false-color three-dimensional rendering. Red areas correspond to passivated Si, blue to Si dangling bonds which were present prior to pattern writing, and green to Si dangling bonds generated by the STM tip. We see in this case that the pattern is extremely sharp, but that several spurious depassivation sites are visible. These defects could be a result of secondary electron emission from the surface.[100] As we will explore in Chapter 4, ultra-sharp STM tips seem to have minimal spurious depassivation, and extremely sharp pattern profiles. The HfB_2 tips shown here have a slightly greater radius of curvature (~4 nm) than ultra-sharp W and Pt-Ir probes used in Chapter 4, and this may account for the small amount of spurious depassivation.

3.4. Discussion

The most apparent conclusions that we draw from the results of this chapter are the conformal coating of ultra-sharp STM tips by HfB_2, particularly in the small-radius apex region, the reduction in radius of curvature afforded by FDSS, and the high-resolution and long-term stability afforded by HfB_2 coated tips.

Like the diamond-like carbon (DLC) tips in Chapter 1, HfB_2 films provide a rounded single-apex tip. However, in contrast to the columnar structure of DLC, HfB_2 films are smooth along the tip shank. The surface roughness observed on CVD films is consistent with earlier studies of CVD-deposited $HfB_{2.}$[108] We do not explore the influence of film thickness on conformality, although it could be the subject of future study.

We find that FDSS affords improved sputter sharpening of HfB_2 films, when compared with the equivalent CSE process. We do note that FDSS-treated HfB_2 tips are slightly blunter than W or Pt-Ir tips, but their radius remains substantially smaller than that of our control tip. Furthermore, it is believed that further optimization by adjustment of FDSS parameters, temperature reduction, and global ion flux reduction may ultimately bring the achievable radius in line with other materials.

As imaging probes, sharpened HfB_2 tips prove exceptionally stable throughout days and weeks of scanning, and provide consistent dimer-resolution imaging and lithography. STS data exhibit constant-spacing spectroscopy typical of Si(100) 2 × 1:H and are remarkably consistent.

Perhaps most importantly, the sharpening of encapsulated probes is a generalizable process. In principle, any conductive coating can be selected, thus enabling us to tailor the properties of our tips to fit specific applications. In addition to having a range of desirable chemical and mechanical properties, tailored probe materials have a range of applications. For example, Ag and Au are favorable for tip-enhanced Raman spectroscopy,[278] while Pd is of interest due to the reversible formation of palladium hydride.[279] Some metals, such as Cu, catalytically form graphene,[280] enabling the formation of graphene-encapsulated tip structures.

3.5. Figures

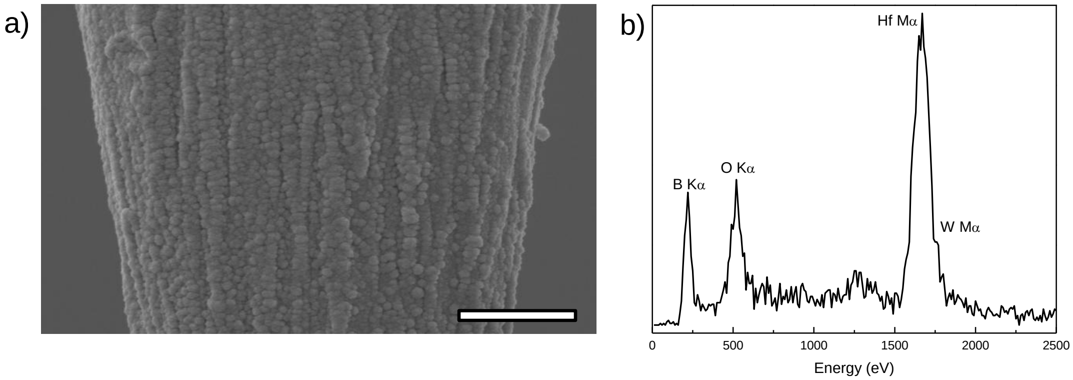

Figure 3.1: Deposition of HfB_2 film on a W core and elemental analysis by energy-dispersive X-ray spectroscopy (EDX). (a) SEM image of the shank of a HfB_2-coated STM tip. Scale bar: 2 μm. (b) EDX spectra from the shank of the tip. The image is primarily composed of Hf, B, O, W. Sensitivity of the instrument to B is low, leading to a small peak. The W signal arises from the W core. The O signal arises from both W oxide in the core and a thin ~1 nm oxidation layer at the suface of the HfB_2.

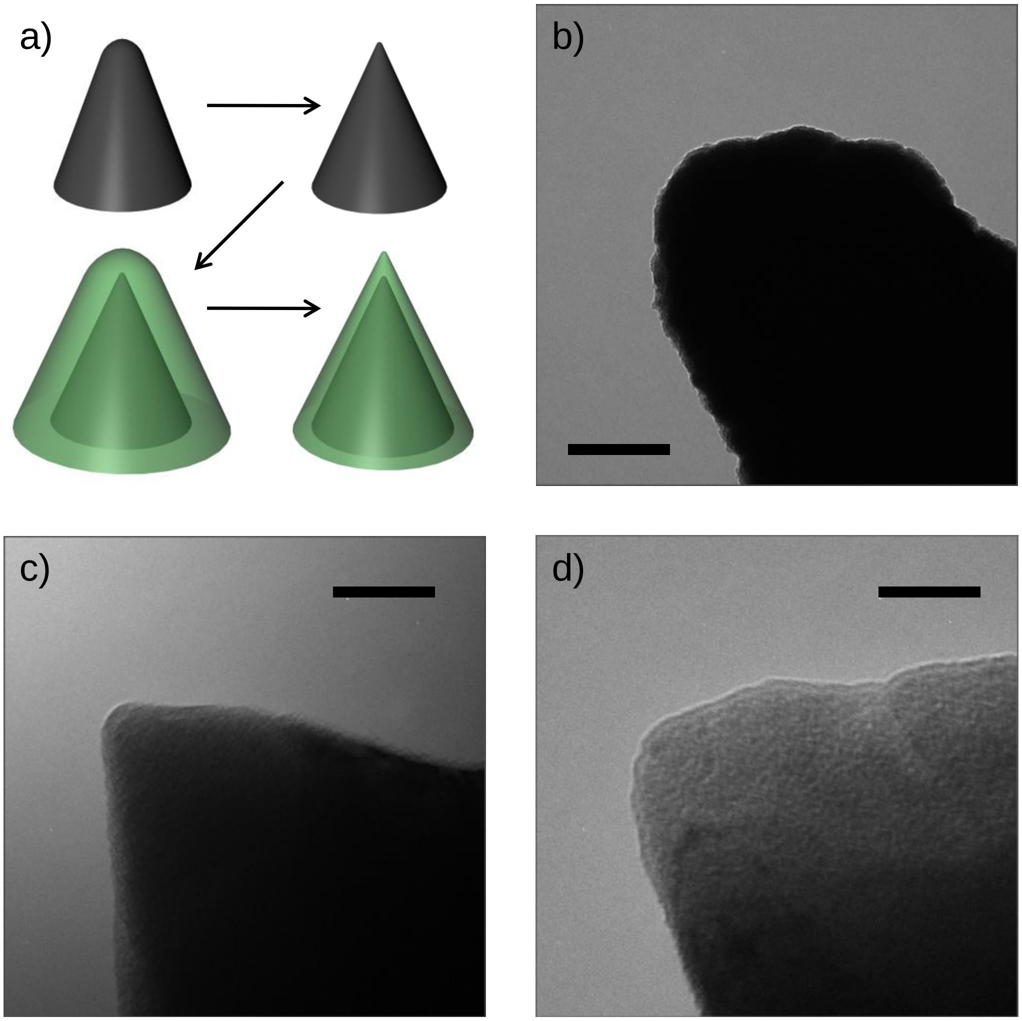

Figure 3.2: Demonstration of hafnium diboride tip sharpening. (a) The process of coating and sharpening the tip is shown schematically. First, a tungsten tip is prepared by ECE, producing a radius of curvature of 10 – 100 nm. Then, the W tip is sharpened by FDSS to produce a radius of curvature <5 nm. The sharpened tip is coated with a uniform film of HfB_2, producing a radius of curvature approximately equal to the film thickness. Finally, the coating is sharpened by FDSS to produce an ultra-sharp HfB_2 tip. (b) W STM tips coated with a 70 nm nominal amorphous HfB_2 coating. The measured radius of curvature is 75 nm and is approximately the sum of the 70 nm thick film and the ~5 nm oxidized W tip. Scale bar: 100 nm. (c) The same tip after FDSS sharpening, with a 4 nm radius of curvature. Scale bar: 20 nm. (d) The results of a control experiment. The tip shown in (c) was further sputtered with the tip bias removed and accelerating voltage reduced to keep landing voltage constant. The resulting radius of curvature increases to 13 nm. Scale bar: 20 nm.

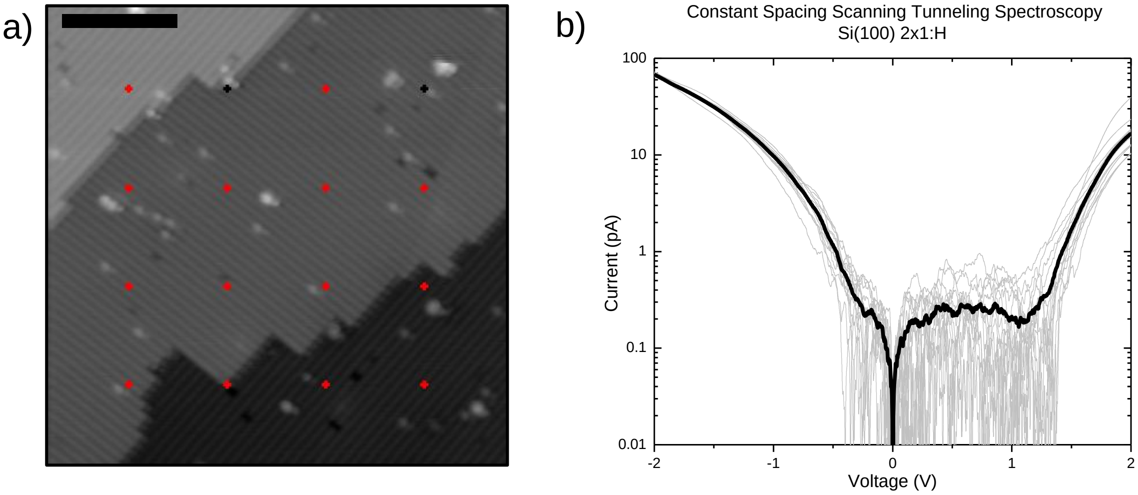

Figure 3.3: STM and STS of Si(100) 2 × 1:H. Data collected with a HfB_2 coated W STM tip. (a) Typical STM image demonstrating dimer-row resolution on the Si(100) 2 × 1-reconstructed surface. The tip is stable, which was typical of imaging over the course of several weeks. Crosshairs correspond to areas where spectroscopy data was taken. Black cross hairs were excluded from analysis due to the presence of a defect in the area. Scale bar: 10 nm. (b) Current-voltage spectroscopy data corresponding to the red crosshairs in (a).

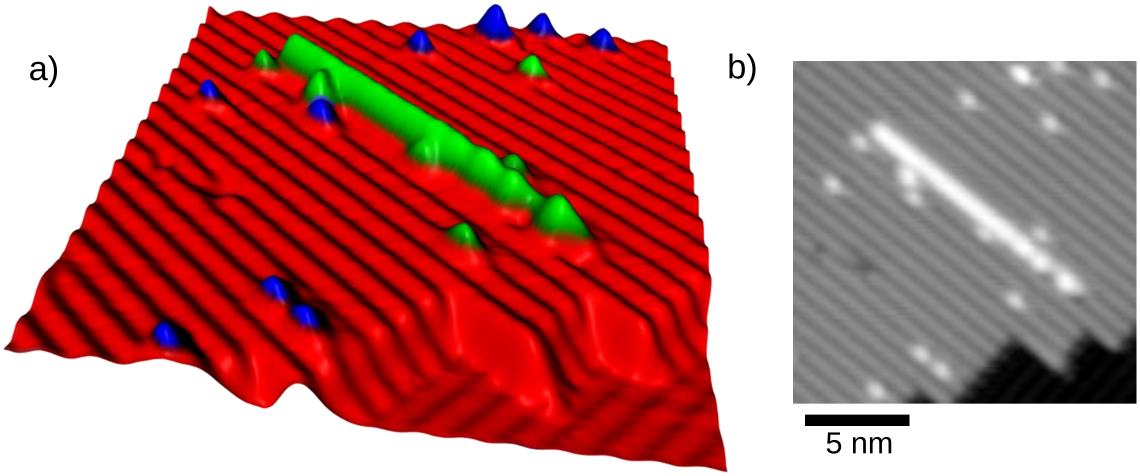

Figure 3.4: Topographic images of nanolithographic patterns generated by HfB_2 STM tips on Si(100) 2 × 1:H. (a) False-color three-dimensional rendering of a dimer-row line. A single dimer row has been depassivated, with some spurious depassivation sites nearby. Red corresponds to passivated Si. Blue corresponds to pre-existing dangling bonds. Green corresponds to dangling bonds generated by the HfB_2 tip. (b) Original 2-D topography of the same pattern.

CHAPTER 4
SCANNING TUNNELING MICROSCOPY AND HIGH-FIDELITY ELECTRON-STIMULATED DESORPTION

The ability to employ probes prepared by FDSS in the UHV-STM is of interest for purposes of atomically-precise substrate modification. In addition to its imaging capabilities, STM offers the potential for selective chemical structuring of the substrate surface. In this case, electrons tunneling from tip to surface will be employed for the selective desorption of hydrogen, generating a chemically-reactive dangling bond within a H-based electron-beam resist. This process can be performed either as a single-electron process in the field emission regime by directly elevating the bonding electron to an antibonding state, or via a vibrational heating mechanism at lower electron energies.

Specifically, FDSS probes produce exceptional electron-stimulated desorption patterns on the Si(100) 2 × 1:H surface.

4.1. High-Fidelity Patterning of the Si(100) 2 × 1:H Surface

The STM provides an excellent tool for tip characterization, although the width of lithographic patterns written by the STM is a less direct measure of probe sharpness than the radius of curvature measured by TEM. However, as lithography is the ultimate goal of this experiment lithographic line widths are arguably the best possible metric. As the spatial distribution of the electron tunneling current is dependent on probe radius, electron-stimulated patterning offers a reasonable technique for probe apex characterization. The quality of FDSS probes in STM can be demonstrated by high-resolution imaging, but more importantly by high-fidelity lithographic patterning.

Substrate patterning can be modeled simply by assuming a Gaussian spatial distribution for the electron tunneling current and a single-electron desorption process. In Figure 4.1 we show a typical tunneling current profile and desorption profile for a sample bias of 6.5 V, tunneling current of 2 nA, line dose of 2×10^{-3} C/cm, 20 nm tip radius, and Pt-Ir probe. The tunneling profile is dependent on tip radius and work function, but the manner in which this distribution translates into a desorption profile depends further on desorption yield and line dose. Thus, for a given tip radius, the desorption profile can be tailored slightly to optimize registry with the atomic lattice. However, there ultimately exists a lower limit to pattern width, at which point full desorption is no longer reliably obtained at the center of the lithographic pattern and the line becomes incomplete.

We can employ a similar model to characterize typical lithographic lines produced under various patterning conditions. In Figure 4.2, five lithographic lines are written with a 2 nA tunneling current and 2×10^{-3} C/cm line dose, using an etched Pt-Ir tip. Sample biases vary and range from 4.5 V (lower left) to 6.5 V (upper right). To analyze these lines, we take a cross section over the area indicated by the red box overlaid on the image. We average over the length of the line, converting the discrete lattice sites into continuous desorption profiles. To model this data as a desorption probability, and assuming that the line is continuous (that is, that the center of the line is fully depassivated), which we cannot assume here for the 4.5 V line, we isolate a single pattern, plane fit to accommodate the tilt of the sample, and normalize the data so that the fully depassivated peak corresponds to a desorption probability of one, while the fully passivated periphery corresponds to a desorption probability of zero.

We can then compare the patterns produced by a specific STM tip to those predicted for given patterning conditions to extract an effective tip radius. In Figure 4.3, we show desorption probabilities for both the 6.5 V and 6.0 V lines from the patterns shown previously. The tip radius that best fits the data is 20 nm.

In order to optimize our patterning procedure, W tips are processed by FDSS, producing sub-5 nm radius probes. These tips can then afford ultra-high resolution lithographic patterning, as shown in Figure 4.4. Here we demonstrate the smallest pitch reliably achieved by FDSS probes. In this case, two dimer rows (each two atoms wide) are patterned with a single two-atom wide dimer row between them. The grayscale 2-D topographic image is shown in Figure 4.4b, and a false-colored 3-D rendering of the image is shown in Figure 4.4a. The coloration identifies the surface's patterning state. Red areas correspond to H-passivated Si. Blue corresponds to Si dangling bonds or adatoms that were present prior to the patterning operation. Green corresponds to Si dangling bonds that were generated by the patterning operation. There are few imperfections in this pattern, although four spurious dangling bonds run along the edge of the rightmost line. These dangling bonds may be a result of imperfect tip registry with the substrate, rather than the spatial distribution of the tunneling current. A similar process is employed in Figure 4.5 to produce a 2-D lithographic box of reactive Si dangling bonds. In both cases, patterning conditions included a sample bias of +4 V, a tunneling current of 2 nA, and a line dose of 2×10^{-3} C/cm. Imaging was performed with a sample bias of −2 V and tunneling current of 50 pA.

4.2. Influence of Field-Directed Sputter Sharpening on Patterning

In order to verify that FDSS has a significant influence on the patterning capabilities of W probes, we perform a series of experiments intended to compare the same tips following a three-step preparation process: etching, FDSS, and CSE as a control. The lines patterned after FDSS consistently have higher resolution than those patterned by etched and control probes.

In this experiment, a single polycrystalline W probe is sequentially sharpened by all three methods; and following each method, the probe is used for ESD of hydrogen from a Si(100) 2 × 1:H surface. When the tip is sharpened by etching, the initial apex (Figure 4.6a) has a 5 ±1 nm radius of curvature (11.5 ±0.5 nm oxide radius). The probe is then degassed above 400 °C for 8 hours in UHV and used repeatedly to write a series of lithographic lines (Figure 4.6b). The tip is then removed from the STM and sharpened by FDSS. From a TEM micrograph (Figure 4.6c) the tip radius is 2 ±1 nm (5.5 ±0.5 nm oxide radius). After the TEM study, the tip is reinserted into our vacuum system and resharpened by FDSS under identical conditions to remove native oxide. After the probe is degassed above 400 °C for 8 hours, it is again used to write a series of lithographic lines (Figure 4.6d). Imaging and patterning resolution improve markedly.

As a control, the tip is then sputtered under CSE conditions with a 1.0 keV ion beam and a grounded probe. Inspection via TEM (Figure 4.6e) shows that the radius of curvature has increased to 8 ±1 nm (12.0 ±0.5 nm oxide radius). The tip is further sputtered under identical conditions to eliminate native oxide and is again degassed above 400 °C for 8 hours before additional patterns are written. Imaging resolution is reduced;

tip instability is enhanced, as indicated by multiple tip changes within the image; and pattern width increases (Figure 4.6f).

The ability to write patterns reproducibly is also markedly better for FDSS-sharpened probes than etched probes (Figure 4.6h). This improvement largely results from the removal of chemisorbed and physisorbed species during sputtering, but also addresses concerns about tip instability resulting from ion-induced radiation damage. Even in the absence of a high-temperature anneal, typical FDSS probes provide immediate and stable dimer resolution imaging.

It is noteworthy that our ECE probe appears exceptionally sharp as judged by TEM (above the 95th percentile of ECE tungsten tips from our facility), making our observation of improvement following FDSS even more significant. Hydrogen resist patterns produced by FDSS probes have reduced line widths compared to those made by both ECE and CSE probes. The FDSS probe generates line widths of 2.2 nm for 4.5 V patterns and 5.8 nm for 5.5 V patterns. By comparison, the ECE probe generates 2.8 and 7.9 nm patterns, whereas the control probe generates 2.7 and 7.3 nm patterns. Thus, the FDSS patterns exhibit a 21% (4.5 V) and 26% (5.5 V) reduction in line width over the ECE probe and an 18% (4.5 V) and 20% (5.5 V) reduction in line width over the control probe. This reduction in patterning width is verified to be statistically significant by a two-tailed Welch’s t-test ($\alpha = 0.10$). A comparison between FDSS and control patterns for both 4.5 V and 5.5 V patterns is presented in Figure 4.6g, and further data are provided in Figure 4.7. Comparing ECE and CSE probes, we cannot reject the null hypothesis for 4.5 V ($p = 0.50$) or 5.5 V ($p = 0.65$) sample bias, allowing for the possibility that CSE offers no improvement over a sharp ECE probe.

In a subsequent experiment, we verify the reproducibility of these results across multiple STM tips, and across multiple tip sputtering cycles. A set of three ECE probes, with a range of apex radii, are selected by TEM (micrographs are shown in Figure 4.8) as clean and potentially stable STM tips. The tips are sharpened and patterns written using the process described above and sample biases from 4 V to 8 V. Each tip was sharpened by FDSS (V_{beam} = 1400 V, V_{tip} = 400 V: V_r = 0.286) and, after patterning, sputtered under CSE conditions (V_{beam} = 1000 V, V_{tip} = 0: V_r = 0). Tip C received damage unrelated to sputtering and scanning before the control experiment, but ECE and FDSS data are shown for completeness. Tip A was FDSS sharpened a second time after CSE patterning, and a second control experiment completed. The resulting pattern widths are shown in Figure 4.9, where we see a clear and reproducible reduction in pattern width as we move from ECE tips to CSE tips and finally to FDSS tips, for which optimal resolution is achieved. It is noteworthy not only that each tip exhibits improved patterning after FDSS, but that the images collected after FDSS achieve atomic resolution patterning from the very first scan (Figure 4.10). Furthermore, the cycling of tip A through multiple FDSS and control cycles further demonstrates the reproducibility of FDSS not only from one tip to the next, but also for a single tip over multiple sputtering cycles.

4.3. Probe Regeneration by Field-Directed Sputter Sharpening

While operating within the STM, probes commonly undergo structural changes due, for example, to surface diffusion or mechanical contact with the substrate being analyzed. Though the result of a “tip change” can be advantageous, for instance, by the creation of an atomically sharp point, more frequently imaging resolution suffers. Often changes are reversible, though the recovery process is rarely deterministic and commonly involves aggressive tip-surface interaction until further structural modification occurs.

Unfortunately, scanned probes remain a consumable item. However, for mildly damaged probes, regeneration by FDSS is possible. In this experiment, a polycrystalline tungsten probe was employed in the STM for imaging and patterning of the silicon surface. Following extended scanning, the probe sustained damage and was unable to provide precise patterning. Figure 4.11a includes a representative pattern produced by the degraded probe. Though evidence of atomic-scale surface structure can be discerned, the electron-stimulated desorption patterns are broadened. Additionally, the probe appears to have multiple apices, each of which provides an STM image of the surface in parallel. As a result, multiple shadow images are visible on the surface for each line. It was believed that the damaged probe used to generate Figure 4.11a would be a good candidate for regeneration via FDSS. Without removal from high vacuum, the probe was subjected to FDSS processing with ion energies of 1.2 keV and a probe bias of 200 V. The probe was not imaged by TEM, but immediately degassed and returned to UHV for further use in the STM.

The regenerated tip enabled stable imaging of the silicon surface, and high-fidelity patterning by electron-stimulated desorption. One representative pattern is shown in Figure 4.11b. Of particular interest is the extreme patterning precision visible in this image. Outside of the immediate patterns, which follow the atomic dimers of the surface, most dangling bonds are randomly distributed and created by imperfect sample preparation, instead of electron-stimulated desorption.

4.4. Discussion

In conclusion, the radius of probes has a marked effect on the width of patterns they produce. We show that the desorption profile is a reasonable metric for the sharpness of a tip. We then show that, under identical patterning conditions, tips prepared by FDSS produce significantly smaller patterns than those produced by ECE or CSE. We also show that FDSS tips produce more consistent and reproducible patterns than etched tips, and that FDSS tips typically provide stable imaging from the first scan.

We also show that the improved patterning capabilities of FDSS-processed tips are reproducible across multiple tips and multiple FDSS/CSE cycles for the same tip. Finally, we demonstrate that FDSS enables the regeneration of damaged tips following STM. Although this process is not a panacea, moderately damaged tips will benefit from subsequent FDSS treatment and can be used and reused numerous times over extended periods of time (sometimes months).

In conclusion, FDSS is a remarkable technique for the improvement of lithographic patterning, which provides consistent and reproducible patterning across multiple tips and moves towards the limit of atomically-registered and atomically-precise lithography.

4.5. Figures

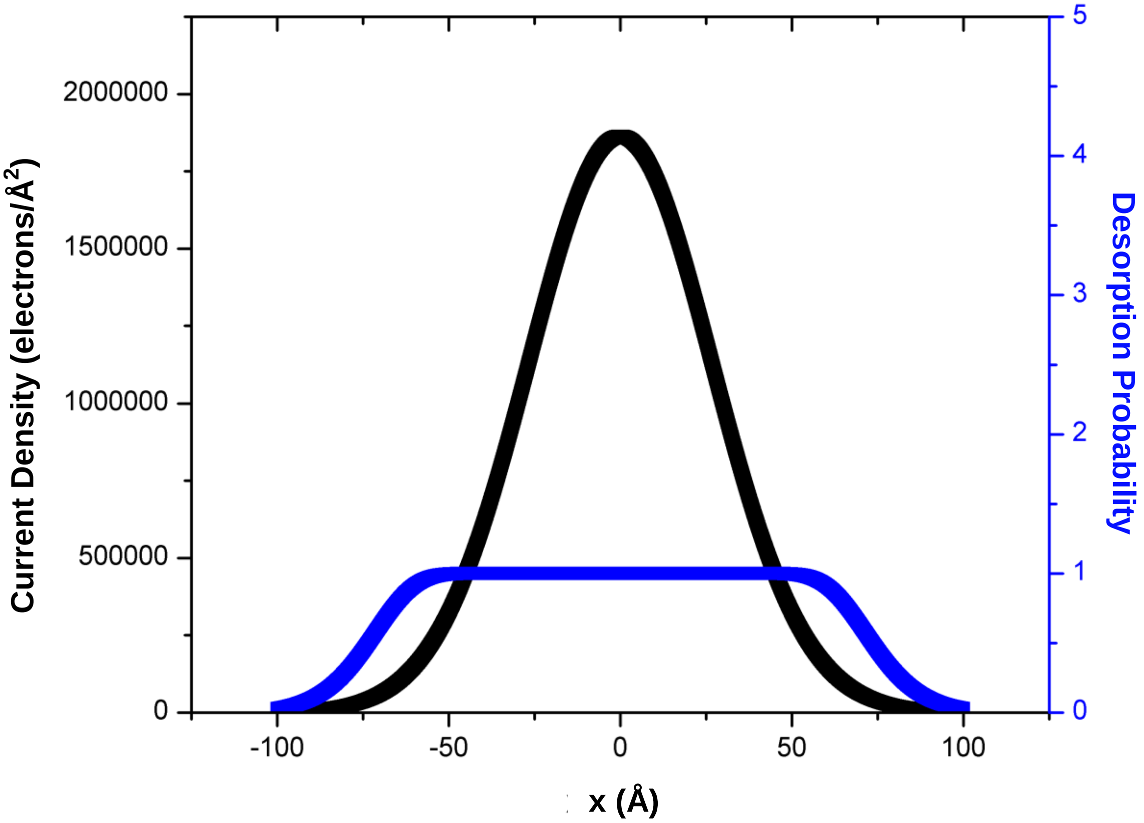

Figure 4.1: Simulated tunneling current profile (black) compared to the resulting desorption probability (blue).

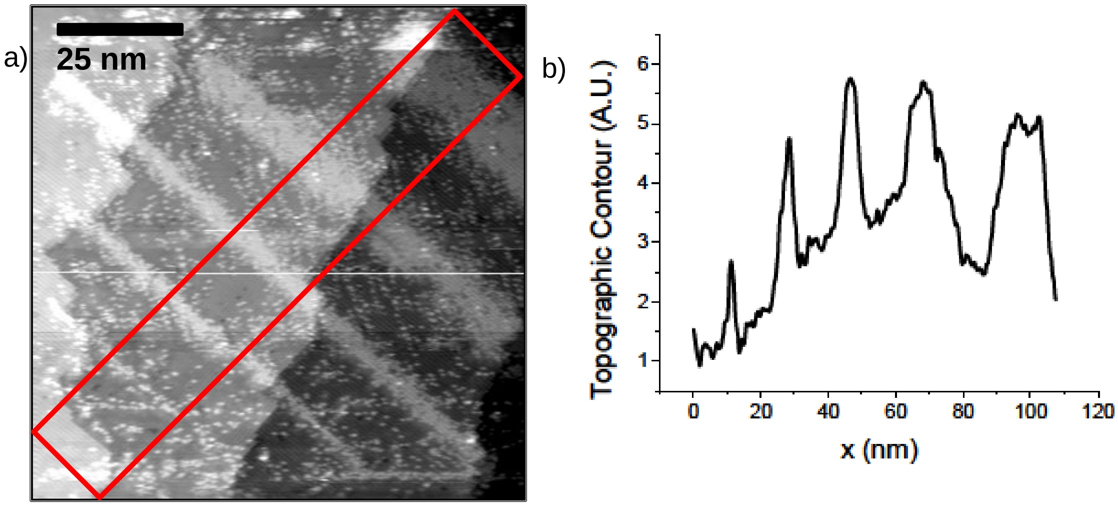

Figure 4.2: Experimental extraction of desorption probability for a variety of lithographic patterns with sample biases. (a) Topographic STM image with patterns written from 4.5 V (lower left) to 6.5 V (upper right). (b) Topographic height is averaged along the length of each line within the red box in (a), producing the topographic contour shown. This data is related to the desorption probability.

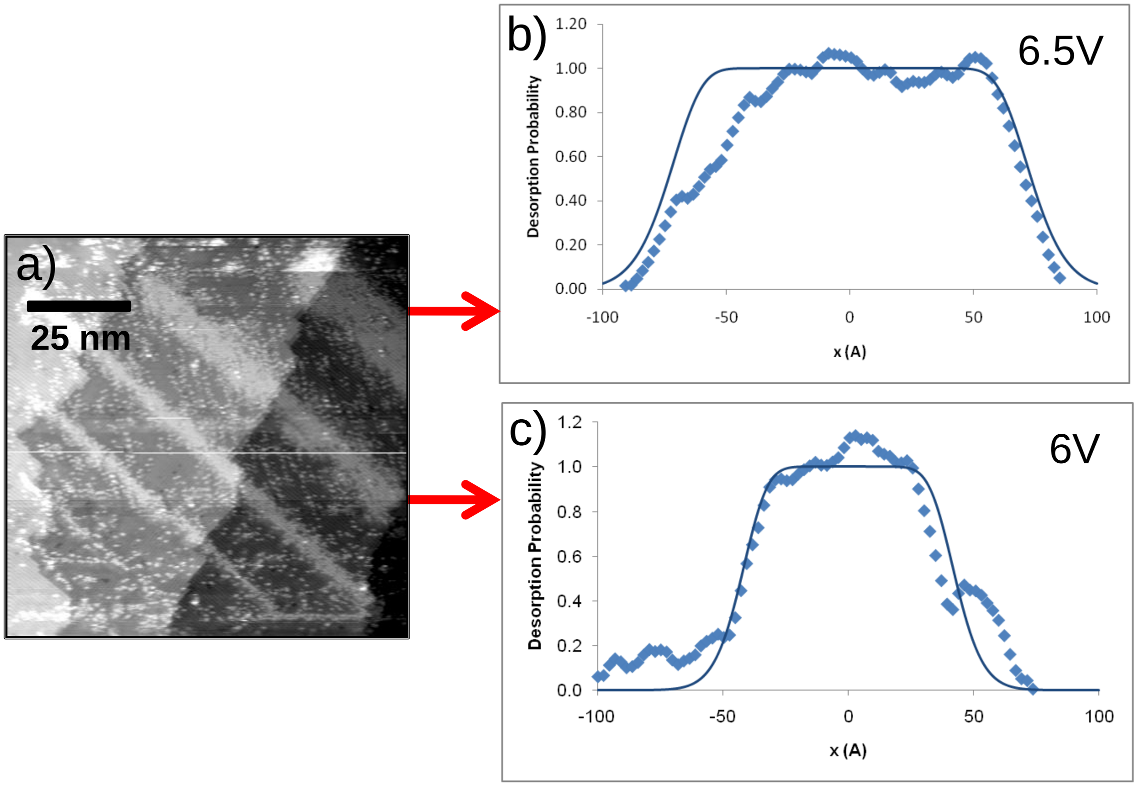

Figure 4.3: Comparison of experimental desorption probability with our model. After normalization, experimental topographic contours are compared to models, and an effective tip radius is extracted. In this case, the tip radius is 20 nm. (a) Topographic image of all lithographic patterns. (b) Desorption probability extracted from 6.5 V pattern (blue) compared to predicted pattern (black). (c) Desorption probability extracted from 6 V pattern (blue) compared to predicted pattern (black).

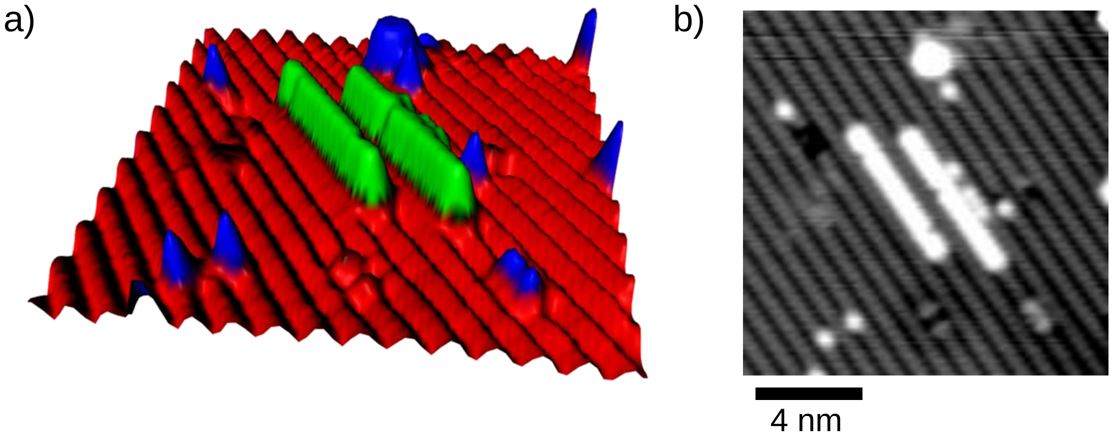

Figure 4.4: A demonstration of atomic-fidelity lithography by electron-stimulated desorption (ESD) of hydrogen from the Si(100) 2 × 1:H surface with a 4 V sample bias, 2 nA current setpoint, 2×10^{-3} C/cm line dose and FDSS-generated tungsten probe. STM images are collected with a sample bias of −2 V and a current setpoint of 50 pA. All scale bars are 4 nm. (a) Dimer-row line width lithography is demonstrated. The image is a false-color three-dimensional rendering where red represents passivated silicon, blue represents background surface features unrelated to patterning, and green represents dangling bonds generated by the ESD process. (b) The same pattern shown in its original form as a two-dimensional STM topograph.

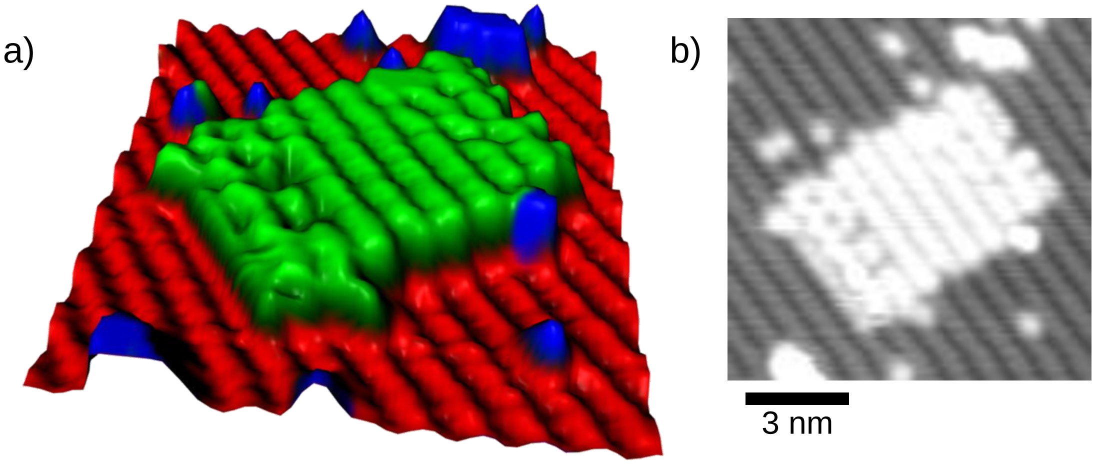

Figure 4.5: (a) A nanolithographic box 20 × 13 atoms in dimension is shown as a false-color three-dimensional rendering similar to that in Figure 4.4a. The feature has been generated by five successive depassivation patterns under identical patterning conditions. (b) Topographic STM data in two dimensions for the nanobox pattern.

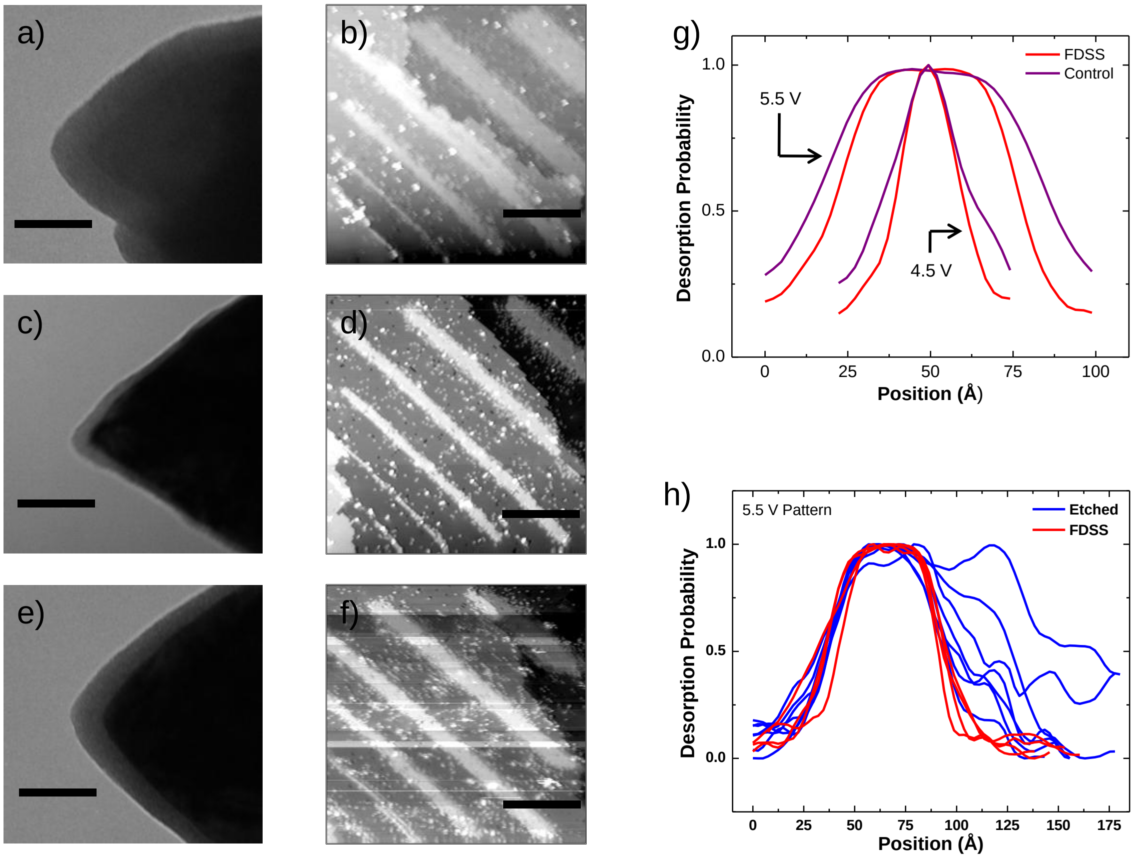

Figure 4.6: The effects of probe sharpening on patterning capabilities. Each hydrogen-resist pattern includes a sequence of lines corresponding to sample biases from lower left to upper right of 4 V, 4.5V, 5 V, 5.5 V, 6 V, and 6.5 V with constant tunneling current of 2 nA and line dose of 2×10^{-3} C/cm. STM images are collected with a sample bias of −2 V and a current set point of 50 pA. All scale bars are 30 nm. (a) Transmission electron micrograph of an exceptionally sharp tungsten probe produced by ECE. (b) A representative pattern on the Si(100) 2×1:H surface written by ESD of H using the ECE probe of (a). (c) Transmission electron micrograph of the probe following an FDSS sharpening procedure (1.4 keV ion energy, $V_r = 0.286$, 38 minutes). (d) A representative pattern created with this FDSS-generated probe. (e) Transmission electron micrograph of the same probe following control experiment sputtering (1.0 keV ion energy, $V_r = 0$, 60 minutes). (f) A representative pattern created with the control probe. (g) Spatial distribution of desorption probability for FDSS and control probe patterns at 5.5 V and 4.5 V sample bias. (h) Pattern stability achieved with an FDSS probe is compared to that of an etched probe. All 5.5 V patterns generated by a probe before and after FDSS are shown.

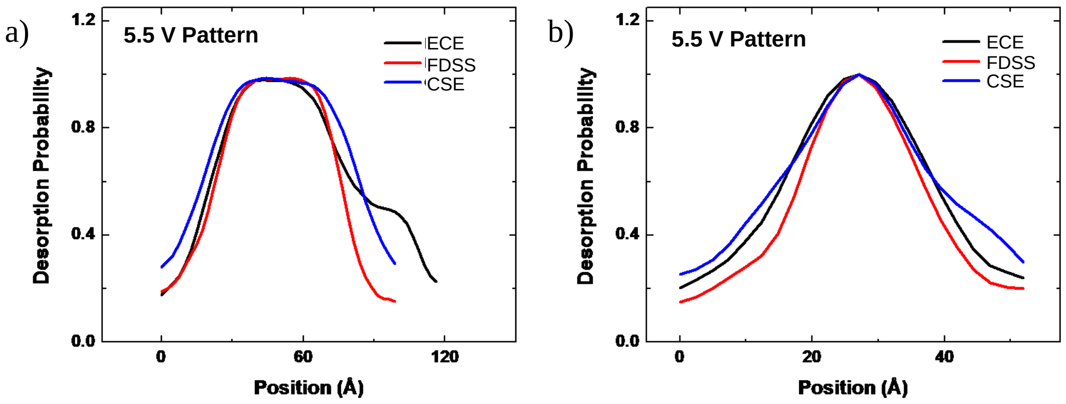

Figure 4.7: Further data from desorption patterns created by etched, FDSS, and control probes. (a) Averaged data from each series of patterns created at 5.5 V sample bias. The variation of widths is visible between FDSS and control cases, and also between FDSS and etched cases, though much of this variation results from a shoulder produced by the probe instability shown in Figure 4.6h. However, the distinction between FDSS and etched probes becomes clearer for 4.5 V sample bias where the effects of any secondary apices in the etched probe are dramatically reduced. (b) Averaged data from each series of patterns created at 4.5 V sample bias. Here a clear distinction is drawn between FDSS and etched probes, and between FDSS and control probes.

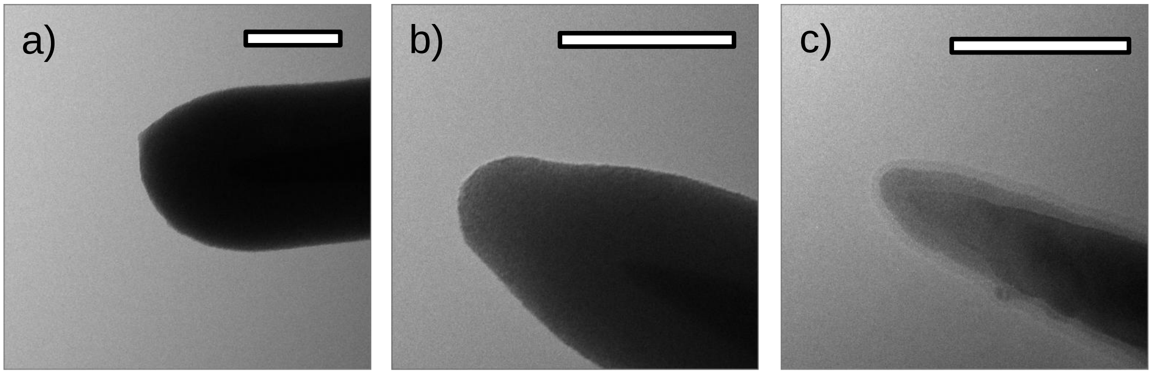

Figure 4.8: Initial TEM micrographs of the tips used to generate Figure 4.9. (a) Initial form of tip A. (b) Initial form of tip B. (c) Initial form of tip C. Scale bars: 50 nm.

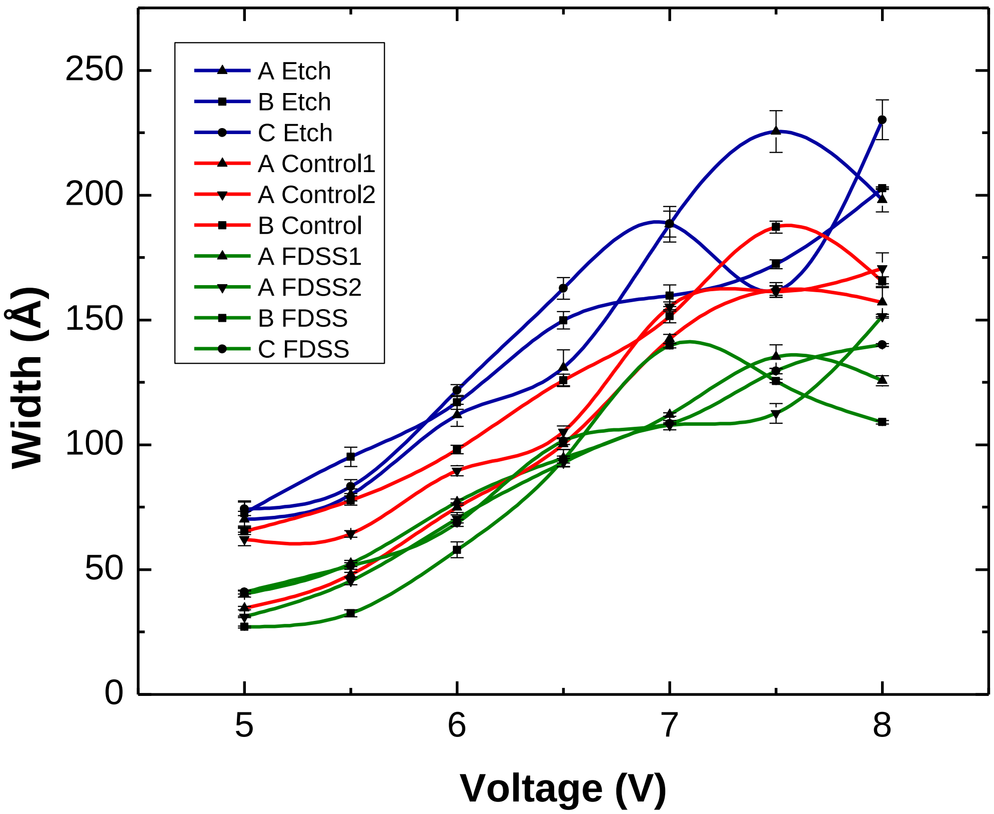

Figure 4.9: Further patterning results from multiple STM tips. Each curve corresponds to a set of patterns written at sample biases between 5 V and 8 V. Blue curves correspond to ECE tips, red to CSE tips, and green to FDSS tips. FDSS clearly produces narrower patterns, and this is most clearly visible at high sample biases.

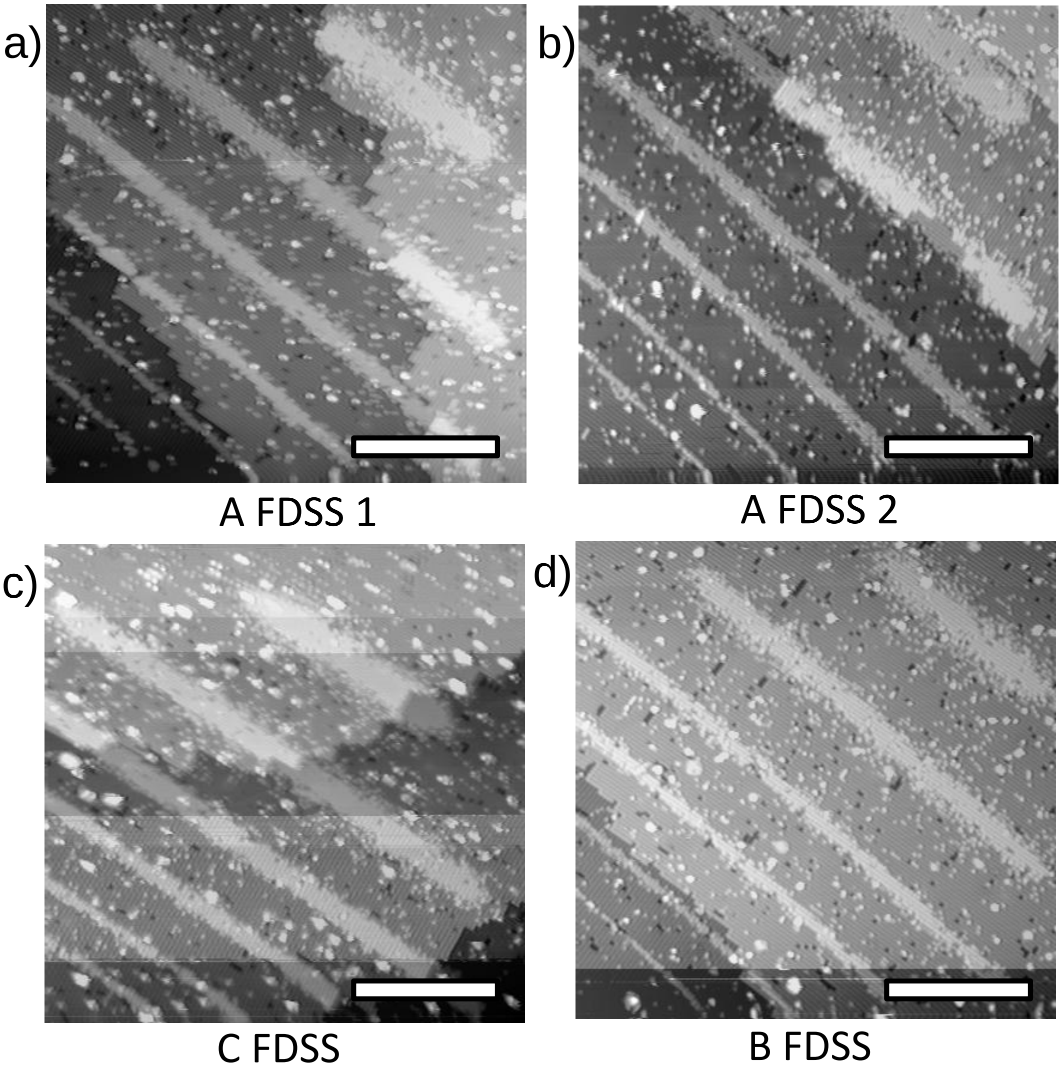

Figure 4.10: Initial imaging and patterning resolution from each of four FDSS cycles and three FDSS-processed probes. In each case the first pattern written is shown, which corresponds to the second image collected. Thermal drift was allowed to subside after the sample was loaded into the STM, but no additional tip treatments were employed to achieve this resolution. In one case (c), the tip likely acquired an adsorbate during imaging, resulting in a slight multiple tip in the top half of this image. This adsorbate became desorbed naturally in the course of the subsequent scan, the tip returned to its initial state, and no lasting effect was observed on the tip's imaging and patterning capabilities, as shown in Figure 4.9. Scale bars: 30 nm

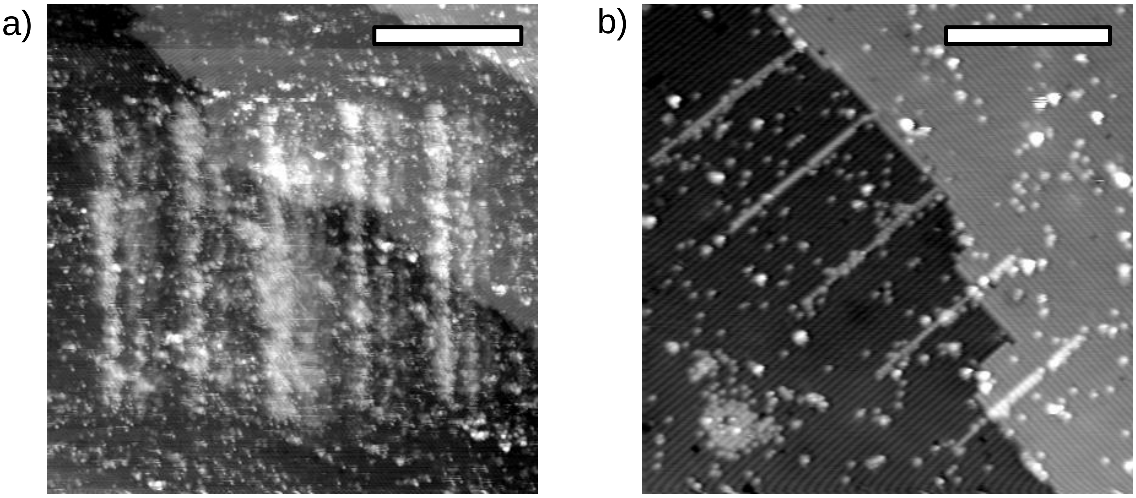

Figure 4.11: Regeneration of damaged STM tips by FDSS. (a) Pattern resulting from ESD of hydrogen from the Si(100) 2 × 1:H surface using a patterning voltage of +4 V and set point current of 2 nA. The STM image was collected with a sample bias of −2 V and a current set point of 50 pA. Scale bar: 30 nm. (b) Equivalent pattern generated by the same probe following FDSS (V_{beam} = 1.2 kV, V_t = 200 V: Vr = 0.167). Patterns were written with a sample bias of +4 V and a current set point of 2 nA. The STM image was taken with a sample bias of −2 V and a current set point of 50 pA. The round pattern visible in the lower left corner was produced by the extended presence of the STM tip at elevated sample bias. Scale bar: 20 nm.

CHAPTER 5
EXFOLIATION AND DECOMPOSITION OF PUCKERED-SHEET GRAPHITE FLUORIDE

The most intuitive method for producing monolayer fluorinated graphene is also among the most difficult. While the “scotch tape” mechanical exfoliation method has proven extremely successful in the production of monolayer graphene from graphite, when exfoliating from bulk graphite fluoride, the story is very different. Despite the efforts of several groups,[17,25,27] exfoliated monolayers of puckered-sheet graphite fluoride are extremely difficult to isolate and prone to rupture. As we shall see, the results of this dissertation further verify this fact, as monolayers produced are small and unstable, ultimately producing fluorine.

In one application, functionalized graphene sheets must be selectively reduced by chemical or electron-stimulated means to generate metallic or semiconducting pathways within the basal plane.[14,249] Scaling of these pathways provides continuous control of the graphene band gap. Therefore, an improved understanding of the mechanism by which this reduction proceeds is desirable.

In this dissertation we demonstrate tip-induced desorption of fluorine from monolayer CF sheets on the Si(100) 2 × 1:H surface, as evidenced by variation in the height of CF flakes and monolayer pitting of the silicon lattice induced by desorbed fluorine. More generally, this dissertation provides the first STM study of monolayer ds-GF, and in particular the first integration of this compound with the Si(100) surface, and indicates that defluorination proceeds under scanning conditions that are commonly non-destructive. These results also suggest the need to explore edge stability in $(CF)_n$, and the importance of single-sided fluorination in order to limit the influence of fluorine on the underlying substrate.

5.1. Characterization of Bulk Exfoliated Graphite Fluoride

Our source material is a commercially available graphite fluoride powder produced by Acros Organics. As this material is primarily intended as a lubricant, its defect density is expected to be very high, and grain size very small. To better understand the nature of our bulk material, we perform TEM and diffraction measurements, as well as X-ray photoelectron spectroscopy (XPS) of the bulk product. For TEM, graphite fluoride powder is deposited on a Formvar-coated Cu TEM grid from n-methylpyrrolidone (NMP). There are a few important limitations to this process. First, on the basis of subsequent observations, we determine that NMP affords the partial reduction of graphite fluoride. However, this is not a major limitation for us, because the observation of long-range structural order in partially reduced CF almost certainly implies similar order in the fully fluorinated bulk material. Second, NMP dissolves Formvar, making this transfer process extremely inefficient. Nevertheless, some small flakes of CF supported on Formvar remain following transfer, enabling the completion of this experiment. For XPS, graphite fluoride powder is pressed into a thin sheet of Au foil and characterized in this form.

The results of transfer to TEM grids and characterization of a thin flake by TEM and diffraction are shown in Figure 5.1. The flake in question is ~1 μm wide, and exhibits the sixfold symmetric diffraction pattern typical of graphite or graphite fluoride, suggesting the presence of structural order in the bulk material and saying little about the prevalence of defects therein.

To better understand the nature of this material, we explore the XPS spectrum of the powder, which is shown in Figure 5.2. The spectrum suggests a range of sp^2 and sp^3 chemical bonding, with multiple fluorine bonding configurations and a high density of defects. However, the prevalence of covalent sp^3 C-F bonding is clear, as expected for graphite fluoride in the puckered-sheet configuration.

5.2. Dry Contact Transfer of Puckered-Sheet Graphite Fluoride

Knowing the difficulties involved in mechanical exfoliation of monolayer graphene fluoride, we explore a technique made popular for the exfoliation of isolated single-walled carbon nanotubes[281,282] and graphene.[283,284] In dry contact transfer (DCT), a fiberglass applicator is impregnated with a dry source powder (e.g. nanotube bundles or HOPG graphite). The applicator is loaded into a UHV system, degassed at appropriate temperatures, and mechanically stamped onto the target substrate. This process leads to the deposition of small monolayer graphene flakes ~10 nm wide, or isolated nanotubes, onto the substrate. In this case we follow closely the technique for monolayer graphene exfoliation, but impregnate the applicator with graphite fluoride powder. Degassing is performed between 100 °C and 150 °C, well within the operating range of the material. Following DCT to Si(100) 2 × 1:H, a microscopic white powder is visible on the surface by optical microscopy, suggesting that large quantities of graphite fluoride have been transferred, including bulk material. However, as we shall see, much of the surface contains small monolayer flakes which can be identified by STM, with a flake density of approximately four flakes per 1 μm^2. Few-layer and multilayer flakes are not observed in this study, possible as a result of the weak interaction between planes in fluorinated graphite.

5.3. Scanning Tunneling Microscopy: Monolayer Fluorinated Graphene

Following DCT, a survey scan of the Si surface reveals a large number of 2-D structures on the surface, which we identify as graphene fluoride. One typical example is shown in Figure 5.3. Figure 5.3a shows a false-color 3-D rendering of a flake, where Si is shown in red, and the CF flake is shown in green. The original 2-D topographic image is shown in Figure 5.3b.

The fluorination of these flakes appears to be non-uniform, as indicated by graphitic regions visible within flakes. For example, in Figure 5.4, the red arrow indicates an area with a topographic height of ~3 Å, typical of graphene and smaller than the 5 – 7.5 Å heights seen in CF flakes.

Following the location and characterization of 12 monolayer CF flakes, we identify them in terms of average flake size and apparent topographic height. We expect the average flake size to be similar to that of DCT-transferred graphene, and the apparent topographic height to be similar to the interlayer spacing of bulk graphite fluoride. This hypothesis is verified by measuring flake heights by STM. A scatterplot of all flake widths and heights is shown in Figure 5.5. The average flake width is 18.7 Å with a large standard deviation of 8.4 Å, and the average apparent flake height is 6.0 Å with a standard deviation of 1.1 Å.

If we exclude the two outliers with heights near 4 Å, this average apparent height goes to 6.4 Å with a standard deviation of 1.1 Å. The interlayer spacing of bulk graphite fluoride is approximately 6.4 Å,[17] which is in reasonable agreement with our measurements. The high variance in flake height is important to note, and is explained in terms of a different substrate (Si instead of CF) and partial reduction of CF flakes. Consequently, we explore the electron-stimulated reduction of graphene fluoride on Si(100).

5.4. Electron-Stimulated Decomposition: Monolayer Fluorinated Graphene

In order to better understand the influence of low-energy electron bombardment on monolayer CF flakes, we perform an extended batch mode scan of a single flake. The flake is scanned repeatedly with a sample bias of −2 V and tunneling current of 8 pA. Following one hour of scanning, with a total electron dose of ~4000 C/cm^2, the apparent topographic height of this flake has been reduced from 6.4 Å (σ^2 = 0.48 Å) to 4.0 Å (σ^2 = 0.47 Å), declining at 0.0014 Å/(C/cm^2) (R^2 = 0.887). A full data set showing flake height versus time is presented in Figure 5.6. Black squares represent apparent flake height in each scan, with purple lines indicating the interlayer spacing of graphite and graphite fluoride. Heights are measured by producing a histogram of the height of the flake and the height of the Si surface. Both have approximately Gaussian distributions, and we take the height as the difference between the means. The error bars are produced by combining the standard deviations of each histogram. As a control, we also plot the apparent height of a Si dangling bond (red circles) from the same image set, allowing us to verify that the observed change in flake height cannot be attributed to a change in the STM tip or the influence of the STM control system.

This change in flake height explains the sizable variance in observed flake height during our initial survey scan, and can likely be attributed to partial defluorination during the scanning process. To further verify and understand this mechanism, we explore the influence that this defluorination process has on the Si substrate.

5.5. Defluorination and Silicon Substrate Etching

We initially discovered accidentally that CF flakes are unstable on the Si surface. In some cases, under normal scanning conditions (−2 V, 8 pA) flakes are removed spontaneously from the surface, leaving the Si substrate behind. In other cases the flakes are cut or otherwise manipulated on the surface, revealing previously hidden Si atoms. Our ability to manipulate flakes provides an opportunity to understand the influence of the flake on the Si substrate.

Although we do not have reliable control over the relocation and removal of CF flakes, in some cases, we are able to take advantage of fortuitous circumstances to explore CF-substrate interaction. In one case, shown in Figure 5.7, a CF flake was scanned several times; in this process the flake was offset slightly by the STM tip to a location within the same scan area. We then performed an extended batch mode over a period exceeding 45 minutes, during which the flake height changed as shown in Figure 5.6. At the end of this time, the flake was removed from the system and could not be relocated. It may have been transferred to the STM tip, as tip resolution also changed concurrent with the transfer. While the Si substrate was initially pristine, following CF transfer and scanning, a large number of monolayer vacancies appear in the Si substrate. We believe that these defects are introduced by exposure to fluorine desorbed from the lower face of the CF flake. The mechanism of fluorine etching of Si is well understood,[285–287] and the energetically favorable transfer of F atoms from fluorocarbon nanostructures to Si(111) has been studied previously.[288]

From this observation of F-induced Si etching and the observed reduction in CF flake height described previously, we conclude that defluorination of CF occurs under mild scanning conditions (−2 V, 8 pA). We also note that flakes often rupture during scanning, which agrees with similar observations made during mechanical exfoliation.

5.6. Discussion

Mechanically exfoliated CF flakes are poorly suited to integration with electronic devices, in part because of their instability, propensity to rupture, and double-sided nature. Because fluorine is trapped between the flake and substrate, fluorine-substrate chemical interaction is possible. We also present the first demonstration of tip-induced defluorination of a fluorocarbon nanostructure, and specifically of monolayer graphene fluoride. Given our ultimate goal of producing graphene structures in fluorinated graphene films, an improved understanding of this desorption mechanism is necessary. Ultimately, we wish to apply the knowledge gleaned from this study to single-sided structures from which fluorine can be desorbed with neither confinement beneath graphene nor deleterious effect on the chosen substrate.

It is also noteworthy that the DCT process is applicable to exfoliation of graphite fluoride, while traditional exfoliation cannot easily produce monolayer films. The success of DCT is not just a testament to the universal applicability of DCT, however; it also follows from the much smaller flake size observed in DCT-prepared samples. Indeed, the largest flake observed by exfoliation in other work is 1 μm,[25] which is much larger that our samples but achieved much less consistently. Ultimately, DCT is a technique applicable to surface science studies of exfoliated CF flakes on prepared conducting or semi-conducting surfaces. Through an atomic-scale understanding of the interaction between CF and various substrates, scalable techniques for the production of fluorinated graphene may be discovered or enabled.

5.7. Figures

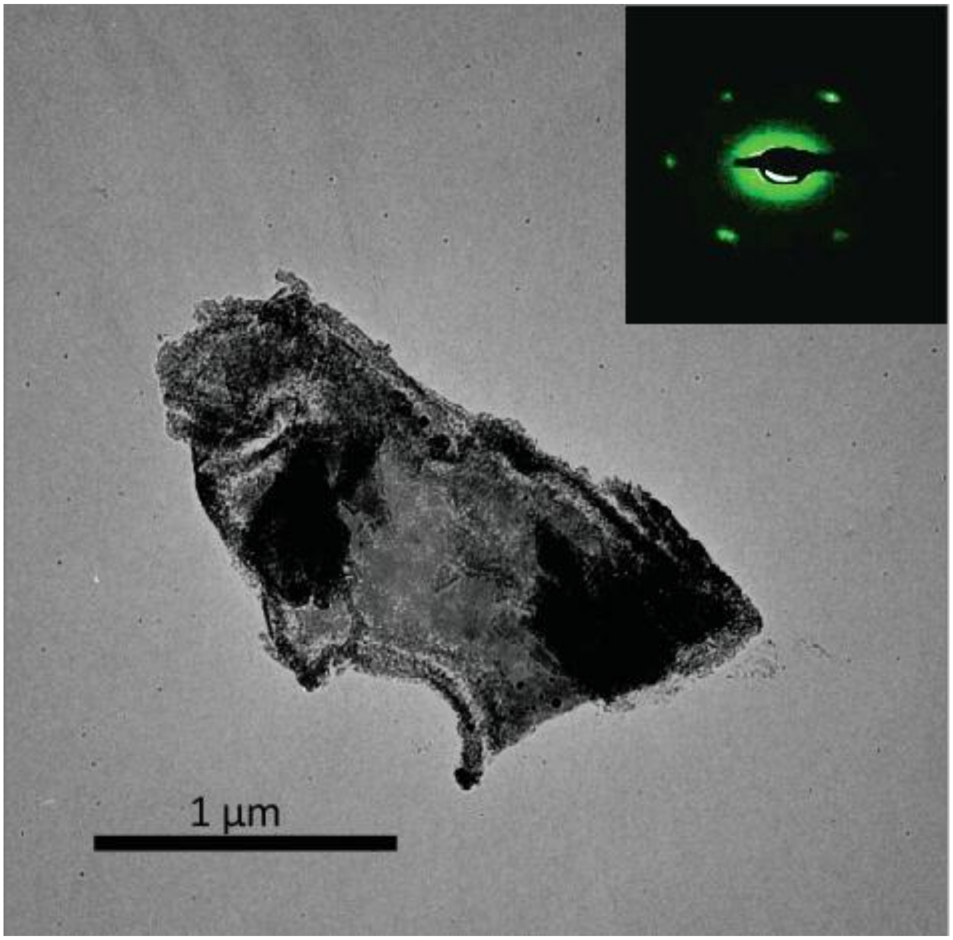

Figure 5.1: TEM micrograph of CF flake on a Formvar grid. The inset shows a diffraction pattern corresponding to this flake, with the expected sixfold symmetry typical of graphitic material. The lattice constant cannot be conclusively determined because the diffraction system was not fully calibrated during this experiment.

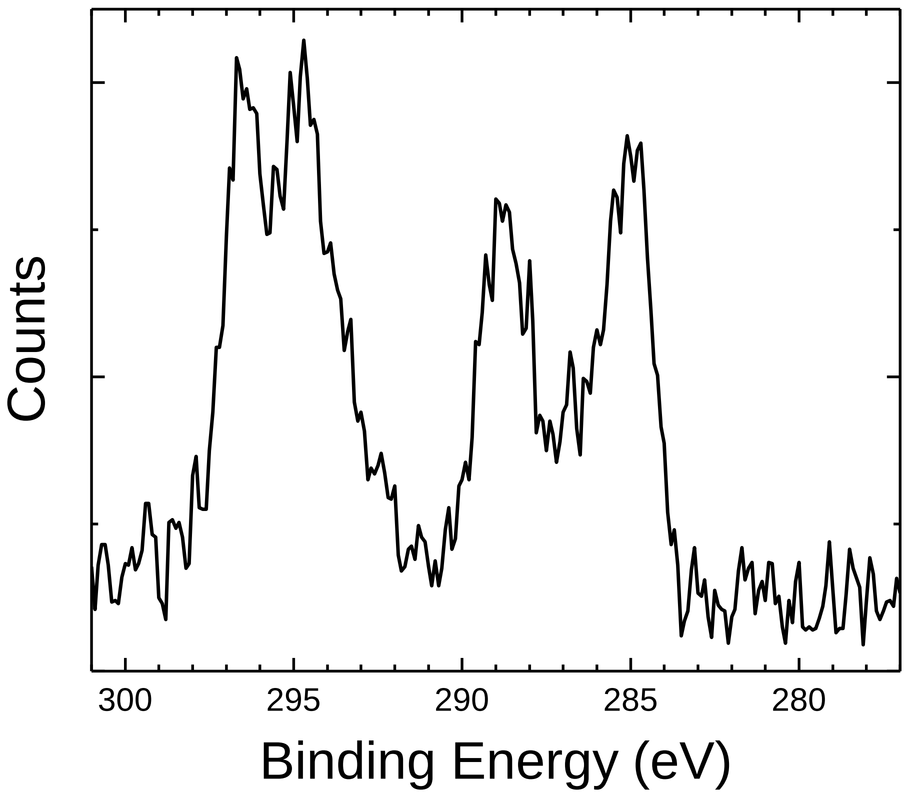

Figure 5.2: XPS spectrum of the C1s peak of fluorinated graphite pressed into Au foil. The spectrum suggests a high degree of fluorination but additionally a high defect density and wide range of C-F bonding configuration, which is consistent with a low-quality sample.

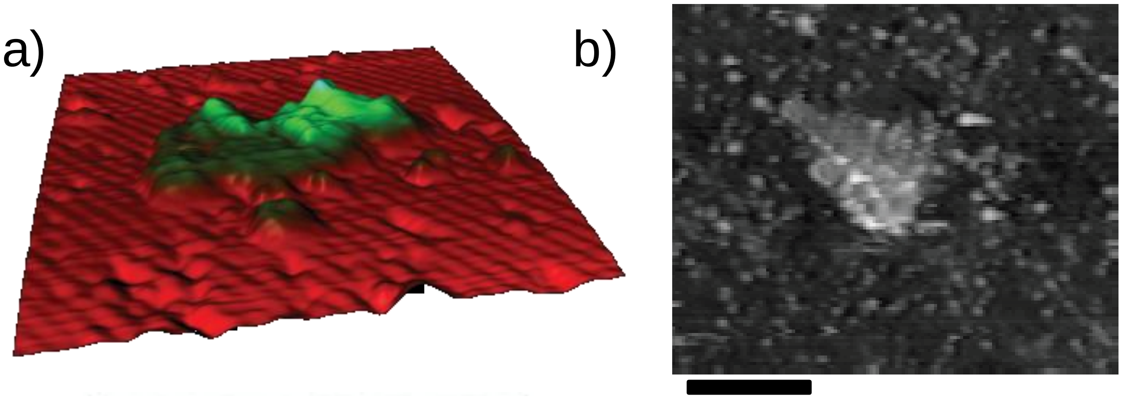

Figure 5.3: Mechanical exfoliation of monolayer CF by dry-contact transfer and characterization by scanning tunneling microscopy (STM). (a) False color, three-dimensional rendering of an exfoliated CF platelet. Green areas represent the CF platelet, and red represents the underlying Si(100) surface. (b) A similarly exfoliated CF flake.

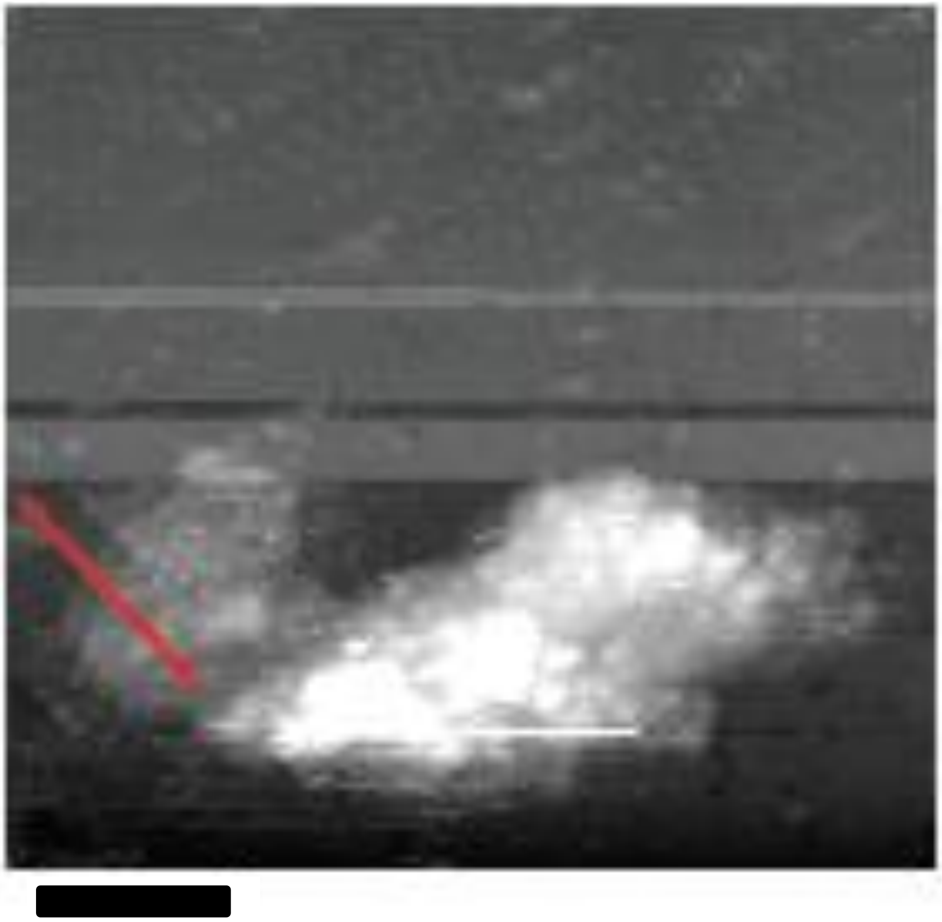

Figure 5.4: A third, larger, flake of CF, demonstrating non-uniformity of fluorination. In this case, a small region of the flake is graphene-like with a topographic height of ~3 Å. The remainder of the flake is fluorinated to varying degrees. Scale bar: 10 nm.

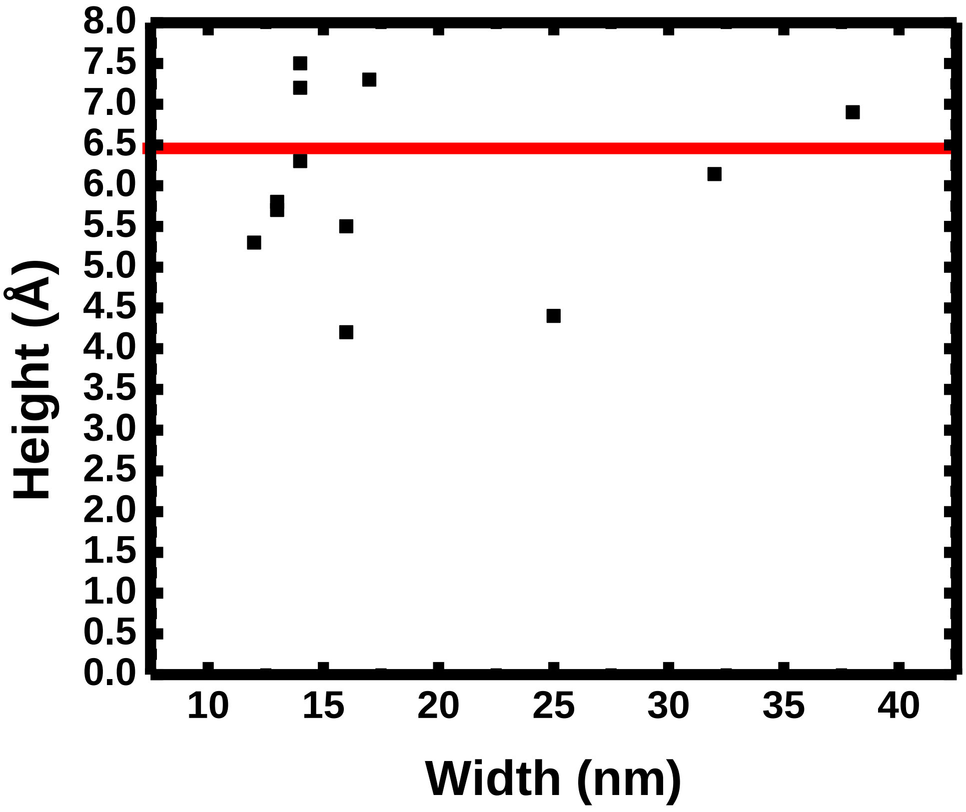

Figure 5.5: Scatter plot of the topographic height and maximum lateral dimension of all CF flakes characterized by STM. Indicated in red is the interlayer spacing of CF[17] for comparison. All of the flakes observed were less than 40 nm in lateral extent. The significant variation observed in topographic height is evidence of the observed non-uniformity in source material fluorination, as well as electron-stimulated modification of the platelets.

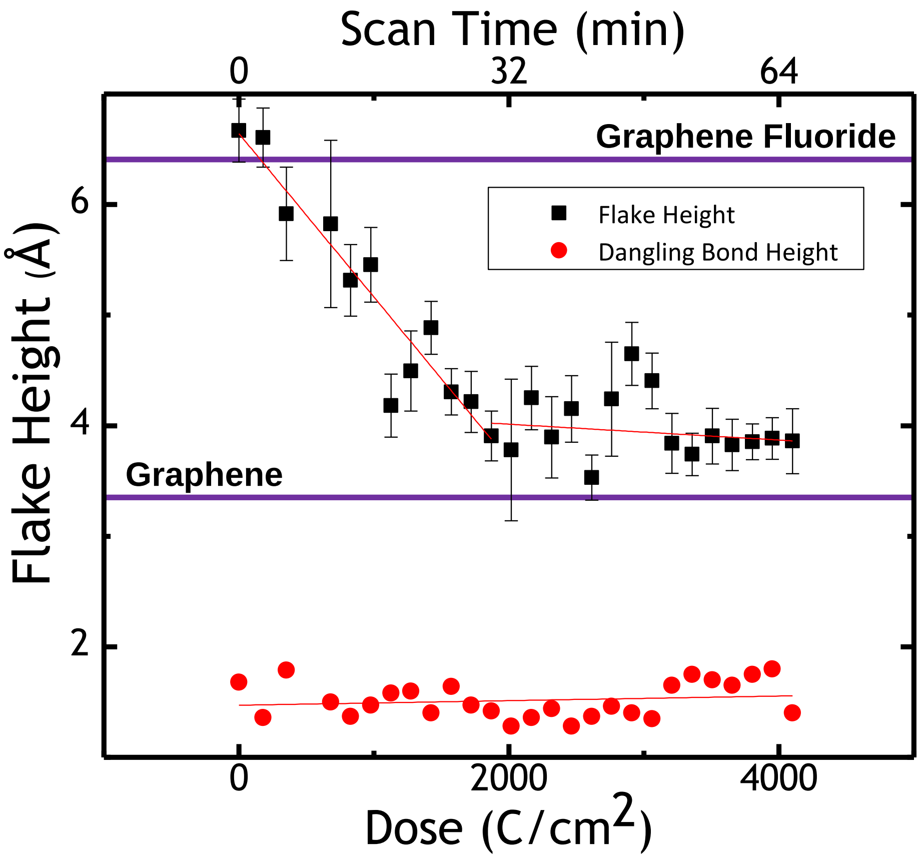

Figure 5.6: Measured height variation of a single CF flake during scanning. Sample bias is −3 V and tunneling current setpoint is 8 pA. Flake height falls linearly under electron bombardment, until saturating at a topographic height of ~4 Å. Also shown as a control is the observed height of silicon dangling bonds on the Si(100) 2 × 1:H surface, taken from the same STM images. Unlike CF flakes, silicon dangling bonds show negligible variations in height throughout the course of the experiment.

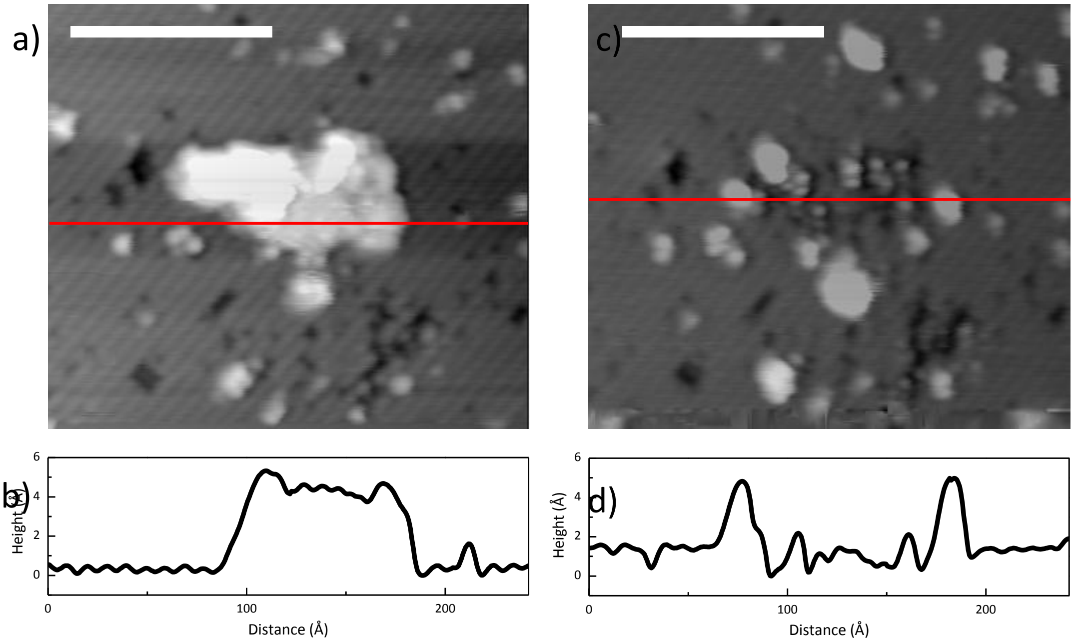

Figure 5.7: Unlike graphene, CF is weakly adhered to the Si substrate. As a result, it can be manipulated by the STM tip, including cutting, pushing, and removal from the surface. After manipulation or removal, fluorine etching of the first atomic layer of the silicon substrate is observed, offering further evidence for electron-stimulated defluorination of CF films. Scale bars: 10 nm. (a) CF flake on Si(100) 2 × 1:H. This flake has undergone extensive scanning (dose: 4000 C/cm^2) and the topographic height has been reduced to ~4 Å. (b) Height contour of flake, demonstrating flake height. (c) Identical silicon substrate after removal of CF flake by STM tip manipulation. The silicon substrate is extensively pitted by fluorine etching. (d) Height contour of the pitted silicon substrate.

CHAPTER 6
ATOMIC AND ELECTRONIC STRUCTURE OF SINGLE-SIDED GRAPHENE FLUORIDE

Fluorinated graphite is produced in puckered and planar forms, distinct in their synthesis and in-plane structure. Fluorination by molecular fluorine between 200 °C and 630 °C produces puckered-sheet graphite fluoride with a puckered sp^3 graphitic backbone of the form CF or C_2F. In contrast, room temperature fluorination by atomic fluorine, often produced from XeF_2, produces a more planar graphite intercalation compound C_xF ($x > 2$) wherein the C_4F in-plane structure is historically known[16] and commonly encountered experimentally.[219] Similar processing has now been applied to monolayer graphene. Although large sheets of substrate-supported monolayer ds-GF are difficult to achieve,[17,27] a form analogous to planar-sheet graphite fluoride can be synthesized by single-sided XeF_2 exposure, leading to ss-GF which saturates as C_4F.[247] Given indications of $C\text{-}F_2$ and $C\text{-}F_3$ bonding[247] and the predominance of variable-range hopping as an electron transport mechanism,[27] the presence of long-range order in ss-GF remains a subject of dispute. Atomic-scale in-plane structure is of profound importance to the application and control of electronic and magnetic properties. For example, atomically-ordered C_4F films have been suggested to serve as a barrier for quantum-confined nanoribbons,[14,249] yet the edge structure of graphene nanoribbons plays an important role. Furthermore, numerous metastable configurations of fluorinated graphene are expected to possess novel carbon-based ferromagnetic or ferrimagnetic properties[289–291] of interest for spin manipulation, but cannot yet be achieved experimentally, and depend heavily on the precise atomic ordering of adsorbed fluorine adatoms.[292] In this study, by STM, STS, and XPS we explore for the first time the atomic-scale structural and electronic characteristics of C_4F ss-GF. We produce the first atomically resolved images of monolayer fluorinated graphene, and find it to possess a wide electronic band gap and structural order on Cu(111) and Cu(311). We further investigate the stability of ss-GF during thermal annealing in vacuum. We find that the underlying Cu substrate exerts a pronounced influence on graphene fluoride, in contrast to CVD graphene films which span defects and topographic modulation on the polycrystalline Cu surface indiscriminately.[161]

Monolayer ss-GF films are produced by a two-step growth and fluorination process. We grow monolayer graphene by CVD on polycrystalline copper foil[158] at 1000 °C for 25 minutes (50 sccm H_2, 850 sccm CH_4). Following growth, the presence of graphene is confirmed by Raman spectroscopy and XPS. Graphene is subsequently fluorinated by exposure to XeF_2 gas at room temperature for 7 minutes in an XACTIX XeF_2 etching system.[247] The films are not removed from the Cu foil, thereby producing the cleanest possible interface and facilitating STM of the wide-gap fluorinated graphene film while minimizing band bending.

6.1. X-ray Photoelectron Spectroscopy and Influence of Annealing

In Figure 6.1, the composition of the resulting film is characterized by XPS, and the effect of thermal annealing explored. We extract by XPS a C/F ratio of 5.3. This ratio is consistent with C_4F, given that approximately 70% of the Cu surface is monolayer with a substantial bilayer component, typical for the growth conditions employed. We identify the following chemical states[293] for carbon atoms in our system: 71.7% C, 6.7% semi-ionic C-F, 7.3% covalent C-F, 4.5% $C\text{-}F_2$, 9.4% $C\text{-}F_3$. The surface contains a significant fraction of C-F_2 and C-F_3 bonding, more than could be explained by sparse point and line defects in CVD graphene.[161] Graphene fluoride is degassed for 17 hours at 120 °C in UHV below 1×10^{-10} torr, and then annealed for 10 minutes between 350 °C and 400 °C in UHV. After imaging the sample by UHV-STM, we collect further XPS data (Figure 6.1c-d) to elucidate the influence of annealing. We measure a C/F ratio of 11.6. Identification of the chemical state of carbon in our annealed system provides the following: 77.1% C, 5% semi-ionic C-F, 10.9% covalent C-F, 0.0% C-F_2, 6.9% C-F_3. We conclude that the UHV thermal reduction process primarily induces desorption of C-F_2 and C-F_3 species, preserving C-F bonded carbon. As we learn by STM, STS, and ARPES studies, this reduction is predominantly restricted to rough Cu surfaces, while long-range order and the wide band gap of C_4F persists on well-ordered Cu(111) and Cu(311) facets. Both before and after annealing, the binding energy of the F 1s electron (calibrated to Cu 2p 3/2 at 932.6 eV) is 689.5 eV, substantially higher than in planar-sheet graphene fluoride.[294] This suggests a strong covalent bond and potentially non-planar structure for ss-GF, and thus we do not adopt the “planar-sheet graphene fluoride” nomenclature.

6.2. Scanning Tunneling Microscopy: Order in Graphene Fluoride

Following anneal, the sample is transferred to a home-built UHV-STM operated at room temperature.[71] Many facets of the polycrystalline copper surface exhibit substantial surface roughness yet are passivated by graphene and remain pristine following atmospheric exposure. This surface passivation effect has been observed previously,[295] and we verify the passivation of our sample by XPS spectra of the Cu 2p doublet (Figure 6.2). While it has been observed that some cold-rolled copper foils exhibit a predominant (100) surface orientation,[296] EBSD data collected on our samples suggest a wide range of surface textures (Figure 6.3). To overcome the inherent roughness of this surface, STM imaging is performed on (111) and (311) facets which are identified by low-resolution batch scanning over a 25 μm^2 area. Scanning is almost universally stable, although clear atomic-resolution imaging of C_4F is achieved exclusively on atomically-flat Cu(111) (Figure 6.4). Covalent fluorine adatoms appear as topographic protrusions in filled-states imaging under conditions selected to avoid the wide gap of the fluorinated graphene overlayer (−4 V sample bias, 10 pA tunneling current), so as to image C_4F rather than the metal-insulator interface. Topographic images of the system clearly indicate a hexagonal in-plane superlattice. In this configuration, F atoms, confined to the top side of the graphene basal plane, are bonded in a super-cell with a lattice constant twice that of graphene (Figure 6.4a-b), disrupting transport and converting semi-metallic graphene into a wide gap semiconductor. The ~4 nm topographic modulations visible in Figure 6.4b constitute a Moiré superstructure which we will explore in greater detail. Identical ordering of fluorine can be found on multiple Cu(111) facets, but cannot be directly observed on high-index Cu. However, as we will see, Cu(311) exhibits a Moiré superstructure consistent with a C_4F overlayer. STS shows a band gap on all studied facets, even high-index surfaces, although the band gap is reduced on high-index surfaces. No other low-index Cu facets were studied, thus we cannot rule out the possibility of a similar result on the Cu(100) or Cu(110) surface. As a control, STM studies of pristine graphene on copper were performed and exhibit the anticipated lattice structure, as shown on an identical scale in Figure 6.4c. These images of graphene on copper are consistent with earlier studies of the material.[161]

Furthermore, by STM we can verify the monolayer nature of our fluorinated graphene films and identify conclusively the underlying Cu substrate and its orientation relative to the ss-GF overlayer. As a near-surface imaging technique, STM is capable of detecting the electronic influence of sub-surface atoms, in this case the Cu substrate. This electronic interaction produces Moiré superstructure arising from lattice misalignment between these two stacked, crystalline materials. In cases where the Moiré pattern is hexagonal (Figure 6.5), we identify the underlying Cu substrate as Cu(111), the only hexagonal low-index surface of Cu thus capable of producing a hexagonal Moiré pattern with C_4F. In one instance, two orthogonal surfaces were visible and identifiable as Cu(111) and Cu(311) (Figure 6.6), and this identification allows the substrate orientation to be precisely defined. To help rule out the possibility that the Moiré pattern could arise from turbostratically stacked bilayer graphene, we model the system from direct observation of the orientation of fluorinated graphene and Cu. The predicted Moiré structures on both Cu(111) (Figure 6.6) and Cu(311) (Figure 6.7) agree with our experimental observations, and we thus conclude that the superstructure results from electronic interaction between C_4F and Cu. As we shall see, this interaction leads also to the visibility of the Cu(111) surface state.

We also show in greater details the superstructure visible on Cu(311). In Figure 6.8, we show a topographic image of C_4F on Cu(311) with a derivative inset in the upper left showing the transition into an adjacent Cu(111) facet where the C_4F atomic structure is visible. Also shown are contour plots running across and along the “beans” of the Moiré superstructure.

6.3. Scanning Tunneling Spectroscopy: Graphene Fluoride Band Structure

Fluorinated graphene is currently of interest for its electronic properties, and for this reason we employ STS to extract the electronic band structure. The predicted (>3 eV) wide-gap electronic structure of fluorinated graphene is observed in all cases (Figure 6.9). Also observed is the presence of a gap state near the Fermi level, which we attribute to the Cu(111) Shockley surface state. Focusing specifically on the well-characterized facets described in Section 6.2, we approximate the local density of states (LDOS) of C_4F by normalized dI/dV calculated from variable-spacing STS (−2 Å).[297] Our results are consistent with theoretical predictions and reproducible between data points and distant Cu facets.

The electronic state visible near −0.6 eV is assigned to the Cu(111) surface state, while the state near 1.7 eV is the C_4F conduction band edge.[298] The observed valence band edge of C_4F is near the Cu d-band state, thus requiring further study to distinguish the two. Comparing STS on Cu(111) and Cu(311) (Figure 6.10) we find C_4F on Cu(311) to be p-doped, an unexpected result that may follow from interaction between ss-GF and periodic charge modulation on the Cu(311) surface.[161] Visibility of the Cu surface state is reasonable given the use of variable-spacing STS, whereby the tip is moved progressively nearer the sample as sample bias approaches zero (−2 Å at the Fermi level). As a result, tip-sample spacing is reduced near the Fermi level and the Cu(111) surface state is discernible. We also note that the surface state persists on Cu(311), but is shifted nearer to the Fermi level, as expected.[299] An observation that cannot yet be explained is the apparent increase in band gap on Cu(311) relative to Cu(111). The band gap of C_4F on Cu(111) is measured to be 3.4 eV, but on Cu(311) this gap increases to 3.7 eV, an unexpected result and the subject of future study.

Additional data is collected on high-index Cu surfaces, on which the surface orientation can be identified (relative to nearby Cu(111)) but atomic resolution of fluorinated graphene is not achieved. In these cases, a wide band gap is seen, and, as expected, the Cu(111) surface state is not seen (Figure 6.11). This indicates that fluorinated graphene spans these regions, but spectroscopic variability of these facets suggests that the surface is partially reduced by annealing, consistent with XPS. This variability is believed to follow from variations in fluorine ordering and concentration and suggests that the substrate plays an important role in the fluorination and reduction of graphene, due either to roughness or superlattice periodicity, as seen in the hydrogenation of graphene on iridium.[244]

As our C_4F sample does not contain any known materials on which our STM tip can be calibrated, we employ the Si(100) 2 × 1:H surface. Immediately following our STS study, the C_4F sample is removed, and a previously prepared Si sample is loaded into the STM. Dimer-resolution imaging of Si(100) 2 × 1 is immediately achieved, and STS data collected (Figure 6.12). An accurate Si band structure is observed, in particular a 1.1 eV band gap, thus indicating the density of states of our STM tip has not significantly convolved the density of states of C_4F.

We note that the orientation of C_4F is identical between distant Cu facets on the same graphene and Cu grains, but this does not necessarily indicate that the initial C_4F

film was ordered between these islands, rather that the islands fall upon a single graphene grain. This identical orientation occurs because, for a single graphene domain, there exist no rotationally distinct configurations of C_4F. While three rotationally equivalent domains exist (Figure 6.13), roughness and lack of atomic resolution on high-index Cu surfaces makes it impossible to identify any such domain boundaries between low-index facets.

6.4. Discussion

In this first atomically resolved study of graphene fluoride, and in particular of ss-GF, we have verified the predicted atomic structure of this novel material, identified specifically the relative orientation of the Cu substrate and C_4F overlayer, and explored the local density of states of this material. Given our identification of the Cu substrate orientation, we are able to explore the influence of various Cu substrates on our fluorinated graphene films. Finally, we verify the expected wide-gap electronic structure of ss-GF, as well as the presence of long-range order within these films.

The C_4F form of ss-GF is a hexagonal fluorine superlattice with a lattice constant twice that of graphene. On the Cu(111) and Cu(311) substrates, these structures appear consistently, and are well ordered within Cu surface facets. On high-index surfaces of Cu we do not achieve atomic resolution imaging of C_4F, but an electronic band gap is preserved. The preservation of a band gap suggests that fluorination persists, albeit with a variable fluorine concentration.

C_4F ss-GF is a wide-gap semiconductor, with a gap larger than 3 eV. On Cu(111) and Cu(311) this band gap is reproducible, but films on rough Cu surfaces are partially reduced during annealing.

6.5. Figures

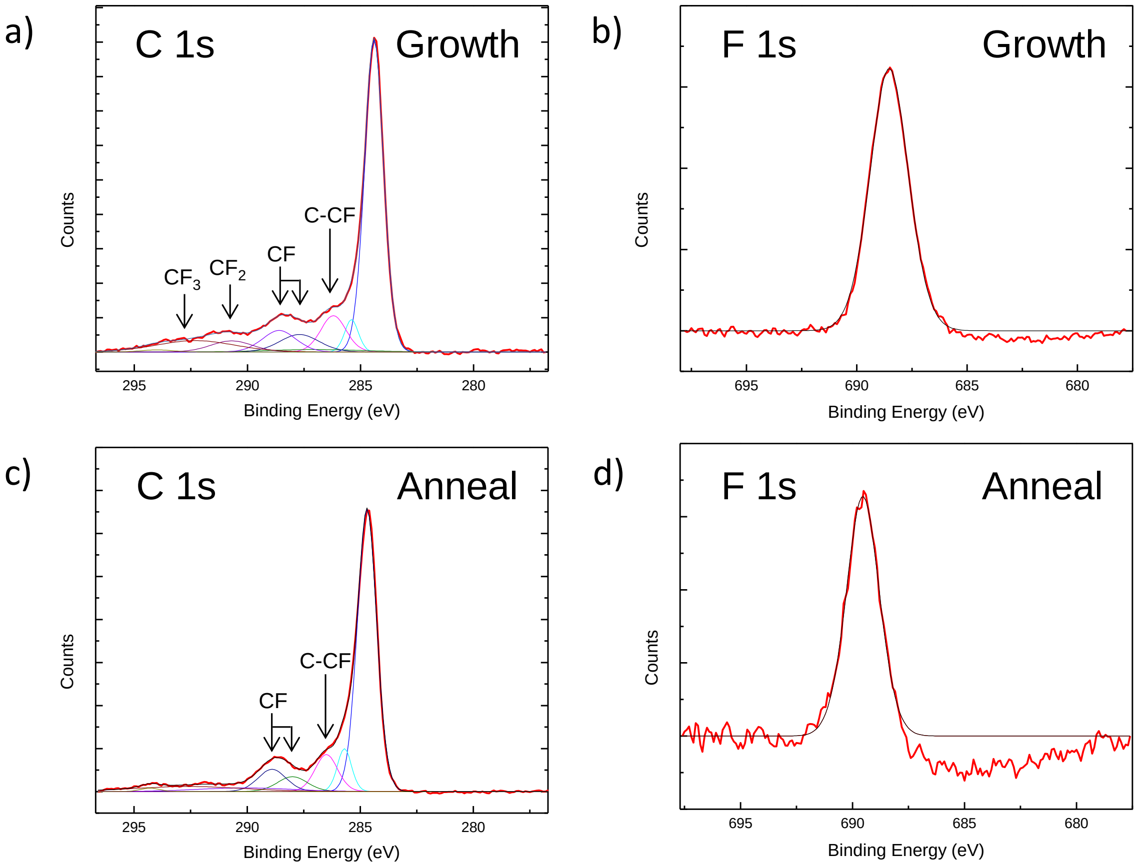

Figure 6.1: X-ray photoelectron spectra of monolayer graphene fluoride following growth, and then following annealing and STM analysis. Plots presented following background subtraction. (a) C 1s peak of graphene fluoride following growth and before annealing, with peaks identified]. (b) F 1s peak of graphene fluoride following growth. (c) C 1s peak of graphene fluoride after annealing and STM, with peaks identified. (d) F 1s peak of graphene fluoride following annealing.

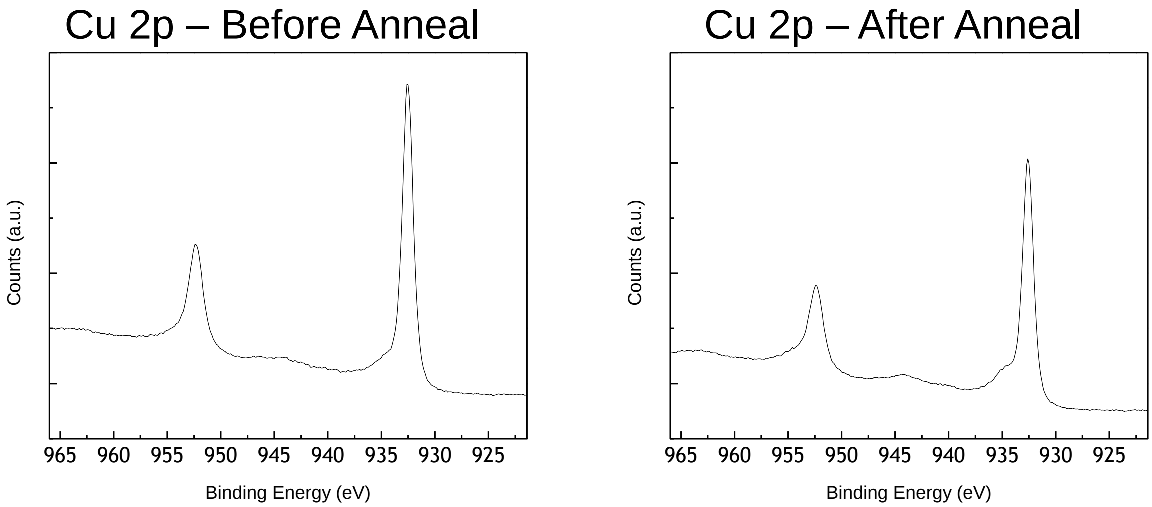

Figure 6.2: High-resolution XPS data of Cu 2p doublet used for calibration and verification of substrate passivation by graphene. In order to calibrate the positions of our C 1s and F 1s peaks, we shift to align the 2p doublet of the nominally pure Cu with its predicted binding energy (Cu 2p 3/2 peak at 932.6 eV). Furthermore, from the Cu 2p doublet we confirm the absence of any significant oxidation or fluorination on the Cu surface both before and after fluorination. The absence of oxidation indicates that the graphene passivation layer remains predominantly continuous during fluorination and annealing, despite evidence for partial reduction of C_4F.

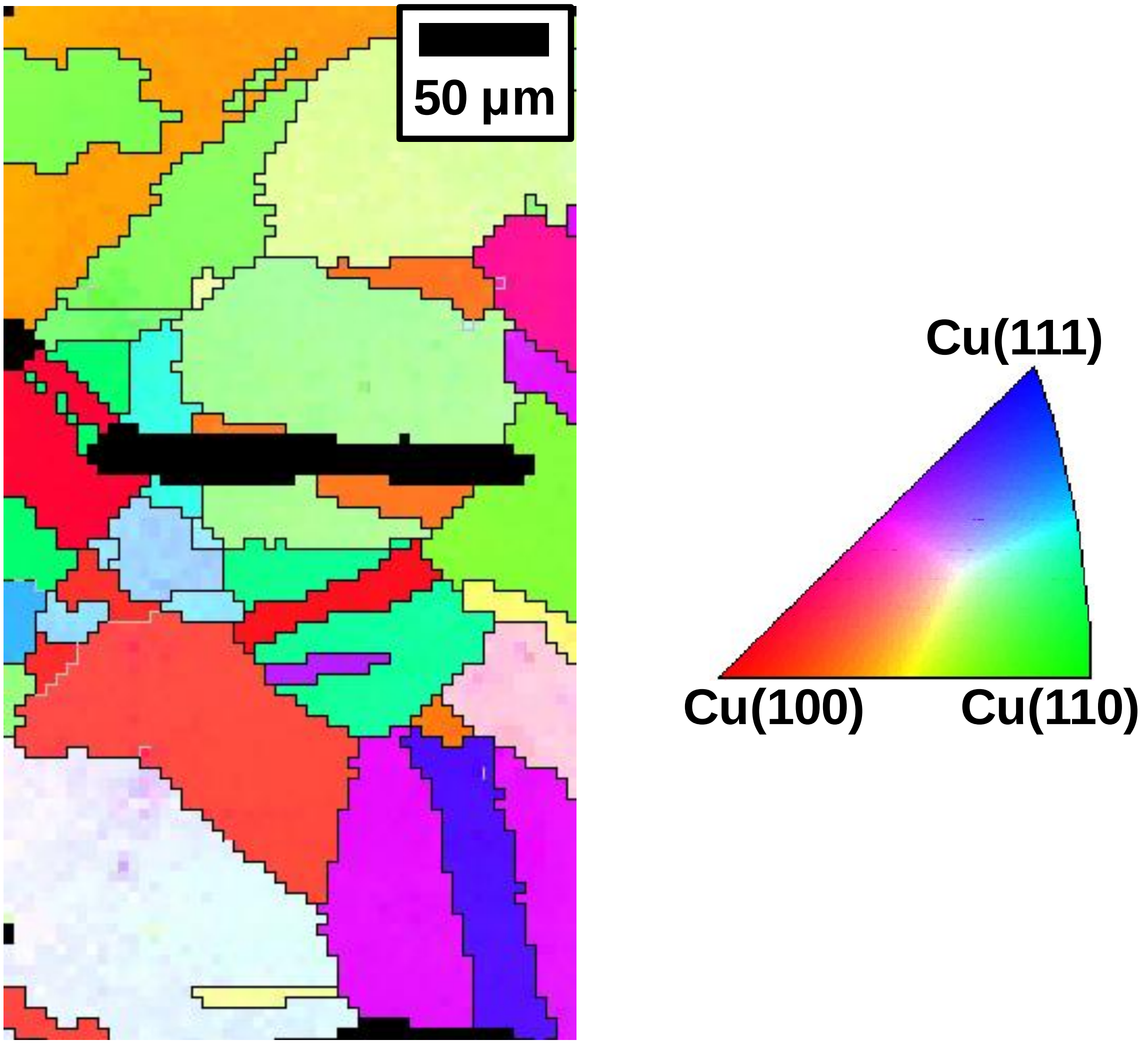

Figure 6.3: During annealing, cold-rolled polycrystalline Cu foils can produce crystallographically preferred surface orientations, often Cu(100) or Cu(111), but in our case the substrate is found predominantly to preserve its highly polycrystalline nature. Using EBSPs collected after the conclusion of the high-temperature graphene CVD process, we verify that the foils used in this experiment contain a wide range of surface orientations, including Cu(100), Cu(111), Cu(110), and a variety of high-index grains.

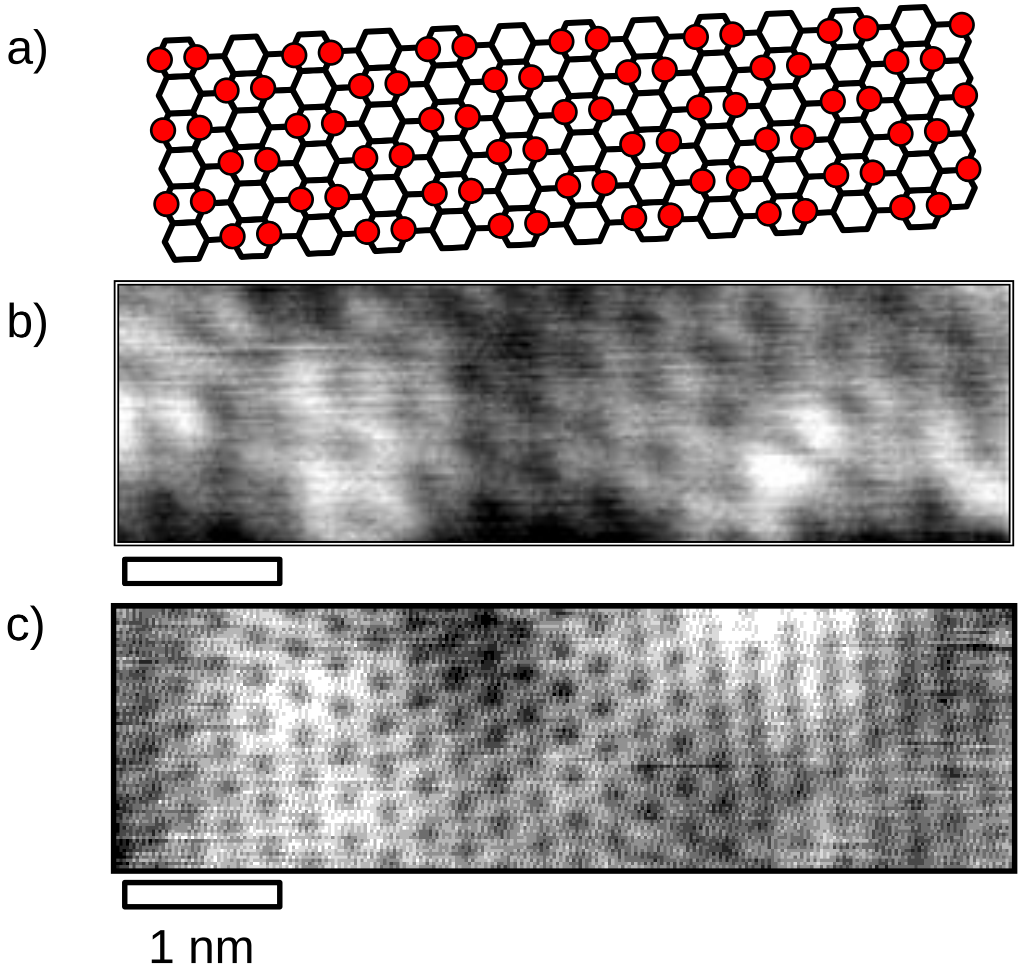

Figure 6.4: Atomic-resolution scanning tunneling microscopy of C_4F on Cu(111). All images on identical scale. Scale bars: 1 nm. (a) Schematic representation of C_4F oriented to the topograph in (b). (b) Topographic image of C_4F on Cu. Fluorine atoms appear as topographic protrusions. Topographic modulations of ~4 nm are elements of a Moiré superstructure. Scanning conditions: −4 V sample bias, 10 pA tunneling current. (c) Spatial derivative of monolayer graphene on Cu from non-fluorinated control experiment. Scanning conditions: −70 mV sample bias, 5 nA tunneling current.

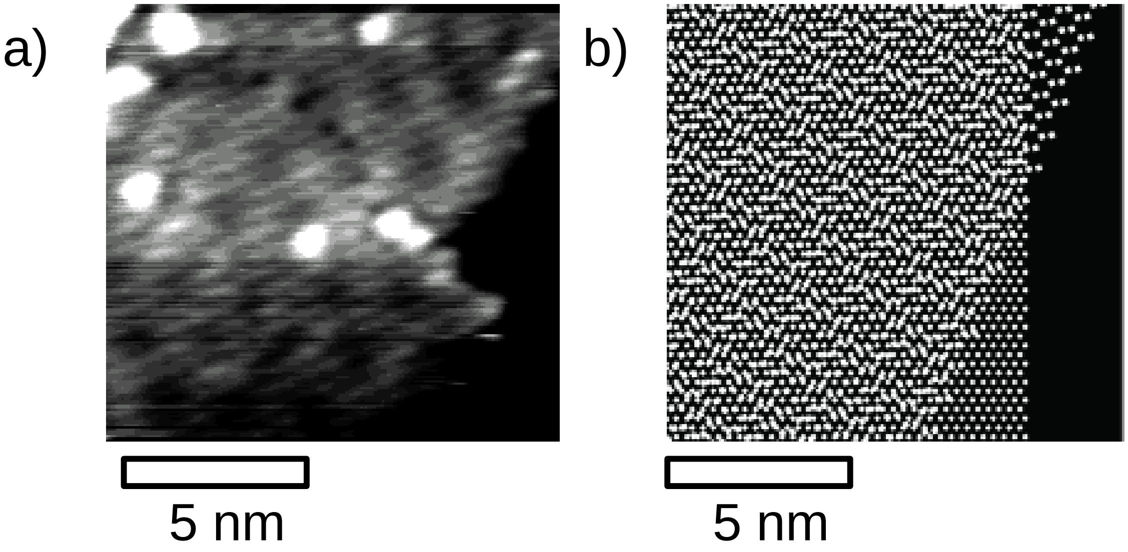

Figure 6.5: (a) Cu(111) facets can be identified by a Moiré pattern arising from the interaction between C_4F and the underlying Cu(111). The presence of this hexagonal pattern uniquely identifies the Cu(111) surface. Scale bar: 5 nm. (b) The orientation of the Cu(111) substrate can be identified by comparison with a theoretical model. This agreement with experiment not only provides the substrate orientation, but also further validation of our C_4F film structure. Scale bar: 5 nm.

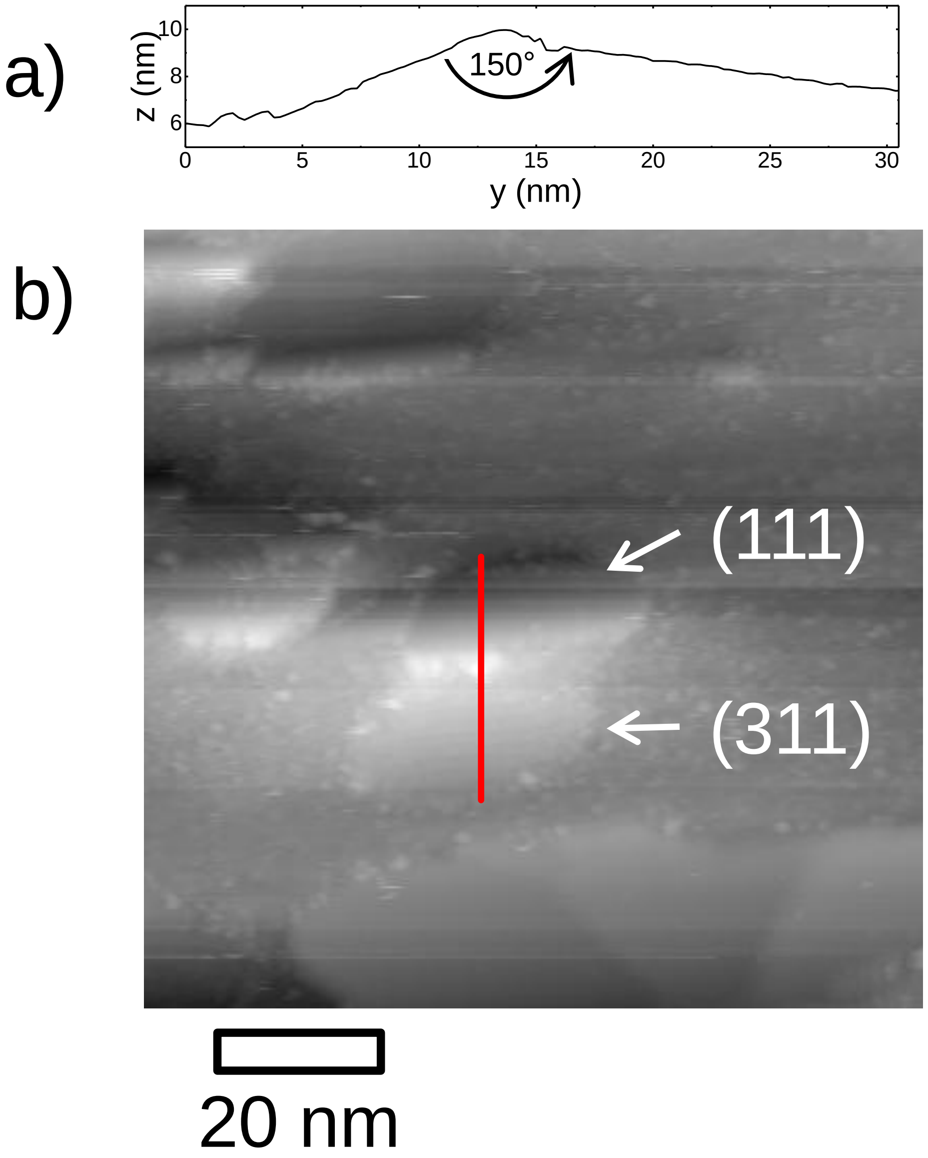

Figure 6.6: (a) 1-D contour plot corresponding to the red line in Figure 6.6b. From the known orientation of the Cu(111) facet, and the measured 150° (30°) angle between facets, we identify the lower facet as Cu(311). (b) Topographic image of Cu(111) and Cu(311) facets within a single grain of polycrystalline Cu. The red line corresponds to the contour plot of Figure 6.6a. Scale bar: 20 nm.

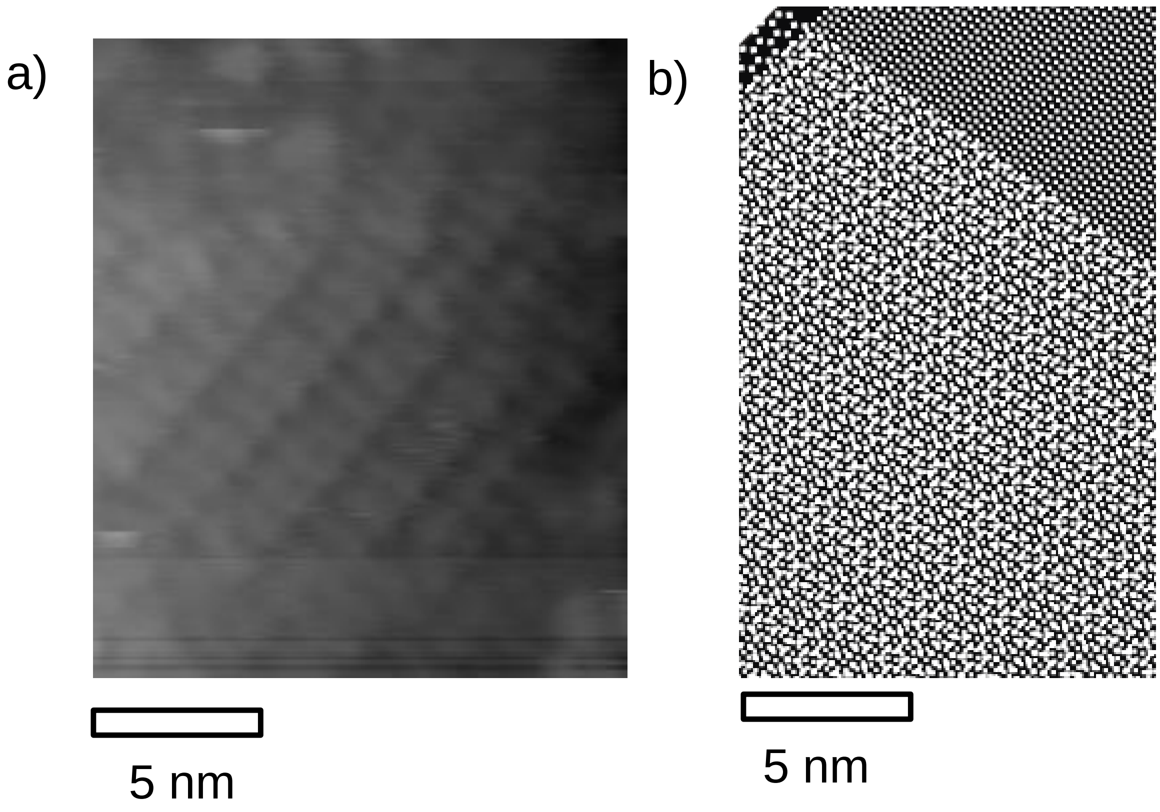

Figure 6.7: (a) Having determined the orientation of the Cu substrate, it is now possible to identify other surfaces, specifically Cu(311) which can be seen in topographic images of the substrate. (b) Moiré pattern model for C_4F on Cu(311) in agreement with experimental observations.

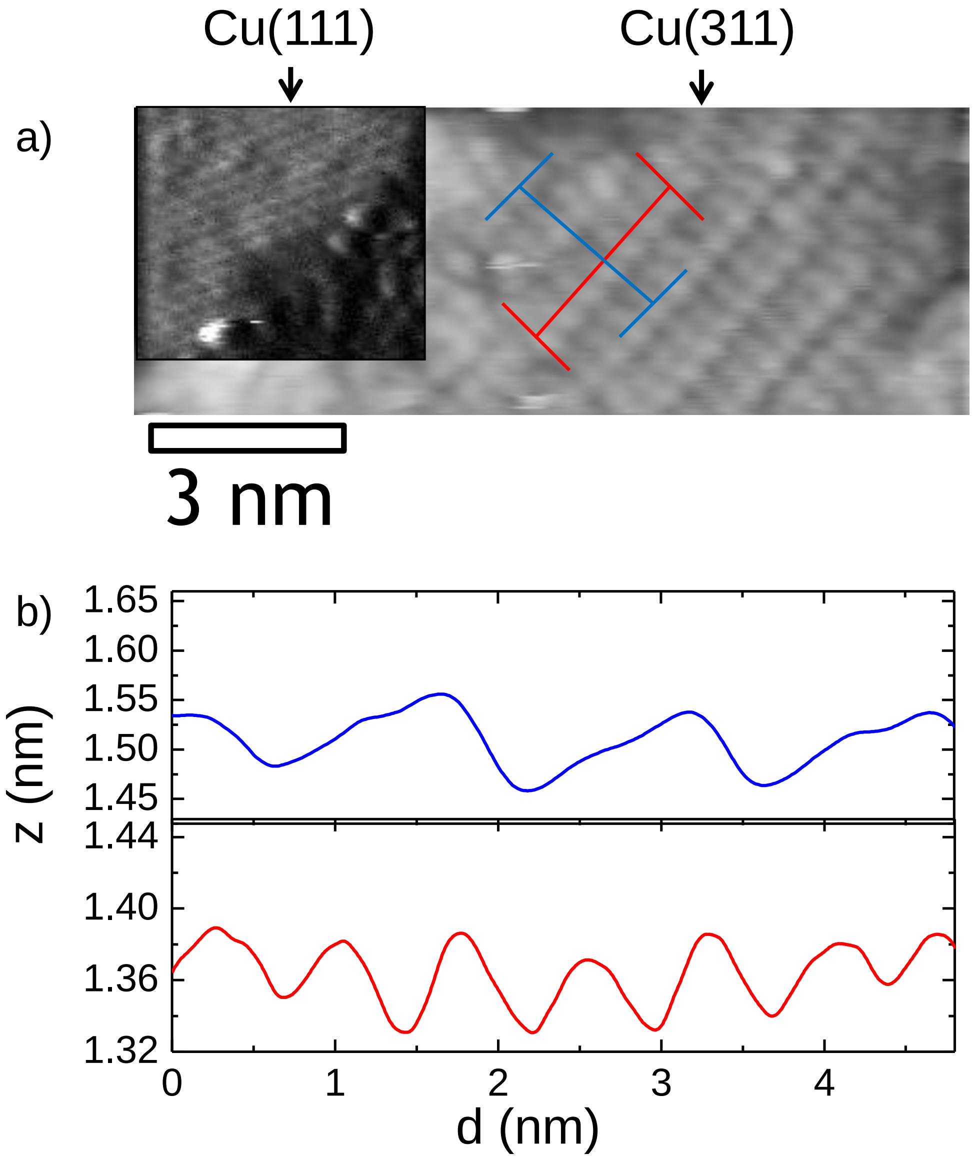

Figure 6.8: Contour plots of the superstructure visible for C_4F on Cu (311). (a) Topographic image of the surface, where Cu(311) abuts Cu(111) (shown in the derivative inset in the upper left corner). (b) Contours below correspond to the red and blue lines in (a).

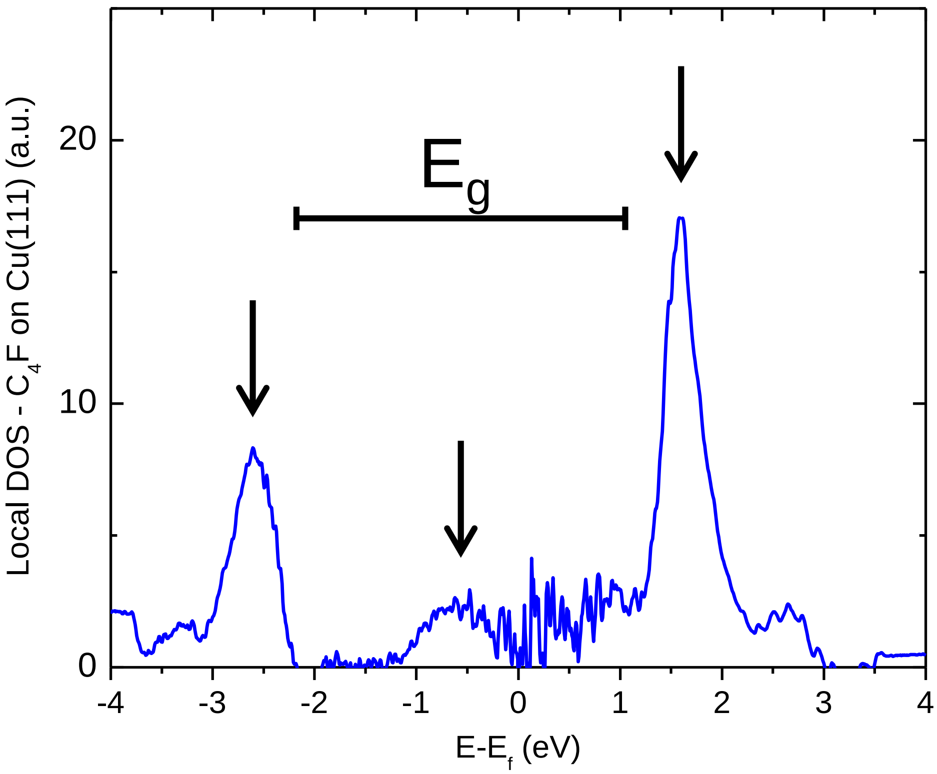

Figure 6.9: Typical local DOS measured on Cu(111) identifying the band gap of C_4F (E_g), the Cu(111) surface state near −0.6 eV, and the conduction and valence band edges.

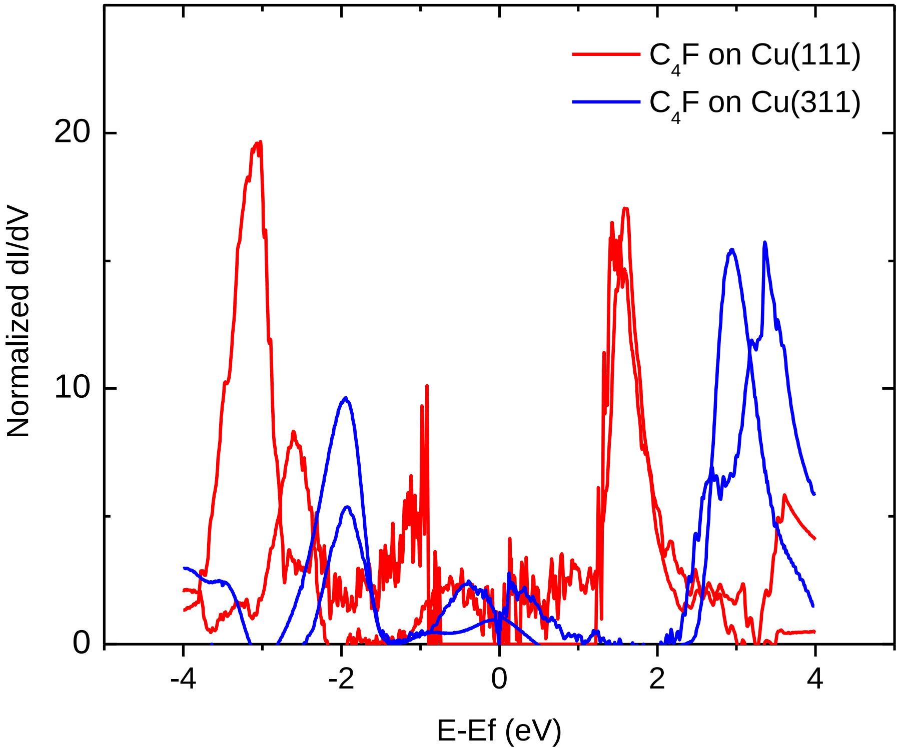

Figure 6.10: Normalized dI/dV spectroscopic data for C_4F graphene fluoride on two independent Cu(111) facets in red and two independent Cu(311) facets in blue.

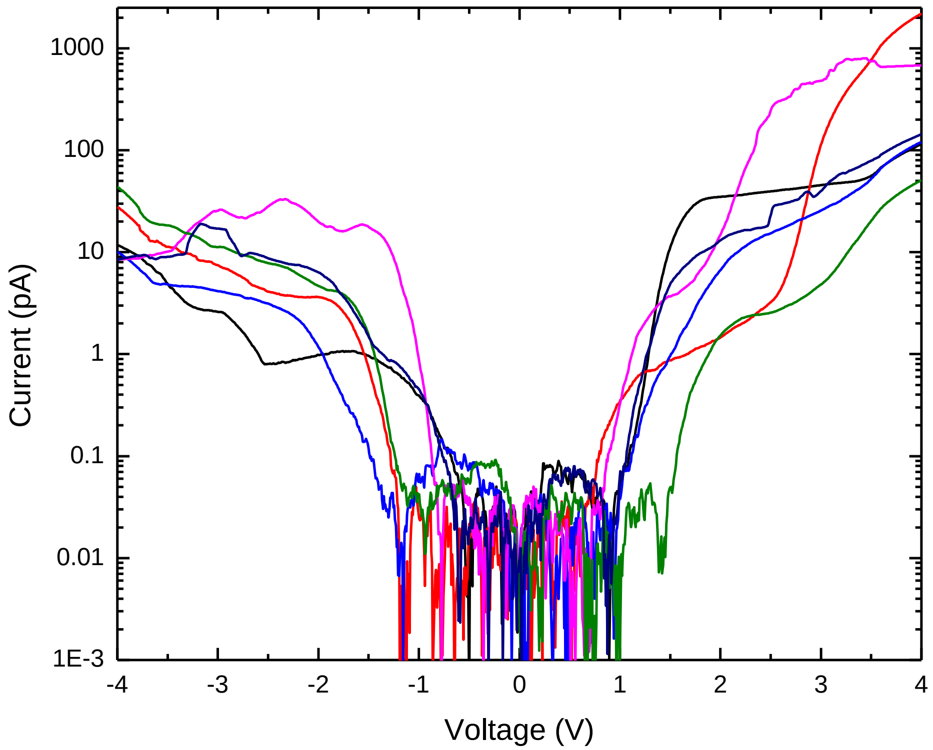

Figure 6.11: Variable spacing IV spectroscopic data from various rough Cu surfaces. A wide band gap of graphene fluoride persists, but as expected the Shockley surface state is not visible. The band gap is smaller and more variable than on Cu(111) or Cu(311) and a state near 2.5 eV appears inconsistently.

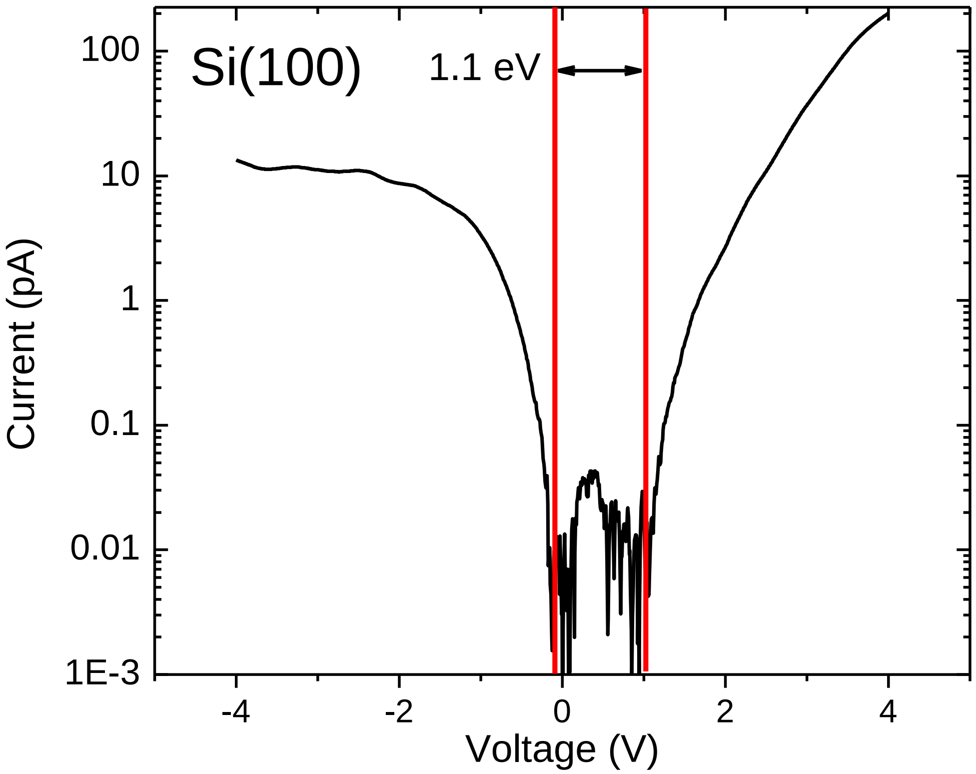

Figure 6.12: Variable spacing IV spectroscopic data from the Si(100) 2 × 1:H surface using the same tip immediately following the spectroscopy study of C_4F.

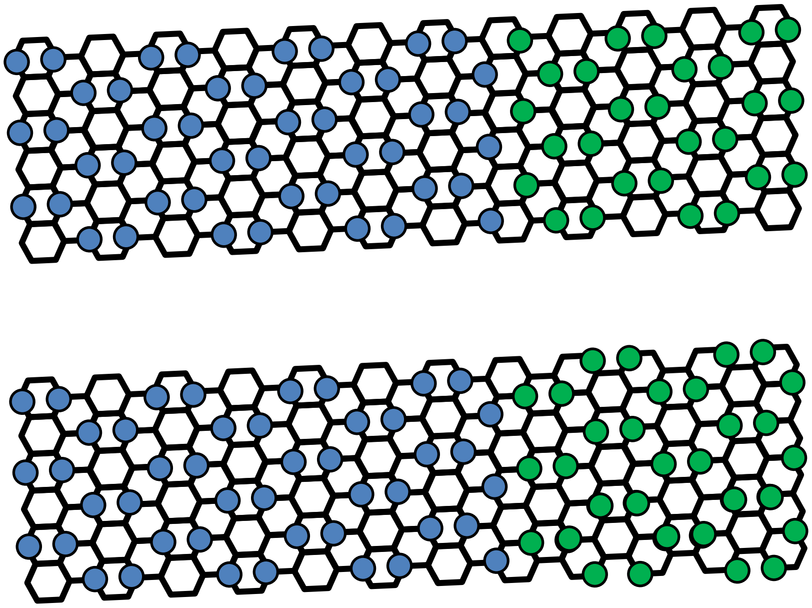

Figure 6.13: While domains in polycrystalline graphene can contain an infinite range of misorientation angles, the fluorination process itself is bound precisely to the orientation of the graphene template. Within a single grain of graphene, no rotationally misoriented domains of fluorine can exist, so long as the C_4F structure is preserved. However, there exist several possible fluorine domains that may arise during the agglomeration of expanding clusters. Two such examples of fluorine grain boundaries are shown, though none are observed experimentally in this study. These diagrams seek to express possible domain orientations, not to strictly demonstrate the preferred atomic configuration of domain boundaries.

CHAPTER 7
CONCLUSIONS AND FUTURE WORK

7.1 Dissertation Summary

This dissertation has explored the process of FDSS, and the nature of single-sided and double-sided forms of fluorinated graphene. We have shown that FDSS produces ultra-sharp metallic tips, that these tips perform significantly better than those prepared by CSE or ECE as electron-sources for ESD of H in the STM, and that the FDSS technique is applicable to HfB_2. We have shown that ds-GF can be exfoliated by DCT, and that the resulting films are unstable under electron bombardment. In contrast, we have shown that ss-GF (C_4F) can be produced on Cu, and that these films are well ordered, wide gapped, and stable.

In Chapter 2 we explored FDSS and, by means of TEM, characterized tips composed of W and Pt-Ir. We demonstrated the sharpest sputter sharpened tip yet produced, and demonstrated that this process was consistent across multiple materials. We explained the influence of off-axis FDSS, and demonstrated the sharpening of DLC films by FDSS, a process that is less effective due to the film's high resistivity.

In Chapter 3 we applied FDSS to a more conductive ultra-hard material, HfB_2. We demonstrated that the sharpening process is effective, and that it affords significant benefits over CSE. We demonstrated the use of HfB_2 as an STM tip material, and verified that it is capable of high-resolution imaging and patterning, as well as stable spectroscopy.

In Chapter 4, we approached the limits of atomically-precise lithography of the Si(100) 2 ×1:H surface. Using ultra-sharp FDSS tips, we demonstrated smaller lithographic pattern widths that ultimately approach reliable atomic-fidelity. We also demonstrated regeneration of tips for ongoing atomic-resolution lithography using FDSS.

Employing the STM and FDSS-processed tips, in Chapter 5 we demonstrated the mechanical exfoliation of puckered-sheet graphene fluoride to the Si(100) 2 × 1:H surface and, consistent with earlier work on fluorocarbon nanostructures, discovered instability inherent to the system which prevents the stable integration of these materials. We demonstrated the tip-induced defluorination of ds-GF, and the ability of the STM to manipulate and remove graphene fluoride flakes from the substrate. We also demonstrated fluorine etching of the silicon substrate as evidence of defluorination and as a possible avenue for further study of fluorine-silicon interaction.

Shifting to a planar-sheet form of graphene fluoride, in Chapter 6 we demonstrated the presence and stability of long-range ordering in C_4F graphene fluoride on polycrystalline copper foil. We found that ordered films of C_4F are formed by XeF_2 treatment followed by UHV anneal between 350 °C and 400 °C, and that C_4F films are comprised predominantly of covalently bonded fluorine with some evidence of semi-ionically bound fluorine and more highly fluorinated carbon structures, likely at grain boundaries and defects. We have measured the density of states of C_4F on copper and found exceptional agreement with theoretical predictions of a wide band gap with a gap state corresponding to the Cu(111) Shockley surface state near the Fermi level.

In conclusion we developed a novel tip sharpening technique which provides the first parallelizable and material independent process for producing sharp metal probes with 1 – 5 nm radii. We have further studied two common forms of graphene fluoride, discovered a non-negligible interaction between ds-GF and the substrate, and subsequently verified the stability of single-sided planar-sheet graphene fluoride on copper. We have resolved uncertainty surrounding the presence of long-range order and a stable band structure in planar-sheet graphene fluoride synthesized by XeF_2 treatment, and pioneered a project for further studies of graphene fluoride and reduced graphene fluoride by STM.

7.2 Future Work

This dissertation represents some of the earliest studies of fluorinated graphene films, and provides an introduction to an extensive program of research, only the earliest stages of which have been realized. Given the ability to produce and characterize fluorinated, and, more generally, chemically modified, graphene with atomic resolution, countless experimental studies are now made possible.

For example, as discussed in Chapter 1, numerous techniques are available for the reduction of fluorinated graphene, each with their own advantages and disadvantages, and none yet understood. Knowing that C_4F is predominantly defect-free, the techniques and results of this study offer a powerful tool for the characterization of each reduction technique, a study that could ultimately optimize the patterning of chemically modified graphene.

Perhaps more directly, the STM offers the potential for ESD of F from C_4F. Future work will explore such direct desorption, as an approach to demonstrating quantum-confined graphene structures in fluorinated graphene films.

Furthermore, there has been much interest in the exploration of the magnetic properties of fluorinated graphene films. Because defects (including F atoms) on each sublattice introduce a specific magnetic polarization to the system,[290,291,300] by confining F atoms to a single sublattice, a ferromagnetic carbon material could be produced. It is not clear that such a structure exists,[292] but it remains an elusive goal for many researchers. The work of this dissertation, particularly in the study of partially reduced graphene fluoride on high-index surfaces, offers some insights and opportunities here. One approach to achieving such ferromagnetic structures may be the use of graphene-substrate interactions to tailor F or H adsorption sites, as in the work of Ng et al.[241]

Our studies of FDSS immediately offer the potential for applications in fabrication of AFM probes and field-emitter arrays. The up-scaling of this technique to a massively parallelizable system (for example, by a raster-scanned ion gun or plasma etching system) would offer the potential for scaling to commercially viable quantities. Furthermore, since the range of novel tip materials is nearly limitless, future work should explore such applications.

Ultimately, the work of this dissertation frames two fields of research, field-directed sputter sharpening and fluorinated graphene, each of which will continue to grow and thrive long into the future.

References

1. Novoselov, K. S. *et al.* Electric field effect in atomically thin carbon films. *Science* **306**, 666–669 (2004).
2. Geim, A. K. & Novoselov, K. S. The rise of graphene. *Nat. Mater.* **6**, 183 (2007).
3. Neto, A. H. C., Guinea, F., Peres, N. M. R., Novoselov, K. S. & Geim, A. K. The electronic properties of graphene. *Rev. Mod. Phys.* **81**, 109–162 (2009).
4. Chen, J. H., Jang, C., Xiao, S., Ishigami, M. & Fuhrer, M. S. Intrinsic and extrinsic performance limits of graphene devices on SiO_2. *Nat. Nanotechnol.* **3**, 206–209 (2008).
5. Han, M. Y., Ozyilmaz, B., Zhang, Y. & Kim, P. Energy band gap engineering of graphene nanoribbons. *Phys. Rev. Lett.* **98**, 206805 (2006).
6. Xia, F., Farmer, D. B., Lin, Y. & Avouris, P. Graphene field-effect transistors with high on/off current ratio and large transport band gap at room temperature. *Nano Lett.* **10**, 715–718 (2010).
7. Giovannetti, G., Khomyakov, P. A., Brocks, G., Kelly, P. J. & van den Brink, J. Substrate-induced band gap in graphene on hexagonal boron nitride: Ab initio density functional calculations. *Phys. Rev. B* **76**, 073103 (2007).
8. Sofo, J. O., Chaudhari, A. S. & Barber, G. D. Graphane: A two-dimensional hydrocarbon. *Phys. Rev. B* **75**, 153401 (2007).
9. Elias, D. C. *et al.* Control of Graphene's Properties by Reversible Hydrogenation: Evidence for Graphane. *Science* **323**, 610–613 (2009).
10. Sessi, P., Guest, J. R., Bode, M. & Guisinger, N. P. Patterning Graphene at the Nanometer Scale via Hydrogen Desorption. *Nano Lett.* **9**, 4343–4347 (2009).
11. Singh, A. K. & Yakobson, B. I. Electronics and Magnetism of Patterned Graphene Nanoroads. *Nano Lett.* **9**, 1540–1543 (2009).
12. Singh, A. K., Penev, E. S. & Yakobson, B. I. Vacancy Clusters in Graphane as Quantum Dots. *ACS Nano* **4**, 3510–3514 (2010).
13. Lin, Y., Ding, F. & Yakobson, B. I. Hydrogen storage by spillover on graphene as a phase nucleation process. *Phys. Rev. B* **78**, 041402 (2008).
14. Ribas, M. A., Singh, A. K., Sorokin, P. B. & Yakobson, B. I. Patterning Nanoroads and Quantum Dots on Fluorinated Graphene. *Nano Res.* **4**, 143 (2011).
15. Ruff, O. & Bretschneider, O. Die Reaktionsprodukte der verschiedenen Kohlenstoffformen mit Fluor II (Kohlenstoff-monofluorid). *Z. Anorg. Chem.* **217**, 1–18 (1934).
16. Rüdorff, W. & Rüdorff, G. Tetrakohlenstoffmonofluorid, eine neue Graphit-Fluor-Verbindung. *Chem. Ber.* **80**, 417–423 (1947).
17. Cheng, S.-H. *et al.* Reversible Fluorination of Graphene: Towards a Two-Dimensional Wide Bandgap Semiconductor. *Phys. Rev. B* **81**, 205435 (2010).
18. Charlier, J.-C., Gonze, X. & Michenaud, J.-P. First-principles study of graphite monofluoride $(CF)_n$. *Phys. Rev. B* **47**, 16162–16168 (1993).
19. Rudorff, W. Graphite intercalation compounds. *Adv. Inorg. Chem. Radiochem.* **1**, 223–265 (1959).
20. Ebert, L. B. *Characterization of Graphite Intercalated by Electron Acceptors* (Ph.D. Thesis, Stanford University: 1975).
21. Watanabe, N. *Graphite Fluorides* (Elsevier, Amsterdam: 1988).

22. Nakajima, T. *Fluorine-Carbon and Fluoride-Carbon Materials: Chemistry, Physics, and Applications* (CRC Press, Boca Raton: 1995).
23. Enoki, T. *Graphite Intercalation Compounds and Applications* (Oxford University Press, Oxford: 2003).
24. Robinson, J. T. *et al.* Properties of fluorinated graphene films. *Nano Lett.* **10**, 3001–3005 (2010).
25. Nair, R. R. *et al.* Fluorographene: A two-dimensional counterpart of Teflon. *Small* **6**, 2877–2884 (2010).
26. Jeon, K.-J. *et al.* Fluorographene: A wide bandgap semiconductor with ultraviolet luminescence. *ACS Nano* **5**, 1042–1046 (2011).
27. Withers, F., Dubois, M. & Savchenko, A. K. Electron properties of fluorinated single-layer graphene transistors. *Phys. Rev. B* **82**, 073403 (2010).
28. Withers, F., Russo, S., Dubois, M. & Craciun, M. F. Tuning the electronic transport properties of graphene through functionalisation with fluorine. *Nanoscale Res. Lett.* **6**, 526 (2011).
29. Withers, F., Bointon, T. H., Dubois, M., Russo, S. & Craciun, M. F. Nanopatterning of fluorinated graphene by electron beam irradiation. *Nano Lett.* **11**, 3912–3916 (2011).
30. Binnig, G. Tunneling through a controllable vacuum gap. *Appl. Phys. Lett.* **40**, 178 (1982).
31. Stoll, E. Resolution of the scanning tunnel microscope. *Surf. Sci.* **143**, L411–L416 (1984).
32. Mayer, T. M., Adams, D. P. & Marder, B. M. Field emission characteristics of the scanning tunneling microscope for nanolithography. *J. Vac. Sci. Technol. B* **14**, 2438–2444 (1996).
33. Binnig, G., Rohrer, H., Gerber, C. & Weibel, E. Surface studies by scanning tunneling microscopy. *Phys. Rev. Lett.* **49**, (1982).
34. Crewe, A. V., Eggenberger, D. N., Wall, J. & Welter, L. M. Electron gun using a field emission source. *Rev. Sci. Instrum.* **39**, 576 (1968).
35. Auciello, O. *et al.* Ion bombardment sharpening of field emitter arrays. *Vacuum Microelectronics Conference, 1995. IVMC., 1995 International* 192–196 (1995).
36. Tsong, T. T. *Atom-probe field ion microscopy : field ion emission and surfaces and interfaces at atomic resolution*. (Cambridge University Press: Cambridge; New York, 1990).
37. Melmed, A. J. The art and science and other aspects of making sharp tips. *J. Vac. Sci. Technol. B* **9**, 601–608 (1991).
38. Morishita, S. & Okuyama, F. Sharpening of monocrystalline molybdenum tips by means of inert-gas ion sputtering. *J. Vac. Sci. Technol. A* **9**, 167–169 (1991).
39. Nam, A. J., Teren, A., Lusby, T. A. & Melmed, A. J. Benign making of sharp tips for STM and FIM: Pt, Ir, Au, Pd, and Rh. *J. Vac. Sci. Technol. B* **13**, 1556 (1995).
40. Watanabe, M. O. & Kinno, T. Rhenium tips for stable scanning tunneling microscopy. *Jpn. J. Appl. Phys.* **32**, 1266–1268 (1993).
41. Iwami, M., Uehara, Y. & Ushioda, S. Preparation of silver tips for scanning tunneling microscopy imaging. *Rev. Sci. Instrum.* **69**, 4010 (1998).
42. Bryant, P. J., Kim, H. S., Zheng, Y. C. & Yang, R. Technique for shaping scanning tunneling microscope tips. *Rev. Sci. Instrum.* **58**, 1115 (1987).

43. Ibe, J. P. *et al.* On the electrochemical etching of tips for scanning tunneling microscopy. *J. Vac. Sci. Technol. A* **8**, 3570 (1990).
44. Morgan, R. An automatic electropolishing supervisor for preparing field ion microscope specimens. *J. Sci. Instrum.* **44**, 808–809 (1967).
45. Gunterschulze, A. & Tollmien, W.V. Neue Untersuchungen über die Kathodenzerstaubung der Glimmentladung. *Z. Phys.* **119**, 685–695 (1942).
46. Sigmund, P. Theory of sputtering. I. Sputtering yield of amorphous and polycrystalline targets. *Phys. Rev.* **184**, 383–416 (1969).
47. Barber, D. J., Frank, F. C., Moss, M., Steeds, J. W. & Tsong, I. S. T. Prediction of ion-bombarded surface topographies using Frank's kinematic theory of crystal dissolution. *J. Mater. Sci.* **8**, 1030–1040 (1973).
48. Carter, G., Colligon, J. S. & Nobes, M. J. The growth of topography during sputtering of amorphous solids. *J. Mater. Sci.* **8**, 1481 (1973).
49. Carter, G. Influence of Surface-Diffusion on Topography Development of an Amorphous Solid during Sputtering. *J. Mater. Sci.* **11**, 1091–1098 (1976).
50. Carter, G., Colligon, J. S. & Nobes, M. J. Analytical Modeling of Sputter Induced Surface Morphology. *Radiat. Eff. Defect. S.* **31**, 65–87 (1977).
51. Sigmund, P. A mechanism of surface micro-roughening by ion bombardment. *J. Mater. Sci.* **8**, 1545–1553 (1973).
52. Carter, G., Nobes, M. J. & Webb, R. P. A 2nd-order erosion slowness theory of the development of surface-topography by ion-induced sputtering. *J. Mater. Sci.* **16**, 2091–2102 (1981).
53. Bradley, R. M., Harper, J. M. E. & Smith, D. A. Theory of thin-film orientation by ion bombardment during deposition. *J. Appl. Phys.* **60**, 4160–4164 (1986).
54. Kubby, J. A. & Siegel, B. M. SEM and TEM observations of 1st and 2nd-order sputter-induced topography. *Nucl. Instrum. Meth. B* **13**, 319–323 (1986).
55. Kubby, J. A. *Ion Beam Micro-Sculpturing* (Ph.D. Thesis, Cornell University: 1986).
56. Hoffrogge, P., Kopf, H. & Reichelt, R. Nanostructuring of tips for scanning probe microscopy by ion sputtering: Control of the apex ratio and the tip radius. *J. Appl. Phys.* **90**, 5322–5327 (2001).
57. Wang, Q. *et al.* Diamond cone arrays with controlled morphologies formed by self-organized selective ions sputtering. *J. Appl. Phys.* **100**, 034312 (2006).
58. Schiller, C., Koomans, A. A., Vanrooy, T. L., Schonenberger, C. & Elswijk, H. B. Decapitation of tungsten field emitter tips during sputter sharpening. *Surf. Sci.* **339**, L925–L930 (1995).
59. Raad, G. J. de, Koenraad, P. M. & Wolter, J. H. Use of the Schiller decapitation process for the manufacture of high quality tungsten scanning tunneling microscopy tips. *J. Vac. Sci. Technol. B* **17**, 1946–1953 (1999).
60. Rezeq, M., Pitters, J. & Wolkow, R. Tungsten nanotip fabrication by spatially controlled field-assisted reaction with nitrogen. *J. Chem. Phys.* **124**, 204716–204716–6 (2006).
61. Rezeq, M., Pitters, J. & Wolkow, R. Nano-tip fabrication by spatially controlled etching. U.S. Patent 7,431,856 (2007).
62. Wehner, G. Influence of the angle of incidence on sputtering yields. *J. Appl. Phys.* **30**, 1762 (1959).

63. Fetz, H. Über die Kathodenzerstäubung bei schiefem Aufparall der Ionen. *Z. Phys. A-Hadron Nucl.* **119**, 590–601 (1942).
64. Frank, F. C. On the kinematic theory of crystal growth and dissolution processes. *Growth and perfection of crystals* 411–419 (1958).
65. Frank, F. C. On the kinematic theory of crystal growth and dissolution processes, II. *Z. Phys. Chem. Neue Fol.* **77**, 84–92 (1972).
66. Anderson, H. H. & Bay, H. L. Sputtering by particle bombardment I. 145 (1981).
67. Wilson, I. H. & Kidd, M. W. A study of cones developed by ion-bombardment of gold. *J. Mater. Sci.* **6**, 1366 (1971).
68. Schmucker, S. W. *Sharpening of Conductive Nanoprobes for Scanning Tunneling Microscopy by Field-Directed Sputter Sharpening* (M.S. Thesis, University of Illinois at Urbana-Champaign: 2009).
69. Cavaille, J. Y. & Drechsler, M. Surface self-diffusion by ion impact. *Surf. Sci.* **75**, 342–354 (1978).
70. Gill, V., Guduru, P. R. & Sheldon, B. W. Electric field induced surface diffusion and micro/nano-scale island growth. *Int. J. Solids Struct.* **45**, 943–958 (2008).
71. Lyding, J. W., Skala, S., Hubacek, J. S., Brockenbrough, R. & Gammie, G. Variable-temperature scanning tunneling microscope. *Rev. Sci. Instrum.* **59**, 1897 (1988).
72. Brockenbrough, R. T. & Lyding, J. W. Inertial tip translator for a scanning tunneling microscope. *Rev. Sci. Instrum.* **64**, 2225 (1993).
73. Janninck, J. R. *Digital Signal Processor Based Control of a Scanning Tunneling Microscope* (M.S. Thesis, University of Illinois at Urbana-Champaign: 1994).
74. Sztelle, M. M. *Stage Design and Improved Vibration Isolation of a Scanning Tunneling Microscope* (M.S. Thesis, University of Illinois at Urbana-Champaign: 2002).
75. Ringger, M., Hidber, H. R., Schlögl, R., Oelhafen, P. & Güntherodt, H. -J Nanometer lithography with the scanning tunneling microscope. *Appl. Phys. Lett.* **46**, 832–834 (1985).
76. McCord, M. A. Lithography with the scanning tunneling microscope. *J. Vac. Sci. Technol. B* **4**, 86 (1986).
77. Becker, R. S., Golovchenko, J. A. & Swartzentruber, B. S. Atomic-scale surface modifications using a tunnelling microscope. *Nature* **325**, 419–421 (1987).
78. Foster, J. S., Frommer, J. E. & Arnett, P. C. Molecular manipulation using a tunneling microscope. *Nature* **331**, 324–326 (1988).
79. Silver, R. M., Ehrichs, E. E. & de Lozanne, A. L. Direct writing of submicron metallic features with a scanning tunneling microscope. *Appl. Phys. Lett.* **51**, 247–249 (1987).
80. Eigler, D. M. & Schweizer, E. K. Positioning single atoms with a scanning tunneling microscope. *Nature* **344**, 524–526 (1990).
81. Redhead, P. A. Interaction of slow electrons with chemisorbed oxygen. *Can. J. Phys.* **42**, 886–905 (1964).
82. Menzel, D. & Gomer, R. Desorption from metal surfaces by low-energy electrons. *J. Chem. Phys.* **41**, 3311–3328 (1964).
83. Menzel, D. & Gomer, R. Electron-impact desorption of carbon monoxide from tungsten. *J. Chem. Phys.* **41**, 3329–3351 (1964).

84. Dempster, A. J. A new method of positive ray analysis. *Phys. Rev.* **11**, 316–325 (1918).
85. Madey, T. E. Electron-stimulated desorption as a tool for studies of chemisorption: A Review. *J. Vac. Sci. Technol.* **8**, 525 (1971).
86. Ramsier, R. D. & Yates Jr., J. T. Electron-stimulated desorption: Principles and applications. *Surf. Sci. Rep.* **12**, 246–378 (1991).
87. McCord, M. A. High resolution, low-voltage probes from a field emission source close to the target plane. *J. Vac. Sci. Technol. B* **3**, 198 (1985).
88. McCord, M. A. Exposure of calcium fluoride resist with the scanning tunneling microscope. *J. Vac. Sci. Technol. B* **5**, 430 (1987).
89. Marrian, C. R. K. & Colton, R. J. Low-voltage electron beam lithography with a scanning tunneling microscope. *Appl. Phys. Lett.* **56**, 755–757 (1990).
90. Avouris, P. Atom-Resolved Surface Chemistry. *Nato. Adv. Sci. I B-Phy.* 513–547 (1991).
91. Dagata, J. A. *et al.* Modification of hydrogen-passivated silicon by a scanning tunneling microscope operating in air. *Appl. Phys. Lett.* **56**, 2001–2003 (1990).
92. Lyo, I. & Avouris, P. Atomic scale desorption processes induced by the scanning tunneling microscope. *J. Chem. Phys.* **93**, 4479–4480 (1990).
93. Becker, R. S., Higashi, G. S., Chabal, Y. J. & Becker, A. J. Atomic-scale conversion of clean Si(111): H-1 × 1 to Si(111)-2 × 1 by electron-stimulated desorption. *Phys. Rev. Lett.* **65**, 1917–1920 (1990).
94. Lyding, J. W., Shen, T. C., Hubacek, J. S., Tucker, J. R. & Abeln, G. C. Nanoscale patterning and oxidation of H-passivated Si(100)-2 × 1 surfaces with an ultrahigh-vacuum scanning tunneling microscope. *Appl. Phys. Lett.* **64**, 2010–2012 (1994).
95. Shen, T. C. *et al.* Atomic-scale desorption through electronic and vibrational-excitation mechanisms. *Science* **268**, 1590–1592 (1995).
96. Hersam, M. C., Guisinger, N. P. & Lyding, J. W. Silicon-based molecular nanotechnology. *Nanotechnol.* **11**, 70–76 (2000).
97. Schofield, S. R. *et al.* Atomically Precise placement of single dopants in Si. *Phys. Rev. Lett.* **91**, 136104 (2003).
98. Fuechsle, M. *et al.* A single-atom transistor. *Nat. Nanotechnol.* In press (2012). doi:10.1038/nnano.2012.21
99. Haider, M. B. *et al.* Controlled coupling and occupation of silicon atomic quantum dots at room temperature. *Phys. Rev. Lett.* **102**, 046805 (2009).
100. Völkel, B. Influence of secondary electrons in proximal probe lithography. *J. Vac. Sci. Technol. B* **15**, 2877 (1997).
101. Wiley, D. E., Manning, W. R. & Hunter Jr., O. Elastic properties of polycrystalline TiB_2, ZrB_2 and HfB_2 from room temperature to 1300 °K. *J. Less-Common Met.* **18**, 149–157 (1969).
102. Bsenko, L. & Lundström, T. The high-temperature hardness of ZrB_2 and HfB_2. *J. Less-Common Met.* **34**, 273–278 (1974).
103. Samsonov, G. V., Kovenskaya, B. A. & Serebryakova, T. I. Some physical characteristics of the diborides of transition metals of groups IV and V. *Sov. Phys. J.* **14**, 11–14 (1973).
104. Juretschke, H. J. & Steinitz, R. Hall effect and electrical conductivity of transition-metal diborides. *J. Phys. Chem. Solids* **4**, 118–127 (1958).

105. Post, B., Glaser, F. W. & Moskowitz, D. Transition metal diborides. *Acta Metall. Mater.* **2**, 20–25 (1954).
106. Chatterjee, A. *et al.* Tribological behavior of hafnium diboride thin films. *Surf. Coat. Tech.* **201**, 4317–4322 (2006).
107. Wuu, D. S., Lee, M. L., Lin, T. Y. & Horng, R. H. Characterization of hafnium diboride thin film resistors by r.f. magnetron sputtering. *Mater. Chem. Phys.* **45**, 163–166 (1996).
108. Jayaraman, S., Yang, Y., Kim, D. Y., Girolami, G. S. & Abelson, J. R. Hafnium diboride thin films by chemical vapor deposition from a single source precursor. *J. Vac. Sci. Technol. A* **23**, 1619 (2005).
109. Jayaraman, S. *Chemical Vapor Deposition of Transition Metal Diborides from Borohydride Precursors* (Ph.D. Thesis, University of Illinois at Urbana-Champaign: 2005).
110. Chatterjee, A. *Tribological Behavior of CVD-Grown Hafnium Diboride Thin Films from Macro to Nano-Length Scales* (Ph.D. Thesis, University of Illinois at Urbana-Champaign: 2008).
111. Kumar, N. *Control of Reaction Surface in Low Temperature CVD to Enhance Nucleation and Conformal Coverage* (Ph.D. Thesis, University of Illinois at Urbana-Champaign: 2009).
112. Thompson, R. The chemistry of metal borides and related compounds. *Prog. Boron Chem.* **2**, 173 (1970).
113. Gebhardt, J. J. & Cree, R. F. Vapor-deposited borides of group IVA metals. *J. Am. Chem. Soc.* **48**, 262–267 (1965).
114. Peshev, P. & Bliznakov, G. On the borothermic preparation of titanium, zirconium and hafnium diborides. *J. Less-Common Met.* **14**, 23–32 (1968).
115. Hoekstra, H. R. & Katz, J. J. The preparation and properties of the group IV-B metal borohydrides. *J. Am. Chem. Soc.* **71**, 2488–2492 (1949).
116. Jensen, J. A., Gozum, J. E., Pollina, D. M. & Girolami, G. S. Titanium, zirconium, and hafnium tetrahydroborates as 'tailored' CVD precursors for metal diboride thin films. *J. Am. Chem. Soc.* **110**, 1643–1644 (1988).
117. Wayda, A. L., Schneemeyer, L. F. & Opila, R. L. Low-temperature deposition of zirconium and hafnium boride films by thermal decomposition of the metal borohydrides ($M[BH_4]_4$). *Appl. Phys. Lett.* **53**, 361–363 (1988).
118. Yang, Y., Jayaraman, S., Kim, D. Y., Girolami, G. S. & Abelson, J. R. Crystalline texture in hafnium diboride thin films grown by chemical vapor deposition. *J. Cryst. Growth* **294**, 389–395 (2006).
119. Jayaraman, S. *et al.* HfB_2 and Hf-B-N hard coatings by chemical vapor deposition. *Surf. Coat. Technol.* **200**, 6629–6633 (2006).
120. van Dorp, W. F. & Hagen, C. W. A critical literature review of focused electron beam induced deposition. *J. Appl. Phys.* **104**, 081301–081301–42 (2008).
121. Ye, W. *et al.* Direct writing of sub-5 nm hafnium diboride metallic nanostructures. *ACS Nano* **4**, 6818–6824 (2010).
122. Wallace, P. R. The band theory of graphite. *Phys. Rev.* **71**, 622–634 (1947).
123. McClure, J. W. Diamagnetism of graphite. *Phys. Rev.* **104**, 666–671 (1956).
124. Slonczewski, J. C. & Weiss, P. R. Band structure of graphite. *Phys. Rev.* **109**, 272–279 (1958).

125. Ajayan, P. M. Nanotubes from carbon. *Chem. Rev.* **99**, 1787–1800 (1999).
126. Dresselhaus, M. S., Dresselhaus, G. & Eklund, P. C. *Science of Fullerenes and Carbon Nanotubes*. (Academic Press: 1996).
127. Saito, R., Dresselhaus, M.S., & Dresselhaus, G. *Physical Properties of Carbon Nanotubes*. (Imperial College Press, London: 1998).
128. Mermin, N. D. Crystalline Order in Two Dimensions. *Phys. Rev.* **176**, 250–254 (1968).
129. Fradkin, E. Critical behavior of disordered degenerate semiconductors. II. Spectrum and transport properties in mean-field theory. *Phys. Rev. B* **33**, 3263–3268 (1986).
130. Boehm, H. P., Clauss, A., Fischer, G. O., & Hofmann, U. Dünnste Kohlenstoff-Folien. *Z. Naturforsch.* **17b**, 150-153 (1962).
131. Boehm, H. P., Clauss, A., Fischer, G. O. & Hofmann, U. Das Adsorptionsverhalten sehr dünner Kohlenstoff-Folien. *Z. Anorg. Allg. Chem.* **316**, 119–127 (1962).
132. McAllister, M. J. *et al.* Single sheet functionalized graphene by oxidation and thermal expansion of graphite. *Chem. Mater.* **19**, 4396–4404 (2007).
133. Dikin, D. A. *et al.* Preparation and characterization of graphene oxide paper. *Nature* **448**, 457–460 (2007).
134. Eda, G., Fanchini, G. & Chhowalla, M. Large-area ultrathin films of reduced graphene oxide as a transparent and flexible electronic material. *Nat. Nanotechnol.* **3**, 270–274 (2008).
135. Mkhoyan, K. A. *et al.* Atomic and electronic structure of graphene-oxide. *Nano Lett.* **9**, 1058–1063 (2009).
136. Dreyer, D. R., Park, S., Bielawski, C. W. & Ruoff, R. S. The chemistry of graphene oxide. *Chem. Soc. Rev.* **39**, 228–240 (2009).
137. Gómez-Navarro, C. *et al.* Atomic structure of reduced graphene oxide. *Nano Lett.* **10**, 1144–1148 (2010).
138. May, J. Platinum surface LEED rings. *Surf. Sci.* **17**, 269–270 (1969).
139. Morgan, A. E. & Somorjai, G. A. Low energy electron diffraction studies of gas adsorption on the platinum (100) single crystal surface. *Surf. Sci.* **12**, 405–425 (1968).
140. Karu, A. E. & Beer, M. Pyrolytic formation of highly crystalline graphite films. *J. Appl. Phys.* **37**, 2179–2181 (1966).
141. Weinberg, W. H., Deans, H. A. & Merrill, R. P. The structure and chemistry of ethylene adsorbed on platinum (111): CFSO-BEBO calculations and experimental studies. *Surf. Sci.* **41**, 312–336 (1974).
142. B., L. A LEED study of the deposition of carbon on platinum crystal surfaces. *Surf. Sci.* **53**, 317–329 (1975).
143. Hamilton, J. C. & Blakely, J. M. Carbon segregation to single crystal surfaces of Pt, Pd and Co. *Surf. Sci.* **91**, 199–217 (1980).
144. Abon, M., Billy, J., Bertolini, J. C. & Tardy, B. Carbon on Pt(111): Characterization and influence on the chemisorptive properties. *Surf. Sci.* **167**, 1–17 (1986).
145. Land, T. A., Michely, T., Behm, R. J., Hemminger, J. C. & Comsa, G. STM investigation of single layer graphite structures produced on Pt(111) by hydrocarbon decomposition. *Surf. Sci.* **264**, 261–270 (1992).
146. Blakely, J. M., Kim, J. S. & Potter, H. C. Segregation of carbon to the (100) Surface of nickel. *J. Appl. Phys.* **41**, 2693–2697 (1970).

147. Shelton, J. C., Patil, H. R. & Blakely, J. M. Equilibrium segregation of carbon to a nickel (111) surface: A surface phase transition. *Surf. Sci.* **43**, 493–520 (1974).
148. Eizenberg, M. & Blakely, J. M. Carbon monolayer phase condensation on Ni(111). *Surf. Sci.* **82**, 228–236 (1979).
149. Eizenberg, M. & Blakely, J. M. Carbon interaction with nickel surfaces: Monolayer formation and structural stability. *J. Chem. Phys.* **71**, 3467–3477 (1979).
150. Gall, Mikhallov, Rut'kov & Tontegode, A. Y. Nature of the adsorption binding between a graphite monolayer and rhenium surface. *Sov. Phys. Solid State* **27**, 1410–1414 (1985).
151. Coraux, J., Busse, C. & Michely, T. Structural coherency of graphene on Ir (111). *Nano Lett.* **8**, 565–570 (2008).
152. T N'Diaye, A. *et al.* Growth of graphene on Ir(111). *New J. Phys.* **11**, 023006 (2009).
153. Kralj, M. *et al.* Graphene on Ir(111) characterized by angle-resolved photoemission. *Phys. Rev. B* **84**, 075427 (2011).
154. Sutter, P. W., Flege, J.-I. & Sutter, E. A. Epitaxial graphene on ruthenium. *Nat. Mater.* **7**, 406–411 (2008).
155. Sutter, E., Acharya, D. P., Sadowski, J. T. & Sutter, P. Scanning tunneling microscopy on epitaxial bilayer graphene on ruthenium (0001). *Appl. Phys. Lett.* **94**, 133101–133101–3 (2009).
156. Sutter, E., Albrecht, P. & Sutter, P. Graphene growth on polycrystalline Ru thin films. *Appl. Phys. Lett.* **95**, 133109–133109–3 (2009).
157. Sutter, P. W., Albrecht, P. M. & Sutter, E. A. Graphene growth on epitaxial Ru thin films on sapphire. *Appl. Phys. Lett.* **97**, 213101–213101–3 (2010).
158. Li, X. *et al.* Large-Area Synthesis of high-quality and uniform graphene films on copper foils. *Science* **324**, 1312–1314 (2009).
159. Li, X., Cai, W., Colombo, L. & Ruoff, R. S. Evolution of graphene growth on Ni and Cu by carbon isotope labeling. *Nano Lett.* **9**, 4268–4272 (2009).
160. Bae, S. *et al.* Roll-to-roll production of 30-inch graphene films for transparent electrodes. *Nat. Nanotechnol.* **5**, 574–578 (2010).
161. Rasool, H. I. *et al.* Continuity of graphene on polycrystalline copper. *Nano Lett.* **11**, 251–256 (2010).
162. Reina, A. *et al.* Large area, few-layer graphene films on arbitrary substrates by chemical vapor deposition. *Nano Lett.* **9**, 30–35 (2008).
163. Li, X., Cai, W., Colombo, L. & Ruoff, R. S. Evolution of graphene growth on Cu and Ni studied by carbon isotope labeling. *Nano Lett.* **9**, 4268–4272 (2009).
164. Yu, Q. *et al.* Graphene segregated on Ni surfaces and transferred to insulators. *Appl. Phys. Lett.* **93**, 113103–113103–3 (2008).
165. Iijima, S. Helical microtubules of graphitic carbon. *Nature* **354**, 56–58 (1991).
166. Iijima, S. High resolution electron microscopy of phase objects: Observation of small holes and steps on graphite crystals. *Optik* **47**, 437–452 (1977).
167. Iijima, S. Thin graphite support films for high resolution electron microscopy. *Micron* **8**, 41–46 (1977).
168. Iijima, S. High resolution electron microscopy of some carbonaceous materials. *Journal of Microscopy* **119**, 99–111 (1980).
169. Acheson, E. G. Manufacture of graphite. US Patent 568,323 (1896).

170. Badami, D. V. X-Ray studies of graphite formed by decomposing silicon carbide. *Carbon* **3**, 53–57 (1965).
171. Van Bommel, A. J., Crombeen, J. E. & Van Tooren, A. LEED and Auger electron observations of the SiC(0001) surface. *Surf. Sci.* **48**, 463–472 (1975).
172. Meyer, F. & Loyen, G. J. Ellipsometry applied to surface problems. *Acta Electron.* **18**, 33–38 (1975).
173. Chang, C. S., Tsong, I. S. T., Wang, Y. C. & Davis, R. F. Scanning tunneling microscopy and spectroscopy of cubic β-SiC(111) surfaces. *Surf. Sci.* **256**, 354–360 (1991).
174. Tsai, M.-H., Chang, C. S., Dow, J. D. & Tsong, I. S. T. Electronic contributions to scanning-tunneling-microscopy images of an annealed β-SiC(111) surface. *Phys. Rev. B* **45**, 1327–1332 (1992).
175. Li, L. & Tsong, I. S. T. Atomic structures of 6H-SiC (0001) and (0001) surfaces. *Surf. Sci.* **351**, 141–148 (1996).
176. Johansson, L. I., Owman, F. & Mårtensson, P. High-resolution core-level study of 6H-SiC(0001). *Phys. Rev. B* **53**, 13793–13802 (1996).
177. Berger, C. *et al.* Ultrathin epitaxial graphite: 2D electron gas properties and a route toward graphene-based nanoelectronics. *J. Phys. Chem. B* **108**, 19912–19916 (2004).
178. Ohta, T., Bostwick, A., Seyller, T., Horn, K. & Rotenberg, E. Controlling the electronic structure of bilayer graphene. *Science* **313**, 951–954 (2006).
179. Rollings, E. *et al.* Synthesis and characterization of atomically thin graphite films on a silicon carbide substrate. *J. Phys. Chem. Solid.* **67**, 2172–2177 (2006).
180. de Heer, W. A. *et al.* Epitaxial graphene. *Solid State Commun.* **143**, 92–100 (2007).
181. Lin, Y.-M. *et al.* 100-GHz transistors from wafer-scale epitaxial graphene. *Science* **327**, 662–662 (2010).
182. Geim, A. K. & Kim, P. Carbon wonderland. *Sci. Am.* **298**, 90–97 (2008).
183. Lu, X., Yu, M., Huang, H. & Ruoff, R. S. Tailoring graphite with the goal of achieving single sheets. *Nanotechnol.* **10**, 269–272 (1999).
184. Novoselov, K. S. *et al.* Two-dimensional gas of massless Dirac fermions in graphene. *Nature* **438**, 197–200 (2005).
185. Zhang, Y., Tan, Y.-W., Stormer, H. L. & Kim, P. Experimental observation of the quantum Hall effect and Berry’s phase in graphene. *Nature* **438**, 201–204 (2005).
186. Geim, A. K. Graphene: Status and prospects. *Science* **324**, 1530–1534 (2009).
187. Dreyer, D. R., Ruoff, R. S. & Bielawski, C. W. From conception to realization: An historial account of graphene and some perspectives for its future. *Angew. Chem. Int. Edit.* **49**, 9336–9344 (2010).
188. Wong, H.-S. P. & Akinwande, D. *Carbon Nanotube and Graphene Device Physics*. (Cambridge University Press: 2011).
189. Jorio, A., Dresselhaus, M. S., Saito, R. & Dresselhaus, G. *Raman Spectroscopy in Graphene Related Systems*. (Wiley-VCH: 2011).
190. Robertson, S. D. Graphite formation from low temperature pyrolysis of methane over some transition metal surfaces. *Nature* **221**, 1044–1046 (1969).
191. Obraztsov, A. N., Obraztsova, E. A., Tyurnina, A. V. & Zolotukhin, A. A. Chemical vapor deposition of thin graphite films of nanometer thickness. *Carbon* **45**, 2017–2021 (2007).

192. Peng, Z., Yan, Z., Sun, Z. & Tour, J. M. Direct growth of bilayer graphene on SiO_2 substrates by carbon diffusion through nickel. *ACS Nano* **5**, 8241–8247 (2011).
193. Mohapatra, C. *Growth and Characterization of Epitaxial Graphene Films by Molecular Beam Epitaxy* (Ph.D. Thesis, University of Illinois at Urbana-Champaign: 2012).
194. Lee, S. -Tong *et al.* Heteroepitaxy of carbon on copper by high-temperature ion implantation. *Appl. Phys. Lett.* **59**, 785–787 (1991).
195. Ong, T. p., Xiong, F., Chang, R. p. h. & White, C. w. Nucleation and growth of diamond on carbon-implanted single crystal copper surfaces. *J. Mater. Res.* **7**, 2429–2439 (1992).
196. López, G. A. & Mittemeijer, E. J. The solubility of C in solid Cu. *Scripta Mater.* **51**, 1–5 (2004).
197. Li, X. *et al.* Graphene films with large domain size by a two-step chemical vapor deposition process. *Nano Lett.* **10**, 4328–4334 (2010).
198. Lagow, R. J. *The Reactions of Elemental Fluorine; A New Approach to Fluorine Chemistry* (Ph.D. Thesis, Rice University: 1970).
199. Ebert, L. B. Intercalation compounds of graphite. *Annu. Rev. Mater. Sci.* **6**, 181–211 (1976).
200. Fusaro, R.L., & Sliney, H.E. Preliminary investigations of graphite fluoride $(CF_x)_n$ as a solid lubricant. *NASA Tech. Note D-5097* (1969).
201. Fusaro, R. L. & Sliney, H. E. Graphite fluoride $(CF_x)_n$—A new solid lubricant. *ASLE Trans.* **13**, 56–65 (1970).
202. Fusaro, R. L. Graphite fluoride lubrication: The effect of fluorine content, atmosphere, and burnishing technique. *ASLE Trans.* **20**, 15–24 (1977).
203. Gisser, H., Petronio, M. & Shapiro, A. Graphite fluoride as solid lubricant, investigating friction coefficient and wear resistance. *Int. Conf. Sol. Lubric., 1st, Denver, Colorado* 217–221 (1971).
204. Fukuda, M. & Iijima, T. Lithium-poly-carbonmonofluoride cylindrical type batteries. *Int. Power Sources Symp., Brighton, Sussex, England* (1974).
205. Nakajima, T. Carbon–fluorine compounds as battery materials. *J. Fluorine Chem.* **100**, 57–61 (1999).
206. Rudorff, W. Graphite intercalation compounds. *Adv. Inorg. Chem.Radiochem.* **1**, 223–265 (1959).
207. Selig, H. & Ebert, L. B. Graphite intercalation compounds. *Adv. Inorg. Chem* **23**, 281–327 (1980).
208. Touhara, H. & Okino, F. Property control of carbon materials by fluorination. *Carbon* **38**, 241–267 (2000).
209. Rüdorff, W. & Rüdorff, G. Zur Konstitution des Kohlenstoff-Monofluorids. *Z. Anorg. Chem.* **253**, 281–296 (1947).
210. Ruff, O. & Bretschneider, O. Die Reaktionsprodukte der verschiedenen Kohlenstoffformen mit Fluor II (Kohlenstoff-monofluorid). *Z. Anorg. Allg. Chem.* **217**, 1–18 (1934).
211. Ruff, O. Reaktionen des festen Kohlenstoffs mit Gasen und Flüssigkeiten. *Z. Elktrochem. Angew. P.* **44**, 333–341 (1938).
212. Palin, D. E. & Wadsworth, K. D. Structure of carbon monofluoride. *Nature* **162**, 925–926 (1948).

213. Gavroglu, K. *Fritz London: A Scientific Biography*. (Cambridge University Press: 1995).
214. Bigelow, L. A. The action of elementary fluorine upon organic compounds. *Chem. Rev.* **40**, 51–115 (1947).
215. Lagow, R. J., Badachhape, R. B., Wood, J. L. & Margrave, J. L. Some new synthetic approaches to graphite–fluorine chemistry. *J. Chem. Soc., Dalton Trans.* 1268–1273 (1974).
216. Worsley, K. A. *et al.* Soluble graphene derived from graphite fluoride. *Chem. Phys. Lett.* **445**, 51–56 (2007).
217. Nakajima, T., Watanabe, N., Kameda, I. & Endo, M. Preparation and electrical conductivity of fluorine-graphite fiber intercalation compound. *Carbon* **24**, 343–351 (1986).
218. Palchan, I., Crespin, M., Estrade-Szwarckopf, H. & Rousseau, B. Graphite fluorides: An XPS study of a new type of C-F bonding. *Chem. Phys. Lett.* **157**, 321–327 (1989).
219. Nakajima, T., Molinier, M. & Motoyama, M. Structure of fluorine-graphite intercalation compounds. *Carbon* **29**, 429–437 (1991).
220. di Vittorio, S. l., Dresselhaus, M. s. & Dresselhaus, G. A model for disorder in fluorine-intercalated graphite. *J. Mater. Res.* **8**, 1578–1585 (1993).
221. Hagiwara, R., Lerner, M. & Bartlett, N. The preparation of planar-sheet graphite fluorides CxF with x < 2. *J. Chem. Soc. Chem. Comm.* 573–574 (1989).
222. Nakajima, T. & Namba, M. Synthesis of highly fluorinated graphite in anhydrous liquid hydrogen fluoride. *Proceedings of the Ninth International Symposium on Molten Salts, San Francisco, CA* 379–384 (1994).
223. Nakajima, T., Molinier, M. & Motoyama, M. Structure of fluorine-graphite intercalation compounds. *Carbon* **29**, 429–437 (1991).
224. Hagiwara, R., Lerner, M. & Bartlett, N. The preparation of planar-sheet graphite fluorides CxF with x < 2. *J. Chem. Soc. Chem. Commun.* 573–574 (1989).
225. Margrave, J. L. Superstroichiometric carbon monofluoride and methods for preparing stable carbon monofluorides of various stoichiometries. US Patent 3,674,432 (1972).
226. Lagow, R. J., Badachhape, R. B., Ficalora, P., Wood, J. L. & Margrave, J. L. A new method of preparation of tetracarbon monofluoride. *Syn. React. Inorg. Met.* **2**, 145–149 (1972).
227. Ikemiya, N., Hara, S., Ogino, K. & Nakajima, T. Surface structure of fluorine-graphite intercalation compounds observed by atomic force microscopy. *Surf. Sci.* **274**, L524–L528 (1992).
228. Daulan, C. *et al.* STM studies of fluorine-intercalated graphite. *J. Solid State Chem.* **107**, 27–33 (1993).
229. Holzwarth, N. A. W., Louie, S. G. & Rabii, S. Electronic structure of graphite intercalation compounds. *MRS Online Proceedings Library* **20** (1982).
230. Ebert, L. B. Intercalation compounds of graphite. *Annu. Rev. Mater. Sci.* **6**, 181–211 (1976).
231. Dresselhaus, M. S. & Dresselhaus, G. Intercalation compounds of graphite. *Adv. Phys.* **51**, 1–186 (2002).

232. Chen, W., Chen, S., Qi, D. C., Gao, X. Y. & Wee, A. T. S. Surface transfer p-type doping of epitaxial graphene. *J. Am. Chem. Soc.* **129**, 10418–10422 (2007).
233. Green, A. A. & Hersam, M. C. Solution phase production of graphene with controlled thickness via density differentiation. *Nano Lett.* **9**, 4031–4036 (2009).
234. Hossain, M. Z. *et al.* Chemically homogeneous and thermally reversible oxidation of epitaxial graphene. *Nat. Chem.* In Press. (2012). doi:10.1038/nchem.1269
235. Neumann, D. *et al.* Interaction of atomic hydrogen with the graphite single-crystal surface. *Appl. Phys. A-Mater.* **55**, 489–492 (1992).
236. Jeloaica, L. & Sidis, V. DFT investigation of the adsorption of atomic hydrogen on a cluster-model graphite surface. *Chem. Phys. Lett.* **300**, 157–162 (1999).
237. Sha, X. & Jackson, B. First-principles study of the structural and energetic properties of H atoms on a graphite (0 0 0 1) surface. *Surf. Sci.* **496**, 318–330 (2002).
238. Schlapbach, L. & Züttel, A. Hydrogen-storage materials for mobile applications. *Nature* **414**, 353–358 (2001).
239. Enoki, T., Sano, M. & Inokuchi, H. Hydrogen in aromatics. III. Chemisorption of hydrogen in graphite–alkali metal intercalation compounds. *J. Chem. Phys.* **78**, 2017–2029 (1983).
240. Enoki, T., Miyajima, S., Sano, M. & Inokuchi, H. Hydrogen-alkali-metal-graphite ternary intercalation compounds. *J. Mater. Res.* **5**, 435–466 (1990).
241. Ng, M. L. *et al.* Controlling hydrogenation of graphene on transition metals. *J. Phys. Chem. C* **114**, 18559–18565 (2010).
242. Zhou, J. *et al.* Ferromagnetism in semihydrogenated graphene sheet. *Nano Lett.* **9**, 3867–3870 (2009).
243. Xiang, H. J., Kan, E. J., Wei, S.-H., Gong, X. G. & Whangbo, M.-H. Thermodynamically stable single-side hydrogenated graphene. *Phys. Rev. B* **82**, 165425 (2010).
244. Balog, R. *et al.* Atomic hydrogen adsorbate structures on graphene. *J. Am. Chem. Soc.***131**, 8744–8745 (2009).
245. Guisinger, N. P., Rutter, G. M., Crain, J. N., First, P. N. & Stroscio, J. A. Exposure of epitaxial graphene on SiC(0001) to atomic hydrogen. *Nano Lett.* **9**, 1462–1466 (2009).
246. Hong, X., Cheng, S.-H., Herding, C. & Zhu, J. Colossal negative magnetoresistance in dilute fluorinated graphene. *Phys. Rev. B* **83**, 085410 (2011).
247. Robinson, J. T. *et al.* Properties of fluorinated graphene films. *Nano Lett.* **10**, 3001–3005 (2010).
248. Zboril, R. Graphene fluoride: A stable stoichiometric graphene derivative and its chemical conversion to graphene. *Small* **6**, 2885–2891 (2010).
249. Shen, N. & Sofo, J. O. Dispersion of edge states and quantum confinement of electrons in graphene channels drawn on graphene fluoride. *Phys. Rev. B* **83**, 245424 (2011).
250. Robinson, J. T., Perkins, F. K., Snow, E. S., Wei, Z. & Sheehan, P. E. Reduced Graphene Oxide Molecular Sensors. *Nano Lett.* **8**, 3137–3140 (2008).
251. Lee, W.-K. *et al.* Chemically isolated graphene nanoribbons reversibly formed in fluorographene using polymer nanowire masks. *Nano Lett.* **11**, 5461–5464 (2011).

252. Juza, R., Jönck, P. & Schmeckenbecher, A. Bildung und Eigenschaften des Chlorgraphits. *Z. Anorg. Allg. Chem.* **292**, 34–45 (1957).
253. Hooley, J. G. A search for intercalation in the graphite-chlorine system. *Carbon* **8**, 333–339 (1970).
254. Hooley, J. G. Isotherms of metal chloride vapors on graphite. *Carbon* **11**, 225–236 (1973).
255. Furdin, G., Bach, B., Herold, A. & Champetier, G. Contribution a l'etude du systeme ternaire graphite-brome-chlore. *C.R. Acad. Sc. Paris* **271**, 683 (1970).
256. Bach & Herald *Bull. Soc. Chim. Fr.* **5**, 1978 (1968).
257. Li, B. *et al.* Photochemical chlorination of graphene. *ACS Nano* **5**, 5957–5961 (2011).
258. Wu, J. *et al.* Controlled chlorine plasma reaction for noninvasive graphene doping. *J. Am. Chem. Soc.* **133**, 19668–19671 (2011).
259. Ijäs, M., Havu, P. & Harju, A. Fracturing graphene by chlorination: A theoretical viewpoint. *Phys. Rev. B* **85**, 035440 (2012).
260. Balog, R. *et al.* Bandgap opening in graphene induced by patterned hydrogen adsorption. *Nat. Mater.* **9**, 315–319 (2010).
261. Havu, P., Ijäs, M. & Harju, A. Hydrogenated graphene on silicon dioxide surfaces. *Phys. Rev. B* **84**, 205423 (2011).
262. Rüdorff, W. Über die Lösung von Brom im Kristallgitter des Graphits, Bromgraphit. *Z. Anorg. Allg. Chem.* **245**, 383–390 (1941).
263. Eeles, W. T. & Turnbull, J. A. The crystal structure of graphite-bromine compounds. *P. Roy. Soc. A-Math Phy.* **283**, 179–193 (1965).
264. Sasa, T., Takahashi, Y. & Mukaibo, T. Crystal structure of graphite bromine lamellar compounds. *Carbon* **9**, 407–416 (1971).
265. Ghosh, D. & Chung, D. D. L. Two-dimensional structure of bromine intercalated graphite. *Mater. Res. Bull.* **18**, 1179–1187 (1983).
266. Erbil, A., Kortan, A. R., Birgeneau, R. J. & Dresselhaus, M. S. Intercalate structure, melting, and the commensurate-incommensurate transition in bromine-intercalated graphite. *Phys. Rev. B* **28**, 6329–6346 (1983).
267. Jung, N. *et al.* Charge transfer chemical doping of few layer graphenes: Charge distribution and band gap formation. *Nano Lett.* **9**, 4133–4137 (2009).
268. Wehling, T. O. *et al.* Molecular doping of graphene. *Nano Lett.* **8**, 173–177 (2007).
269. Wang, X., Tabakman, S. M. & Dai, H. Atomic layer deposition of metal oxides on pristine and functionalized graphene. *J. Am. Chem. Soc.* **130**, 8152–8153 (2008).
270. Wang, Q. H. & Hersam, M. C. Nanofabrication of heteromolecular organic nanostructures on epitaxial graphene via room temperature feedback-controlled lithography. *Nano Lett.* **11**, 589–593 (2010).
271. Yavari, F. *et al.* Tunable bandgap in graphene by the controlled adsorption of water molecules. *Small* **6**, 2535–2538 (2010).
272. Wang, Q. H. & Hersam, M. C. Room-temperature molecular-resolution characterization of self-assembled organic monolayers on epitaxial graphene. *Nat. Chem.* **1**, 206–211 (2009).
273. Kubby, J. A. & Siegel, B. M. High-resolution structuring of emitter tips for the gaseous field-ionization source. *J. Vac. Sci. Technol. B* **4**, 120–125 (1986).

274. Musselman, I. H. & Russell, P. E. Method of fabricating scanning tunneling microscope tips. US Patent 5,085,746 (1992).
275. DLC Coatings | Diamond-Like Carbon Coatings | Titankote | HIPIMS technology. at <http://www.richterprecision.com/dlc-coatings.html> (2012).
276. Cordani, B. *The Kepler Problem : Group Theoretical Aspects, Regularization and Quantization, with Application to the Study of Perturbations*. (Birkhäuser Verlag: Basel; Boston: 2003).
277. Hartmann, A. K., Kree, R., Geyer, U. & Kölbel, M. Long-time effects in a simulation model of sputter erosion. *Phys. Rev. B* **65**, 193403 (2002).
278. Anderson, M. S. Locally enhanced Raman spectroscopy with an atomic force microscope. *Appl. Phys. Lett.* **76**, 3130–3132 (2000).
279. Manchester, F. D., San-Martin, A. & Pitre, J. M. The H-Pd (hydrogen-palladium) system. *J. Phase Equilib.* **15**, 62–83 (1994).
280. Li, X. *et al.* Large-area synthesis of high-quality and uniform graphene films on copper foils. *Science* **324**, 1312–1314 (2009).
281. Albrecht, P. M. & Lyding, J. W. Ultrahigh-vacuum scanning tunneling microscopy and spectroscopy of single-walled carbon nanotubes on hydrogen-passivated Si (100) surfaces. *Appl. Phys. Lett.* **83**, 5029 (2003).
282. Ruppalt, L. B., Albrecht, P. M. & Lyding, J. W. Atomic resolution scanning tunneling microscope study of single-walled carbon nanotubes on GaAs (110). *J. Vac. Sci. Technol. B* **22**, 2005 (2004).
283. Ritter, K. A. & Lyding, J. W. Characterization of nanometer-sized, mechanically exfoliated graphene on the H-passivated Si (100) surface using scanning tunneling microscopy. *Nanotechnol.* **19**, 015704 (2008).
284. Ritter, K. A. & Lyding, J. W. The influence of edge structure on the electronic properties of graphene quantum dots and nanoribbons. *Nat. Mater.* **8**, 235–242 (2009).
285. Chen, D. *A scanning Tunneling Microscopy and Density Functional Theory Study of Halogen Dynamics and Etching Reaction on the Silicon(100) Surfaces* (Ph.D. Thesis, University of North Carolina at Chapel Hill: 2003).
286. Winters, H. F. & Coburn, J. W. Surface science aspects of etching reactions. *Surf. Sci. Rep.* **14**, 162–269 (1992).
287. Nakayama, K. S. & Weaver, J. H. Si(100)- (2 × 1) Etching with fluorine: Planar removal versus three dimensional pitting. *Phys. Rev. Lett.* **83**, 3210–3213 (1999).
288. Fujikawa, Y. *et al.* Fluorine etching on the Si(1 1 1)-7 × 7 surfaces using fluorinated fullerene. *Surf. Sci.* **521**, 43–48 (2002).
289. Lehtinen, P. O., Foster, A. S., Ma, Y., Krasheninnikov, A. V. & Nieminen, R. M. Irradiation-induced magnetism in graphite: A density functional study. *Phys. Rev. Lett.* **93**, 187202 (2004).
290. Yazyev, O. V. & Helm, L. Defect-induced magnetism in graphene. *Phys. Rev. B* **75**, 125408 (2007).
291. Chen, J.-H., Li, L., Cullen, W. G., Williams, E. D. & Fuhrer, M. S. Tunable Kondo effect in graphene with defects. *Nat. Phys.* **7**, 535–538 (2011).
292. Nair, R. R. *et al.* Spin-half paramagnetism in graphene induced by point defects. *Nat. Phys.***8**, 199–202 (2012).

293. Lee, J.-M. *et al.* A high resolution XPS study of sidewall functionalized MWCNTs by fluorination. *J. Ind. Eng. Chem.* **15**, 66–71 (2009).
294. Touhara, H. *et al.* Fluorine-graphite HOPG intercalation compounds. *Synthetic Met.* **23**, 461–466 (1988).
295. Chen, S. *et al.* Oxidation resistance of graphene-coated Cu and Cu/Ni alloy. *ACS Nano* **5**, 1321–1327 (2011).
296. Wofford, J. M., Nie, S., McCarty, K. F., Bartelt, N. C. & Dubon, O. D. Graphene islands on Cu foils: The interplay between shape, orientation, and defects. *Nano Lett.* **10**, 4890–4896 (2010).
297. Stroscio, J. A., Feenstra, R. M. & Fein, A. P. Electronic structure of the Si(111)2 × 1 surface by scanning-tunneling microscopy. *Phys. Rev. Lett.* **57**, 2579–2582 (1986).
298. Sahin, H., Topsakal, M. & Ciraci, S. Structures of fluorinated graphenes and their signatures. *Phys. Rev. B* **83**, 115432 (2011).
299. Lobo, J. & Mascaraque, A. Observation of the noble-metal L-gap surface state in Cu(311). *J. Phys.-Condens. Mat.* **18**, L395–L400 (2006).
300. Ugeda, M. M., Brihuega, I., Guinea, F. & Gómez-Rodríguez, J. M. Missing atom as a source of carbon magnetism. *Phys. Rev. Lett.* **104**, 096804 (2010).
301. Sztelle, M. M. *Low Temperature Selective Silicon Epitaxy at the Nanometer Scale* (Ph.D. Thesis, University of Illinois at Urbana-Champaign: 2008).
302. Zhang, F. *Modification of an Ultra-High-Vacuum Scanning Tunneling Microscope for Silicon Nanostructure Fabrication* (M.S. Thesis, University of Illinois at Urbana-Champaign: 2011).

APPENDIX A
FLOW-THROUGH COOLING FOR UHV DIPSTICK

We present the design of a flow-through cooling system for a preparation chamber “dipstick” in the “Chamber A” UHV system located in the Lyding STM Laboratory at the Beckman Institute. Presented is the design of the original dipstick as well as proposed modifications under construction at the time of writing. The modified dipstick design with flow-through cooling was designed jointly by the author, Professor Joseph Lyding, and Scott McDonald of the ECE department machine shop. Original dipstick designs are shown with a gray background, and the new flow-through cooling dipstick design is shown with a black background.

We first present an earlier dipstick design employed on most Lyding lab UHV-STM systems prior to 2012. The purpose of the dipstick is fourfold: in situ positioning and rotation, heating, cooling, and temperature measurement.

The dipstick is designed to interface with a variety of assemblies, including but not limited to sample holders, tip heaters, and molecular dosers. All of these assemblies will be generically referred to as “holders.” In all cases, the interface between dipstick and holder provides for two electrically isolated sides separated by an insulating center-piece. While the holder is held from above, it is fixed in place vertically by spring-steel clips and quartz rollers which interface with depressions in the side of each holder. Lateral stability is provided by two pins which protrude into the insulating center-piece of the holder.

Positioning of the holder in three dimensions is enabled by the use of an xyz stage and welded bellows. Rotational manipulation is enabled by a differentially pumped rotational stage. The use of differential pumping to enable rotation (with gasket seals and three vacuum stages: UHV, turbo pump, roughing pump) is not ideal, but is necessitated in the current design by the need to rotate both electrical feedthroughs and, more importantly, gas feedthroughs employed for sample cooling. These feedthroughs cannot be rotated without implementing a poorly sealed rotating vacuum feedthrough. A diagram of this rotational system with feedthroughs is found in Figure A.1. Alternate designs have variously employed a cooling plate design to replace the dipstick cooling assembly[301,302] and a stage design where the entire dipstick assembly is replaced by various fixed stages on which holders are positioned by use of a "wobble stick" vacuum manipulator.

Two heating mechanisms are provided, including filament heating and resistive sample heating. In the former case, heating is through a tungsten filament affixed to the side of the dipstick stack. The filament is generally enshrouded in a metal foil housing which optimizes thermal transfer. Filament heating is employed to heat the entire dipstick and mounted holder to a temperature typically below 150 °C and in all cases below 200 °C. While filament heating is sufficient to remove water from inert samples, frequently higher temperature processing is required for sample preparation or tip degassing. For example, Si(100) samples are prepared by flashing briefly to 1200 °C, and STM tips are typically degassed above 600 °C before use. In these cases, samples are heated by independently biasing both sides of the dipstick, allowing current to flow through the holder directly. For fairly resistive samples, including Si, high temperatures (1200 °C) are easily achieved, although care should be taken to avoid thermal runaway when heating lightly doped semiconductors. For highly electrically and thermally conductive samples, such as Cu foil, extremely high currents would be necessary to achieve high temperatures, and in these cases a more resistive film (typically Si) is mounted behind an insulating film as a resistive heating element while the conductor is electrically contacted only on one side for sample biasing in the STM. Resistive sample heating allows for high processing temperatures without imparting extreme thermal stresses on the dipstick. The dipstick can also be simultaneously cooled to limit dipstick temperature.

Dipstick and holder cooling is enabled by the flow of a cooling gas or liquid through the dipstick during processing. Two sealed steel tubes extend from the top of the dipstick down to its head. The tubes are sealed, but cooling is enabled by pressing a second inner tube down into the outer tube (Figure A.2). Care must be taken to electrically isolate the inner tube from the outer tube where it exits the chamber, because the inner tube will be in electrical contact with the biased head of the dipstick. Gas (typically N_2) or cryogenic liquid (LN_2 is not recommended due to thermal stressing of silver braze joints between the steel tubes and Cu dipstick head) is passed in the inner tube and then out the outer tube to provide a rudimentary flow-through cooling system.

Temperature measurement is provided by two thermocouple feedthroughs. One thermocouple is affixed to the Cu dipstick head (it is spot welded to a foil clip which is then bolted to the dipstick). This thermocouple provides measurement of the dipstick temperature during processing. A second thermocouple feedthrough is attached to the aforementioned pins which prevent lateral movement of the holder on the dipstick. In this way, a thermocouple can be mounted on each holder and interfaced with the dipstick thermocouple feedthroughs for in situ sample temperature measurement. Thermocouples are typically Type K (alumel and chromel) or Type C (tungsten-rhenium) depending on system design and application.

In order to electrically isolate each side of the dipstick from the chamber ground, alumina isolators from Ceramtec (for example, model #8002-01-W) are welded into the steel tubing (Figure A.3). The precise model employed in the original dipstick is unknown, but the new design employs cryogenic isolators with an operating temperature ranging from −269 °C to 450 °C, compatible with all low-temperature and high-temperature dipstick processing employed in the Lyding STM Lab. Cu wires sheathed in fiberglass are then clamped to each cooling tube below the isolator and connected to a high-current electrical feedthrough. To prevent overheating and warping of the dipstick during high current, high-temperature processing, braided copper wire is run along the length of the stainless steeling tubing to improve thermal and electrical conductivity (Figure A.4).

At the bottom of the dipstick (Figure A.5), both stainless steel cooling tubes are brazed to copper blocks with a silver-based solder. These Cu blocks are similarly brazed to Cu tubes which pass to the dipstick head itself, where they are brazed. Hollows for gas-flow pass through these junctions into the dipstick head, where they terminate. Due to the geometry of the dipstick head, the inner cooling tube cannot pass beyond the upper Cu block, and therefore gas beneath this level is not forced but moved only by convection, reducing cooling efficiency. The six braze joints and the approximate locations of the inner cooling tubes are indicated in Figure A.6.

The original dipstick of the Chamber A STM system failed between 2010 and 2011. The mode of failure was the formation of a microfracture in one of the braze joints at the dipstick head. The time and expense required to repair this damage would equal or exceed the cost of building a new dipstick, due in part to the unknown composition of the existing silver solder and therefore the need to fully remove this material before inserting a new braze joint. As a result, we took this opportunity to design a modified dipstick which allowed flow-through cooling directly to the base of the dipstick, and simultaneously reduced the number of braze joints, which had proven to be a likely point of failure.

The modified dipstick design includes four stainless steel tubes which pass through the outer shell of the UHV chamber, through four staggered ceramic isolators, and down to the head of the dipstick, incorporating a similar electrical contact and braided copper wire for thermal and electrical conductivity. This modified design is shown in Figure A.7.

Electrically, each side of the dipstick includes two ¼ inch stainless steel tubes which are wired in parallel to increase conductivity and minimize the effect of thermally induced warping. A close-up view of the wiring mechanism and copper braid is shown in Figure A.8.

At the bottom of the modified dipstick, each stainless steel cooling tube is brazed directly to the dipstick head (Figure A.9), reducing the total number of joints from six to four. The geometry of the head is modified, while maintaining the necessary dimensions to fit within the translational and rotational manipulation assemblies. The interface between dipstick and sample holder remains unchanged, to maintain compatibility with all existing holders and processes.

Flow-through cooling is implemented by joining the cooling tubes within the copper block of the dipstick head, as shown in Figure A.10. This modification enables gas flow through the dipstick head, increasing cooling efficiency and eliminating the need for inner cooling tubes.

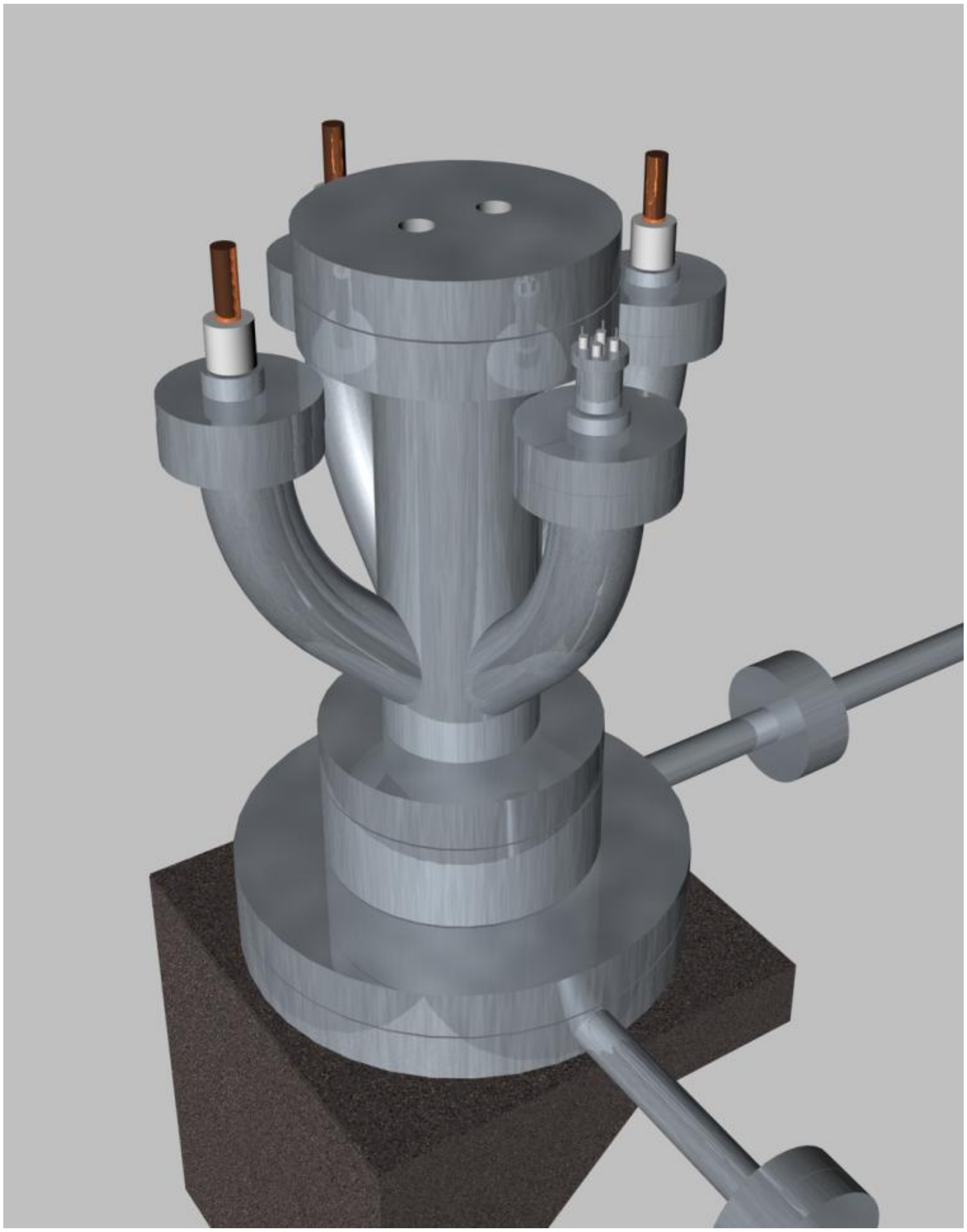

Figure A. 1

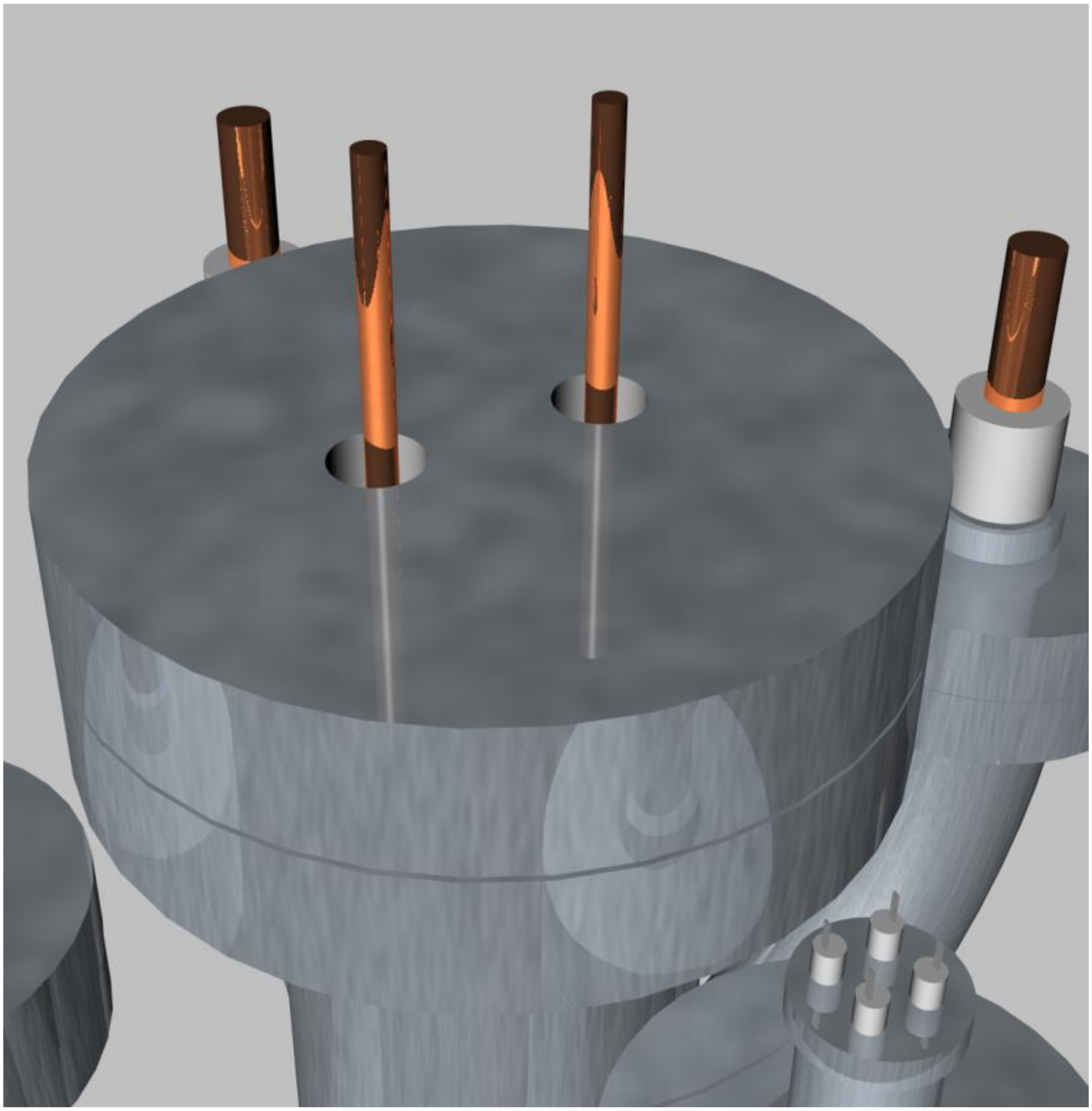

Figure A. 2

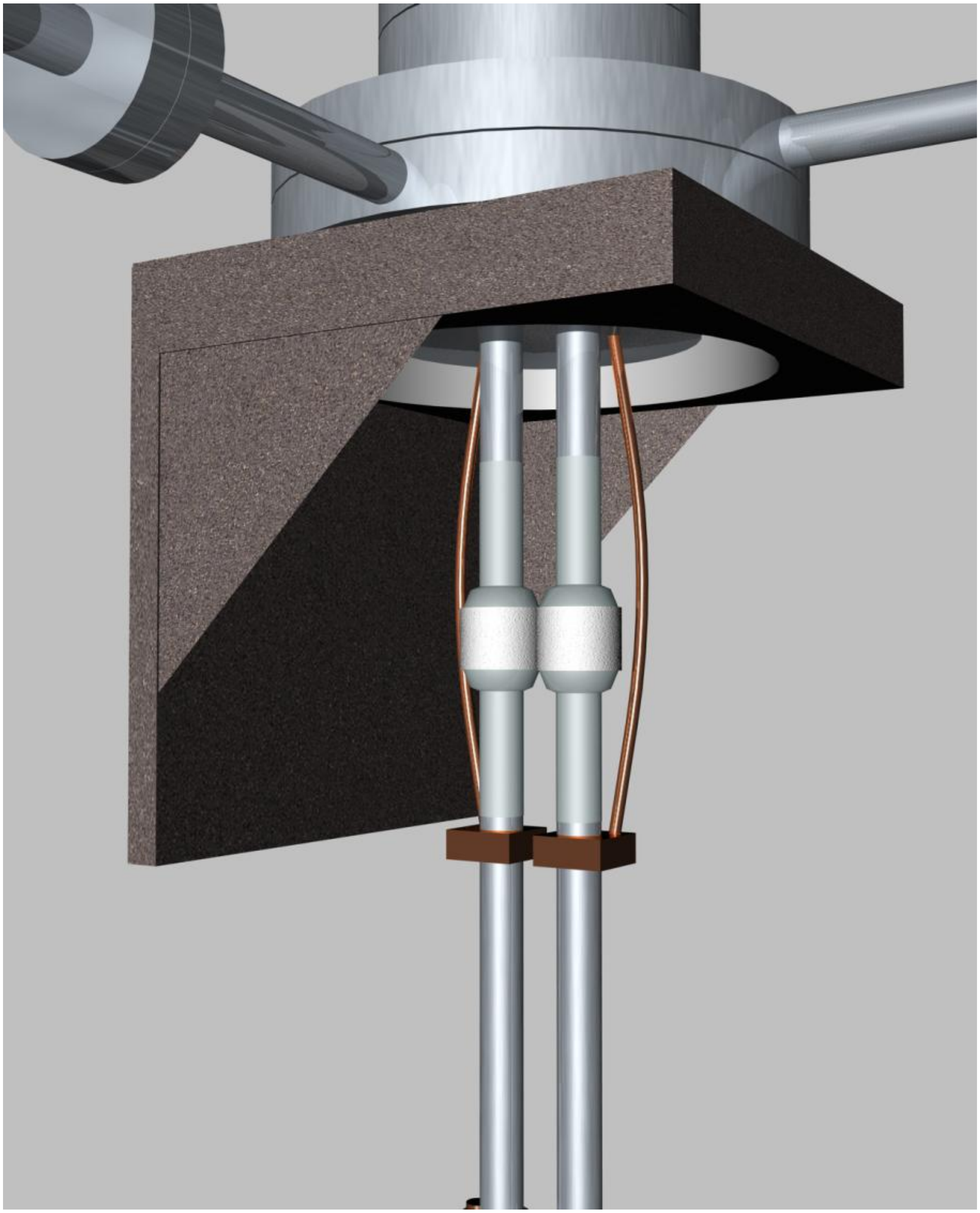

Figure A. 3

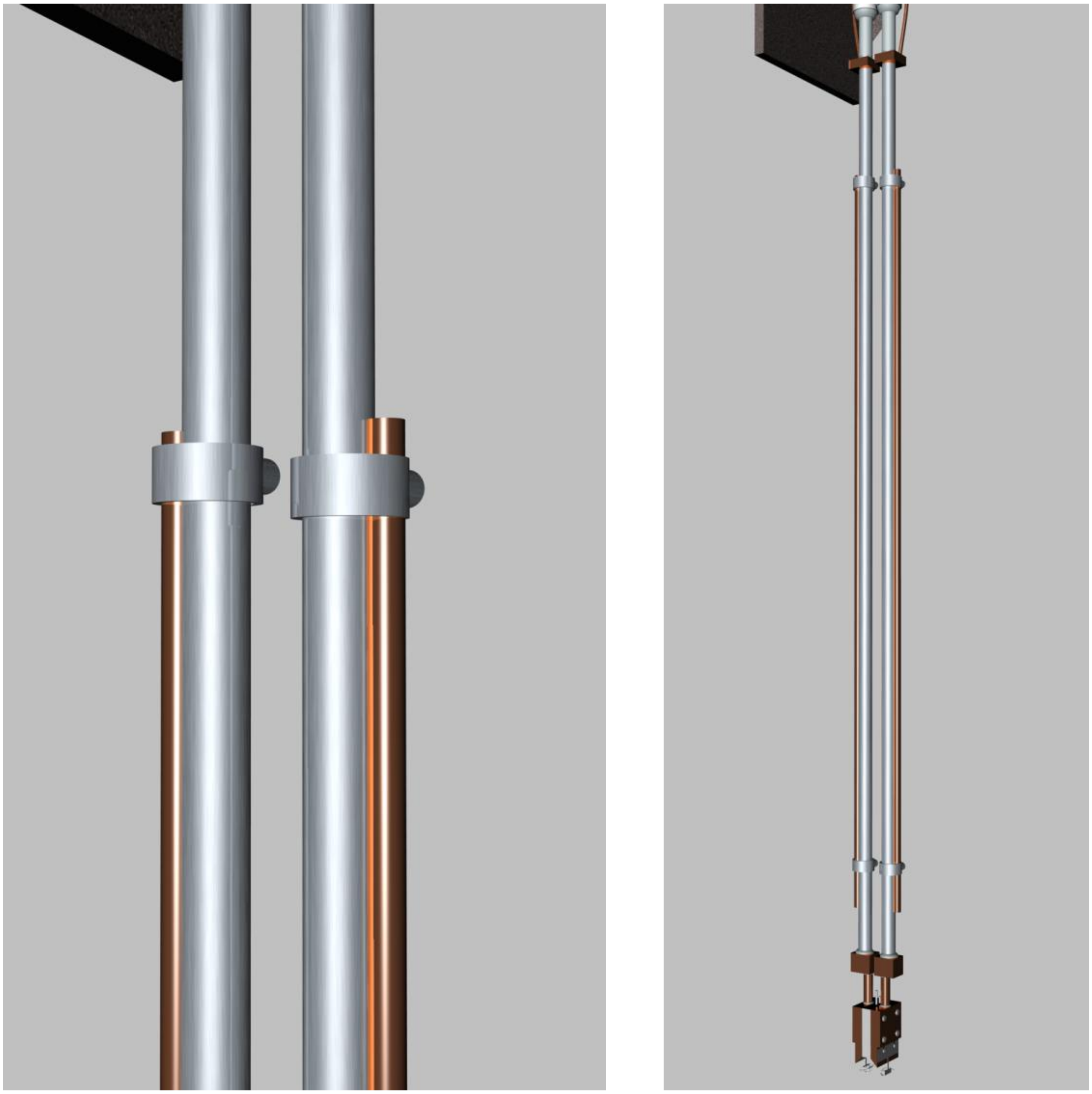

Figure A. 4

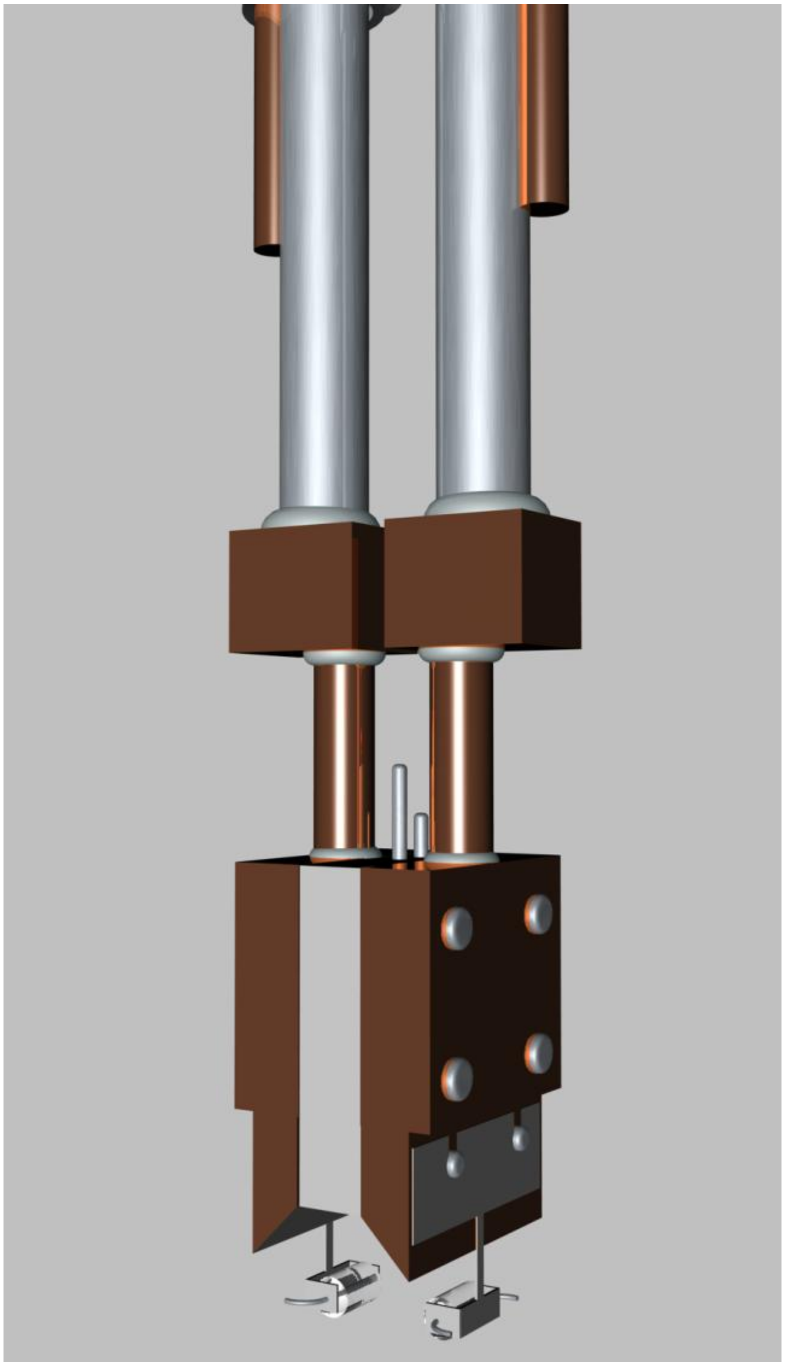

Figure A. 5

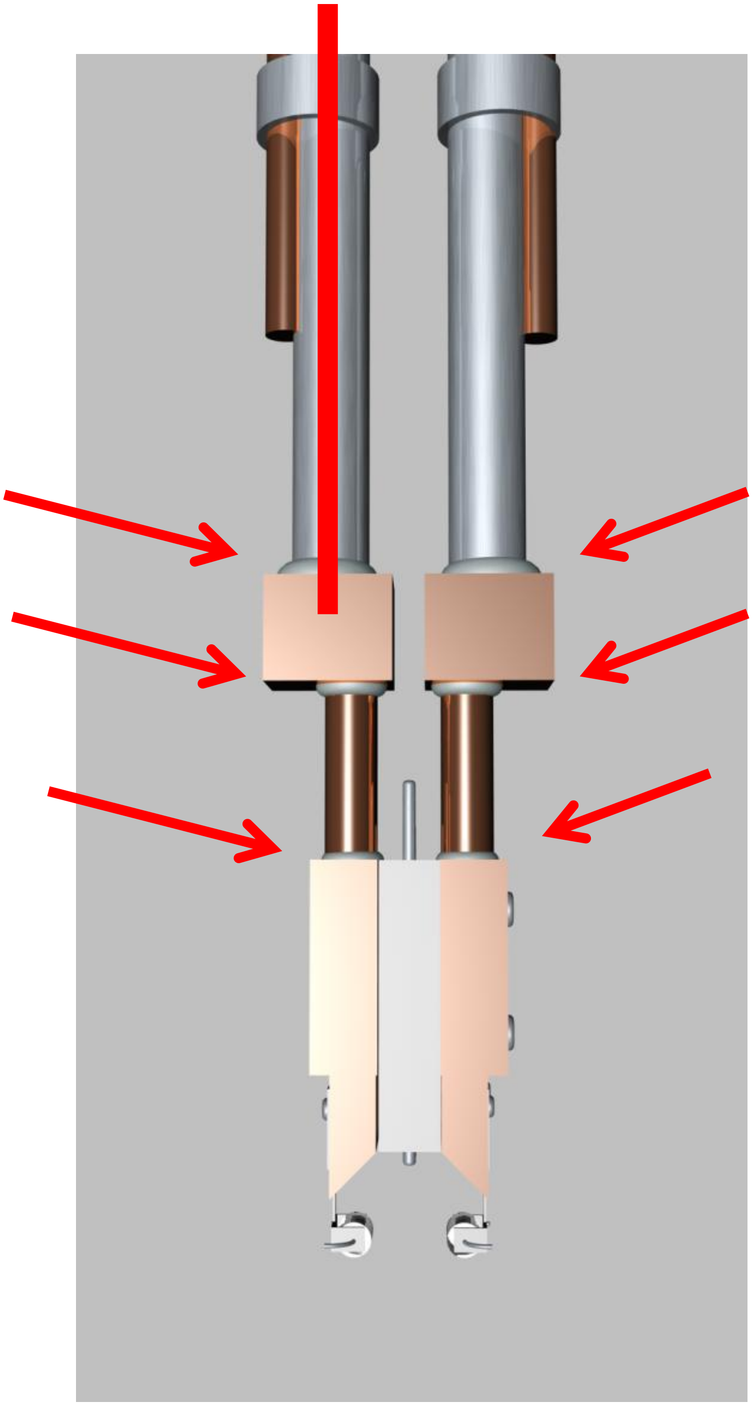

Figure A. 6

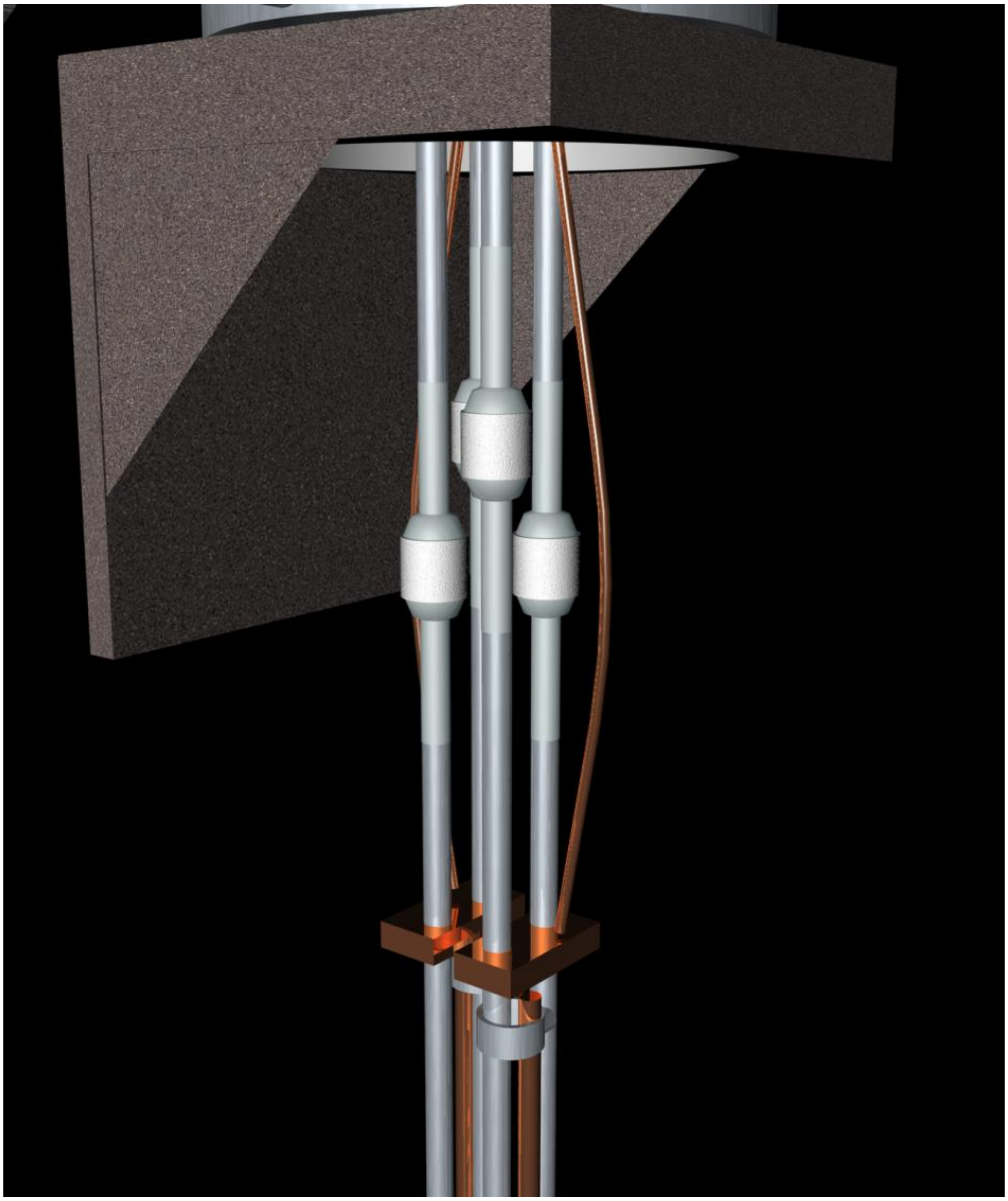

Figure A. 7

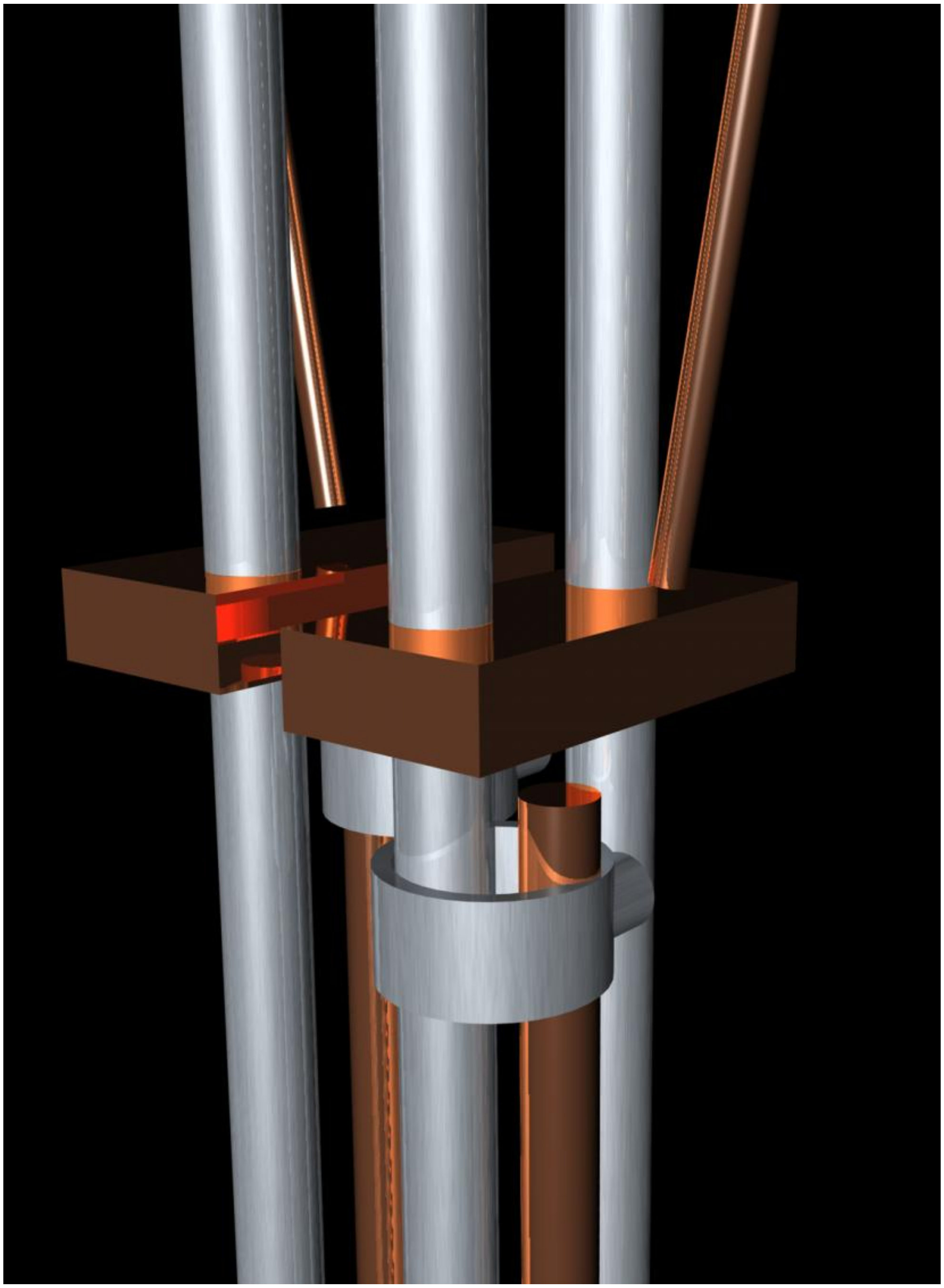

Figure A. 8

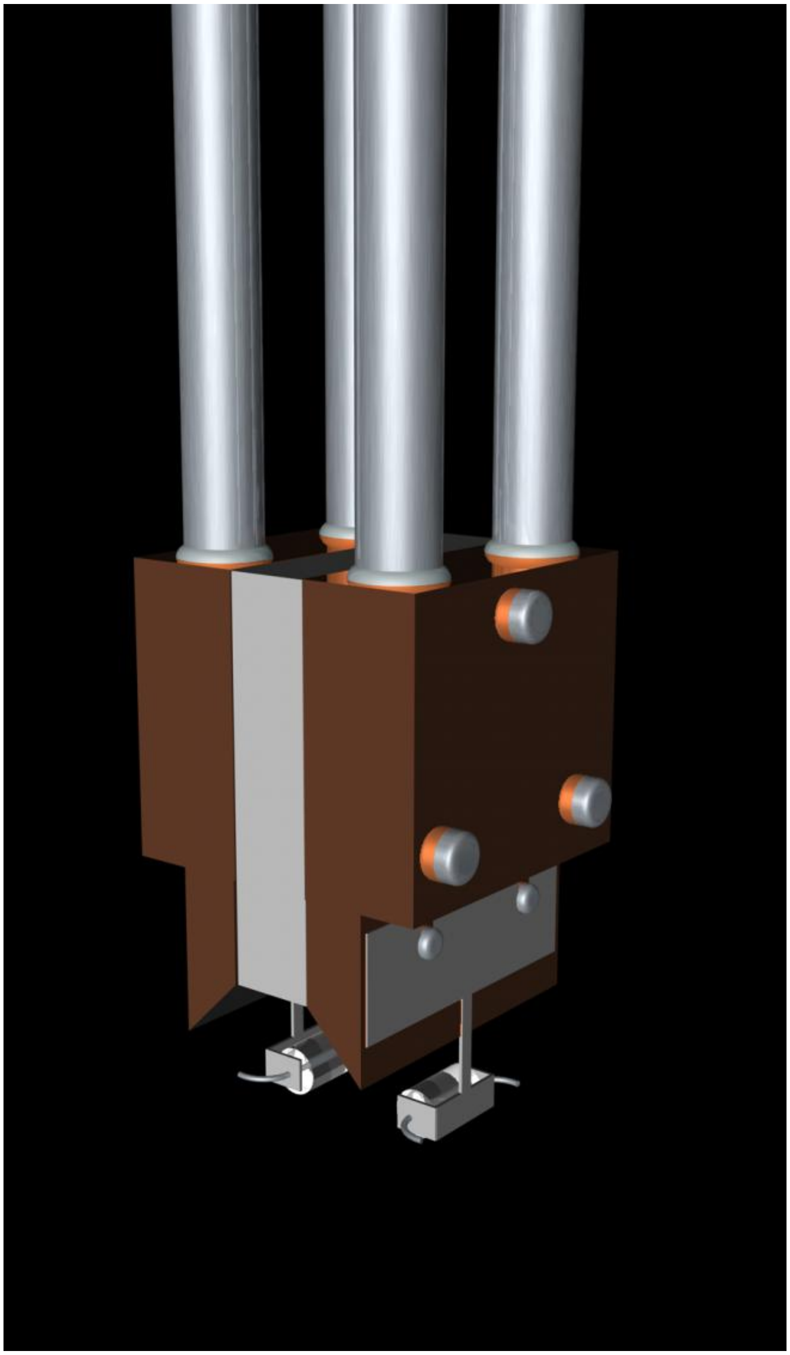

Figure A. 9

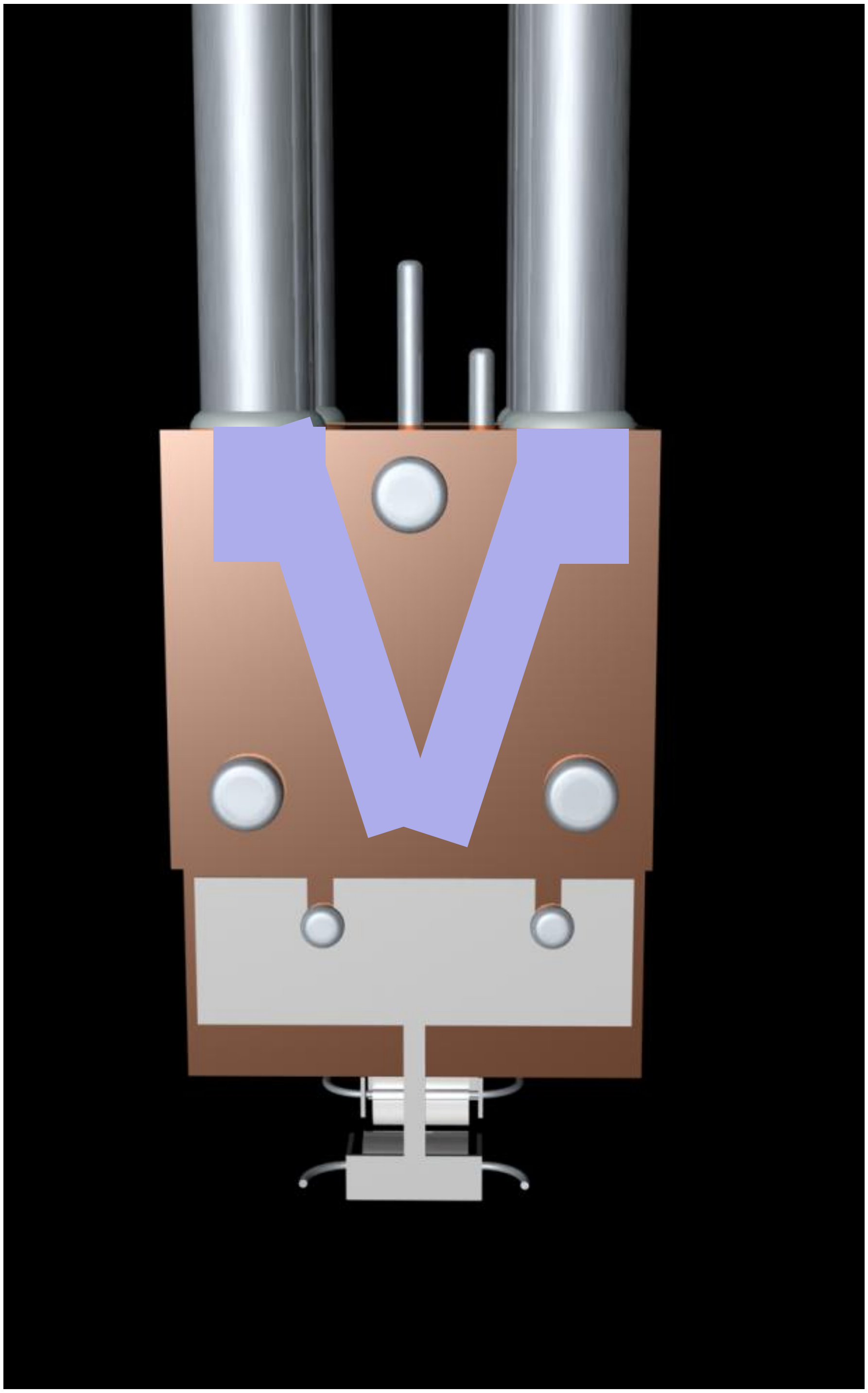

Figure A. 10

APPENDIX B
LYDING TO GWYDDION FILE CONVERSION SOFTWARE

The STM control software employed in the Lyding STM Lab at the University of Illinois was written by Joseph Lyding and Roger Brockenbrough, and has been updated repeatedly through its developmental history. The software outputs STM data in a file format specific to the Lyding STM program which incorporates topographic buffers, spectroscopic buffers, and lithographic parameters into a single data file. Each version of the Lyding STM software is backwards compatible with prior versions of the data file format. No complete documentation exists describing the file format.

Gwyddion is a freely available, open source, modular software package distributed under the GNU general public license. It is used for the analysis of scanned probe microscopy data sets, including topographic buffers and spectroscopic buffers. Its modular and extensible structure further enables the incorporation of additional data types such as lithographic writing parameters. Gwyddion is a popular tool in the SPM community, and continues to undergo development. In order to employ Gwyddion for the analysis of Lyding STM data files, it became necessary to implement conversion software to take the originally formatted Lyding STM data into a Gwyddion-compatible format. A first release of this conversion software is available, with the following features and limitations:

- Parses Lyding STM data files (Version 4.0) to extract the following information:
    - Image buffers (topograph, current, dig. topograph, lock-in, error, d^2I/dV^2)
    - Spectroscopy data and relevant parameters
    - CITS spectra and image buffers
    - Scanning variables and details of the electronic configuration
    - Textual scan log input by the user
- Creates a Gwyddion-formatted output file (.gwy) containing the following information:
    - Image buffers (topography, current, dig. topograph, lock-in, error, d^2I/dV^2)
- Limitation:
    - Can not parse data files containing embedded lithography parameters. Such data files must be resaved with lithography data excluded.

What follows is C++ code for a portion of the conversion software. Specifically, I have included the code for the stmfile class which handles the parsing of Lyding STM data.

```
#include <stdlib.h>
#include <stdio.h>
#include <string.h>

using namespace std;

int parsestring(FILE *out, char *outchar, char *name, int length, int errorcode);
int parsekeyword(FILE *out, char *keyword, int errorcode);
int parseshort(FILE *out, short *siout, char *name, int errorcode);
int parseint(FILE *out, int *iout, char *name, int errorcode);
int parsefloat(FILE *out, float *floatout, char *name, int errorcode);
FILE *fp;

struct globalvars_type {
       char rev_lab[40];    // File type revision label
       char samp_lab[80];
       short year;   // Year that data file was collected
       short month;  // Month that data file was collected
       short day;    // Day that data file was collected
       short hour;   // Hour that data file was collected
       short minute; // Minute that data file was collected
       short second; // Second that data file was collected
       char stm_revision_label[40];
       char stm_id[16];
       char stm_electronics[16];
       short stm_revision_year;
       short stm_revision_month;
       short stm_revision_day;
       short stm_revision_hour;
       short stm_revision_minute;
       short usedsp;
       short usekeithley;
```

```
	float iscan;
	float vscan;
	float tsamp;
	short bias_to_probe;
	short atodsign;
	float dsp_atod_max_v;
	float dsp_dtoa_max_v;
	short dtoa_max_value;

	// Gain factors and amplifier (lin/log)
	float cur_gain;
	float hv_gain;
	float amplif;

	// A/D Converter Variables
	float top_ad_ver;
	float top_ad_max_gain;
	float top_ad_gain;
	float cur_ad_ver;
	float cur_ad_gain;
	float err_ad_ver;
	float err_ad_gain;
	float lock_ad_ver;
	float lock_ad_gain;

	// STM Electronics Variables
	float prop_gain;
	float intg_gain;
	float der_gain;
	float atod1_gain;
	float atod2_gain;
	short atod1_chanl;
	short atod2_chanl;

	globalvars_type()
	{
		atodsign = 0;
		dsp_atod_max_v = 2.75;
		dsp_dtoa_max_v = 3.0;
	}
};

struct messagebox_type {
	short num_message_lines;
	char **message_lines;

	messagebox_type()
	{
		num_message_lines = 0;
		message_lines = NULL;
	}
};

struct heatvars_type {
	char heat_cal_data_filename[60];   // Calibration file
	char heat_cal_data_label[60];      // Calibration data label
	short heat_cal_num_points;  // Number of points in heater calibration data
set
```

```
        float *heat_cal_current;    // Current array (size = heat_cal_num_points)
        float *heat_cal_temperature;       // Temperature array (size =
heat_cal_num_points)
        float heat_cal_slope;
        float heat_cal_intercept;
        float heat_cal_correlation;
        short heat_cal_valid_regression;

        heatvars_type()
        {
                heat_cal_num_points = 0;
                heat_cal_current = NULL;
                heat_cal_temperature = NULL;
        }
};

struct stsblock_type {
        short spec_block_data_type;
        char spec_block_label[80];
        short spec_mode;
        short max_spec_per_coord;
        short spec_num_spec;
        short spec_pt_per_spec;
        short spec_avg_num_spec;
        short spec_hex_num_spec;
        short spec_x_num_spec;
        short spec_y_num_spec;
        short spec_u_num_spec;
        float spec_spread_type;
        short spec_lead_pts;
        float spec_settle;
        float spec_vstrt;
        float spec_vfnsh;
        float spec_istrt;
        float spec_ifnsh;
        float spec_pt_del;
        float spec_zstrt;
        float spec_zfnsh;
        float spec_zscan;
        float spec_avg_del;
        float spec_x_spec_inc;
        float spec_y_spec_inc;
        float spec_r_x_cen;
        float spec_r_y_cen;
        float spec_rect_angl;
        float spec_u_x_cen;
        float spec_u_y_cen;
        float spec_user_angl;
        float spec_hex_pt_sep;
        float spec_h_x_cen;
        float spec_h_y_cen;
        float spec_hex_angl;
        short spec_lock_in_der;
        float spec_lock_in_range;
        float spec_lock_in_tau;
        float spec_dith_ampl;
        float spec_dith_freq;
        short spec_cusp_index;
```

```
       float spec_lock_in_point_delay;
       float spec_lock_in_full_scale_v;
       short spec_skip_endpoint_ramps;
       short spec_pt_num_average;
       float spec_pt_avg_delay;
       short spec_potentiometry;
       short spec_potentio_use_samp_intv;
       float spec_potentio_samp_interval;
       float spec_potentio_lower_rail_v;
       float spec_potentio_upper_rail_v;
       short spec_potentio_lower_rail_fixed;
       short spec_potentio_upper_rail_fixed;
       short spec_initial_v_use_scan_value;
       short spec_initial_i_use_scan_value;
       short spec_initial_trans_together;
       short spec_initial_trans_i_first;
       float spec_initial_v;
       float spec_initial_v_trans_time;
       float spec_initial_i;
       float spec_initial_i_trans_time;
       float spec_cusp_voltage;
       float spec_delay_before_atod;
       short spec_set_initial_ds;
       float spec_initial_ds;
       float spec_initial_ds_trans_time;
       short spec_current_channel_0_on;
       short spec_current_channel_1_on;
       short spec_current_channel_2_on;
       short spec_current_channel_3_on;
       short spec_current_average_mode;
       short spec_dither_only;
       short spec_leave_dither_on;

       // Coordinates
       short *cols;         // Size = spec_num_spec
       short *rows;         // Size = spec_num_spec

       float ***stsdata;    // Array of array of floats (array of floats for each 
spectra)

       stsblock_type()
       {
              cols = NULL;
              rows = NULL;
              stsdata = NULL;
       }
};

struct stsvars_type {
       short valid_spec;
       short spec_num_blocks;
       short spec_mode;
       float spec_array_offset;
       short spec_max_points_per_spec;
       short spec_max_spec_per_coord;
       short spec_max_num_spec;
       short spec_active_block;
       stsblock_type *stsblocks;          // size = spec_num_blocks
```

```
       stsvars_type()
       {
              valid_spec = 0;
              spec_num_blocks = 0;
              stsblocks = NULL;
       }
};

struct citsbuff_type {
       float cits_bias;
};

struct citsblock_type {
       short cits_block_mode;
       short cits_block_data_type;
       char cits_block_text[80];
       short cits_spec_raw_deglitch;
       short cits_spec_raw_glitch_threshold;
       short cits_spec_raw_smooth;
       short cits_spec_raw_smooth_order;
       short cits_spec_raw_smooth_n_fit;

       float **realdata;                  // holds data array if data type = 1,
else null
       short **intdata;                   // holds data array if data type = 0,
else null

       citsblock_type()
       {
              realdata = NULL;
              intdata = NULL;
       }
};

struct citsvars_type {
       short cits_on;
       short valid_cits;

       short spec_mode;
       short cits_num_buff;
       short cits_num_blocks;
       short cits_analysis_block;
       short cits_display_block;
       short cits_oversample_mult;
       float spec_vstrt;
       float spec_vfnsh;
       float spec_pt_del;
       short spec_avg_num_spec;
       float spec_avg_del;
       float spec_lock_in_point_delay;
       short cits_log_temperature;
       short cits_temperature_pts;
       short cits_temperature_atod_channel;
       float cits_temperature_log_interval;
       float cits_temperature_log_sampl_dt;
       float cits_temperature_conv_factor;
       short spec_dither_only;
```

```
	short cits_topo_average;
	short cits_topo_num_average;
	short cits_spec_fit;
	short cits_spec_fit_pts;
	float spec_istrt;
	float spec_ifnsh;
	float spec_zstrt;
	float spec_zfnsh;
	float spec_zscan;

	char *cits_temperature_array;		// length = 4 *
cits_temperature_pts
	citsbuff_type *citsbuffs;		// size = cits_num_buff
	citsblock_type *citsblocks;		// size = cits_num_blocks

	citsvars_type()
	{
		cits_on = 0;
		valid_cits = 0;
		cits_num_buff = 0;
		cits_num_blocks = 0;
		cits_temperature_pts = 0;
		cits_temperature_array = NULL;
		citsbuffs = NULL;
		citsblocks = NULL;
	}
};

struct colormap_type {
	float h_min;
	float h_max;
	float s_min;
	float s_max;
	float i_min;
	float i_max;
	short n_min;
	short n_max;
	short d_min;
	short d_max;
	float dp_min;
	float dp_max;
	short dpr_min;
	short dpr_max;
	short col_fit_type;
};

struct colormap_arr_type {
	short num_colormaps; // Min(NUM_BUFFERS,NUM_MAPS)
	colormap_type *maps;		// Array of color maps (size = num_colormaps)

	colormap_arr_type()
	{
		num_colormaps = 0;
		maps = NULL;
	}
};

struct scanvars_type {
```

```
	short scan_mode;
	float xst;
	float xfin;
	float xinc;
	float x_ofset;
	float yst;
	float yfin;
	float yinc;
	float y_ofset;
	float scnxin;
	float scnyin;
	float theta;
	float scan_del;
	short scan_ad_check;
	short scan_up_dwn;
	short scanning_up;
	short nsampl;
	short nscans;
	short xnum;
	short ynum;
	float jj_z_gain; // Jim Janninck Z Gain? Constant 3.35

	// Variable speed scanning parameters
	float topo_ad_delay;
	short ad_max_change;
	short max_num_ad_check;

	// Sub-interval scanning variables
	short use_scan_inc;
	float scan_del_intv;
	short scan_xnum;
	short scan_ynum;

	// I'm not sure what this does, it is saved together with the scan 
direction for each buff
	short retrace_num_average;

	// Scan line delay constants
	float delay_before_next_scan_line;
	float delay_after_i_and_v_setting;

	// Total scan time
	float scantime;

	// Calibration and vernier settings
	float xcal;
	float ycal;
	float zcal;
	float xver;
	float yver;
	float zver;

	scanvars_type()
	{
		jj_z_gain = (float)3.35;
	}
};
```

```
struct buffdata {
       short active;                     // Buffer active flag
       float voltage1;                          // Lower rail voltage
       float voltage2;                          // Upper rail voltage
       float current;                           // Current setpoint
       short scan_mode;                  // Scan mode for each buffer
       short scan_direction;                    // Scan direction (up/down)
       short image_buffer_data_type;     // Data type (0 = integer, 1 = real)
       float **realdata;                 // holds data array if data type = 1,
else null
       short **intdata;                  // holds data array if data type = 0,
else null

       // Plane fit parameters for each buffer
       short valid_plane;
       short plane_sub;
       short line_by_line_sub;
       float a23;
       float a24;
       float a25;
       short pl_avg;
       float plane_x_len;
       short plane_xpts;
       float plane_angle;

       buffdata()
       {
              realdata = NULL;
              intdata = NULL;
       }
};


class stmfile
{
public:
       stmfile(char *file);
       ~stmfile();
       int is_valid;
       char *filename;
       short num_buffers;
       short display_buffer;
       char *keyword;
       globalvars_type globalvars;
       buffdata *buffer_data;
       heatvars_type heatvars;
       colormap_arr_type colormap_arr;
       messagebox_type messagebox;
       scanvars_type scanvars;
       stsvars_type stsvars;
       citsvars_type citsvars;
private:
       int i,j,k,x,y,ec;
       int spc;
};

stmfile::stmfile(char *file)
{
```

```
       is_valid = 1;
       keyword = new char[8];
       filename = new char[strlen(file)+1];
       strcpy_s(filename, strlen(file)+1, file);
       buffer_data = NULL;
       heatvars.heat_cal_current = NULL;
       heatvars.heat_cal_temperature = NULL;
       colormap_arr.maps = NULL;
       messagebox.message_lines = NULL;
       // Check the number of arguments to verify that we have
       // all the information that we need.
       // Open specified file for reading
       if(fopen_s(&fp, file, "rb")!=0)
       {
              perror(file);
              is_valid = 0;
              exit(1);
       }

       ec=1;
       if(!parsestring(stdout,globalvars.rev_lab,"REV_LAB",40,ec++))
              {is_valid = 0;exit(1);}
       if(!parsekeyword(stdout,keyword,ec++))
              {is_valid = 0;exit(1);}
       if(!parsestring(stdout,globalvars.samp_lab,"SAMP_LAB",80,ec++))
              {is_valid = 0;exit(1);}
       if(!parseshort(stdout,&globalvars.year,"YEAR",ec++))
              {is_valid = 0;exit(1);}
       if(!parseshort(stdout,&globalvars.month,"MONTH",ec++))
              {is_valid = 0;exit(1);}
       if(!parseshort(stdout,&globalvars.day,"DAY",ec++))
              {is_valid = 0;exit(1);}
       if(!parseshort(stdout,&globalvars.hour,"HOUR",ec++))
              {is_valid = 0;exit(1);}
       if(!parseshort(stdout,&globalvars.minute,"MINUTE",ec++))
              {is_valid = 0;exit(1);}
       if(!parseshort(stdout,&globalvars.second,"SECOND",ec++))
              {is_valid = 0;exit(1);}

       while(strncmp(keyword,"EOF     ",8)!=0 && !feof(fp))
       {
               if(!parsekeyword(stdout,keyword,ec++))
                       {is_valid = 0;exit(1);}
              if(strncmp(keyword,"ATODSIGN",8)==0)
              {
                     //printf("switch ATODSIGN\n");
                     globalvars.atodsign = 1;
              }

              else if(strncmp(keyword,"HEATCAL ",8)==0)
              {
                     //printf("switch heatcal\n");

       if(!parsestring(NULL,heatvars.heat_cal_data_filename,"HEAT_CAL_DATA_FILENAM
E",60,ec++)) {is_valid = 0;exit(1);}

       if(!parsestring(NULL,heatvars.heat_cal_data_label,"HEAT_CAL_DATA_LABEL",60,
ec++)) {is_valid = 0;exit(1);}
```

```
       if(!parseshort(stdout,&heatvars.heat_cal_num_points,"HEAT_CAL_NUM_POINTS",e
c++)) {is_valid = 0;exit(1);}
                     heatvars.heat_cal_current = new
float[heatvars.heat_cal_num_points];
                     heatvars.heat_cal_temperature = new
float[heatvars.heat_cal_num_points];
                     for(i=0;i<heatvars.heat_cal_num_points;i++)
                     {

       if(!parsefloat(stdout,&heatvars.heat_cal_current[i],"HEAT_CAL_CURRENT",ec++
)) {is_valid = 0;exit(1);}

       if(!parsefloat(stdout,&heatvars.heat_cal_temperature[i],"HEAT_CAL_TEMPERATU
RE",ec++)) {is_valid = 0;exit(1);}
                     }

       if(!parsefloat(stdout,&heatvars.heat_cal_slope,"HEAT_CAL_SLOPE",ec++))
{is_valid = 0;exit(1);}

       if(!parsefloat(stdout,&heatvars.heat_cal_intercept,"HEAT_CAL_intercept",ec+
+)) {is_valid = 0;exit(1);}

       if(!parsefloat(stdout,&heatvars.heat_cal_correlation,"HEAT_CAL_correlation"
,ec++)) {is_valid = 0;exit(1);}

       if(!parseshort(stdout,&heatvars.heat_cal_valid_regression,"HEAT_CAL_VALID_R
EGRESSION",ec++)) {is_valid = 0;exit(1);}
              }
              else if(strncmp(keyword,"REVISION",8)==0)
              {
                     //printf("switch revision\n");

       if(!parsestring(NULL,globalvars.stm_revision_label,"STM_REVISION_LABEL",40,
ec++)) {is_valid = 0;exit(1);}

       if(!parseshort(stdout,&globalvars.stm_revision_year,"STM_REVISION_YEAR",ec+
+)) {is_valid = 0;exit(1);}

       if(!parseshort(stdout,&globalvars.stm_revision_month,"STM_REVISION_MONTH",e
c++)) {is_valid = 0;exit(1);}

       if(!parseshort(stdout,&globalvars.stm_revision_day,"STM_REVISION_DAY",ec++)
) {is_valid = 0;exit(1);}

       if(!parseshort(stdout,&globalvars.stm_revision_hour,"STM_REVISION_HOUR",ec+
+)) {is_valid = 0;exit(1);}

       if(!parseshort(stdout,&globalvars.stm_revision_minute,"STM_REVISION_MINUTE"
,ec++)) {is_valid = 0;exit(1);}
              }
                else if(strncmp(keyword,"BUFF_0  ",8)==0)
                {
                        //printf("switch buff_0\n");
                        if(!parseshort(stdout,&num_buffers,"NUM_BUFFERS",ec++))
{is_valid = 0;exit(1);}
                     buffer_data = new buffdata[num_buffers];
                }
```

```
                else if(strncmp(keyword,"BUFF_1  ",8)==0)     // Display buffer,
scan buffer voltages, currents and flags
                {
                        //printf("switch buff_1\n");

if(!parseshort(stdout,&display_buffer,"DISPLAY_BUFFER",ec++)) {is_valid =
0;exit(1);}
                     for(i=0;i<num_buffers;i++)
                     {

       if(!parseshort(stdout,&(buffer_data[i].active),"SCAN_BUFFER_ACTIVE",ec++))
{is_valid = 0;exit(1);}

       if(!parsefloat(stdout,&(buffer_data[i].voltage1),"VSCAN_1",ec++)) {is_valid
= 0;exit(1);}

       if(!parsefloat(stdout,&(buffer_data[i].current),"ISCAN",ec++)) {is_valid =
0;exit(1);}
                     }
                }
                else if(strncmp(keyword,"BUFF_2  ",8)==0)     // Upper rail
voltage buffer
                {
                        //printf("switch buff_2\n");
                        for(i=0;i<num_buffers;i++)
                        {

if(!parsefloat(stdout,&(buffer_data[i].voltage2),"VSCAN_2",ec++)) {is_valid =
0;exit(1);}
                        }
                }
                else if(strncmp(keyword,"NANO_1  ",8)==0)  // Nanolithography data
                {
                        //printf("switch NANO_1\n");
                }
                else if(strncmp(keyword,"C_MAPS_1",8)==0)  // Color map data
                {
                        //printf("switch c_maps_1\n");

       if(!parseshort(stdout,&colormap_arr.num_colormaps,"NUMCMAPS",ec++))
{is_valid = 0;exit(1);}
                     colormap_arr.maps = new
colormap_type[colormap_arr.num_colormaps];
                     for(i=0;i<colormap_arr.num_colormaps;i++)
                     {

       if(!parsefloat(stdout,&colormap_arr.maps[i].h_min,"H_MIN",ec++)) {is_valid
= 0;exit(1);}

       if(!parsefloat(stdout,&colormap_arr.maps[i].h_max,"H_MAX",ec++)) {is_valid
= 0;exit(1);}

       if(!parsefloat(stdout,&colormap_arr.maps[i].s_min,"S_MIN",ec++)) {is_valid
= 0;exit(1);}

       if(!parsefloat(stdout,&colormap_arr.maps[i].s_max,"S_MAX",ec++)) {is_valid
= 0;exit(1);}
```

```
       if(!parsefloat(stdout,&colormap_arr.maps[i].i_min,"I_MIN",ec++)) {is_valid
= 0;exit(1);}

       if(!parsefloat(stdout,&colormap_arr.maps[i].i_max,"I_MAX",ec++)) {is_valid
= 0;exit(1);}

       if(!parseshort(stdout,&colormap_arr.maps[i].n_min,"N_MIN",ec++)) {is_valid
= 0;exit(1);}

       if(!parseshort(stdout,&colormap_arr.maps[i].n_max,"N_MAX",ec++)) {is_valid
= 0;exit(1);}

       if(!parseshort(stdout,&colormap_arr.maps[i].d_min,"D_MIN",ec++)) {is_valid
= 0;exit(1);}

       if(!parseshort(stdout,&colormap_arr.maps[i].d_max,"D_MAX",ec++)) {is_valid
= 0;exit(1);}

       if(!parsefloat(stdout,&colormap_arr.maps[i].dp_min,"DP_MIN",ec++))
{is_valid = 0;exit(1);}

       if(!parsefloat(stdout,&colormap_arr.maps[i].dp_max,"DP_MAX",ec++))
{is_valid = 0;exit(1);}

       if(!parseshort(stdout,&colormap_arr.maps[i].dpr_min,"DPR_MIN",ec++))
{is_valid = 0;exit(1);}

       if(!parseshort(stdout,&colormap_arr.maps[i].dpr_max,"DPR_MAX",ec++))
{is_valid = 0;exit(1);}

       if(!parseshort(stdout,&colormap_arr.maps[i].col_fit_type,"COL_FIT_TYPE",ec+
+)) {is_valid = 0;exit(1);}
                     }
                }
                else if(strncmp(keyword,"DSP     ",8)==0)  // DSP and Keithley
usage flags
                {
                        //printf("switch DSP\n");
                     if(!parseshort(stdout,&globalvars.usedsp,"USEDSP",ec++))
{is_valid = 0;exit(1);}
                     if(globalvars.usedsp)
                     {
                            globalvars.dtoa_max_value = 32767;
                     }
                     else
                     {
                            globalvars.dtoa_max_value = 4095;
                     }

       if(!parseshort(stdout,&globalvars.usekeithley,"USEKEITHLEY",ec++))
{is_valid = 0;exit(1);}
                }
                else if(strncmp(keyword,"ID      ",8)==0)  // STM and electronics
ID numbers
                {
                        //printf("switch ID\n");
```

```
                    if(!parsestring(NULL,globalvars.stm_id,"STM_ID",16,ec++))
{is_valid = 0;exit(1);}

       if(!parsestring(NULL,globalvars.stm_electronics,"STM_ELECTRONICS",16,ec++))
{is_valid = 0;exit(1);}
                }
                else if(strncmp(keyword,"MESSG   ",8)==0)  // Message box data
                {
                        //printf("switch MESSG\n");

       if(!parseshort(stdout,&messagebox.num_message_lines,"MESSG_LINES",ec++))
{is_valid = 0;exit(1);}
                    messagebox.message_lines = new
char*[messagebox.num_message_lines];
                    for(i=0;i<messagebox.num_message_lines;i++)
                    {
                           messagebox.message_lines[i] = new char[60];

       if(!parsestring(stdout,messagebox.message_lines[i],"MESSG",60,ec++))
{is_valid = 0;exit(1);}
                    }
                }
                else if(strncmp(keyword,"I_V_T   ",8)==0)  // IVT parameters
                {
                        //printf("switch I_V_T\n");
                        if(!parsefloat(stdout,&globalvars.iscan,"ISCAN",ec++))
{is_valid = 0;exit(1);}
                        if(!parsefloat(stdout,&globalvars.vscan,"VSCAN",ec++))
{is_valid = 0;exit(1);}
                        if(!parsefloat(stdout,&globalvars.tsamp,"TSAMP",ec++))
{is_valid = 0;exit(1);}
                }
                else if(strncmp(keyword,"SCAN    ",8)==0)  // Scanning parameters
                {
                        //printf("switch SCAN\n");

if(!parseshort(stdout,&scanvars.scan_mode,"SCANMODE",ec++)) {is_valid =
0;exit(1);}
                        if(!parsefloat(stdout,&scanvars.xst,"XST",ec++)) {is_valid
= 0;exit(1);}
                        if(!parsefloat(stdout,&scanvars.xfin,"XFIN",ec++))
{is_valid = 0;exit(1);}
                        if(!parsefloat(stdout,&scanvars.xinc,"XINC",ec++))
{is_valid = 0;exit(1);}
                        if(!parsefloat(stdout,&scanvars.x_ofset,"X_OFSET",ec++))
{is_valid = 0;exit(1);}
                        if(!parsefloat(stdout,&scanvars.yst,"YST",ec++)) {is_valid
= 0;exit(1);}
                        if(!parsefloat(stdout,&scanvars.yfin,"YFIN",ec++))
{is_valid = 0;exit(1);}
                        if(!parsefloat(stdout,&scanvars.yinc,"YINC",ec++))
{is_valid = 0;exit(1);}
                        if(!parsefloat(stdout,&scanvars.y_ofset,"Y_OFSET",ec++))
{is_valid = 0;exit(1);}
                        if(!parsefloat(stdout,&scanvars.scnxin,"SCNXIN",ec++))
{is_valid = 0;exit(1);}
                        if(!parsefloat(stdout,&scanvars.scnyin,"SCNYIN",ec++))
{is_valid = 0;exit(1);}
```

```
                        if(!parsefloat(stdout,&scanvars.theta,"THETA",ec++))
{is_valid = 0;exit(1);}
                        if(!parsefloat(stdout,&scanvars.scan_del,"SCAN_DEL",ec++))
{is_valid = 0;exit(1);}

if(!parseshort(stdout,&scanvars.scan_ad_check,"SCAN_AD_CHECK",ec++)) {is_valid =
0;exit(1);}

if(!parseshort(stdout,&scanvars.scan_up_dwn,"SCAN_UP_DOWN",ec++)) {is_valid =
0;exit(1);}

if(!parseshort(stdout,&scanvars.scanning_up,"SCANNING_UP",ec++)) {is_valid =
0;exit(1);}
                        if(!parseshort(stdout,&scanvars.nsampl,"NSAMPL",ec++))
{is_valid = 0;exit(1);}
                        if(!parseshort(stdout,&scanvars.nscans,"NSCANS",ec++))
{is_valid = 0;exit(1);}
                        if(!parseshort(stdout,&scanvars.xnum,"XNUM",ec++))
{is_valid = 0;exit(1);}
                        if(!parseshort(stdout,&scanvars.ynum,"YNUM",ec++))
{is_valid = 0;exit(1);}
                }
                else if(strncmp(keyword,"SCAN_1  ",8)==0)  // VARIABLE SPEED
SCANNING PARAMETERS
                {
                        //printf("switch SCAN_1\n");

if(!parsefloat(stdout,&scanvars.topo_ad_delay,"TOPO_AD_DELAY",ec++)) {is_valid =
0;exit(1);}

if(!parseshort(stdout,&scanvars.ad_max_change,"AD_MAX_CHANGE",ec++)) {is_valid =
0;exit(1);}

if(!parseshort(stdout,&scanvars.max_num_ad_check,"MAX_NUM_AD_CHECK",ec++))
{is_valid = 0;exit(1);}
                }
                else if(strncmp(keyword,"SCAN_2  ",8)==0)  // SUB-INTERVAL
SCANNING VARIABLES
                {
                        //printf("switch SCAN_2\n");

if(!parseshort(stdout,&scanvars.use_scan_inc,"USE_SCAN_INC",ec++)) {is_valid =
0;exit(1);}

if(!parsefloat(stdout,&scanvars.scan_del_intv,"SCAN_DEL_INTV",ec++)) {is_valid =
0;exit(1);}

if(!parseshort(stdout,&scanvars.scan_xnum,"SCAN_XNUM",ec++)) {is_valid =
0;exit(1);}

if(!parseshort(stdout,&scanvars.scan_ynum,"SCAN_YNUM",ec++)) {is_valid =
0;exit(1);}
                }
                else if(strncmp(keyword,"S_MODE_1",8)==0)  // SCAN MODES FOR ALL
IMAGE BUFFERS
                {
                        //printf("switch S_MODE_1\n");
                     for(i=0;i<num_buffers;i++)
```

```
if(!parseshort(stdout,&buffer_data[i].scan_mode,"SCAN_MODE",ec++)) {is_valid =
0;exit(1);}
                }
                else if(strncmp(keyword,"SCAN_3  ",8)==0)  // SCAN DIRECTIONS FOR
ALL IMAGE BUFFERS
                {
                        //printf("switch SCAN_3\n");
                     for(i=0;i<num_buffers;i++)

if(!parseshort(stdout,&buffer_data[i].scan_direction,"SCAN_DIRECTION",ec++))
{is_valid = 0;exit(1);}

if(!parseshort(stdout,&scanvars.retrace_num_average,"RETRACE_NUM_AVERAGE",ec++))
{is_valid = 0;exit(1);}
                }
                else if(strncmp(keyword,"SCAN_4  ",8)==0)  // SCAN LINE DELAY
CONSTANTS
                {
                        //printf("switch SCAN_4\n");

if(!parsefloat(stdout,&scanvars.delay_before_next_scan_line,"DELAY_BEFORE_NEXT_SCA
N_LINE",ec++)) {is_valid = 0;exit(1);}

if(!parsefloat(stdout,&scanvars.delay_after_i_and_v_setting,"DELAY_AFTER_I_AND_V_S
ETTING",ec++)) {is_valid = 0;exit(1);}
                }
                else if(strncmp(keyword,"SCAN_5  ",8)==0)  // IMAGE BUFFER DATA
TYPE FOR ALL IMAGE BUFFERS (OLD VERSION)
                {
                        //printf("switch SCAN_5\n");
                     for(i=0;i<num_buffers;i++)
                     {

       if(!parseshort(stdout,&buffer_data[i].image_buffer_data_type,"IMAGE_BUFFER_
DATA_TYPE",ec++)) {is_valid = 0;exit(1);}
                     }
                }
                else if(strncmp(keyword,"SCAN_5A ",8)==0)  // IMAGE BUFFER DATA
TYPE FOR ALL IMAGE BUFFERS
                {
                        //printf("switch SCAN_5A\n");
                     for(i=0;i<num_buffers;i++)
                     {

       if(!parseshort(stdout,&(buffer_data[i].image_buffer_data_type),"IMAGE_BUFFE
R_DATA_TYPE",ec++)) {is_valid = 0;exit(1);}
                     }
                }
                else if(strncmp(keyword,"SCAN_6  ",8)==0)  // TOTAL SCAN TIME
                {
                        //printf("switch SCAN_6\n");

       if(!parsefloat(stdout,&scanvars.scantime,"ELAPSED_SCAN_TIME",ec++))
{is_valid = 0;exit(1);}
                }
                else if(strncmp(keyword,"PLANE_2 ",8)==0)  // PLANE FIT PARAMETERS
FOR EACH BUFFER
```

```
                {
                        //printf("switch PLANE_2\n");
                     for(i=0;i<num_buffers;i++)
                     {

if(!parseshort(stdout,&buffer_data[i].valid_plane,"VALID_PLANE",ec++)) {is_valid =
0;exit(1);}

if(!parseshort(stdout,&buffer_data[i].plane_sub,"PLANE_SUB",ec++)) {is_valid =
0;exit(1);}

if(!parseshort(stdout,&buffer_data[i].line_by_line_sub,"LINE_BY_LINE_SUB",ec++))
{is_valid = 0;exit(1);}
                            if(!parsefloat(stdout,&buffer_data[i].a23,"A23",ec++))
{is_valid = 0;exit(1);}
                            if(!parsefloat(stdout,&buffer_data[i].a24,"A24",ec++))
{is_valid = 0;exit(1);}
                            if(!parsefloat(stdout,&buffer_data[i].a25,"A25",ec++))
{is_valid = 0;exit(1);}
                   if(!parseshort(stdout,&buffer_data[i].pl_avg,"PL_AVG",ec++))
{is_valid = 0;exit(1);}

       if(!parsefloat(stdout,&buffer_data[i].plane_x_len,"PLANE_X_LEN",ec++))
{is_valid = 0;exit(1);}

if(!parseshort(stdout,&buffer_data[i].plane_xpts,"PLANE_XPTS",ec++)) {is_valid =
0;exit(1);}

       if(!parsefloat(stdout,&buffer_data[i].plane_angle,"PLANE_ANGLE",ec++))
{is_valid = 0;exit(1);}
                     }
                }
                else if(strncmp(keyword,"CAL     ",8)==0)  // CALIBRATION AND
VERNIER SETTINGS
                {
                        //printf("switch CAL\n");
                     if(!parsefloat(stdout,&scanvars.xcal,"XCAL",ec++)) {is_valid =
0;exit(1);}
                     if(!parsefloat(stdout,&scanvars.ycal,"YCAL",ec++)) {is_valid =
0;exit(1);}
                     if(!parsefloat(stdout,&scanvars.zcal,"ZCAL",ec++)) {is_valid =
0;exit(1);}
                     if(!parsefloat(stdout,&scanvars.xver,"XVER",ec++)) {is_valid =
0;exit(1);}
                     if(!parsefloat(stdout,&scanvars.yver,"YVER",ec++)) {is_valid =
0;exit(1);}
                     if(!parsefloat(stdout,&scanvars.zver,"ZVER",ec++)) {is_valid =
0;exit(1);}
                }
                else if(strncmp(keyword,"GAIN_1  ",8)==0)  // GAIN FACTORS AND
AMPLIFIER (LIN/LOG) TYPE
                {
                        //printf("switch GAIN_1\n");
                     if(!parsefloat(stdout,&globalvars.cur_gain,"CUR_GAIN",ec++))
{is_valid = 0;exit(1);}
                     if(!parsefloat(stdout,&globalvars.hv_gain,"HV_GAIN",ec++))
{is_valid = 0;exit(1);}
```

```
                    if(!parsefloat(stdout,&globalvars.amplif,"AMPLIF",ec++))
{is_valid = 0;exit(1);}
                }
                else if(strncmp(keyword,"ATOD    ",8)==0)  // A/D CONVERTOR
VARIABLES
                {
                        //printf("switch ATOD\n");

       if(!parsefloat(stdout,&globalvars.top_ad_ver,"TOP_AD_VER",ec++)) {is_valid
= 0;exit(1);}

       if(!parsefloat(stdout,&globalvars.top_ad_max_gain,"TOP_AD_MAX_GAIN",ec++))
{is_valid = 0;exit(1);}
                    globalvars.top_ad_gain = (float)1.0 +
(globalvars.top_ad_ver/(float)10.0)*globalvars.top_ad_max_gain;

       if(!parsefloat(stdout,&globalvars.cur_ad_ver,"CUR_AD_VER",ec++)) {is_valid
= 0;exit(1);}

       if(!parsefloat(stdout,&globalvars.cur_ad_gain,"CUR_AD_GAIN",ec++))
{is_valid = 0;exit(1);}

       if(!parsefloat(stdout,&globalvars.err_ad_ver,"ERR_AD_VER",ec++)) {is_valid
= 0;exit(1);}

       if(!parsefloat(stdout,&globalvars.err_ad_gain,"ERR_AD_GAIN",ec++))
{is_valid = 0;exit(1);}

       if(!parsefloat(stdout,&globalvars.lock_ad_ver,"LOCK_AD_VER",ec++))
{is_valid = 0;exit(1);}

       if(!parsefloat(stdout,&globalvars.lock_ad_gain,"LOCK_AD_GAIN",ec++))
{is_valid = 0;exit(1);}
                }
                else if(strncmp(keyword,"ELEC1   ",8)==0)  // FOR NEW ELECTRONICS
WRITE ADDITIONAL VARIABLES
                {
                        //printf("switch ELEC1\n");
                    if(!parsefloat(stdout,&globalvars.prop_gain,"PROP_GAIN",ec++))
{is_valid = 0;exit(1);}
                    if(!parsefloat(stdout,&globalvars.intg_gain,"INTG_GAIN",ec++))
{is_valid = 0;exit(1);}
                    if(!parsefloat(stdout,&globalvars.der_gain,"DER_GAIN",ec++))
{is_valid = 0;exit(1);}

       if(!parsefloat(stdout,&globalvars.atod1_gain,"ATOD1_GAIN",ec++)) {is_valid
= 0;exit(1);}

       if(!parsefloat(stdout,&globalvars.atod2_gain,"ATOD2_GAIN",ec++)) {is_valid
= 0;exit(1);}

if(!parseshort(stdout,&globalvars.atod1_chanl,"ATOD1_CHANL",ec++)) {is_valid =
0;exit(1);}

if(!parseshort(stdout,&globalvars.atod2_chanl,"ATOD2_CHANL",ec++)) {is_valid =
0;exit(1);}
                }
```

```
                else if(strncmp(keyword,"FLAG    ",8)==0)  // FLAGS USED TO
INDICATE VARIOUS THINGS
                {
                        //printf("switch FLAG\n");

if(!parseshort(stdout,&stsvars.valid_spec,"VALID_SPEC",ec++)) {is_valid =
0;exit(1);}

if(!parseshort(stdout,&globalvars.bias_to_probe,"BIAS_TO_PROBE",ec++)) {is_valid =
0;exit(1);}
                        if(!parseshort(stdout,&citsvars.cits_on,"CITS_ON",ec++))
{is_valid = 0;exit(1);}
                }
                else if(strncmp(keyword,"FLAG_1  ",8)==0)  // FLAG SPECIFYING
WHETHER OR NOT THERE IS VALID CITS DATA
                {
                        //printf("switch FLAG_1\n");
                        //printf(“The .t.r.e.a.s.u.r.e. is in …\n");

if(!parseshort(stdout,&citsvars.valid_cits,"VALID_CITS",ec++)) {is_valid =
0;exit(1);}
                }
                else if(strncmp(keyword,"SPEC_M1 ",8)==0)  // SPECTROSCOPY DATA
                {
                        //printf("switch SPEC_M1\n");

if(!parseshort(stdout,&stsvars.spec_num_blocks,"SPEC_NUM_BLOCKS",ec++)) {is_valid
= 0;exit(1);}

       if(!parsefloat(stdout,&stsvars.spec_array_offset,"SPEC_ARRAY_OFFSET",ec++))
{is_valid = 0;exit(1);}

if(!parseshort(stdout,&stsvars.spec_max_points_per_spec,"SPEC_MAX_POINTS_PER_SPEC"
,ec++)) {is_valid = 0;exit(1);}

if(!parseshort(stdout,&stsvars.spec_max_spec_per_coord,"SPEC_MAX_SPEC_PER_COORD",e
c++)) {is_valid = 0;exit(1);}

if(!parseshort(stdout,&stsvars.spec_max_num_spec,"SPEC_MAX_NUM_SPEC",ec++))
{is_valid = 0;exit(1);}

if(!parseshort(stdout,&stsvars.spec_active_block,"SPEC_ACTIVE_BLOCK",ec++))
{is_valid = 0;exit(1);}
                     if(stsvars.spec_num_blocks>0)
                            stsvars.stsblocks = new
stsblock_type[stsvars.spec_num_blocks];
                     for(i=0;i<stsvars.spec_num_blocks;i++)
                     {

       if(!parseshort(stdout,&stsvars.stsblocks[i].spec_block_data_type,"SPEC_BLOC
K_DATA_TYPE",ec++)) {is_valid = 0;exit(1);}

       if(!parsestring(stdout,stsvars.stsblocks[i].spec_block_label,"SPEC_BLOCK_LA
BEL",80,ec++)) {is_valid = 0;exit(1);}

       if(!parseshort(stdout,&stsvars.stsblocks[i].spec_mode,"SPEC_MODE",ec++))
{is_valid = 0;exit(1);}
```

```
       if(!parseshort(stdout,&stsvars.stsblocks[i].spec_num_spec,"SPEC_NUM_SPEC",e
c++)) {is_valid = 0;exit(1);}

       if(!parseshort(stdout,&stsvars.stsblocks[i].spec_pt_per_spec,"SPEC_PT_PER_S
PEC",ec++)) {is_valid = 0;exit(1);}

       if(!parseshort(stdout,&stsvars.stsblocks[i].spec_avg_num_spec,"SPEC_AVG_NUM
_SPEC",ec++)) {is_valid = 0;exit(1);}

       if(!parseshort(stdout,&stsvars.stsblocks[i].spec_hex_num_spec,"SPEC_HEX_NUM
_SPEC",ec++)) {is_valid = 0;exit(1);}

       if(!parseshort(stdout,&stsvars.stsblocks[i].spec_x_num_spec,"SPEC_X_NUM_SPE
C",ec++)) {is_valid = 0;exit(1);}

       if(!parseshort(stdout,&stsvars.stsblocks[i].spec_y_num_spec,"SPEC_Y_NUM_SPE
C",ec++)) {is_valid = 0;exit(1);}

       if(!parseshort(stdout,&stsvars.stsblocks[i].spec_u_num_spec,"SPEC_U_NUM_SPE
C",ec++)) {is_valid = 0;exit(1);}

       if(!parsefloat(stdout,&stsvars.stsblocks[i].spec_spread_type,"SPEC_SPREAD_T
YPE",ec++)) {is_valid = 0;exit(1);}

       if(!parseshort(stdout,&stsvars.stsblocks[i].spec_lead_pts,"SPEC_LEAD_PTS",e
c++)) {is_valid = 0;exit(1);}

       if(!parsefloat(stdout,&stsvars.stsblocks[i].spec_settle,"SPEC_SETTLE",ec++)
) {is_valid = 0;exit(1);}

       if(!parsefloat(stdout,&stsvars.stsblocks[i].spec_vstrt,"SPEC_VSTRT",ec++))
{is_valid = 0;exit(1);}

       if(!parsefloat(stdout,&stsvars.stsblocks[i].spec_vfnsh,"SPEC_VFNSH",ec++))
{is_valid = 0;exit(1);}

       if(!parsefloat(stdout,&stsvars.stsblocks[i].spec_istrt,"SPEC_ISTRT",ec++))
{is_valid = 0;exit(1);}

       if(!parsefloat(stdout,&stsvars.stsblocks[i].spec_ifnsh,"SPEC_IFNSH",ec++))
{is_valid = 0;exit(1);}

       if(!parsefloat(stdout,&stsvars.stsblocks[i].spec_pt_del,"SPEC_PT_DEL",ec++)
) {is_valid = 0;exit(1);}

       if(!parsefloat(stdout,&stsvars.stsblocks[i].spec_zstrt,"SPEC_ZSTRT",ec++))
{is_valid = 0;exit(1);}

       if(!parsefloat(stdout,&stsvars.stsblocks[i].spec_zfnsh,"SPEC_ZFNSH",ec++))
{is_valid = 0;exit(1);}

       if(!parsefloat(stdout,&stsvars.stsblocks[i].spec_zscan,"SPEC_ZSCAN",ec++))
{is_valid = 0;exit(1);}

       if(!parsefloat(stdout,&stsvars.stsblocks[i].spec_avg_del,"SPEC_AVG_DEL",ec+
+)) {is_valid = 0;exit(1);}
```

```
        if(!parsefloat(stdout,&stsvars.stsblocks[i].spec_x_spec_inc,"SPEC_X_SPEC_INC",ec++)) {is_valid = 0;exit(1);}

        if(!parsefloat(stdout,&stsvars.stsblocks[i].spec_y_spec_inc,"SPEC_Y_SPEC_INC",ec++)) {is_valid = 0;exit(1);}

        if(!parsefloat(stdout,&stsvars.stsblocks[i].spec_r_x_cen,"SPEC_R_X_CEN",ec++)) {is_valid = 0;exit(1);}

        if(!parsefloat(stdout,&stsvars.stsblocks[i].spec_r_y_cen,"SPEC_R_Y_CEN",ec++)) {is_valid = 0;exit(1);}

        if(!parsefloat(stdout,&stsvars.stsblocks[i].spec_rect_angl,"SPEC_RECT_ANGL",ec++)) {is_valid = 0;exit(1);}

        if(!parsefloat(stdout,&stsvars.stsblocks[i].spec_u_x_cen,"SPEC_U_X_CEN",ec++)) {is_valid = 0;exit(1);}

        if(!parsefloat(stdout,&stsvars.stsblocks[i].spec_u_y_cen,"SPEC_U_Y_CEN",ec++)) {is_valid = 0;exit(1);}

        if(!parsefloat(stdout,&stsvars.stsblocks[i].spec_user_angl,"SPEC_USER_ANGL",ec++)) {is_valid = 0;exit(1);}

        if(!parsefloat(stdout,&stsvars.stsblocks[i].spec_hex_pt_sep,"SPEC_HEX_PT_SEP",ec++)) {is_valid = 0;exit(1);}

        if(!parsefloat(stdout,&stsvars.stsblocks[i].spec_h_x_cen,"SPEC_H_X_CEN",ec++)) {is_valid = 0;exit(1);}

        if(!parsefloat(stdout,&stsvars.stsblocks[i].spec_h_y_cen,"SPEC_H_Y_CEN",ec++)) {is_valid = 0;exit(1);}

        if(!parsefloat(stdout,&stsvars.stsblocks[i].spec_hex_angl,"SPEC_HEX_ANGL",ec++)) {is_valid = 0;exit(1);}

        if(!parseshort(stdout,&stsvars.stsblocks[i].spec_lock_in_der,"SPEC_LOCK_IN_DER",ec++)) {is_valid = 0;exit(1);}

        if(!parsefloat(stdout,&stsvars.stsblocks[i].spec_lock_in_range,"SPEC_LOCK_IN_RANGE",ec++)) {is_valid = 0;exit(1);}

        if(!parsefloat(stdout,&stsvars.stsblocks[i].spec_lock_in_tau,"SPEC_LOCK_IN_TAU",ec++)) {is_valid = 0;exit(1);}

        if(!parsefloat(stdout,&stsvars.stsblocks[i].spec_dith_ampl,"SPEC_DITH_AMPL",ec++)) {is_valid = 0;exit(1);}

        if(!parsefloat(stdout,&stsvars.stsblocks[i].spec_dith_freq,"SPEC_DITH_FREQ",ec++)) {is_valid = 0;exit(1);}

        if(!parseshort(stdout,&stsvars.stsblocks[i].spec_cusp_index,"SPEC_CUSP_INDEX",ec++)) {is_valid = 0;exit(1);}

        if(!parsefloat(stdout,&stsvars.stsblocks[i].spec_lock_in_point_delay,"SPEC_LOCK_IN_POINT_DELAY",ec++)) {is_valid = 0;exit(1);}
```

```
        if(!parsefloat(stdout,&stsvars.stsblocks[i].spec_lock_in_full_scale_v,"SPEC
_LOCK_IN_FULL_SCALE_V",ec++)) {is_valid = 0;exit(1);}

        if(!parseshort(stdout,&stsvars.stsblocks[i].spec_skip_endpoint_ramps,"SPEC_
SKIP_ENDPOINT_RAMPS",ec++)) {is_valid = 0;exit(1);}

        if(!parseshort(stdout,&stsvars.stsblocks[i].spec_pt_num_average,"SPEC_PT_NU
M_AVERAGE",ec++)) {is_valid = 0;exit(1);}

        if(!parsefloat(stdout,&stsvars.stsblocks[i].spec_pt_avg_delay,"SPEC_PT_AVG_
DELAY",ec++)) {is_valid = 0;exit(1);}

        if(!parseshort(stdout,&stsvars.stsblocks[i].spec_potentiometry,"SPEC_POTENT
IOMETRY",ec++)) {is_valid = 0;exit(1);}

        if(!parseshort(stdout,&stsvars.stsblocks[i].spec_potentio_use_samp_intv,"SP
EC_POTENTIO_USE_SAMP_INTV",ec++)) {is_valid = 0;exit(1);}

        if(!parsefloat(stdout,&stsvars.stsblocks[i].spec_potentio_samp_interval,"SP
EC_POTENTIO_SAMP_INTERVAL",ec++)) {is_valid = 0;exit(1);}

        if(!parsefloat(stdout,&stsvars.stsblocks[i].spec_potentio_lower_rail_v,"SPE
C_POTENTIO_LOWER_RAIL_V",ec++)) {is_valid = 0;exit(1);}

        if(!parsefloat(stdout,&stsvars.stsblocks[i].spec_potentio_upper_rail_v,"SPE
C_POTENTIO_UPPER_RAIL_V",ec++)) {is_valid = 0;exit(1);}

        if(!parseshort(stdout,&stsvars.stsblocks[i].spec_potentio_lower_rail_fixed,
"SPEC_POTENTIO_LOWER_RAIL_FIXED",ec++)) {is_valid = 0;exit(1);}

        if(!parseshort(stdout,&stsvars.stsblocks[i].spec_potentio_upper_rail_fixed,
"SPEC_POTENTIO_UPPER_RAIL_FIXED",ec++)) {is_valid = 0;exit(1);}

        if(!parseshort(stdout,&stsvars.stsblocks[i].spec_initial_v_use_scan_value,"
SPEC_INITIAL_V_USE_SCAN_VALUE",ec++)) {is_valid = 0;exit(1);}

        if(!parseshort(stdout,&stsvars.stsblocks[i].spec_initial_i_use_scan_value,"
SPEC_INITIAL_I_USE_SCAN_VALUE",ec++)) {is_valid = 0;exit(1);}

        if(!parseshort(stdout,&stsvars.stsblocks[i].spec_initial_trans_together,"SP
EC_INITIAL_TRANS_TOGETHER",ec++)) {is_valid = 0;exit(1);}

        if(!parseshort(stdout,&stsvars.stsblocks[i].spec_initial_trans_i_first,"SPE
C_INITIAL_TRANS_I_FIRST",ec++)) {is_valid = 0;exit(1);}

        if(!parsefloat(stdout,&stsvars.stsblocks[i].spec_initial_v,"SPEC_INITIAL_V"
,ec++)) {is_valid = 0;exit(1);}

        if(!parsefloat(stdout,&stsvars.stsblocks[i].spec_initial_v_trans_time,"SPEC
_INITIAL_V_TRANS_TIME",ec++)) {is_valid = 0;exit(1);}

        if(!parsefloat(stdout,&stsvars.stsblocks[i].spec_initial_i,"SPEC_INITIAL_I"
,ec++)) {is_valid = 0;exit(1);}

        if(!parsefloat(stdout,&stsvars.stsblocks[i].spec_initial_i_trans_time,"SPEC
_INITIAL_I_TRANS_TIME",ec++)) {is_valid = 0;exit(1);}
```

```
       if(!parsefloat(stdout,&stsvars.stsblocks[i].spec_cusp_voltage,"SPEC_CUSP_VO
LTAGE",ec++)) {is_valid = 0;exit(1);}

       if(!parsefloat(stdout,&stsvars.stsblocks[i].spec_delay_before_atod,"SPEC_DE
LAY_BEFORE_ATOD",ec++)) {is_valid = 0;exit(1);}

       if(!parseshort(stdout,&stsvars.stsblocks[i].spec_set_initial_ds,"SPEC_SET_I
NITIAL_DS",ec++)) {is_valid = 0;exit(1);}

       if(!parsefloat(stdout,&stsvars.stsblocks[i].spec_initial_ds,"SPEC_INITIAL_D
S",ec++)) {is_valid = 0;exit(1);}

       if(!parsefloat(stdout,&stsvars.stsblocks[i].spec_initial_ds_trans_time,"SPE
C_INITIAL_DS_TRANS_TIME",ec++)) {is_valid = 0;exit(1);}

       if(!parseshort(stdout,&stsvars.stsblocks[i].spec_current_channel_0_on,"SPEC
_CURRENT_CHANNEL_0_ON",ec++)) {is_valid = 0;exit(1);}

       if(!parseshort(stdout,&stsvars.stsblocks[i].spec_current_channel_1_on,"SPEC
_CURRENT_CHANNEL_1_ON",ec++)) {is_valid = 0;exit(1);}

       if(!parseshort(stdout,&stsvars.stsblocks[i].spec_current_channel_2_on,"SPEC
_CURRENT_CHANNEL_2_ON",ec++)) {is_valid = 0;exit(1);}

       if(!parseshort(stdout,&stsvars.stsblocks[i].spec_current_channel_3_on,"SPEC
_CURRENT_CHANNEL_3_ON",ec++)) {is_valid = 0;exit(1);}

       if(!parseshort(stdout,&stsvars.stsblocks[i].spec_current_average_mode,"SPEC
_CURRENT_AVERAGE_MODE",ec++)) {is_valid = 0;exit(1);}

       if(!parseshort(stdout,&stsvars.stsblocks[i].spec_dither_only,"SPEC_DITHER_O
NLY",ec++)) {is_valid = 0;exit(1);}

       if(!parseshort(stdout,&stsvars.stsblocks[i].spec_leave_dither_on,"SPEC_LEAV
E_DITHER_ON",ec++)) {is_valid = 0;exit(1);}
                                  stsvars.stsblocks[i].cols = new
short[stsvars.stsblocks[i].spec_num_spec];
                                  stsvars.stsblocks[i].rows = new
short[stsvars.stsblocks[i].spec_num_spec];
                                  stsvars.stsblocks[i].stsdata = new
float**[stsvars.stsblocks[i].spec_num_spec];

       for(j=0;j<stsvars.stsblocks[i].spec_num_spec;j++)
                                  {
                                         spc = 1;

       if(stsvars.stsblocks[i].spec_potentiometry &&
(stsvars.stsblocks[i].spec_mode==1 || stsvars.stsblocks[i].spec_mode==4))
                                                spc = 2;
                                         if(stsvars.stsblocks[i].spec_lock_in_der)
                                                spc = 2;
                                         stsvars.stsblocks[i].max_spec_per_coord =
spc;

                                         stsvars.stsblocks[i].stsdata[j] = new
float*[spc];

                                         for(k=0;k<spc;k++)
                                         {
```

```
                                                stsvars.stsblocks[i].stsdata[j][k]
= new float[stsvars.stsblocks[i].spec_pt_per_spec];
                                          }
                                   }
                     }
                }
                else if(strncmp(keyword,"CITS    ",8)==0)  // CITS DATA
                {
                        //printf("switch CITS\n");

if(!parseshort(stdout,&citsvars.spec_mode,"SPEC_MODE",ec++)) {is_valid =
0;exit(1);}

if(!parseshort(stdout,&citsvars.cits_num_buff,"CITS_NUM_BUFF",ec++)) {is_valid =
0;exit(1);}

if(!parseshort(stdout,&citsvars.cits_oversample_mult,"CITS_OVERSAMPLE_MULT",ec++))
{is_valid = 0;exit(1);}
                     if(!parsefloat(stdout,&citsvars.spec_vstrt,"SPEC_VSTRT",ec++))
{is_valid = 0;exit(1);}
                     if(!parsefloat(stdout,&citsvars.spec_vfnsh,"SPEC_VFNSH",ec++))
{is_valid = 0;exit(1);}

       if(!parsefloat(stdout,&citsvars.spec_pt_del,"SPEC_PT_DEL",ec++)) {is_valid
= 0;exit(1);}

if(!parseshort(stdout,&citsvars.spec_avg_num_spec,"SPEC_AVG_NUM_SPEC",ec++))
{is_valid = 0;exit(1);}

       if(!parsefloat(stdout,&citsvars.spec_avg_del,"SPEC_AVG_DEL",ec++))
{is_valid = 0;exit(1);}

       if(!parsefloat(stdout,&citsvars.spec_lock_in_point_delay,"SPEC_LOCK_IN_POIN
T_DELAY",ec++)) {is_valid = 0;exit(1);}
                     citsvars.citsbuffs = new
citsbuff_type[citsvars.cits_num_buff];
                     for(i=0;i<citsvars.cits_num_buff;i++)
                     {

       if(!parsefloat(stdout,&citsvars.citsbuffs[i].cits_bias,"CITS_BIAS",ec++))
{is_valid = 0;exit(1);}
                     }
                }
                else if(strncmp(keyword,"CITS_1  ",8)==0)  // MORE CITS DATA
                {
                        //printf("switch CITS_1\n");

if(!parseshort(stdout,&citsvars.spec_dither_only,"SPEC_DITHER_ONLY",ec++))
{is_valid = 0;exit(1);}

if(!parseshort(stdout,&citsvars.cits_topo_average,"CITS_TOPO_AVERAGE",ec++))
{is_valid = 0;exit(1);}

if(!parseshort(stdout,&citsvars.cits_topo_num_average,"CITS_TOPO_NUM_AVERAGE",ec++
)) {is_valid = 0;exit(1);}

if(!parseshort(stdout,&citsvars.cits_spec_fit,"CITS_SPEC_FIT",ec++)) {is_valid =
0;exit(1);}
```

```
if(!parseshort(stdout,&citsvars.cits_spec_fit_pts,"CITS_SPEC_FIT_PTS",ec++))
{is_valid = 0;exit(1);}
                }
                else if(strncmp(keyword,"CITS_2  ",8)==0)  // MORE CITS DATA
                {
                        //printf("switch CITS_2\n");

if(!parseshort(stdout,&citsvars.cits_num_blocks,"CITS_NUM_BLOCKS",ec++)) {is_valid
= 0;exit(1);}

if(!parseshort(stdout,&citsvars.cits_analysis_block,"CITS_ANALYSIS_BLOCK",ec++))
{is_valid = 0;exit(1);}

if(!parseshort(stdout,&citsvars.cits_display_block,"CITS_DISPLAY_BLOCK",ec++))
{is_valid = 0;exit(1);}
                     citsvars.citsblocks = new
citsblock_type[citsvars.cits_num_blocks];
                     for(i=0;i<citsvars.cits_num_blocks;i++)
                     {

if(!parseshort(stdout,&citsvars.citsblocks[i].cits_block_mode,"CITS_BLOCK_MODE",ec
++)) {is_valid = 0;exit(1);}
                     }
                }
                else if(strncmp(keyword,"CITS_3  ",8)==0)  // NEW CITS VARIABLES
FOR ARIOUS SPECTROSCOPY MODES
                {
                        //printf("switch CITS_3\n");
                     if(!parsefloat(stdout,&citsvars.spec_istrt,"SPEC_ISTRT",ec++))
{is_valid = 0;exit(1);}
                     if(!parsefloat(stdout,&citsvars.spec_ifnsh,"SPEC_IFNSH",ec++))
{is_valid = 0;exit(1);}
                     if(!parsefloat(stdout,&citsvars.spec_zstrt,"SPEC_ZSTRT",ec++))
{is_valid = 0;exit(1);}
                     if(!parsefloat(stdout,&citsvars.spec_zfnsh,"SPEC_ZFNSH",ec++))
{is_valid = 0;exit(1);}
                     if(!parsefloat(stdout,&citsvars.spec_zscan,"SPEC_ZSCAN",ec++))
{is_valid = 0;exit(1);}
                }
                else if(strncmp(keyword,"CITS_4  ",8)==0)  // NEW CITS VARIABLES
FOR ARIOUS SPECTROSCOPY MODES
                {
                        //printf("switch CITS_4\n");
                     for(i=0;i<citsvars.cits_num_blocks;i++)
                     {

if(!parseshort(stdout,&citsvars.citsblocks[i].cits_block_data_type,"CITS_BLOCK_DAT
A_TYPE",ec++)) {is_valid = 0;exit(1);}

       if(!parsestring(stdout,citsvars.citsblocks[i].cits_block_text,"CITS_BLOCK_T
EXT",80,ec++)) {is_valid = 0;exit(1);}
                     }
                }
                else if(strncmp(keyword,"CITS_5  ",8)==0)  // CITS TEMPERATURE
LOGGING VARIABLES AND ARRAY
                {
                        //printf("switch CITS_5\n");
```

```
if(!parseshort(stdout,&citsvars.cits_log_temperature,"CITS_LOG_TEMPERATURE",ec++))
{is_valid = 0;exit(1);}
                     if(citsvars.cits_log_temperature)
                     {

if(!parseshort(stdout,&citsvars.cits_temperature_pts,"CITS_TEMPERATURE_PTS",ec++))
{is_valid = 0;exit(1);}

if(!parseshort(stdout,&citsvars.cits_temperature_pts,"CITS_TEMPERATURE_ATOD_CHANNE
L",ec++)) {is_valid = 0;exit(1);}

       if(!parsefloat(stdout,&citsvars.cits_temperature_log_interval,"CITS_TEMPERA
TURE_LOG_INTERVAL",ec++)) {is_valid = 0;exit(1);}

       if(!parsefloat(stdout,&citsvars.cits_temperature_log_sampl_dt,"CITS_TEMPERA
TURE_LOG_SAMPL_DT",ec++)) {is_valid = 0;exit(1);}

       if(!parsefloat(stdout,&citsvars.cits_temperature_conv_factor,"CITS_TEMPERAT
URE_CONV_FACTOR",ec++)) {is_valid = 0;exit(1);}
                            if(citsvars.cits_temperature_pts>0)
                            {
                                   if(citsvars.cits_temperature_array==NULL)
                                          citsvars.cits_temperature_array = new
char[4*citsvars.cits_temperature_pts];

       if(!parsestring(NULL,citsvars.cits_temperature_array,"CITS_TEMPERATURE_ARRA
Y",4*citsvars.cits_temperature_pts,ec++)) {is_valid = 0;exit(1);}
                            }
                     }
                }
                else if(strncmp(keyword,"CITS_6  ",8)==0)  // CITS RAW DATA
PROCESSING PARAMETERS
                {
                        //printf("switch CITS_6\n");

if(!parseshort(stdout,&citsvars.spec_dither_only,"SPEC_DITHER_ONLY",ec++))
{is_valid = 0;exit(1);}

if(!parseshort(stdout,&citsvars.cits_topo_average,"CITS_TOPO_AVERAGE",ec++))
{is_valid = 0;exit(1);}

if(!parseshort(stdout,&citsvars.cits_topo_num_average,"CITS_TOPO_NUM_AVERAGE",ec++
)) {is_valid = 0;exit(1);}
                     for(i=0;i<citsvars.cits_num_blocks;i++)
                     {

if(!parseshort(stdout,&citsvars.citsblocks[i].cits_spec_raw_deglitch,"CITS_SPEC_RA
W_DEGLITCH",ec++)) {is_valid = 0;exit(1);}

if(!parseshort(stdout,&citsvars.citsblocks[i].cits_spec_raw_glitch_threshold,"CITS
_SPEC_RAW_GLITCH_THRESHOLD",ec++)) {is_valid = 0;exit(1);}

if(!parseshort(stdout,&citsvars.citsblocks[i].cits_spec_raw_smooth,"CITS_SPEC_RAW_
SMOOTH",ec++)) {is_valid = 0;exit(1);}

if(!parseshort(stdout,&citsvars.citsblocks[i].cits_spec_raw_smooth_order,"CITS_SPE
C_RAW_SMOOTH_ORDER",ec++)) {is_valid = 0;exit(1);}
```

```
if(!parseshort(stdout,&citsvars.citsblocks[i].cits_spec_raw_smooth_n_fit,"CITS_SPE
C_RAW_SMOOTH_N_FIT",ec++)) {is_valid = 0;exit(1);}
                    }

       if(!parsestring(NULL,NULL,"CITS_6_BUFF",6+10*citsvars.cits_num_blocks,ec++)
) {is_valid = 0;exit(1);}
                }
                else if(strncmp(keyword,"IMG_BUF ",8)==0)  // IMAGE BUFFERS
                {
                        //printf("switch IMG_BUF\n");
                    if(scanvars.xnum<0 || scanvars.ynum<0)
                    {
                           //printf("Parse Error: Required values are not defined
(xnum, or ynum)\n");
                           return;
                    }
                    for(i=0;i<num_buffers;i++)
                    {
                           if(buffer_data[i].image_buffer_data_type==0)    // Int
values
                           {
                                  buffer_data[i].intdata = new
short*[scanvars.xnum];
                                  for(j=0;j<scanvars.xnum;j++)
                                         buffer_data[i].intdata[j] = new
short[scanvars.ynum];
                           }
                           else if(buffer_data[i].image_buffer_data_type==1)
       // Real values
                           {
                                  buffer_data[i].realdata = new
float*[scanvars.xnum];
                                  for(j=0;j<scanvars.xnum;j++)
                                         buffer_data[i].realdata[j] = new
float[scanvars.ynum];
                           }
                           for(x=0;x<scanvars.xnum;x++)
                           {
                                  for(y=0;y<scanvars.ynum;y++)
                                  {

       if(buffer_data[i].image_buffer_data_type==0)    // Integer values
                                         {

       if(!parseshort(NULL,&(buffer_data[i].intdata[y][x]),"zval",ec++)) {is_valid
= 0;exit(1);}
                                         }
                                         else
if(buffer_data[i].image_buffer_data_type==1)    // Real values
                                         {

       if(!parsefloat(NULL,&(buffer_data[i].realdata[y][x]),"rval",ec++))
{is_valid = 0;exit(1);}
                                         }
                                  }
                           }
                    }
```

```
                     if(citsvars.valid_cits)
                     {
                            for(i=0;i<citsvars.cits_num_blocks;i++)
                            {

                                if(citsvars.citsblocks[i].cits_block_data_type==0)
// Int values
                                {
                                        citsvars.citsblocks[i].intdata = new
short*[scanvars.xnum];
                                        for(j=0;j<scanvars.xnum;j++)
                                                citsvars.citsblocks[i].intdata[j]
= new short[scanvars.ynum];
                                }
                                else
if(citsvars.citsblocks[i].cits_block_data_type==1)       // Real values
                                {
                                        citsvars.citsblocks[i].realdata = new
float*[scanvars.xnum];
                                        for(j=0;j<scanvars.xnum;j++)
                                                citsvars.citsblocks[i].realdata[j]
= new float[scanvars.ynum];
                                }
                                for(x=0;x<scanvars.xnum;x++)
                                {
                                        for(y=0;y<scanvars.ynum;y++)
                                        {

if(citsvars.citsblocks[i].cits_block_data_type==0)    // Integer values

       {

if(!parseshort(NULL,&(citsvars.citsblocks[i].intdata[y][x]),"cits_zval",ec++))
{is_valid = 0;exit(1);}

       }

       else if(citsvars.citsblocks[i].cits_block_data_type==1)       // Real
values

       {

       if(!parsefloat(NULL,&(citsvars.citsblocks[i].realdata[y][x]),"cits_rval",ec
++)) {is_valid = 0;exit(1);}

       }
                                                                             }
                                }



                            }
                     }
                }
                else if(strncmp(keyword,"SPC_MDAT",8)==0)  // OUTPUT 32-BIT
SPECTROSCOPY DATA
                {
                        //printf("switch SPC_MDAT\n");
```

```
                     for(i=0;i<stsvars.spec_num_blocks;i++)
                     {
                            // Read columns
                            for(j=0;j<stsvars.stsblocks[i].spec_num_spec;j++)
                            {

       if(!parseshort(stdout,&stsvars.stsblocks[i].cols[j],"sts_column",ec++))
{is_valid = 0;exit(1);}
                            }
                            // Read rows
                            for(j=0;j<stsvars.stsblocks[i].spec_num_spec;j++)
                            {

       if(!parseshort(stdout,&stsvars.stsblocks[i].rows[j],"sts_row",ec++))
{is_valid = 0;exit(1);}
                            }
                     }
                     for(i=0;i<stsvars.spec_num_blocks;i++)
                     {
                            for(j=0;j<stsvars.stsblocks[i].spec_num_spec;j++)
                            {

       for(k=0;k<stsvars.stsblocks[i].spec_pt_per_spec;k++)
                                   {

       if(!parsefloat(NULL,&stsvars.stsblocks[i].stsdata[j][0][k],"rval",ec++))
{is_valid = 0;exit(1);}
                                   }

                                   if(stsvars.stsblocks[i].max_spec_per_coord==2)
                                   {

       for(k=0;k<stsvars.stsblocks[i].spec_pt_per_spec;k++)
                                          {

       if(!parsefloat(NULL,&stsvars.stsblocks[i].stsdata[j][1][k],"rval",ec++))
{is_valid = 0;exit(1);}
                                          }
                                   }
                            }
                     }
                }



              else if(strncmp(keyword,"EOF     ",8)==0)
              {
                     //printf("switch EOF\n");
              }
              else
              {
                     //printf("Keyword Parse Error: %s\n", keyword);
                     return;
              }
       }


       // Close the file
```

```
	fclose(fp);
}

stmfile::~stmfile()
{
	if(filename!=NULL)
		delete [] filename;
	if(colormap_arr.maps!=NULL)
		delete [] colormap_arr.maps;
	if(stsvars.stsblocks!=NULL)
	{
		for(i=0;i<stsvars.spec_num_blocks;i++)
		{
			if(stsvars.stsblocks[i].cols!=NULL)
				delete [] stsvars.stsblocks[i].cols;
			if(stsvars.stsblocks[i].rows!=NULL)
				delete [] stsvars.stsblocks[i].rows;
			if(stsvars.stsblocks[i].stsdata!=NULL)
			{
				for(k=0;k<stsvars.stsblocks[i].spec_num_spec;k++)
				{

	for(j=0;j<stsvars.stsblocks[i].max_spec_per_coord;j++)
					{
						delete []
stsvars.stsblocks[i].stsdata[k][j];
					}
					delete [] stsvars.stsblocks[i].stsdata[k];
				}
				delete [] stsvars.stsblocks[i].stsdata;
			}
		}
		delete [] stsvars.stsblocks;
	}
	if(buffer_data!=NULL)
	{
		for(i=0;i<num_buffers;i++)
			if(buffer_data->realdata!=NULL)
			{
				for(j=0;j<scanvars.xnum;j++)
					delete [] (buffer_data->realdata)[j];
				delete [] buffer_data->realdata;
			}
			if(buffer_data->intdata!=NULL)
			{
				for(j=0;j<scanvars.xnum;j++)
					delete [] (buffer_data->intdata)[j];
				delete [] buffer_data->intdata;
			}
	}
	delete [] buffer_data;
	delete [] keyword;
}

int parsestring(FILE *out, char *outchar, char *name, int length, int errorcode)
{
	int i,x;
```

```
#ifdef VERBOSE
	if(out!=NULL)
		fprintf(out,"%s: [", name);
	fflush(out);
#endif

	for(i=0;i<length;i++)
	{
		x = fgetc(fp);
		if(x==EOF)
		{
			return 0;
		}

		if(outchar!=NULL)
			outchar[i] = x;

#ifdef VERBOSE
		if(out!=NULL)
			fprintf(out,"%c",x);
#endif
	}
#ifdef VERBOSE
	if(out!=NULL)
		fprintf(out,"]\n");
#endif

	return 1;
}

int parseshort(FILE *out, short *siout, char *name, int errorcode)
{
	int x;
	short si;

#ifdef VERBOSE
	if(out!=NULL)
		fprintf(out,"%s: [", name);
#endif

	x = fread(&si,sizeof(short),1,fp);
	if(x<1)
	{
		return 0;
	}

#ifdef VERBOSE
	if(out!=NULL)
	{
		fprintf(out,"%i",si);
		fprintf(out,"]\n");
	}
#endif

	if(siout!=NULL)
		*siout = si;

	return 1;
```

```
}

int parseint(FILE *out, int *iout, char *name, int errorcode)
{
	int x;
	int i;

#ifdef VERBOSE
	if(out!=NULL)
		fprintf(out,"%s: [", name);
	fflush(out);
#endif

	x = fread(&i,sizeof(int),1,fp);
	if(x<1)
	{
		return 0;
	}
#ifdef VERBOSE
	if(out!=NULL)
	{
		fprintf(out,"%x",i);
		fprintf(out,"]\n");
	}
#endif

	if(iout!=NULL)
		*iout = i;

	return 1;
}

int parsefloat(FILE *out, float *floatout, char *name, int errorcode)
{
	int x;
	float i;


#ifdef VERBOSE
	if(out!=NULL)
		fprintf(out,"%s: [", name);
	fflush(out);
#endif

	x = fread(&i,sizeof(float),1,fp);
	if(x<1)
	{
		return 0;
	}
#ifdef VERBOSE
	if(out!=NULL)
	{
		fprintf(out,"%E",i);
		fprintf(out,"]\n");
	}
#endif

	if(floatout!=NULL)
```

```
            *floatout = i;

      return 1;
}

int parsekeyword(FILE *out, char *keyword, int errorcode)
{
        int i;

#ifdef VERBOSE
      if(out!=NULL)
              fprintf(out,"%KEY_WORD: [");
      fflush(out);
#endif

        for(i=0;i<8;i++)
        {
                keyword[i] = fgetc(fp);
                if(keyword[i]==EOF)
                {
                        return 0;
                }
#ifdef VERBOSE
             if(out!=NULL)
                      fprintf(out,"%c",keyword[i]);
#endif
        }
#ifdef VERBOSE
      if(out!=NULL)
              fprintf(out,"]\n");
#endif

        return 1;
}
```